Recirculation zone developing downstream of an expansion in a shallow open-channel flow

Lei Han

N° d'ordre 2015-ISAL–0005 Année 2015

THÈSE

Recirculation à l'aval de l'élargissement brusque d'un écoulement à surface libre peu profond

Présentée devant

l'Institut National des Sciences Appliquées de Lyon

pour obtenir

le GRADE DE DOCTEUR

École doctorale :

Mécanique, Énergétique, Génie Civil, Acoustique

Spécialité :

MÉCANIQUE des FLUIDES

par

Lei HAN

Soutenue le 05 Février devant la Commission d'examen

Jury

M. DENIS DARTUS	Professeur (INPT, Toulouse)	Rapporteur
M. JOSÉ VAZQUEZ	Professeur (ENGEES, Strasbourg)	Rapporteur
M. RICHARD PERKINS	Professeur (Ecole Centrale de Lyon)	Président
M. SÉBASTIEN PROUST	Chercheur (IRSTEA, Lyon)	Examinateur
M. SÉBASTIEN ROUX	I.R. (CNR, Lyon)	Examinateur
M. EMMANUEL MIGNOT	Maître de Conférences (INSA, Lyon)	Co-directeur de thèse (Invité)
M. NICOLAS RIVIÈRE	Professeur (INSA, Lyon)	Directeur de thèse

LMFA - UMR CNRS 5509 - INSA de Lyon
20, avenue Albert Einstein, 69621 Villeurbanne Cedex (FRANCE)

INSA Direction de la Recherche - Ecoles Doctorales – Quinquennal 2011-2015

SIGLE	ECOLE DOCTORALE	NOM ET COORDONNEES DU RESPONSABLE
CHIMIE	**CHIMIE DE LYON** **http://www.edchimie-lyon.fr** Sec : Renée EL MELHEM Bat Blaise Pascal 3e etage 04 72 43 80 46 Insa : R. GOURDON	M. Jean Marc LANCELIN Université de Lyon – Collège Doctoral Bât ESCPE 43 bd du 11 novembre 1918 69622 VILLEURBANNE Cedex Tél : 04.72.43 13 95 directeur@edchimie-lyon.fr
E.E.A.	**ELECTRONIQUE, ELECTROTECHNIQUE, AUTOMATIQUE** **http://edeea.ec-lyon.fr** Sec : M.C. HAVGOUDOUKIAN eea@ec-lyon.fr	M. Gérard SCORLETTI Ecole Centrale de Lyon 36 avenue Guy de Collongue 69134 ECULLY Tél : 04.72.18 60.97 Fax : 04 78 43 37 17 Gerard.scorletti@ec-lyon.fr
E2M2	**EVOLUTION, ECOSYSTEME, MICROBIOLOGIE, MODELISATION** **http://e2m2.universite-lyon.fr** Sec : Safia AIT CHALAL Bat Darwin - UCB Lyon 1 04.72.43.28.91 Insa : H. CHARLES	Mme Gudrun BORNETTE CNRS UMR 5023 LEHNA Université Claude Bernard Lyon 1 Bât Forel 43 bd du 11 novembre 1918 69622 VILLEURBANNE Cédex Tél : 06.07.53.89.13 e2m2@ univ-lyon1.fr
EDISS	**INTERDISCIPLINAIRE SCIENCES-SANTE** **http://www.ediss-lyon.fr** Sec : Safia AIT CHALAL Hôpital Louis Pradel - Bron 04 72 68 49 09 Insa : M. LAGARDE Safia.ait-chalal@univ-lyon1.fr	Mme Emmanuelle CANET-SOULAS INSERM U1060, CarMeN lab, Univ. Lyon 1 Bâtiment IMBL 11 avenue Jean Capelle INSA de Lyon 696621 Villeurbanne Tél : 04.72.68.49.09 Fax :04 72 68 49 16 Emmanuelle.canet@univ-lyon1.fr
INFOMATHS	**INFORMATIQUE ET MATHEMATIQUES** **http://infomaths.univ-lyon1.fr** Sec :Renée EL MELHEM Bat Blaise Pascal 3e etage infomaths@univ-lyon1.fr	Mme Sylvie CALABRETTO LIRIS – INSA de Lyon Bat Blaise Pascal 7 avenue Jean Capelle 69622 VILLEURBANNE Cedex Tél : 04.72. 43. 80. 46 Fax 04 72 43 16 87 Sylvie.calabretto@insa-lyon.fr
Matériaux	**MATERIAUX DE LYON** **http://ed34.universite-lyon.fr** Sec : M. LABOUNE PM : 71.70 –Fax : 87.12 Bat. Saint Exupéry Ed.materiaux@insa-lyon.fr	M. Jean-Yves BUFFIERE INSA de Lyon MATEIS Bâtiment Saint Exupéry 7 avenue Jean Capelle 69621 VILLEURBANNE Cedex Tél : 04.72.43 83 18 Fax 04 72 43 85 28 Jean-yves.buffiere@insa-lyon.fr
MEGA	**MECANIQUE, ENERGETIQUE, GENIE CIVIL, ACOUSTIQUE** **http://mega.universite-lyon.fr** Sec : M. LABOUNE PM : 71.70 –Fax : 87.12 Bat. Saint Exupéry mega@insa-lyon.fr	M. Philippe BOISSE INSA de Lyon Laboratoire LAMCOS Bâtiment Jacquard 25 bis avenue Jean Capelle 69621 VILLEURBANNE Cedex Tél :04.72 .43.71.70 Fax : 04 72 43 72 37 Philippe.boisse@insa-lyon.fr
ScSo	**ScSo*** **http://recherche.univ-lyon2.fr/scso/** Sec : Viviane POLSINELLI Brigitte DUBOIS Insa : J.Y. TOUSSAINT	Mme Isabelle VON BUELTZINGLOEWEN Université Lyon 2 86 rue Pasteur 69365 LYON Cedex 07 Tél : 04.78.77.23.86 Fax : 04.37.28.04.48 viviane.polsinelli@univ-lyon2.fr

*ScSo : Histoire, Géographie, Aménagement, Urbanisme, Archéologie, Science politique, Sociologie, Anthropologie

Remerciements

Dans cette partie individuelle, je voudrais rédiger en français et aussi chinois en raison de remercier les amis français et chinois qui me soutient pendant 3 ans et demi laquelle a commencé par Septembre, 2011.
Je tiens à exprimer mes plus vifs remerciements à Nicolas RIVIÈRE qui fut pour moi un directeur de thèse attentif et disponible. Il est un professeur rigoureux et responsable. Il a proposé des idées pour les manipulation et le réduction de thèse. Surtout, comme un ami, il est gentil et sympathique quelquefois aussi humoriste. Emmanuel MIGNOT comme le co-directeur m'aide beaucoup sur le programmation et me pousser toujours avance de la thèse. Pendant le période de son travail en Chili, j'ai reçu quand mÍme énorme recommandations de la thèse et les articles. Merci a toi!
Évidemment, je vais remercier les deux rapporteurs de ma thèse : Denis DARTUS et José VAZQUEZ. Leur rigueurs et les avis pertinents ont amélioré la qualité de la thèse. J'ai également eu la chance de compter dans mon jury: Richard PERKINS , Sébastien PROUST et Sébastien ROUX.
Dans notre laboratoire, les gens sont gentils et m'aident cordialement. Dans ma deuxième année, Marc CHATELAIN fait son Master chez nous. J'ai bénéficié les résultats numérique dans ma thèse je lui remercie pour son partage. Je voudrais merci à les renseignant dans notre LMFA c'est à dire Gilbert TRAVIN, Jean-Yves CHAMPAGNE, Valéry BOTTON, Mahmoud El Hajem, Cyril MAUGER et Serge SIMOËNS. Le voisin de mon bureau est Daniel HENRY, Directeur de Recherche de CNRS, je lui remercie aussi pour m'accompagne travail pendant 2 ans. Merci à notre technicien Cedric MARMOUNIER pour ses belles productions dans les manipulations.
Les thésards de LMFA sont dynamiques, je n'oublie pas de la première diner de fromage fondu avec Yann PELTIER, Pierre VALIORGUE, Nicolas SOUZY et Trong DAÏ, ils ont me renseigne la commence de vie de la thésard en France. En plus, les étudiants entrain de finir leur thèse comme Wei CAI, Gaby LAUNAY et Virgile TAVERNIER ont partagé leur techniques avec moi et j'apprends plus que les connaissance dans le livre. Il y a un chercheur de IRSTEA qui m'a renseigné les détails de manipulations au début de mon arriver, il est Sébastien PROUST, merci beaucoup pour d'être un jury de ma soutenance en même temp.
Dans la côté du bourse, je veux remercier CSC (China Scholarship Council) et le programme "UT-INSA" pour me soutenir financement.

在这特别的一段文字里， 我要感谢我的妻子，**蒋晓璐**。在法国读博士的 42 个月里，是你，在我最需要关怀和鼓励的时候站在了我的身边，不能想象没有你的三年将是怎样的黑暗和无助，感谢上天在里昂把你赐给了我，让我的生活中永远充满着光明和希望！我爱你！

Abstract

The present research focuses on the recirculation zone developing downstream of an expansion in a shallow open-channel flow with a specific attention on its length. The work consists of combined experimental and numerical approaches.

The dimensional analysis and previous studies permit to express the dimensionless recirculation length as a function of 3 parameters: the friction number S, the ratio between the water depth and the expansion step h/d and the geometrical aspect ratio R_b. Nevertheless, varying either S or h/d on the experimental set-up without affecting the other is a complicated task which was not performed by previous studies. Following this approach permitted to obtain an unexpected bell shape for the L/d=f(S) curve, differing form the literature results.

In order to improve the approach and vary S and h/d independently, a 3D numerical campaign was performed and proved that L/d actually depends both on S and h/d parameters and that the bell shape is in fact the consequence of the opposite influence of both parameters.

Moreover, the precise experimental analysis of the mixing layer at the frontier between the main flow and the recirculation for flows with different S and h/d values showed that the recirculation length is governed by the lateral confinement due to the reattachment wall and the size of the eddies present in the mixing layer.

Hence, an integral approach is adopted, using balances of momentum and of energy at the whole flow scale, showing: i) that the shear force exerted along the mixing layer is negligible compared to the other forces and ii) that the meaning of S parameter is to quantify the intensity of the bottom friction of the whole flow on these balance. The following regimes can thus be encountered: i) according to the bed friction S values, the flow can be non-frictional (small S) or frictional (large S) and ii) according to the relative water depth, the flow can be vertically unconfined (large h/d) or confined (small h/d).

An empirical correlation permitting to estimate the recirculation length L/d as a function of S, R_b and h/d is finally obtained and appears to fairly fit the numerical calculations and experimental measurements.

KEY WORD: Shallow flows, Open-channel expansion, Recirculation, Mixing layer, Backward-facing step, Experiments, Numerical simulations, Hydraulic models

Résumé

Le travail présenté ici a pour objet l'étude de la zone de recirculation qui se développe à l'aval d'un élargissement brusque ayant lieu dans un canal à surface libre, avec une attention particulière portée sur la longueur de recirculation. Ce travail consiste en une approche combinée expérimentale et numérique.

L'analyse dimensionnelle ainsi que les travaux préliminaires antérieurs à cette thèse montrent que la longueur de recirculation adimensionnée dépend de 3 paramètres que sont : le nombre de frottement S, la hauteur d'eau adimensionnée par la taille de l'élargissement h/d et enfin le rapport géométrique de l'élargissement R_b. Cependant, faire varier dans les expériences S ou h/d sans affecter l'autre paramètre s'avère être une tâche très délicate qui a été négligée dans les études précédentes. En utilisant cette même approche, les résultats présentés ici font état d'une forme de cloche très inattendue de la courbe : $L/d = f(S)$. Ces résultats sont en fort désaccord avec ceux de la litérature.

Afin d'améliorer notre approche et de faire varier S et h/d indépendament, une campagne de modélisation numérique 3D est menée et prouve que L/d dépend en fait des deux paramètres considérés S et h/d et que la forme de cloche résulte des influences opposées de ces deux paramètres.

De plus, l'analyse de la couche de mélange qui prend place entre la zone de recirculation et l'écoulement principal, mesurée expérimentalement pour 4 écoulements à différentes valeurs de S et h/d montre que la longueur de la zone de recirculation est gouvernée par le confinement latéral dû à la paroi latérale et à la taille des cellules turbulentes advectée le long de la couche de mélange.

Pour aller plus loin, les bilans de quantité de mouvement et d'énergie à l'échelle de l'écoulement dans son ensemble montrent que i) la force de cisaillement exercée le long de la couche de mélange est négligeable par rapport aux autres forces mises en jeu et ii) que la réelle signification de S est de quantifier l'intensité du frottement du fond à l'échelle de l'écoulement global intervenant dans ces bilans. Les différents régimes d'écoulement qui peuvent être rencontrés dépendent donc: i) selon la valeur du nombre de frottement S l'écoulement peut être frictionnel (S élevé) ou non-frictionnel (S faible) et ii) selon la valeur de la hauteur d'eau adimensionnelle, l'écoulement peut être confiné verticalement (faible valeur de h/d) ou non-confiné (forte valeur de h/d).

Une corrélation empirique permettant d'estimer la longueur de la zone de recirculation L/d en fonction des paramètres S, R_b and h/d est finalement obtenue. Elle s'avère être en bon accord avec les calculs numériques et les mesures expérimentales.

MOTS CLÉS: Écoulements à surface libre peu profonds, Élargissement, Recirculation, Couche de mélange, Marche descendante, Expériences, Simulations numériques, Modélisations hydrauliques

INSA INSTITUT NATIONAL DES SCIENCES APPLIQUÉES LYON

FOLIO ADMINISTRATIF

THÈSE SOUTENUE DEVANT L'INSTITUT NATIONAL DES SCIENCES APPLIQUÉES DE LYON

NOM : HAN
(avec précision du nom de jeune fille, le cas échéant)

DATE de SOUTENANCE : 05 Février, 2015

Prénoms : Lei

TITRE : Recirculation à l'aval de l'élargissement brusque d'un écoulement à surface libre peu profond

NATURE : Doctorat

Numéro d'ordre : 2015ISAL0005

Ecole doctorale : **M**écanique, **É**nergétique, **G**enie Civil, **A**coustique

Spécialité :
MÉCANIQUE des FLUIDES

RESUME :
Le travail présenté ici a pour objet l'étude de la zone de recirculation qui se développe à l'aval d'un élargissement brusque ayant lieu dans un canal à surface libre, avec une attention particulière portée sur la longueur de recirculation. Ce travail consiste en une approche combinée expérimentale et numérique.

L'analyse dimensionnelle ainsi que les travaux préliminaires antérieurs à cette thèse montrent que la longueur de recirculation adimensionnée dépend de 3 paramètres que sont : le nombre de frottement S, la hauteur d'eau adimensionnalisée par la taille de l'élargissement h/d et enfin le rapport d'aspect géométrique de l'expansion R_b. Cependant, faire varier expérimentalement S ou h/d sans affecter l'autre paramètre s'avère être une tâche très délicate qui a été négligée dans les études précédentes. En utilisant cette même approche, les résultats présentés ici font été d'une forme de cloche très inattendue de la courbe : $L/d=f(S)$. Ces résultats sont alors en fort désaccord avec ceux de la litérature.
Afin d'améliorer notre approche et de faire varier S et h/d indépendament, une champagne de modélisation numérique 3D est menée et prouve que L/d dépend en fait des deux paramètres considérés S et h/d et que la forme de cloche résulte de l'impact opposé de ces deux paramètres.

De plus, l'analyse de la couche de mélange, ayant lieu entre la zone de recirculation et l'écoulement principal, mesurée expérimentalement pour 4 écoulements à différentes valeurs de S et h/d montre que la longueur de la zone de recirculation est gouvernée par le confinement latéral dû à la paroi latérale et à la taille des cellules turbulentes advectée le long de la couche de mélange.

Pour aller plus loin, les bilans de quantité de mouvement et d'énergie à l'échelle de l'écoulement dans son ensemble montrent que i) la force de cisaillement exercée le long de la couche de mélange est négligeable par rapport aux autres forces mises en jeu et ii) que la réelle signification de S est de quantifier l'intensité du frottement pariétal de l'écoulement global intervenant dans ces bilans. Les différents régimes d'écoulement qui peuvent être rencontrés dépendent donc: i) selon la valeur du nombre de frottement S l'écoulement peut être frictionnel (S élevé) ou non-frictionnel (S faible) et ii) selon la valeur de la hauteur d'eau adimensionnelle, l'écoulement peut être confiné verticalement (faible valeur de h/d) ou non-confiné (forte valeur de h/d).

Une corrélation empirique permettant d'estimer la longueur de la zone de recirculation L/d en fonction des paramètres S, R_b and h/d est finalement obtenue s'avère être en bon accord avec les calculs numériques et les mesures expérimentales.

MOTS-CLÉS : Recirculation, Expérience, Élargissement, Marche descendante en arrière, Moyenne de Reynolds Navier-Stokes, Couche de mélange , Grande echelle vortice.

Laboratoire (s) de recherche : LMFA - Laboratoire de Mécanique des Fluides et d'Acoustique

Directeur de thèse:
Nicolas RIVIÈRE

Président de jury : PERKINS Richard

Composition du jury : MIGNOT Emmanuel (Invité), PERKINS Richard, PROUST Sébastien, RIVIÈRE Nicolas, ROUX Sébastien,DARTUS Denis, VAZQUEZ José.

Contents

List of Figures

List of Tables

Notation

Subscript or superscripts

0	Position in the middle of the width of the channel in the expansion section
w	Bottom wall
s	Side wall
PVC	PVC bottom
x	The streamwise direction
y	The transverse direction
z	The vertical direction
c	Correction by the ADV rotation
e	Section of the expansion
reg	Data from the regress progress
num	Data from numerical simulation
exp	Data from experiments

Abbreviation

ADV	**A**coustic **D**oppler **V**elocimeter
DNS	**D**irect **N**avier-Stokes **S**imulation
GRPs	**G**round **R**eference **P**oints
LMFA	**L**aboratoire de **M**ecanique des **F**luides et **A**coustique
LSPIV	**L**arge **S**cale **PIV**
RANS	**R**eynolds-**A**veraged **N**avier-Stokes equations
IA	**I**nterrogation **A**rea
SA	**S**earching **A**rea
PIV	**P**article **I**mage **V**elocimetry
HD	**H**igh **D**efinition
CCD	**C**harge-**c**oupled **D**evice
LDV	**L**aser **D**oppler **V**elocimetry
RMS	**R**oot **M**ean **S**quare
FFT	**F**ast **F**ourier **T**ransform
VOF	**V**olume **O**f **F**luid
TKE	**T**urbulent **K**inetic **E**nergy

UDF	**U**ser **D**efined **F**unction
Condition A	The expansion fixing at 2.36m
Condition B	The expansion fixing at 2.96m
Condition C	The expansion fixing at 3.56m
Condition D	The expansion fixing at 4.16m

Mathematical operator

$E(..)$	Expect value of..
$\overline{(..)}$	Average value of ..
$(..)'$	Operator of fluctuation
$\Pi(..)$	Dimensionless operation

Symbols

symbol	description	unit
α	Mixing layer spreading rate coefficient in Chapter 5 Coriolis kinetic coefficient in Chapter 6	[-] [-]
β	Boussinesq momentum coefficient	[-]
ε	Equivalent sand grain roughness of the bed	[m]
ε_{PVC}	Equivalent sand grain roughness of the PVC bed	[m]
ε_{ROU}	Equivalent sand grain roughness of the roughness bed	[m]
L_t	Total length of the channel	[m]
L_b	Distance from the water tank to the enlargement	[m]
B	Total channel width	[m]
d	Enlargement width	[m]
So, x	Bottom mean slope in the x-wise direction	[%]
g	Gravitational acceleration (g=9.81)	[m/s^2]
ν	Kinematic viscosity of water (1.3×10^{-6} at $10°C$)	[m^2/s]
ν_T	Kinematic viscosity of turbulence	[m^2/s]
μ	Dynamic viscosity of water	[N.s/m^2]
L	Length of the recirculation	[m]
h	Water depth	[m]
h_{air}	Measured depth between the water surface and probe	[m]
h_{bottom}	Measured depth between the channel bottom and probe	[m]
x	x position with the dimensionless of L	[-]
x^*	dimensionless streamwise distance	[-]
y	y position with the dimensionless of L	[-]
X	x position of the flume	[m]
Y	y position of the flume	[m]
a	Parameters for calculating Ground Reference Points	[-]
R	Autocorrelation function of the velocity	[-]

R_{uv}	Reynolds Stress Tensor	[N]
M_i	x direction length of the interrogation areas	[pixel]
M_j	y direction length of the interrogation areas	[pixel]
A_{ij}	Distribution of the gray-level intensities of photo n	[-]
B_{ij}	Distribution of the gray-level intensities of photo $n+1$	[-]
R_b	Expansion ratio	[-]
u	Instantaneous longitudinal velocity	[m/s]
v	Instantaneous transverse velocity	[m/s]
w	Instantaneous vertical velocity	[m/s]
S	Global Bed friction number	[-]
$S(x)$	Local bed-friction number in section x	[-]
ξ_i	Independent, identically distributed, standard, normal, random variable	[-]
N	Number of samples in a series	[-]
φ	Coefficient of the mixing length associated to the shear	[-]
F_p	Force of pressure	[N]
F_{xy}	Force of interface between recirculation and main stream	[N]
F_w	Force of friction near the wall	[N]
λ_U	Universal threshold	[-]
$\hat{\sigma}$	Estimate of the standard deviation	[-]
θ	Angle between the ADV and the flume reference frames	[°]
θ_U	Rotation angel of principle axis of $\Delta^2 u_i$ and u_i	[°]
F_s	Sampling rate	[Hz]
E_{uu}	Energy density	[m^2/s^2/Hz]
f	Frequency	[Hz]
F_r	Froude number	[-]
R_e	Reynolds number	[-]
h_n	Normal depth of the flow	[m]
h_L	Water depth downstream the expansion	[m]
R_h	Hydraulic radius	[m]
λ	Darcy-Weisbach friction coefficient	[-]
C	Chézy coefficient	[$m^{1/2}$/s]
c_f	Bed-friction coefficient	[-]
t	Time	[t]
u'	Fluctuation of streamwise velocity u	[m/s]
v'	Fluctuation of transverse velocity v	[m/s]
u_c	The “center” velocity in the mixing layer	[m/s]
u_1	Outer velocity of mixing layer	[m/s]
u_2	Inter velocity of mixing layer	[m/s]
Δu	Outer velocity difference of the mixing layer	[m/s]
$\delta(x)$	Width of mixing layer in section x	[m]

$y_{maxgradient}$	Position with the maximum gradient in the mixing layer	[m]
ω	Dimensionless vorticity magnitude	[-]
K_s	Strickler's coefficient	[$m^{1/3}/s$]
k	Kinetic energy of the mean motion per unit of mass	[J/kg]
$\nu_T(x)$	Turbulent viscosity in each section x	[m^2/s]
S_{ij}	Mean rate of strain tensor	[m^2/s]
$\nu_{T-Prandtl}$	Prandtl horizontal eddy viscosity	[m^2/s]
l_m	Prandtl mixing length	[m]
ε	Viscous dissipation term	[m^2/s^3]
F_k	Turbulent flux terms	[m^3/s^3]
Adv	Turbulent advention terms	[m^2/s^3]
P	Turbulent production terms	[m^2/s^3]
p	Total pressure	[Pa]
υ	Velocity scale in $k-\varepsilon$ equation	[m/s]
l	Length scale in $k-\varepsilon$ equation	[m]
R_b	Expansion ratio	[-]
J_f	Head loss due to the bottom friction	[J]
J_r	Head loss in the recirculation	[J]
M	Terms in the momentum balance analysis	[-]
T	Terms in the head balance analysis	[-]

Chapter 1

Introduction and scientific issue

After a brief overview of practical situations involving open-channel shallow flows, this chapter provides a literature review concerning different phenomena involved in the shallow water flow. The expansion is then simplified as our experimental configuration. It is related to the classical backward facing step. Then the mixing layer, notably influenced by the shallowness and existing studies on the shallow water expansion are introduced. Finally, the scientific issues stemming from this literature review are listed and the thesis structure is detailed.

Contents

1.1 Shallow flow conceptions

Environmental shallow flows often involve a wide range of eddy length scales, ranging from micro-scale vortices [Nezu and Nakagawa, 1993] up to large-scale coherent structures with horizontal length scales that are much larger than the water depth ($L >> H$) [Talstra, 2011] . There are shallow shear flows as the compound flow in the river as FIG.1.1. Another shallow flow is the shallow recirculation flow as the groyne in FIG.1.2 [Talstra, 2011]. Shallow recirculating flows are very common in the nature. They are observed in bays and harbors ([Ouellet et al., 1986], [Langendoen et al., 1994], [Bijvelds et al., 1999] and [Winterwerp, 2005]), behind islands [Wolanski et al., 1984] and as coastal effluents reattach to the shoreline [Chu and Jirka, 1986]. In natural streams, these regions have a major implication for transport of scalar [Babarutsi and Chu, 1991] or sediment [Wang et al., 2011] then the limited velocities make the recirculation a privileged zone of material deposition.

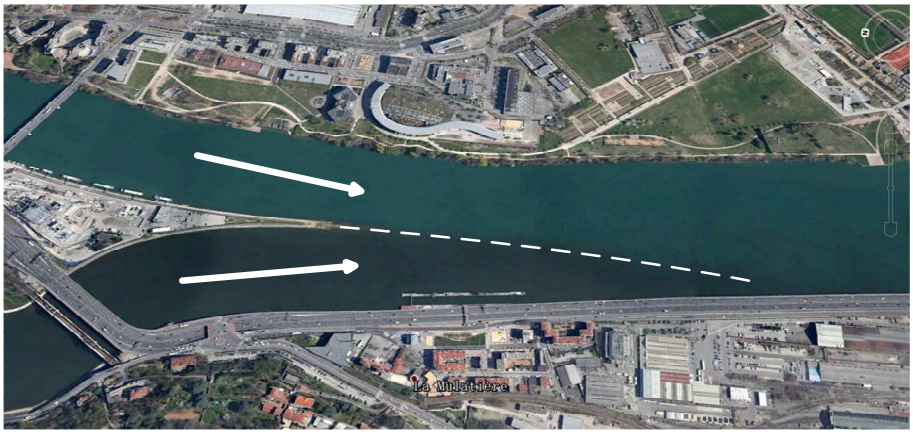

Figure 1.1: Confluence of Lyon. From Google Earth.

This thesis deals with the recirculation zones occurring downstream sudden lateral expansions of open channels. Such recirculations are essential in river engineering. They form silting zones which importance depends on their streamwise extent and thus influences the forming of the river-bed ([Nassiri and Babarutsi, 1997] and [Altai and Chu, 1997]). These dead zones also favour the development of specific fauna and flora, which are influenced by the exchanges through the mixing layer separating the main flow and the recirculation. Finally, they present strong analogies with the recirculations occurring within groyne fields used for river engineering.

Following an applied science approach, this research focuses on a simplified geometry of shallow open channel flow expansion, which is described in next section.

Figure 1.2: Separating and recirculating flow in groyne fields along the river. [Talstra, 2011]

1.2 Expansion geometry and characteristics

The sudden expansion of an open-channel, shallow water flow can be considered as the juxtaposition of different elementary flow situations (FIG.1.3). In the whole study, we consider an expansion with a sharp edge and a flow separation always occurs. Thus, a recirculation zone forms downstream of the expansion, which is a zero-discharge zone, with positive and negative streamwise velocities. Apart from this zone, the flow is referred to ”free-stream” hereafter. It expends and reaches the right wall at the flow reattachment point which is the downstream end of the recirculation. From the flow separation location, a mixing layer develops, which separates the free-stream and the recirculation. From these considerations, our problem could correspond to a “classical” backward facing step situation, in a horizontal plane. Nevertheless, our flow is strongly influenced by the shallowness. Considering shallow flows, *i.e.* with a water depth very smaller than the horizontal length scales ($h << B$), the flow is confined between the bottom and the free-surface. The whole flow is influenced by the bottom friction whilst 3D developments of turbulent structure are limited by the water depth.

This chapter provides a literature review concerning the different phenomena involved in the shallow water flow expansion: (i) backward facing step, (ii) mixing layer, notably influenced by the shallowness, (iii) existing studies on the shallow water expansion. It then ends by the scientific issues stemming from this literature review.

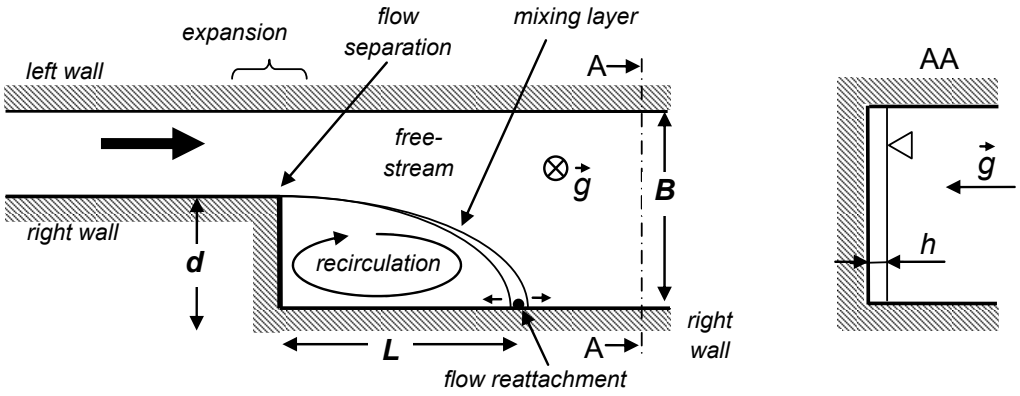

Figure 1.3: Recirculation zone downstream of the expansion
Note: top view (left) and 'AA' cross section (right).

1.3 Backward-facing steps

The backward facing step is an abrupt expansion, considered usually in a vertical plane, and unbounded laterally as in FIG.1.4. It is a classical problem that was abundantly addressed in the literature, notably for its use as a "benchmark" problem to evaluate 3D numerical simulation tools (*e.g.* [Le et al., 1997], [Dubief and Delcayre, 2000], [Toschi et al., 2006] and [Wu et al., 2013]). When focusing on the length of the recirculation zone, [Abbott and Kline, 1962] observed no influence of the Reynolds number, provided the flow is turbulent and fully developed. When Reynolds numbers Re are in magnitude of 1.2×10^4, the skin friction coefficient strongly dependent of Re [Tihon et al., 2001]. For Reynolds numbers Re$<$400, the flow past the backward-facing step can be predicted successfully by two-dimensional computations [Biswas et al., 2004]. [Armaly et al., 1983] proposes experiments showing the huge variations of the recirculation length from the laminar to the turbulent regime. [Adams and Johnston, 1988] confirm that the recirculation length is influenced by the development of the boundary layer but also by the ratio of the channel widths upstream and downstream of the expansion. This last point is confirmed by the numerical study of [Kitoh et al., 2007]. The case of double backward facing step was studied by [Abbott and Kline, 1962]. A possible loss of symmetry, namely recirculations of different sizes, was observed due to interaction between the two recirculation zones. Thus, such cases were not considered in the present work. Recent studies were reviewed by [Peltier et al., 2014], with applications to settling or retention basins. The recirculation zone downstream an expansion seems similar to the recirculation that occurs in the classical backward facing step situation. In both cases, the boundary of the recirculation zone is a mixing layer, where instabilities develop [Chen and Jirka, 1995], producing detached vortices advected along the mixing layer. Nevertheless, significant differences with the present configuration originate due to the so-called vertical confinement effect [Chu et al., 1983], as detailed hereafter.

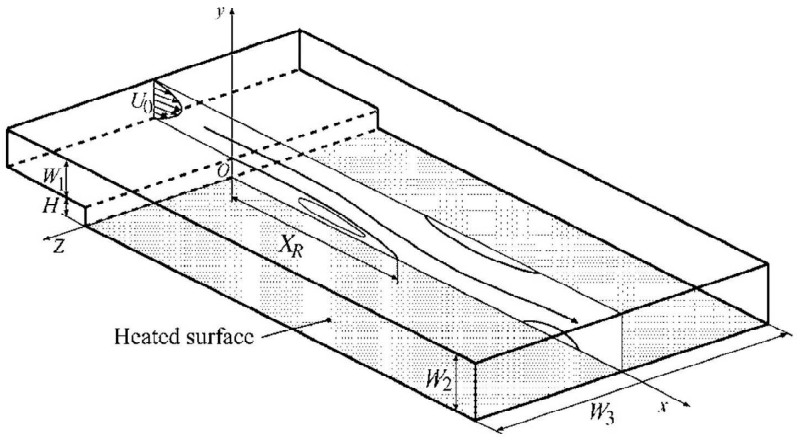

Figure 1.4: Backward-facing flow configurations from [Kitoh et al., 2007]

1.4 Mixing layers

As detailed above, in an open channel sudden expansion, the approaching flow separates from the corner of the expansion and reattaches further downstream. This separating streamline is thus the frontier between i) on one side: the main flow which decelerates due to an increased section and ii) on the side of the expansion: a so called "recirculation zone". One specificity of the recirculation zone is its low velocity magnitude compared to the mean flow. As a consequence, the separating streamline is a location of very high velocity gradient, named "mixing layer", see [Pope, 2008].

Mixing layers are very common in the field or in the literature, both for gas or liquid flows and thus have been deeply studied in the literature ([De Serres et al., 1999], [Rhoads and Sukhodolov, 2008]). Different types of mixing layers exist depending on their specificity. To start with, authors such as [Wygnanski and Fiedler, 1970], [Bell and Mehta, 1990] and [Loucks and Wallace, 2012] studied the simpler configuration for a mixing layer with two parallel flows of different velocities suddenly released one next to the other (see FIG.1.5). Authors also studied mixing layers in more complex configurations, among others are: mixing layers in accelerated [Fiedler et al., 1991] or curved flows ([Margolis and Lumley, 1965], [Gibson and Younis, 1983], [Plesniak et al., 1996]), at the edge of a plate [Ruderich and Fernholz, 1986], in a downward-facing step ([Kasagi and Matsunaga, 1995] and [Jovic and Driver, 1994]), of a square-shaped submerged obstacle [Simoens et al., 2007], of a forward-facing step ([Largeau and Moriniere, 2007] and [Sherry et al., 2010]), of a macro-roughness emerging from a gravel-bed [Mignot et al., 2009] or of the inner bank of a sharp bend [Blanckaert et al., 2012], and of course of a sudden lateral expansion [Babarutsi et al., 1989].

Moreover, apart from the specific geometry in which the mixing layer is observed, the mixing layer may be confined, either laterally [Mignot et al., 2014a] and [Biancofiore, 2014]) due to the side walls located close enough from the mixing layer

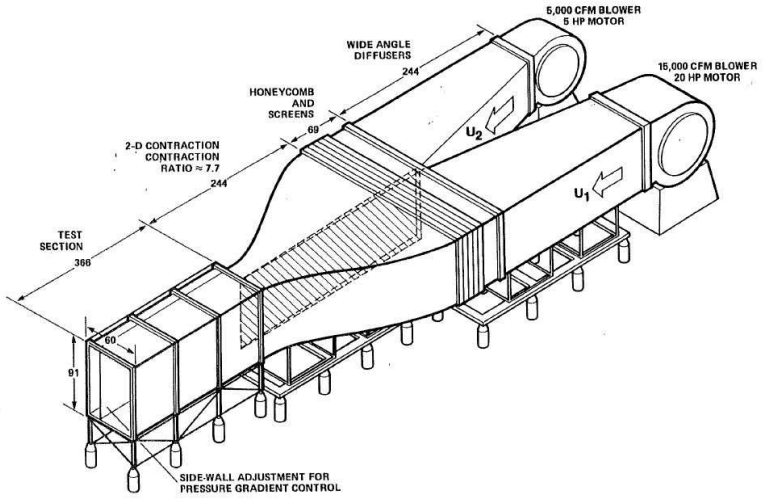

Figure 1.5: Schismatic of mixing layer wind tunnel. [Bell and Mehta, 1990]

to impact it and/or vertically due to the limited depth (for a liquid flow) or channel height (for a gas flow, see [Biancafiore et al., 2011]).

1.4.1 Common characteristics of all mixing layers

As summarized by [Mignot et al., 2014b], measurements in the literature agree that:
→ for high velocity gradients, the inflection of the mean transverse velocity profiles lead to Kelvin-Helmholtz instabilities (see the comprehensive description by [Raupach et al., 1996]. This gives birth to coherent turbulent structures that are shed from the upstream end and advected along the mixing layer with increasing typical size and time-scale (seeFIG.1.6)
→ the width of the mixing layer increases along its development length (see FIG.1.7)
→ the maximum turbulent intensities and Reynolds shear stress across the mixing layer occur at its centerline. After an initial increase, they tend to decrease in magnitude with distance from the upstream boundary condition. (see FIG.1.8)

These three characteristics of the mixing layers are always encountered but their details vary from one configuration to another.

1.4.2 Consequences of the mixing layers

The turbulent structures present in the mixing layer have important consequences, among which:
→ The transfer of momentum from one side to the other
→ The transfer of mass, either passive scalar, sediments, gazes, nutriments *etc*. from one side to the other. An example proposed here [Weitbrecht et al., 2008] is the exchange

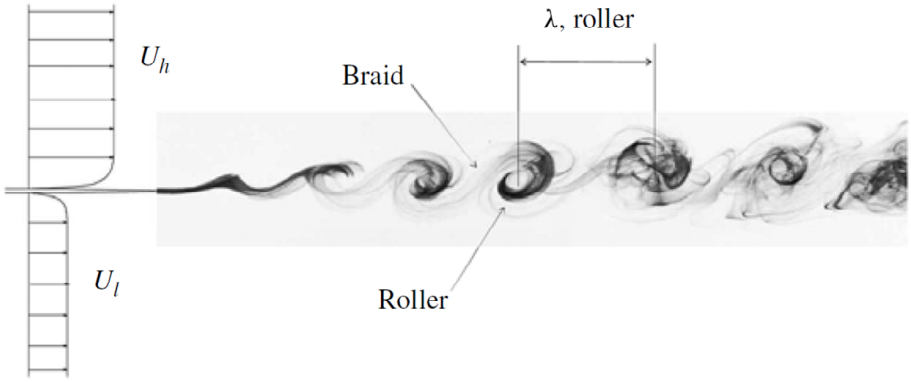

Figure 1.6: Visualization of vortices in the mixing layer. [Loucks and Wallace, 2012]

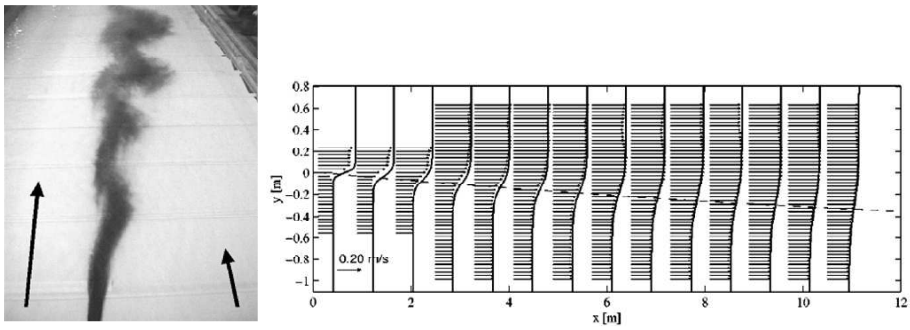

Figure 1.7: Development of the mixing layer. [Van Prooijen and Uijttewaal, 2002]

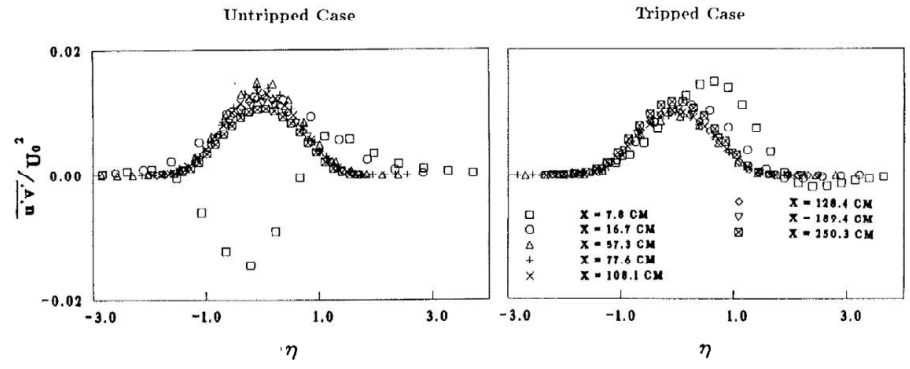

Figure 1.8: Profiles of turbulent shear stress. [Bell and Mehta, 1990]

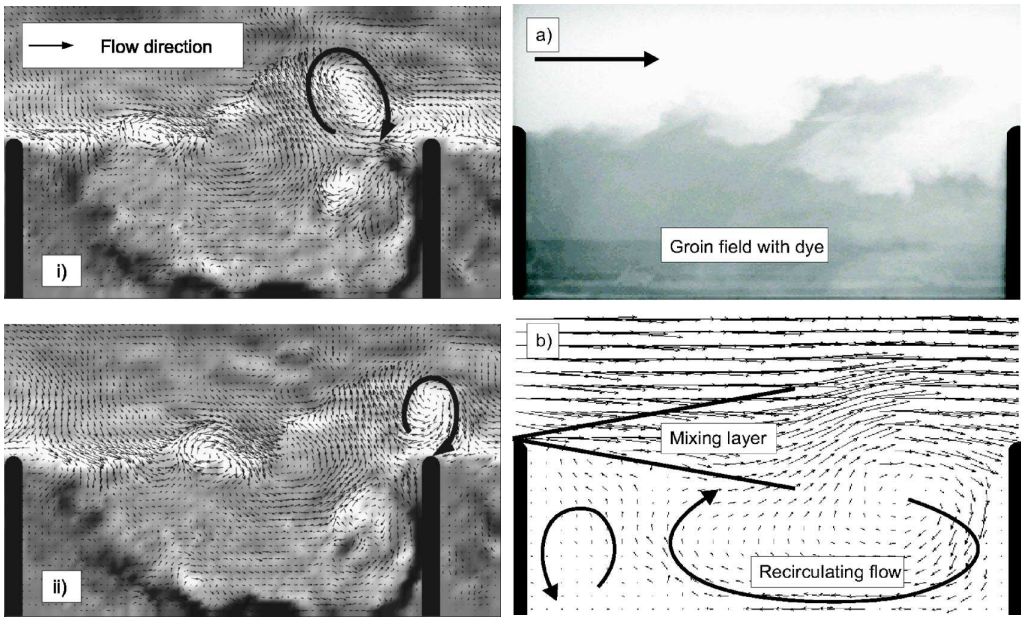

Figure 1.9: Visualization of 2DLCS and Flow dynamics in groin fields. [Weitbrecht et al., 2008]

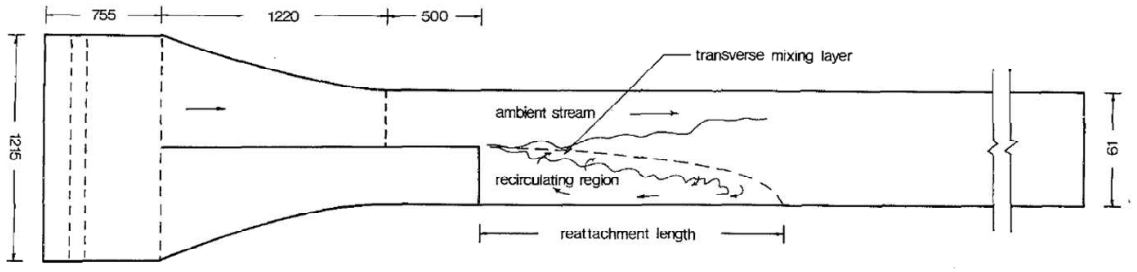

Figure 1.10: Shallow open channel flow with sudden expansion. [Babarutsi et al., 1989]

through the mixing layer at the interface between a main flow and a dead zone (as seen in FIG.1.9).

1.4.3 The present mixing layer, how is it?

The mixing layer taking place along the separating streamline at the sudden expansion of an open-channel flow (FIG.1.10) is:
→ Bounding a recirculation zone
→ Confined laterally by the reattachment wall
→ Confined vertically in a shallow flow, with limited water depth

[Li and Djilali, 1995] listed the most common geometries giving birth to a recirculation zone (see FIG.1.11). Within the recirculation zone, the net discharge is null with positive streamwise velocities near the separating streamline and negative reverse veloci-

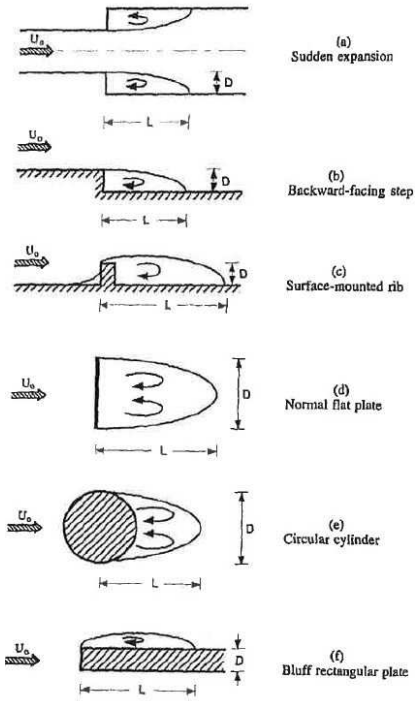

Figure 1.11: Schematic view of some reattaching flows. [Li and Djilali, 1995]

ties near the side wall.

The specificity of mixing layers in separating flows are that:
→ the centerline of the mixing layer turns along its development from the separation to the rattachment point (see [Mignot et al., 2014a]).
→ the velocity gradient is very high, the mean flow being an order of magnitude more rapid than the recirculating flow.

Nevertheless, the main characteristics detailed above for all mixing layers are retrived (see data from [Rouse and Appel, 1965] in FIG.1.12)

1.4.4 Specific case of the shallow flows (vertical confinement)

In limited water depth, the flow is confined between a stick condition on the bed and a zero vertical but free horizontal slip velocity at the free-surface. This confinement creates a strong vertical velocity gradient and thus additional turbulence generated in the near wall region. [Uijttewaal and Booij, 2000] estimate that additionally, the vertical confinement may induce secondary circulation which could also affect the development of the mixing layer.

The impact of the vertical confinement on the mixing layer was deeply investigated on the river scale (see [Sukhodolov et al., 2010]) as in FIG.1.13 or on channel scale (see

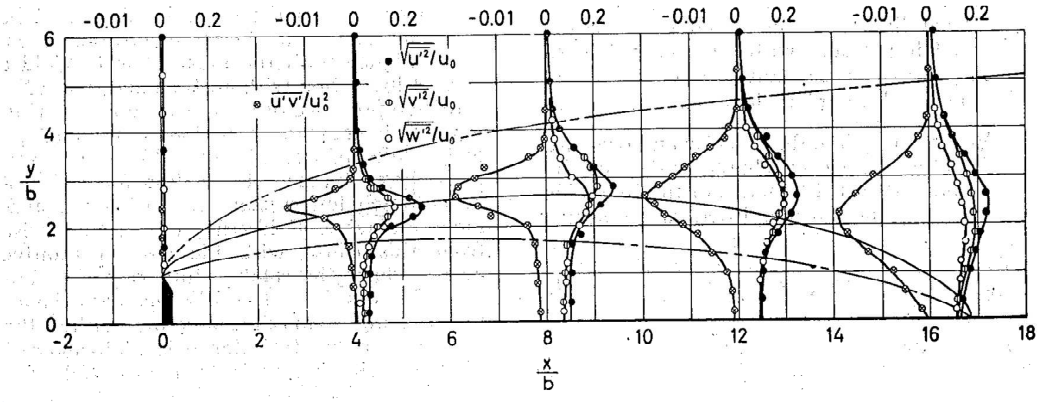

Figure 1.12: Main characteristics detailed in mixing layer. [Rouse and Appel, 1965]

[Uijttewaal and Booij, 2000]) as in FIG.1.14.

1.4.5 What about the lateral confinement

In open-channel sudden lateral expansions, as in backward facing steps, the recirculation zone is constrained by two perpendicular walls and closed along the third side by the separating streamline. For the mixing layer downstream backward facing steps authors such as [Chandrsuda and Bradshaw, 1981], [Jovic and Driver, 1994] and [Kasagi and Matsunaga, 1995] show that:
→ The axis of the mixing layer just downstream the separation is parallel to the inflow while further downstream, the mixing layer approaches the downstream wall with an increasing angle.
→ in the upstream part of the recirculation the mixing layer strongly resembles typical free-mixing layers (see section 1.4.1 above) with a maximum turbulent activity occurring along the centerline of the mixing layer.
→ Further downstream, the mixing layer becomes affected by the side wall. In this reattachment region, the authors show that the location of maximum Reynolds stress and turbulent production is shifted from the side wall at a distance which is not clearly measured (we aim to do it in the present work).

1.4.6 Pioneering work from McGill University research team

Regarding the analysis of mixing layers in this configuration, to the author's knowledge, the only available study was performed by the research team of McGill University, Canada. [Babarutsi et al., 1989] confirmed that the streamwise fluctuation is maximum along the separating streamline and decreases on both sides (See FIG.1.16).

They also confirmed what was written above :
→ The velocity on the slow flow side is very limited, as for all recirculation zones.
→ The curvature of the mixing layer trajectory increases when approaching the reattachment point, as for all recirculation zones.

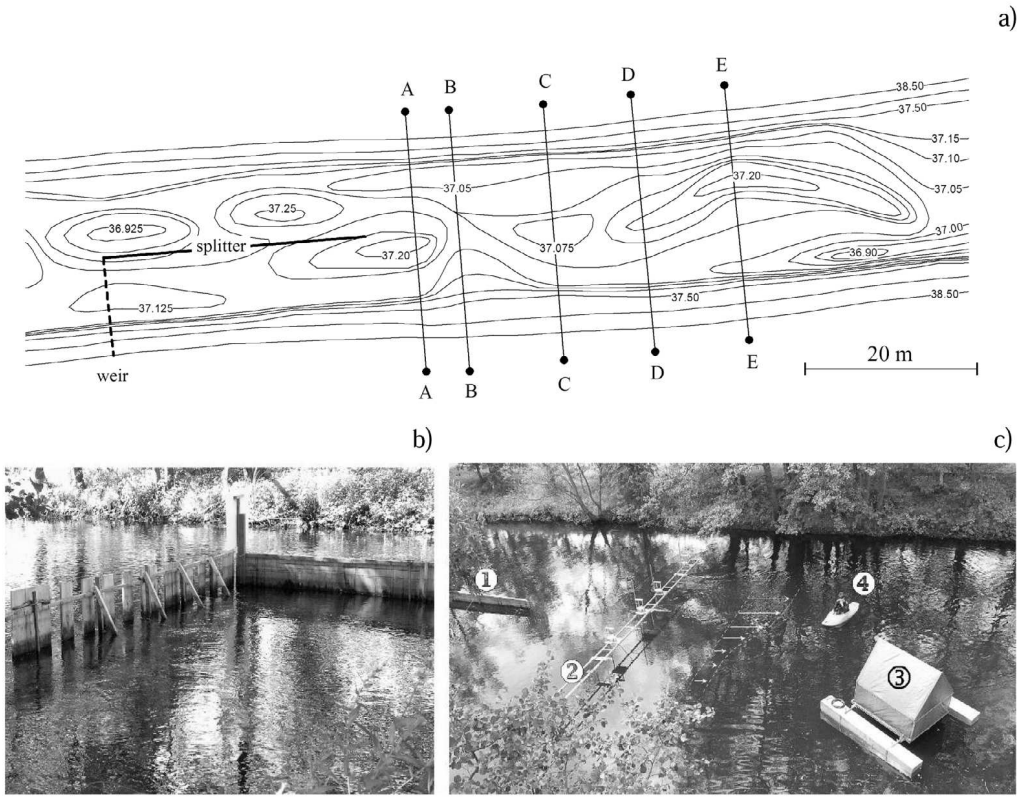

Figure 1.13: Experimental facilities and setup in the river. [Sukhodolov et al., 2010]

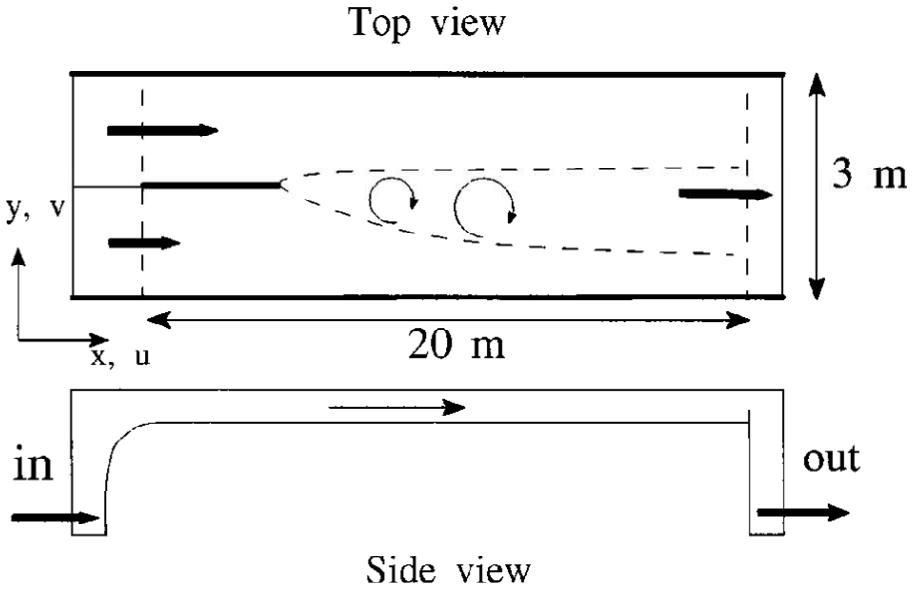

Figure 1.14: Schematic view of the channel with mixing layer (−−). [Uijttewaal and Booij, 2000]

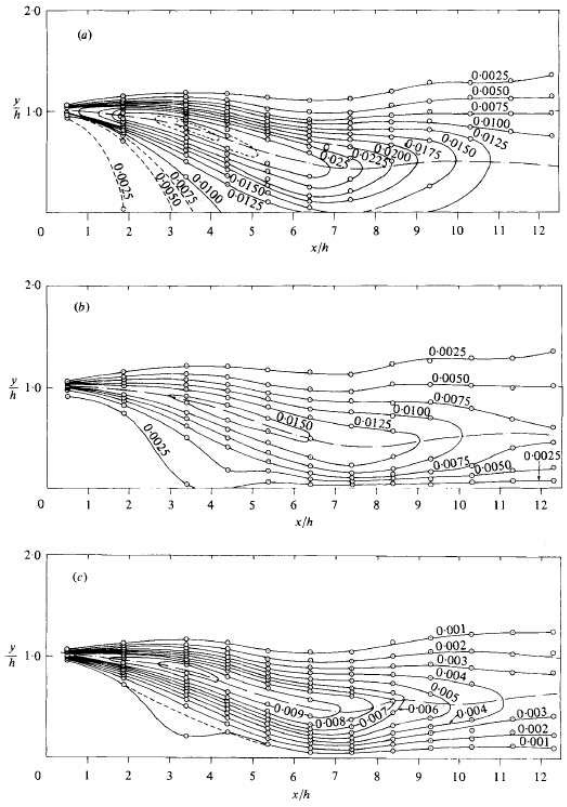

Figure 1.15: Reynolds stress contours. [Chandrsuda and Bradshaw, 1981]
(a) $\overline{u'^2}$ (b)$\overline{v'^2}$ (c)$\overline{u'v'}$

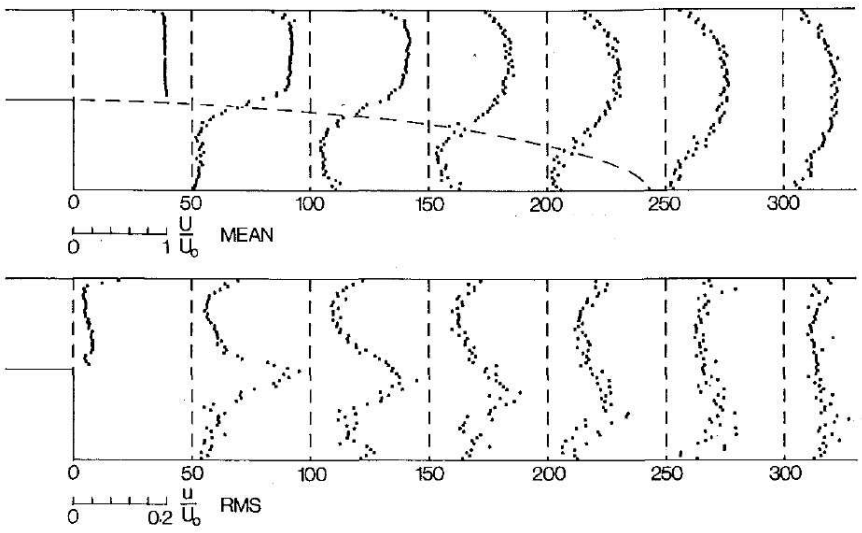

Figure 1.16: Mean and r.m.s. profiles for test 3 of [Babarutsi et al., 1989]

→ The lateral confinement due to the side wall strongly influences the mixing layer, as for all laterally confined mixing layers.

The same research team then measured [Babarutsi and Chu, 1991] the capacity of such a mixing layer to transfer scalar from the recirculating zone towards the mean flow and provided the interest of studying in details the mixing layer characteristics.

1.5 Length of the recirculation

1.5.1 Pioneering work from McGill University

To our knowledge, the main contribution related to our problem was again performed in McGill University, in Montreal, Canada. Considering that the mixing layer is the leading phenomena in the flow, these authors studied the effects of the shallowness on the behaviour of the recirculation : its capacity to exchange passive scalars with the free-stream ([Nassiri and Babarutsi, 1997] and [Altai and Chu, 1997]) and its extent, through the reciruclation length L/d, see FIG.1.17. Our work focuses on the second point, the recirculation length. The bed friction number S was proved to account for the shallowness effects on the mixing layer. As the mixing layer width increases from the separation to the reattachment, [Babarutsi et al., 1989] derive S adopting as transverse length scale the expansion width d (FIG.1.3) and as vertical length scale the flow depth h. Thus, considering the friction coefficient c_f (linked to the Darcy-Weisbach head loss coefficient $\lambda = 4c_f$

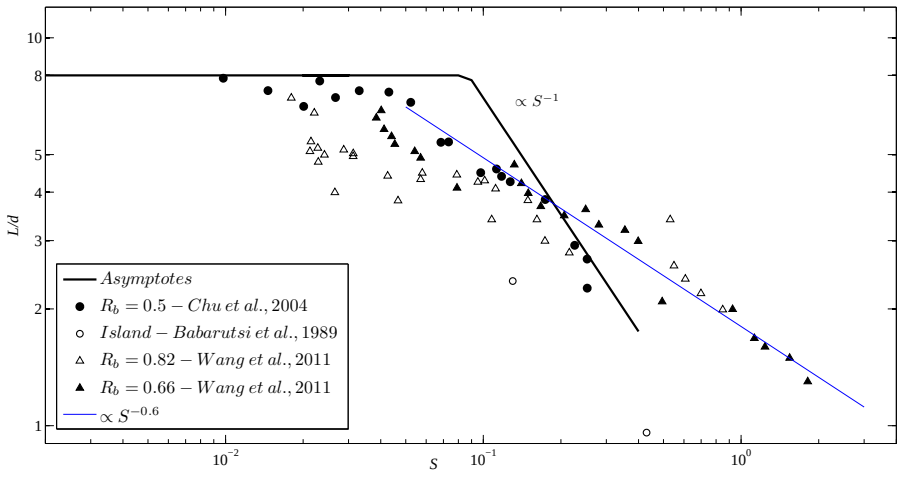

Figure 1.17: Evolution of L/d with S as detailed in literatures

in fully developed flow), the bed friction number S reads:

$$S = \frac{\lambda d}{8h} \tag{1.1}$$

Small values of the bed friction number (S <0.05) are refereed to “non-frictional flows” [Chu et al., 2004] or “deep water flows” [Babarutsi et al., 1989]. The bed friction has a limited influence on the flow pattern in this case. According to [Chu et al., 2004], the length L of the recirculation zone depends only on the transverse length scale:

$$\frac{L}{d} = 8 \tag{1.2}$$

which is consistent but slightly higher than values for backward facing steps reported by [Adams and Johnston, 1988] and [Ramamurthy et al., 1991] for Reynolds numbers higher than 10^4.

Oppositely, high values of the bed friction number (S >0.1) are referred to “frictional flows” [Chu et al., 2004] or “shallow water flows” [Babarutsi et al., 1989]. In such a case, the recirculation is broader and its length depends also on the vertical length scale h/c_f :

$$\frac{L}{d} = a\frac{2h}{c_f d} = \frac{a}{S} \tag{1.3}$$

where the constant a was successively corrected: a=0.6 for [Babarutsi et al., 1989], a=0.5 for [Babarutsi et al., 1996] and finally a=0.7 for [Chu et al., 2004]. In FIG.1.17, the two asymptotic regimes (Eqs.(1.2) and (1.3)) are compared with the experimental results gathered in the most recent publication from McGill [Chu et al., 2004]; from a laboratory channel in closed symbols, from islands in the St.Laurent river in open symbols). The agreement is fair in the non-frictional regime. It is more questionable in the frictional regime, considering the logarithmic scale. Another question stems from the expansion

ratio B/d, *i.e.* the ratio of the channel downstream width and of the expansion width. In all the laboratory experiments reported by [Chu et al., 2004], the expansion ratio was always $B/d = 2$. Yet, this ratio was found to have an influence on the length of backward facing steps (section 1.3) . This seems to be confirmed for shallow expansions by the case of islands in the St.Laurent River: the ratio B/d is considerably larger, and the reported dimensionless recirculation length noticeably smaller as in FIG.1.17.

1.5.2 Wang and co-authors' experiments

Recently, [Wang et al., 2011] performed other experiments. They increased the bed roughness to obtain high values of the bed friction number S. Their results are plotted on FIG.1.17, accounting for their definition of S that is twice the one used in our work. They confirm that L/d decreases with S but, even for S reaching 2, the S^{-1} asymptotic regime is never observed. Conversely, L/d follows a $\sim S^{-0.6}$ law. The dimensionless recirculation lengths observed for two different expansion widths seem to be different but the huge scattering observed for $B/d = 5.8$ prevents from emitting definite conclusions.

1.5.3 Previous studies of our team at LMFA

From this last assessment, preliminary works were performed in our team to examine the influence of additional dimensionless parameters. During their Masters of Science, Badin (2005) and Bomchill (2006) [Rivière et al., 2008] showed that the upstream Froude number has no influence, at least as long as the flow remains sub-critical, whilst the expansion ratio strongly affects the dimensionless recirculation length L/d. Gautier (2010) [Riviere et al., 2011] confirmed the increase in size of the large scale, vertical axis vortices when decreasing S, by means of increasing the water depth. These studies used the same technique to characterize the reattachment, namely long time exposure photographs of floating sawdust. The results were very dependent on the choice of the time exposure, and suffered of bias due to capillary effects that modify the sawdust particles trajectories. Hence, a quantitative estimation of the influence of the expansion ratio was not possible. Moreover, due the moderate length of our laboratory channel, the backwater curve from the downstream weir was able to affect the length of the longest recirculations.

1.6 Scientific issue and structure of the manuscript

The literature review and the previous studies performed in LMFA team lead to the following informations:
$\rightarrow$ The shallow, open channel flow expansion studied here exhibits similarities with the classical backward facing step problem: a flow separation creating a recirculation zone bounded by a mixing layer and two perpendicular walls, where instabilities develop, producing detached vortices advected along the mixing layer and for which the mixing layer reattaches at the wall.

→ Nevertheless, an additional complexity is that shallow expansions are confined between the bed and the free surface. This shallowness may promote substantial differences with unbounded backward facing steps.
→ The action of the shallowness on mixing layers between 2 parallel flows has been studied, but very few results are available for the impact of the shallowness, bounded, curved mixing layers as the one delimiting our recirculation zone and the impact of this shallowness on the interaction of the mixing layer with the lateral wall.
→ In the literature, bed friction number S is the parameter used to characterize the shallowness of expansion flows. The recirculation length follows two asymptotical behaviours according to the values of this parameter S: one for large S (very shallow flow) and one for small S (deep flow).
→ However, existing studies hardly examine the influence of other dimensionless parameters describing the flow, such as the expansion ratio, which was yet found influence for backward-facing steps.
→ Preliminary studies performed at LMFA before this Ph.D. confirmed that additional parameters must be taken into account but provide no definite conclusions due to experimental limitations.

The objective of present studies are (i) establishing all the parameters influencing the flow expansion and particularly the recirculation length, (ii) characterizing their influence on this length, (iii) characterizing this influence on the mixing layer characteristics (local scale) , iv) explaining this influence at the flow scale (recirculation length) and at the local scale (mixing layer).

The manuscript is organized as follows:
↬ Chapter 2 describes the experimental devices and measurement techniques to characterize the mixing layer and to obtain precise estimations of the recirculation length, coping with the source of errors encountered in the previous studies at LMFA.
↬ Chapter 3 presents the experimental results, discusses the fact that the bed friction number is not the only dimensionless parameters that must be considered in shallow flow expansion, and casts doubt on the asymptotic behaviours of the recirculation length related in the literature.
↬ In Chapter 4, as two dimensionless parameters cannot vary independently in the experiments, numerical simulations are performed to establish definitely the influence of each of the dimensionless parameters on the recirculation length.
↬ Chapter 5 details the characteristics of the specific mixing layer, bounded by the lateral wall and investigates their evolution as a function of the shallowness of the flow.
↬ Chapter 6, applies momentum and energy balances at the scale of the flow in the separate region. The aim is to investigate the physical role of friction on the bed (accounted for through the bed friction number S, shallowness (relative water depth h/d) and expansion ratio (R_b). It shows the necessity to distinguish the friction effect and the vertical confinement, though they both contribute to the shallowness.
↬ Chapter 7 proposes some conclusions and prospects.

Chapter 2

Experimental set-up and measuring devices

In this chapter, the experimental flume and its specific devices are first presented. The characteristics of the measuring devices (ADV, LSPIV and Ultrasonic probe) used for our experiments are then exposed. Finally, the calibration of the instruments are done to be ready to accomplish the further experiments.

Contents

2.1 Experimental set-up

Experiments presented in this thesis were conducted in a straight open-channel flume located in the Laboratory of Fluids Mechanics and Acoustics (LMFA) of Lyon, France.

2.1.1 Main characteristics of the channel

Experiments were conducted in an 8 meters long and 0.8 meters wide experimental flume located at LMFA, INSA. This flume is straight with a symmetrical rectangular cross-section and has a streamwise mean slope of $S_{o,x}$ =0.18 %. The channel is PVC made and its surface state is smooth with a typical roughness which is $\varepsilon \sim 5 \times 10^{-5}$ m (See FIG.2.1). Geometrical parameters and the values are displayed in FIG.2.2.

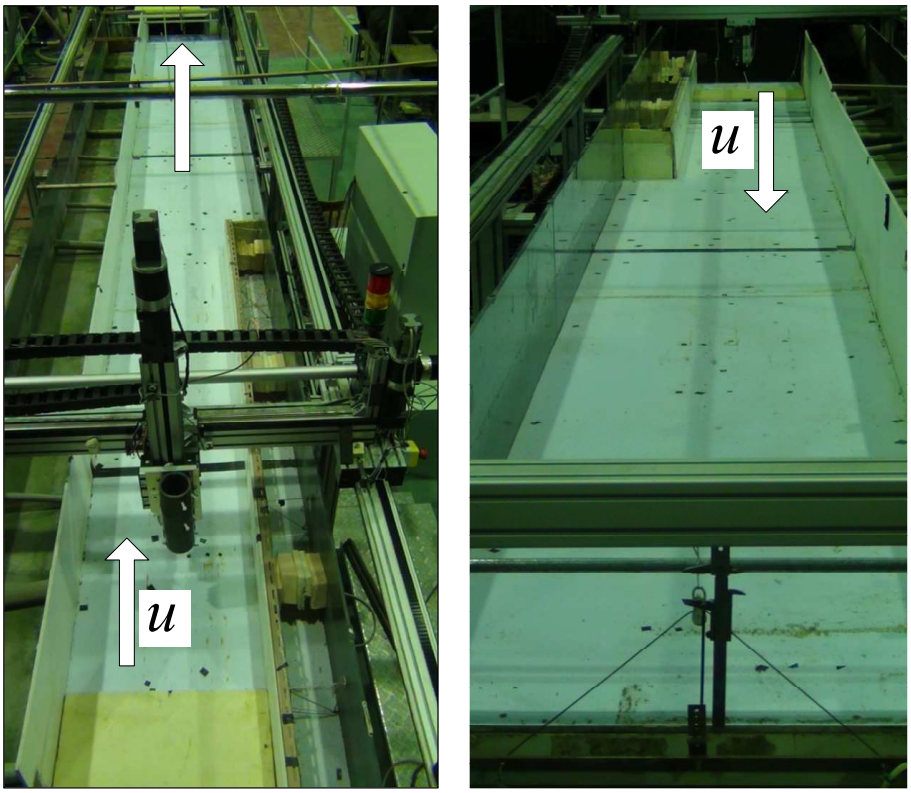

Figure 2.1: Top looking structure of the open-channel flume.
Note: left one is upstream view and the right one is the downstream view

A PVC board is added flexibly for changing the width B and so R_b, as shown in FIG.2.3. FIG.2.3(right) is captured in the direction towards the inlet with $B = 0.3$m, d=0.2, so $R_b = \frac{(B-d)}{B} = 0.33$. In order to avoid the leak between the two parts of the channel, a flow with the same water depth is setted in the other side of the PVC wall. The values of L_b and d can be also adjusted by displacing the impervious block. This block is

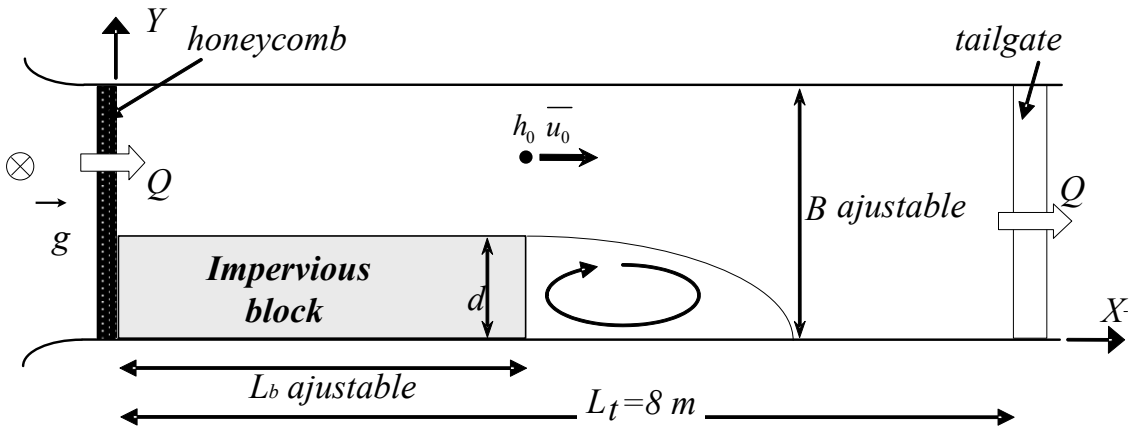

Figure 2.2: Top view definition sketch of the channel

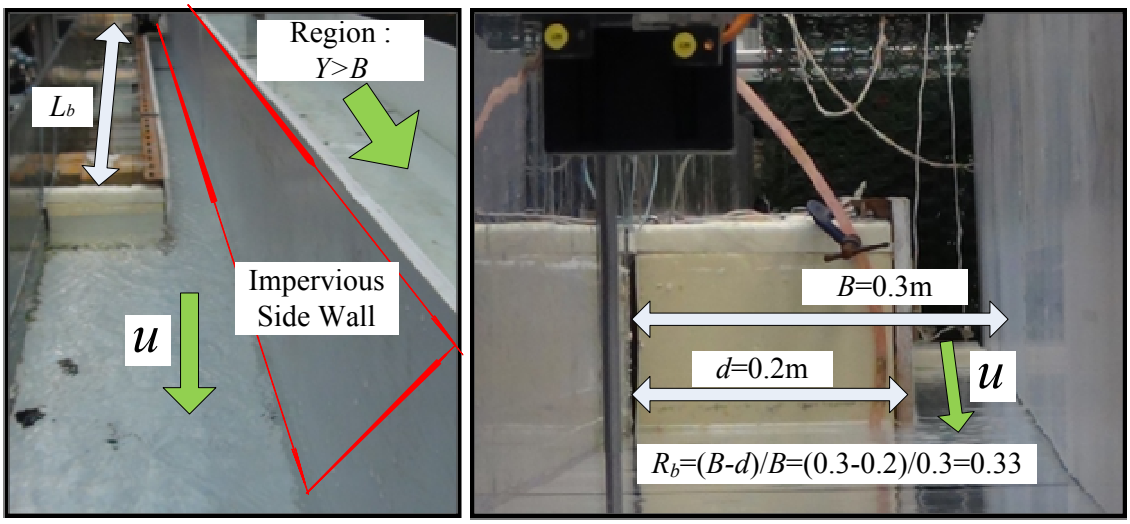

Figure 2.3: Configuration for changing the R_b in the experiments

also filled with water inside which has the same depth as in the channel in order to avoid any leak between the two.

As depicted in FIG.2.4(a) and (b), the flume is equipped by a metal frame which supports an automatic traversing device. This frame is independent of the channel and follows the same mean slope $S_{o,x}$ as the channel. Measuring devices are fixed on the traversing device in order to measure the flow parameters such as water depth and the velocity. The instantaneous velocity components along the streamwise, transverse and the vertical directions will be noted as *u*, *v* and *w*, which are plotted in the FIG.2.4(a).

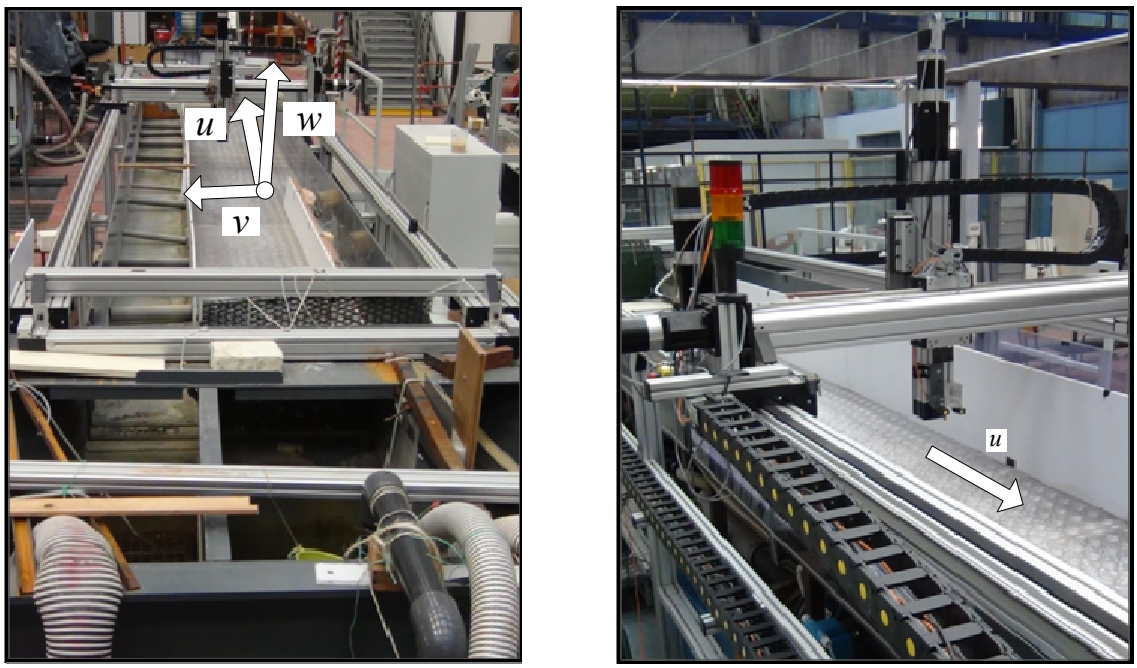

(a) (b)

Figure 2.4: Inlet of the channel (a) and the metal traversing device (b)

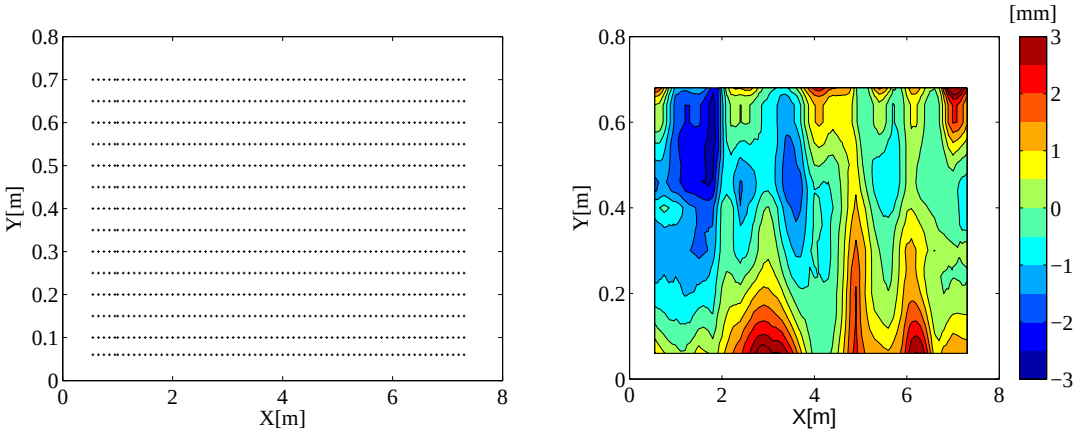

(a) Measuring mesh

(b) absolute variations of the bottom topography

Figure 2.5: Measuring mesh and absolute variations of the bottom topography.

2.1.2 Topography of the channel bottom

The longitudinal mean-slope $S_{o,x}$ of the bottom of the flume was first surveyed using a theodolite: $S_{o,x}$ = 1.8 $\pm$ 0.36 mm/m [Peltier, 2011]. Afterwards, the slope of the surrounding metal frame was set at the same averaged value in order to avoid any problems of protuberance between the reference frame attached to the flume and the reference frame attached to the traversing device. The flume topography was then surveyed using an ultrasonic probe (uncertainty: $\pm$ 0.3 mm) which measured the distance between the traversing device and the bottom. Measurements were carried out following the mesh displayed in FIG.2.5(a). Then by assuming that both slopes of the flume and metal frame were equal to 1.8 mm/m, this slope was subtracted to measurements. Resulting data FIG.2.5(b) finally represents the variations of the bottom around the mean-slope of the flume and they therefore enable to estimate the positions of protuberances.

In the middle of the flume, the bottom is nearly flat along the streamwise and the transverse direction. The topographic protuberance can be observed near the right bank of the flume, there are three protuberances at 3m, 5m and 6m. The first one is totally covered by the expansion block. The other two will influence the recirculation zone (See section after). So another PVC bottom with less conjoint was fixed on the ancient bottom to avoid the projection. The new topography is shown in FIG.2.6(a). The white block is the region of the expansion. The region of the protuberance decreases compared with the first one. When introducing the rough bottom (See section 3.4.3.2), the survey is done in the similar methodology. The topography does not change much as in FIG.2.6(b), the protuberance is acceptable for the experiment.

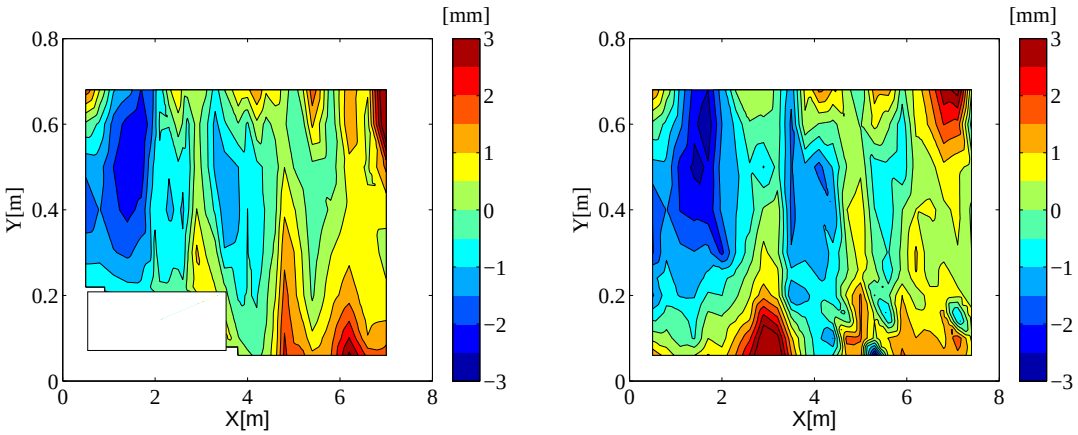

(a) repaired PVC bottom (b) aluminium tear plate bottom

Figure 2.6: Absolute variations of the bottom topography for different bottom

2.1.3 Upstream and the downstream boundary condition

The upstream boundary condition consists of a honeycomb followed by a succession of a grid buffer with small mesh (FIG.2.7 (a), the succession of grids is 1 cm wide). The honeycomb enables to refine the fluid coming from the tank but is responsible for a decrease of the water depth. The grid buffer stabilizes the outflow of the honeycomb in order to avoid the creation of a hydraulic jump due to a too strong diminution in the water depth which is located just in the output of the honeycomb. Finally, after the two grids, a float board made of extruded polystyrene lies on the free surface in order to release the free surface oscillations on the flow.
The downstream boundary condition consists two parts (FIG.2.7 (b)):
$\rightarrow$ Adjustable tailgate. The tailgate can be rotated from horizontal to vertical direction which permits to precisely adjust the downstream water depth. It is referenced with a permanent ruler connected in the top (uncertainty equal to $\pm$ 0.1 mm).
$\rightarrow$ Vent pipe. Due to the surface tension of the water, when the flow discharge is small, the backwater flows along the back face of the tailgate influences the outlet. A vent pipe permit to ensure a detached flow, and makes the flow outlet as free outlet as expected.

2.1.4 Closed-loop water flow system

2.1.4.1 Pump: Grundfos SP125-1-A

As the flow leaves the flume, it is collected in the main tank. For supporting the flow continuity, the underground tank is used which has the capacity of 300 m^3 water. In the tank, a submersible helical pump (Grundfos, SP125-1-A;FIG.2.8 a) is used. The pump is 400 V three-phased with a nominal power of 7.5 kW, a nominal discharge of 125 m^3/h and a nominal manometer head of 13 m. During experiments, the pump is always used out of its nominal characteristics. So a regulator (Danfoss FC202P11KT4E55G,

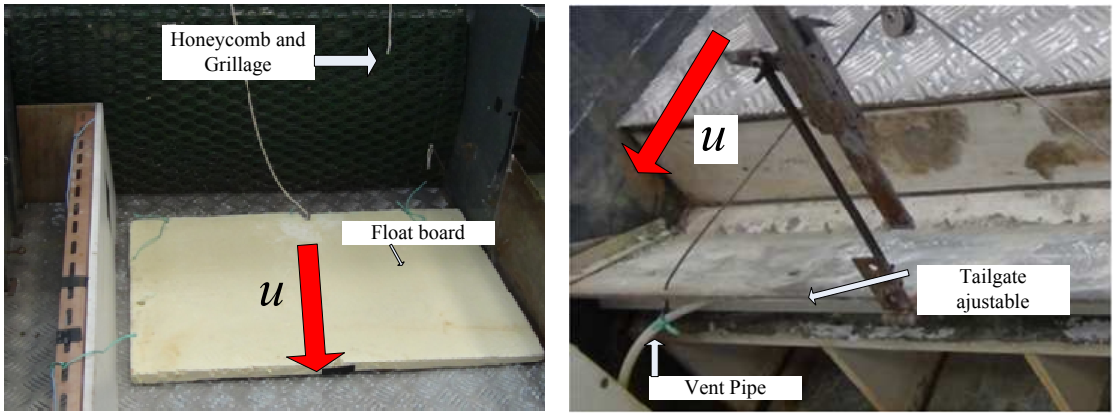

Figure 2.7: The upstream condition and the downstream condition

maximal intensity of 20 A, as in the FIG.2.8) is used to obtain the required discharges transported in the pipe loop and to ensure that the upstream discharge in the flume remains constant all along the experiment. A feedback control was set up on the regulator from the flowmeters using a Proportional-Integral-Derivative controller (constant of time equal to 10 s) to ensure a quick and stable response of the flow system. With a fully-open pipe, the engine of the pumps could not properly spin under a frequency of 16 Hz, *i.e.* it could not deliver a discharge smaller than 4 l/s. For flows with low discharge, another pump was then used which can reach a stable minimum discharge about 0.5 l/s. The flow discharge is adjusted by the valve in the middle of the pipe. And we use electromagnetic flowmeter downstream of the valve for surveying the required discharges.

2.1.4.2 Electromagnetic flowmeters

The injected discharge is controlled on each supply line by an electromagnetic flowmeter (Endress-Hauser, Promag 10, see in FIG.2.9 (a). The uncertainty on the discharge is given by the manufacturer, *i.e.* the uncertainty is equal to 0.5 percent of the maximal working range of the pump: for the Grundfos pump is 0.2 l/s. For the low discharge pump, an electromagnetic flowmeter (Endress-Hauser, Promag 50, see in FIG.2.9 (b) is used. The uncertainty on the discharge is 0.05 l/s which is given by the manufacturer.

2.2 Measurement techniques and calibration

2.2.1 Data acquisition system with LabVIEW

Thanks to [Peltier, 2011], the channel and the equipments for measuring were all ready to use. Here we recall all the characteristics and redo the calibration for the measurement. For the measurement device, we improve some functions for adjusting to our experiments. In the experiment, all the measuring devices are fixed on the traversing device moving on

(a) Pump (b) Regulater

Figure 2.8: Grundfos pump and the Danfoss regulator for closing the water cycling

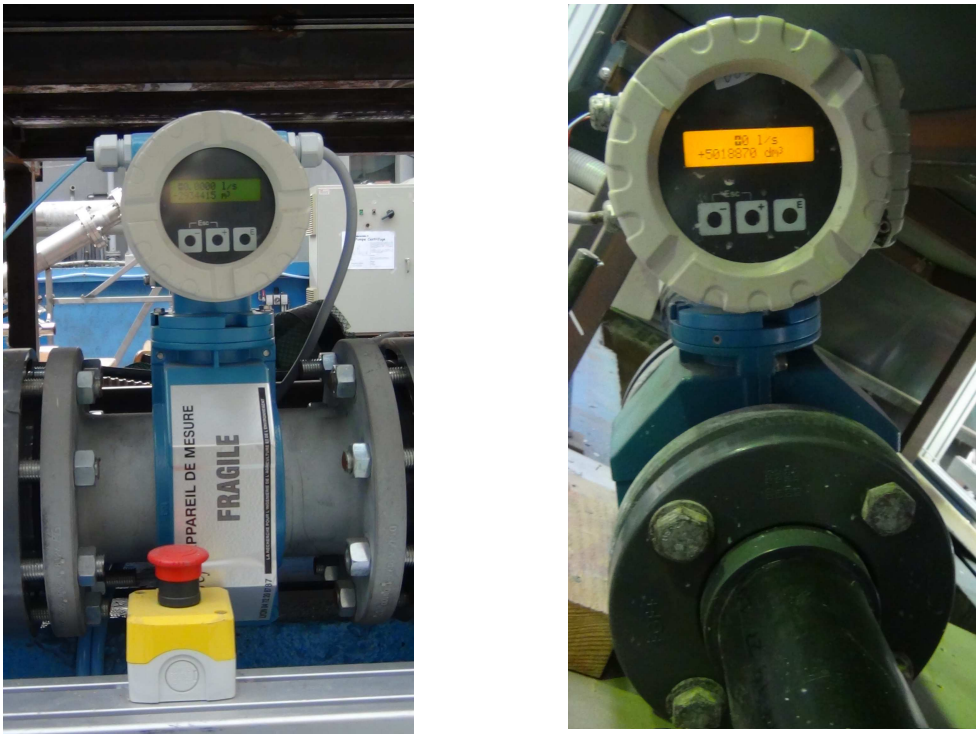

(a) Endress-Hauser, Promag 10 (b) Endress-Hauser, Promag 50

Figure 2.9: Two electromagnetic flowmeters for different discharge

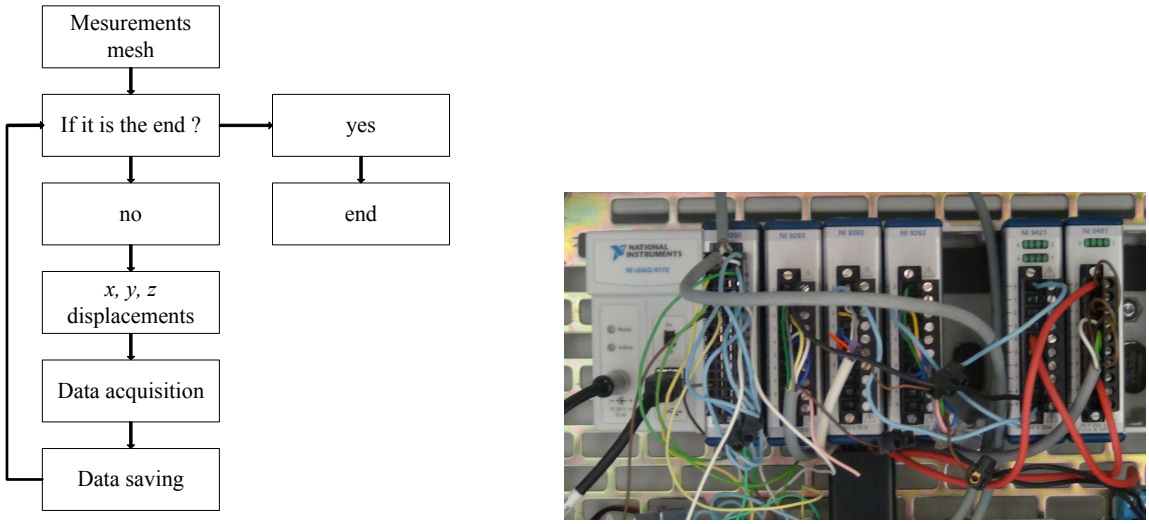

(a) (b)

Figure 2.10: LabVIEW controlling flow chart and the acquisition module

the metal frame surrounding the flume. Thanks to LabVIEW, all the data can be measured automatically by changing the acquisition position and storing the readable data files. With the automation work, it is not necessary to interact with the devices. The data acquisition was performed through a cDAQ-9172card (See FIG.2.10 (b)). The traversing device is driven by a stepper motor controlled through LabVIEW which precision equals to 0.2 mm in the streamwise direction (X-direction) and in the transverse direction (Y-direction). The measurement procedure follows the operation scheme resumed in FIG.2.10 (a). Firstly, the mesh files should be built up including the X and Y (Z if necessary) position and the duration for acquisition. Then the file is read by the program. After defining the initial position of the automate, the transverse devices starts moving towards the next position and stops. Then the data measurement acquisition can start which terminates with writing the data into a file which the name previously affected. The program check if it is the end of the mesh file: if yes, the program stops; if no, the progress continues with a next position until the end of the mesh file. Along all boundaries of the flume, protectors are fixed which cuts the electricity when the displacement reaches given positions. That protects the metal frame and also the measuring devices.

One of the program used for the ADV (described in section 2.2) is introduced here. The front board interaction is illustrated in FIG.2.11. The information is simple to read from the interface. The left region is designed for all the configuration files such as the meshing file and position for storing the data files. The right region give the instant information of acquisition such as the velocity and SNR (describe next).

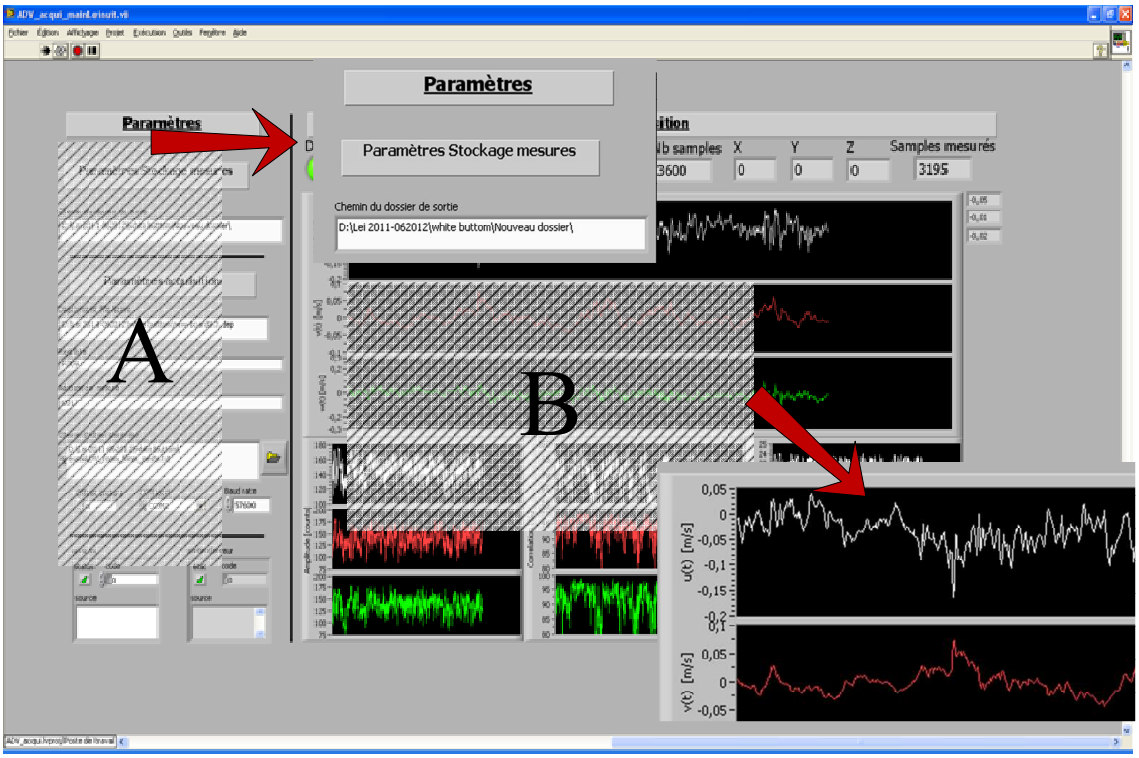

Figure 2.11: Front board of LabVIEW acquisition system

2.2.2 The water depth measurement

For the experiment, the uniform flow condition is expected so the measurement of water depth along the streamwise direction is required. In this thesis, the free surface level and the bottom level were measured using an ultrasonic probe (Baumer Electric, UNDK 20I 6912 S35A, as showed in FIG.2.12). These two probes are fixed on the transverse frame. The minimum distance between the surface and the probe equals to 5 mm. The accuracy of the probe is equal to $\pm$ 0.3 mm and the reproducibility between two measurements is equal to $\pm$ 0.5 mm.The ultrasonic probe is composed of one cylindrical transmitter rounded by one receiver (FIG.2.12). The transmitter sends a series of waves that reflects on the object to be detected (bottom of the flume or free water surface) and then return to the receiver. The distance h_{bottom} (from the probe to the bottom) and h_{air} (from the free surface to the probe) are obtained by the time to travel round trip. So h_{water}=h_{bottom}-h_{air} is then calculated for the flow.

To evaluate the convergence of the time-series signal, long-time measurements were done with the ultrasonic probe. As shown in FIG.2.13, the cumulative mean of the measured distance is about and constant after 30 s. As a consequence, we chose to measure levels during 30 s in the future experiments.

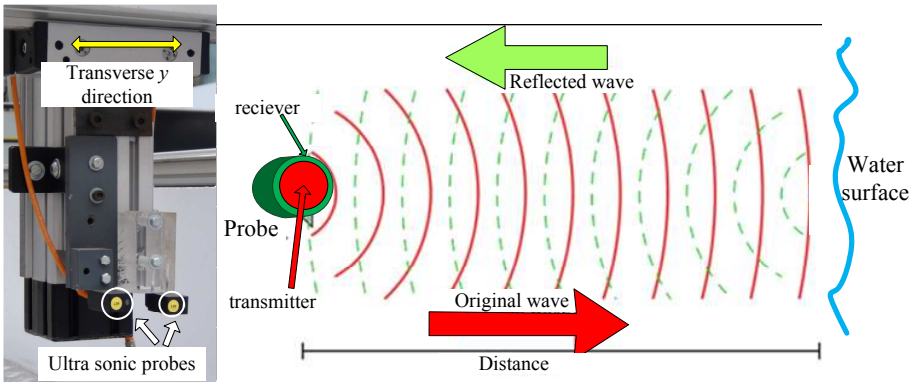

Figure 2.12: Working principle of the Ultrasonic Doppler probe

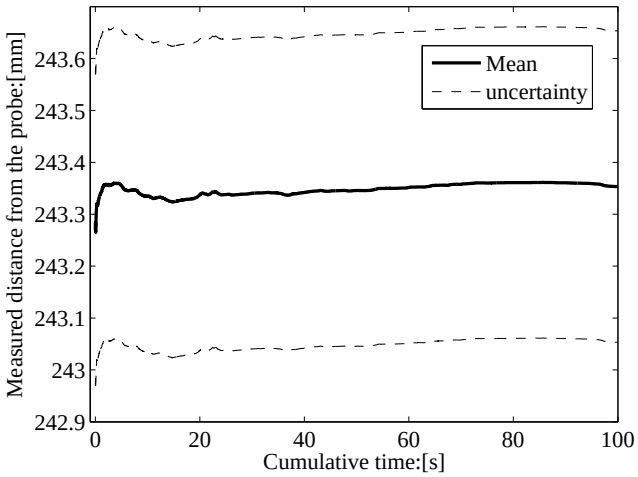

Figure 2.13: Cumulative mean water depth measured by the ultrasound probe.

2.2.3 Acoustic Doppler Velocimetry

For measuring the mean and fluctuating velocity field, many instruments have been used in the recent years such as the hot-film anemometer [Babarutsi et al., 1989], laser Doppler anemometry [Uijttewaal and Tukker, 1998] , PIV [Talstra, 2011]. Here, the ADV (Acoustic Doppler Velocimetry) is selected. For the condition with the water depth is smaller than 20 mm, the ADV cannot be used due to a too large intrusion in such shallow flow. This is caused by the diameter of the sound transmitter. So the LSPIV (Large Scale Particle Imaging Velocimetry) is then carried out for measuring the velocity field as we want.

2.2.3.1 Operating principle

The Vectrino (Nortek, Vectrino+, Fs = 1-200 Hz) is a high-resolution acoustic Velocimeter used to measure 3D water velocity in a wide variety of applications from the laboratory to the ocean. The basis measurement technology is the coherent Doppler processing, which is characterized by accurate data with no appreciable zero offset [website Nortek]. There are many types of ADV instruments such as the down-looking or side-looking and with or without the rigid stem. For this thesis, we use the Vectrino side looking fixed probe (FIG.2.14 in the red frame) especially adapted for shallow flows. As displayed in FIG.2.14, the probe (part 4) is mounted on a fixed stem (part 3) connected to the main housing (part 2) through the probe end bell.

It uses the Doppler effect to measure flow velocity by transmitting a short pulse of sound, receiving its echo and measuring the change in pitch or frequency of the echo. Different from the standard Doppler profilers, the Vectrino separates the sender part and the receiver part as shown in FIG.2.14. It transmits the signals through the central beam and receives them through four beams displaced in one side. All the four beams focus on the same sampling volume which is 5 cm distance from the center of the sending beam. The sampling volume is cylinder with a fixed diameter of 6mm. The height can be adjusted from 3mm-15mm. And so the receiver will “listen” the data in this sampling volume and then give out the instantaneous velocity. The side-looking ADV was mounted on the carriage of the automatic displacement and was moved through LabVIEW. The ADV moving and data acquisition was controlled by LabVIEW automatically. The velocity fluctuations can be measured at a maximal frequency of 200 Hz, which is useful for having a well described turbulent spectrum.

2.2.3.2 Measuring characteristics

During the measurement process, SNR (Signal Noise Ratio) is surveyed, which equals $20log_{10}\left(\frac{Amplitude_{signal}}{Amplitude_{noise}}\right)$ according to Nortek Manual. It influences the precision. As the method used by [Hurther and Lemmin, 2001] is too complex and gives lots of data, so it is not used for our experiments. However, according to the study of [Strom and Papanicolaou, 2007], the noise has a negligible effect on the mean velocities ,and Reynolds normal stress τ_{yy} and Reynolds shear stress τ_{xy}. Only τ_{xx} is noised, but

Figure 2.14: Working principle of the side looking probe

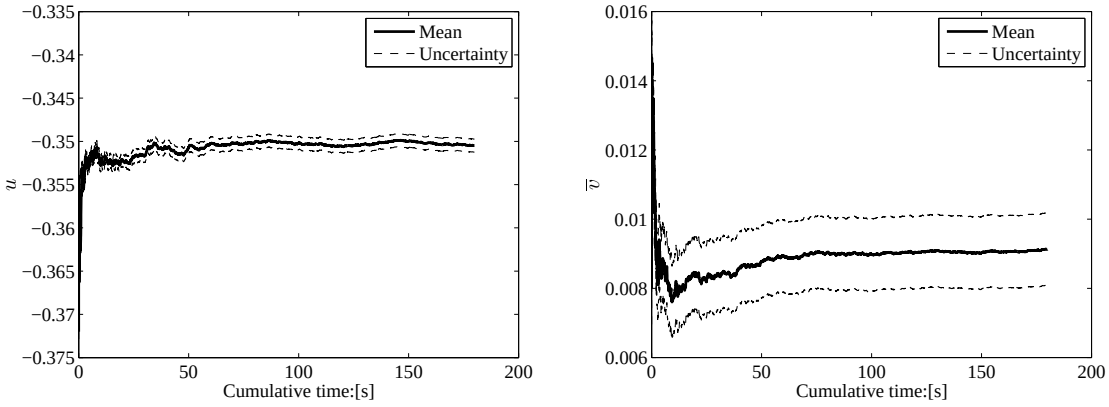

Figure 2.15: Cumulative mean velocity in streamwise and transverse direction

according to [McLelland and Nicholas, 2000], when the SNR is bigger than 20 db, the noise influences very little.

For increasing the received Doppler signal intensity in the sampling, spherical micro-particles of glass (Dantek, HGS 10-20 μm) were injected in the upstream tank of the flume; the spherical micro-particles of glass is sufficient for the whole velocity field. However particles cannot recirculate so we decided to use a cheaper method: electrolysis of water for producing enough small bubbles in the upstream section of the channel instead of the spherical micro-particles of glass. In addition, the diameter of the air bubble is extraordinary small and should not influence the velocity field.

For measuring the turbulence characteristics in the mixing layer, the frequency is fixed to 30 Hz. For testing the average velocity, a long-time data acquisition is in the FIG.2.15. The uncertainty is about $\pm 0.5\%(\overline{u},\overline{v})\pm 1$mm/s. For finding the end of the recirculation, only the direction of the mean velocity is required so the time-average velocity convergence is used and 120 s is enough. However, for the measurement of turbulence characteristics, 3 minutes is used to get a good convergence of the cross-power spectrum densities in the most productive zone of turbulence, as in FIG.5.4(b).

2.2.3.3 Despiking the ADV data

Comparing with the traditional methodology for measuring the outdoor hydraulic flume such as PIV and LDV, the ADV is more rapid and practical. However, it presents two main disadvantages. The first one is aliasing of the signal emitted by the ADV. That appears as the phase-shift between the outgoing and incoming pulse lies outside the range between $+180^\circ$ and -180°. And so the ambiguity will introduce a spike in the recording data [Goring and Nikora, 2002] and [Nikora and Goring, 1998], as shown in FIG.2.16 (R_b= 0.75, S= 0.023, X=3.94m, Y=0.065m). A spike also occurs when the flow velocity range exceeds the pre-set velocity range or there exits an contamination by the complex boundary geometry in the channel and also when a large bubble passes.

In FIG.2.16, the red ellipsoids tag some spikes in the time series of the streamwise

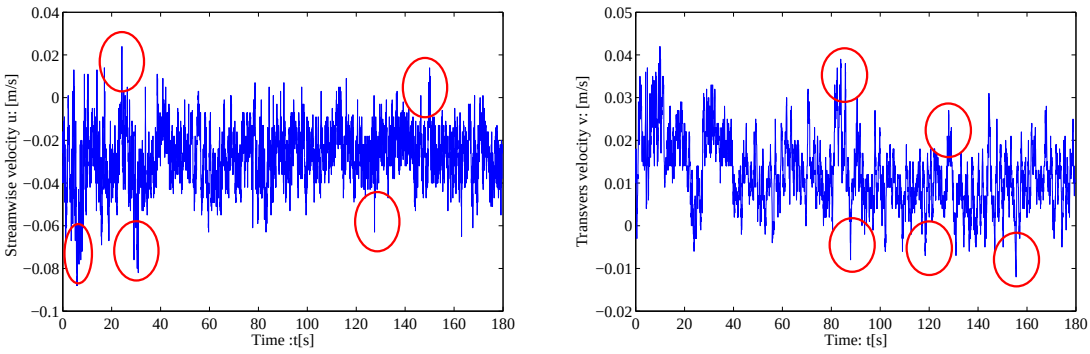

Figure 2.16: Spiked Adv data without correction in the velocity derection.

and the transversal velocities measured for the point (Note: the signal is measured at R_b= 0.75, S= 0.023, X=3.94m, Y=0.065m). The magnitude of these spikes is at least twice larger than the average magnitude of the signal. The pre-set of the velocity range is large enough for this flow velocity, so these peaks are related to other processes and artificially increase the variance of the signal. Hence, these peaks have to be removed from the signal. The spikes are removed using a correction of the method developed by [Goring and Nikora, 2002]. This method is called "Phase-Space Thresholding Method" and is widely used by most of the ADV users. The basic thought is simple which includes two parts: (1) detecting the spikes and (2) replacing the spikes with corrected data.
$\longmapsto$ Detecting. The threshold arises from a theoretical result from normal probability distribution theory which says that for n independent, identically distributed, standard, normal, random variables ξ_i the expected absolute maximum is $E(|\sigma_i|_{max}) = \sqrt{2lnN} = \lambda_U$ where λ_U is called the universal threshold. For a normal, random variable whose standard deviation is estimated by $\hat{\sigma}$ and the mean is 0, the expected absolute maximum $\lambda_U\hat{\sigma} = \sqrt{2lnN}\hat{\sigma}$. In the FIG.2.17, it is apparent that most of the data points are enclosed in the ellipsoid cloud and the spikes are outside. So, the points spiked are found out.
$\longmapsto$ Replacing. [Goring and Nikora, 2002] have tried many method for replacing the holes. It's said that a third-order polynomial through 12 points on either side of the spike is the best choice which can be adorable for the sampling rate changes from 25Hz to 100Hz.

However, there is a disadvantage in the algorithm: If more than 10 % of the time series is spiked, the series is simply invalidated. So in this thesis, we use the methodology introduced by [Peltier, 2011], which improves the equation of [Goring and Nikora, 2002], for calculating $\lambda_U\hat{\sigma}$ as shown below.

$$\theta_U = \tan^{-1}\left(\Sigma u_i \Delta^2 u_i / \Sigma {u_i}^2\right) \tag{2.1}$$

θ_U is the angle of rotation of principle axis of $\Delta^2 u_i$ versus u_i. When the second derivative $\Delta^2 u_i$ is one order smaller (or even more) than the variable u_i, the angle becomes very small and it is impossible to follow the real slope of the cloud, so [Peltier, 2011] improved the

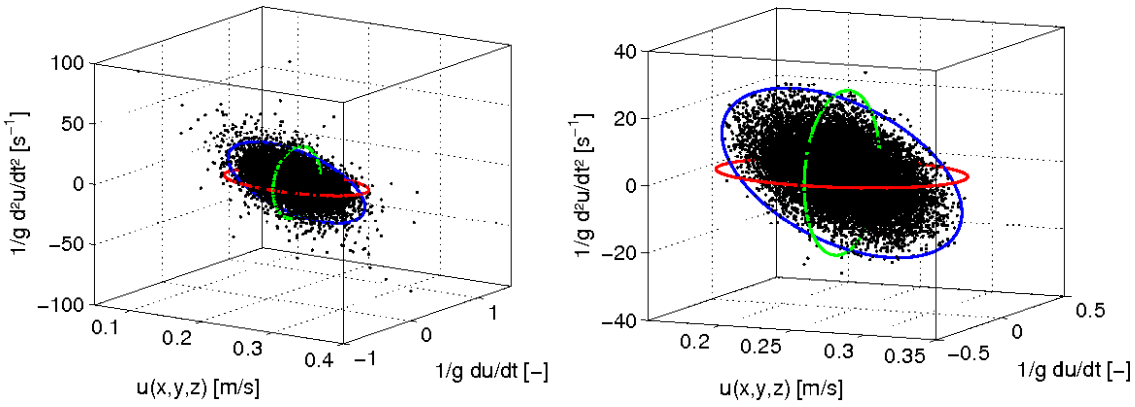

Figure 2.17: Application of the Phase-Space Thresholding Method. [Peltier, 2011]

equation for $\overline{U_i}$ which can be written as below:

$$\theta_U = \tan^{-1}[\Sigma(u_i - \overline{u_i})(\Delta^2 u_i - \overline{\Delta^2 u_i})/\Sigma(u_i - \overline{u_i})^2] \tag{2.2}$$

This despiking method is less restrictive than the original method. So, the despiked data signal is obtained in the FIG.2.18. It illustrates that most of the peaks seen on the original data are removed by the despiking method and are replaced with the interpolated data.

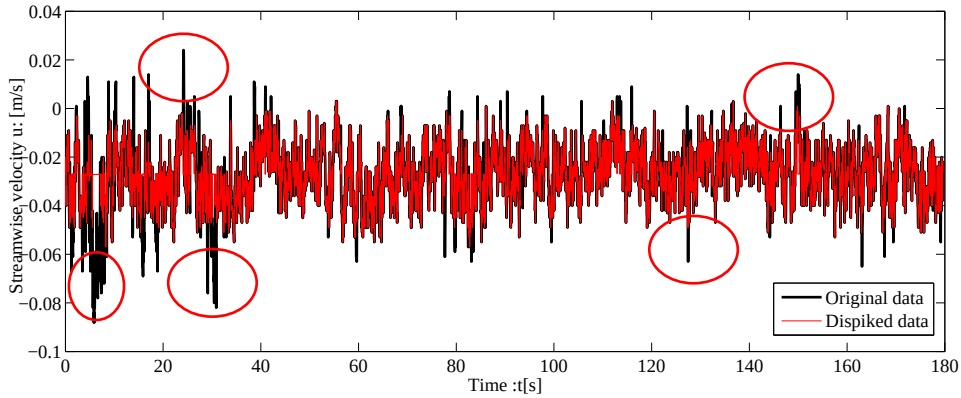

Figure 2.18: Results of the Phase-Space Thresholding Method application

2.2.3.4 Reposition de rotation of the ADV

ADV data is very sensitive to the probe orientation. For example, an error of $\pm 1^\circ$ on the probe orientation may produce ± 1 cm/s additional transversal velocity. So before measurements, orientation verification of all the velocity should be done as perfectly as we can especially for streamwise direction. The ADV probe has three rotation axes. For vertical and transverse axes we use the ruler with a bubble level. Because of the slope of

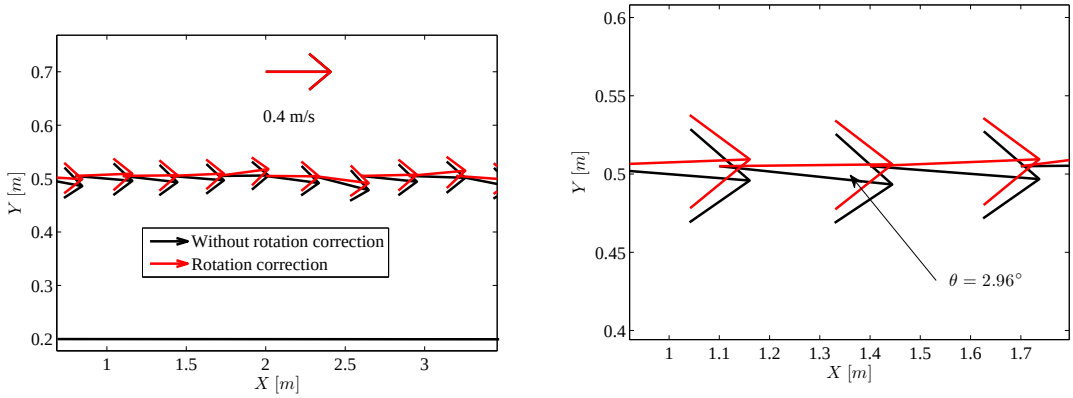

Figure 2.19: Application of the rotation for the ADV.

bottom ($S_{0,x}$=0.0018), we should keep the vertical direction with the same slope. For the direction longitudinal, the influence of the error angle is more sensitive to the accuracy of the velocity. So the four beams should be strictly fixed parallel to the side wall. But, from calibration of the bubble ruler, a small angel still remains. Hence, a correction method is introduced in processing the data. Theoretically, in the upstream of uniform flow upstream the enlargement, the component of transverse velocity v should be 0. We selected about 15 points measured along the centre line of the channel in the upstream flow (Y=500mm) as shown in the FIG.2.19.

As the working theory of the ADV, if the ADV frame and the flume reference have an angle of θ, the corrected velocities are computed as the following equations,see [Peltier, 2011] and [Peltier et al., 2013] .

$$\begin{pmatrix} u_c \\ v_c \end{pmatrix} = \begin{pmatrix} \cos\theta & -\sin\theta \\ \sin\theta & \cos\theta \end{pmatrix} \begin{pmatrix} u \\ v \end{pmatrix} \tag{2.3}$$

Using the Reynolds decomposition, velocity correction can be written as following equations,

$$\begin{pmatrix} \overline{u_c} + u_c\prime \\ \overline{v_c} + v_c\prime \end{pmatrix} = \begin{pmatrix} \cos\theta & -\sin\theta \\ \sin\theta & \cos\theta \end{pmatrix} \begin{pmatrix} \overline{u} + u\prime \\ \overline{v} + v\prime \end{pmatrix} \tag{2.4}$$

As we known, the total velocity includes two parts, the instantaneous and the mean term, with the average of the two terms, they write as below:
$\overline{\overline{u_c} + u_c\prime} = \overline{u_c}$
$\overline{\overline{v_c} + v_c\prime} = \overline{v_c}$
So the time-averaged velocities and the instantaneous velocities can be described separately and the time-averaged velocities are written as the equation below:

$$\begin{pmatrix} \overline{u_c} \\ \overline{v_c} \end{pmatrix} = \begin{pmatrix} \cos\theta & -\sin\theta \\ \sin\theta & \cos\theta \end{pmatrix} \begin{pmatrix} \overline{u} \\ \overline{v} \end{pmatrix} \tag{2.5}$$

Actually, the aim of the correction is to find out θ which minimizes $\Sigma_{upstream}(\overline{v_c})^2$. As

shown in FIG.2.18, the velocity corrected velocity vector are marked red which has small v component and flows along the streamwise direction.

2.2.3.5 Spectrum analysis for the turbulence and denoise progress

The second disadvantage of the ADV is that the Doppler noise appears at high frequency section and creates an additional variance that increases the turbulent intensity such as in the Reynolds stress tensor [Nikora and Goring, 1998] and [Voulgaris and Trowbridget, 1997]. Here the spectrum analysis is used for detecting and deleting the noise as the [Peltier, 2011].

The spectrum densities are calculated using the method of the short modified periodograms [Welch, 1967]: *i.e.* estimates the power spectral density of the input signal vector x using Welch's averaged modified periodograms method of spectral estimation. Here, the vector x is the despiked time-series. The characteristics of the computations are given below:
1. We start with the fluctuation velocity signal. It was equal to $N \sim 5400$ for 3 min of measurements at F_s = 30 Hz. Nevertheless, the FFT algorithms need a number of samples equal to a power 2 number, the required number of samples used for our FFT calculations was et equal to NFFT = 2×N=10800. The signal is divided into NFFT length segments and then, the last segment is padded with zeros.
2. A Hanning window of 512 samples wide was then applied on the new signal with an overlapping of 50 %, therefore cutting the signal in (NFFT/512 $\times$ 2−1) segments (the window is used to reduce the aliasing in the spectrum density and it improves the resolution of the spectrum).
3. In the sequence, the FFT of each segment and their periodograms were calculated. The average of all the periodograms finally gives the estimate of the one-sided spectral density, as shown as the black one in the FIG.2.20.
4. The level of noise is identified at high frequencies as white noise on the power-spectrum (green plateau at the end of the despiked signal in FIG.2.20). The noise is finally subtracted to the despiked signal, therefore giving a despiked and denoised power spectrum density.
5. The denoised signal (the red one) has the more apparent tendency of the Kolmogorov's -5/3 rules and the integral of the E_{uu} is the corrected Reynolds stress [Voulgaris and Trowbridget, 1997].

2.2.4 Large Scale Particle Imaging Velocimetry

In the condition with water depths smaller than 20 mm, the ADV can not access the measurement as the probe diameter exceeds the water depth. So LSPIV (Large Scale Particle Image Velocimetry) is carried out to measure the mean velocity field in order to find the point of reattachment. LSPIV has the same working principle as the traditional PIV but applied to a large scale. LSPIV uses macroscopic seeding floating on the free

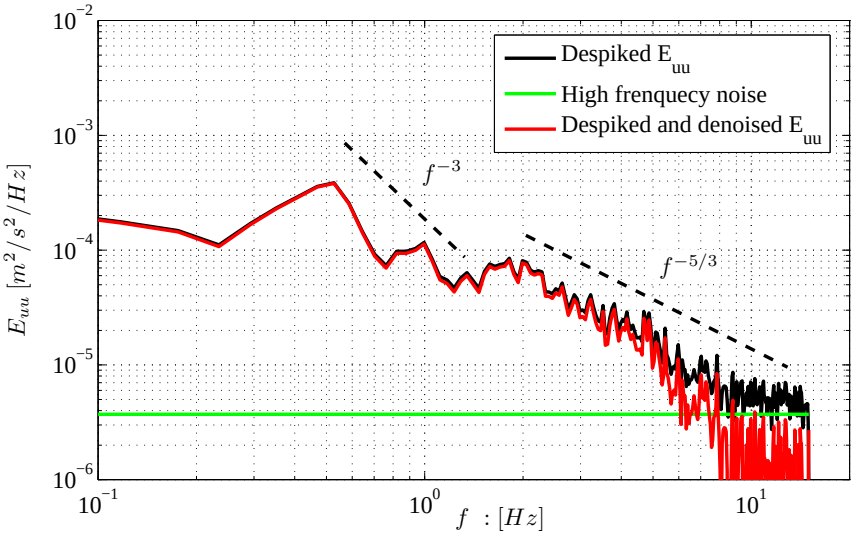

Figure 2.20: Application of denoise progress.

surface which are cheap and easy to obtain. In the other hand, it is very clean for the flume and easy to collect in the end of the channel for reusing.

2.2.4.1 Operating principle

The operating principle is based on the theory of [Hauet, 2006] as shown in the FIG.2.21. Sony HDR-PJ10E is used for recording the film of the flow stream. It is the a high definition video camera with 3 CCD sensors. The format of sequences is HD Blue-ray, the frame-rate of the video-camera is 50 frames (can be change) per second and image resolution is 1920 $\times$ 1080 pixels (3.3 million pixels totally) which enables to have a good precision on the details of the images even for very large view field. For the particle, the wooden sawdust (about 1mm$\times$2mm) is chosen. They has smaller capillarity than the bigger ones and can be floated at the surface of the flow. As shown in FIG.2.21, a zone including the reattachment point is captured by the camera and recorded along 3000 consecutive photos (25 p/s $\times$120 s).

With the several known Ground Reference Points (GRPs) (red points in FIG.2.21), the sequence of images is then orthorectified. The object is to solve the equation below:

$$\begin{aligned} X &= \frac{a_1 i + a_2 j + a_3}{a_7 i + a_8 j + 1} \\ Y &= \frac{a_4 i + a_5 j + a_6}{a_7 i + a_8 j + 1} \end{aligned} \tag{2.6}$$

So, with at least 8 GRPs and the least-square method, the orthorectification is performed as in the FIG.2.21. Displacement of the flow tracers is calculated by a classical cross-correction algorithm. It calculates the correlation R between the interrogation area (IA) centred on a point a_{ij} in the n image and the area centred in the (n+1) image taken with a

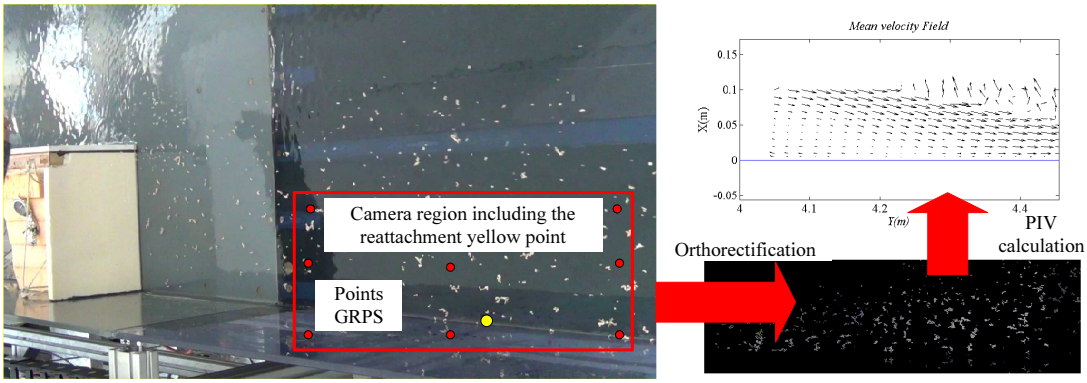

Figure 2.21: Working principle of the LSPIV

time interval of Δt (for us Δt=0.04 s). The correlation coefficient $R(a_{ij}, b_{ij})$ is a similarity index for the gray-scale in density of a group of pixels contained in the two compared areas, expressed as:

$$R(a_{ij}, a_{ij}) = \frac{\Sigma_{i=1}^{M_i}\Sigma_{j=1}^{M_j}[(A_{ij} - \overline{A_{ij}})(B_{ij} - \overline{B_{ij}})]}{[\Sigma_{i=1}^{M_i}\Sigma_{j=1}^{M_j}(A_{ij} - \overline{A_{ij}})^2\Sigma_{i=1}^{M_i}\Sigma_{j=1}^{M_j}(B_{ij} - \overline{B_{ij}})^2]^{1/2}} \tag{2.7}$$

Where M_i and M_j are the size of the interrogation areas (unit in pixel), and A_{ij} and B_{ij} are the distribution of the gray-level intensities in the two areas calculated by the photos. All the calculations are only computed in the searching area (SA). The region size is selected according to the characteristics of the flow condition such as the estimated velocity direction and magnitude in the region. Supposedly, the region should ensure that the displacement of the tracer from the n image is contained in the SA of the (n+1) image. And so, the displacement will be calculated and the mean velocity field is shown in the FIG.2.21.

2.2.4.2 Measurement characteristics

The precision of the LSPIV depends on the physics of the measured flow. For example, the size of the seeding should be changed (2 mm and 4 mm) with the flow mean velocity; the daylight is too intense, so that a peach of black cloth is added on top of the measurement area to prevent any light reflection on the free surface. With the same experimental condition, it is obvious that to have the best mean surface velocity is to start with a very long video-sequence. In our experiments, the video sequences are selected as 2 min. As shown in the FIG.2.22 (R_b= 0.75, S= 0.07, X= 4.3502, Y= 0.0198); the convergence is well obtained after about 2 min. The error of the LSPIV system is hard and complex to estimate [Peltier, 2011]. The relative error product by the size of the sawdust can be estimated as 0.3%(which is obtained in the case with the shortest recirculation zone). However, LSPIV is used here just to detect the reattachment point, the velocity field is not so much focused herein.

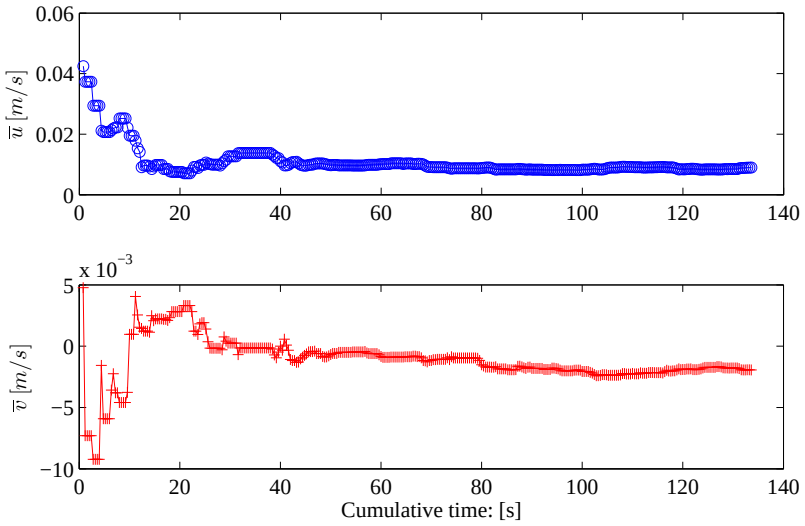

Figure 2.22: Cumulative mean velocity of the point measured by the LSPIV.

2.3 Chapter conclusion

Previous chapter, thanks to a literature review, established the functionalities required by our experiments: modifiable expansion ratio, adjustable water depth with no backwater influence, precise measurements of depth, of velocity and associated turbulent characteristics, detection of the reattachment point.

Firstly, the channel was modified: flexible left wall to adjust the channel width B (and so R_b), modification of the bed to limit topography effects, upstream stilling conditions, additional roughness.

Secondly, all the instruments for measuring the velocity (ADV and LSPIV) and the water depth h (ultrasonic probes) were taken in charge and calibrated.

With all the required functionalities and techniques available, experiments are undertaken, as detailed in next chapter.

Chapter 3

Experimental measurement of the recirculation length

For the length of the recirculation, the literatures pay few attention to the dimensionless analysis or to the experimental method for detecting the attachment point precisely. So in this chapter, we begin with the dimensional analysis for the expansion flow, and then verify the influence of the experimental details. With the preliminary experiments, the main characteristics of this data-set are explained. Finally, the results of the experiments are obtained and compared with literatures.

Contents

3.1 Dimensional analysis

Vaschy-Buckingham Π theorem is a key theorem in dimensional analysis. So here it is used for determining the relationship between the length of the recirculation and the geometrical and flow parameters of the experiments. Given the geometry of the flume and the various physical parameters between the mean physical parameters of the experiments, 11 variables are identified for solving the Vaschy-Buckingham Π theorem. They are summarized in TAB.3.1.

Table 3.1: Consistent parameters in the system

Parameters	Description of the parameters	Scale
L	The unknown recirculation length	[L]
$\overline{u}$	Mean velocity upstream the expansion	[LT^{-1}]
$\overline{u}_L$	Mean velocity downstream the expansion	[LT^{-1}]
h	Flow depth upstream the expansion	[L]
h_L	Flow depth downstream the expansion	[L]
B	Channel width	[L]
d	Enlargement width	[L]
ε	Equivalent sand grain roughness of the bed	[L]
ρ	Density of the liquid in the flume	[ML^{-3}]
μ	Dynamic viscosity of the liquid in the flume	[ML^{-1}T^{-1}]
g	Gravitational acceleration	[LT^{-2}]

Some of these variables are not independent and can be expressed as function of the others. For instance, following literature and as detailed hereafter, the water depth is assumed constant from the upstream to downstream region of the recirculation which writes: $h_L = h$. Therefore, $\overline{u}$ and $\overline{u}_L$ can be related through the constant discharge: $\overline{u}_L = \overline{u}(B-d)/B$. As a result, there are 9 individual parameters in the system. For solving the dimensional analysis, the parameters can be described using three dimensions:
(1) Time scale $[T]$ is defined as $h/\overline{u}$;
(2) Length scale $[L]$is defined as h;
(3) Mass scale $[M]$ is defined as ρh^3.
According to the Vaschy-Buckingham Π theorem, the dimensional analysis yields to 6 dimensionless parameters as equation below:

$$\Pi\left(\frac{L}{h}, \frac{\varepsilon}{h}, \frac{\rho\overline{u}h}{\mu}, \frac{d}{h}, \frac{\overline{u}}{\sqrt{gh}}, \frac{B}{h}\right) = 0 \tag{3.1}$$

By introducing the upstream hydraulic radius as $R_h = \frac{(B-d)h}{2h+(B-d)} = h$, and the expansion ratio $R_b = \frac{B-d}{B}$, the Eq.(3.1) can be written with the classical dimensionless numbers as:

$$\frac{L}{d} = f\left(\frac{\varepsilon}{R_h}, Re, \frac{h}{d}, Fr, \frac{B}{d}\right) \tag{3.2}$$

Where Re and Fr are the upstream Reynolds Re$= (4\overline{u}R_h)/\mu$ and Froude number $\overline{u}/\sqrt{gh}$. The relative bed roughness ε/R_h and the Reynolds number define the Darcy friction coefficient λ in the upstream section through the Colebrook-White equation Eq.(3.3).

$$\frac{1}{\sqrt{\lambda}} = -2\log_{10}\left(\frac{\varepsilon}{3.71\times 4R_h} + \frac{2.51}{Re\sqrt{\lambda}}\right) \tag{3.3}$$

Then λ and h/d define the bed friction number $S = \lambda d/8h$. Eq.(3.2) can thus be rewritten as:

$$\frac{L}{d} = f\left(S, Fr_0, R_{b0}, Re_0, \frac{h_0}{d}\right) \tag{3.4}$$

where the parameters are defined with subscript 0 that refers to the position of the expansion section. Eq.(3.4) indicates that, apart from S (which impact was already studied in the literature especially by [Chu et al., 2004], four additional parameters may influence the dimensionless recirculation length L/d.

The study will investigate the impact of all geometry and flow parameters on the flow recirculation length. To achieve this, we need to establish a set of data that covers a wide range of flow conditions. Then, the characteristics of the data set are given and discussed. For setting the data of the experiments, the following steps are considered:
1. the width of the channel B and the expansion width d are defined.
2. the desired value of S is selected and the parameters λ and $h_0 = h_n$ where $h_n(Q, S_{o,x})$ is the uniform flow depth in the upstream channel, are then computed (as this condition was observed as the best way to obtain a quasi-constant depth over the whole recirculation zone). To do so, Eq.(3.5) is solved firstly:

$$Q = \frac{K_s(bh_0)^{5/3}}{(b+2h_0)^{2/3}} S_0^{1/2} \tag{3.5}$$

where Q is the discharge, K_s is the Strickler's coefficient which can be linked to Chézy coefficient C through the equation:

$$C = K_s \times R_h^{1/6} \tag{3.6}$$

Where C is related to the Darcy-Weisbach friction coefficient factor λ through $C = \sqrt{(2g/c_f)}$ and $c_f = \lambda/4$.

The relative bed roughness ε/R_h and the Reynolds number define the Darcy friction coefficient λ in the upstream section through the Colebrook-White Eq.(3.3). This set of equations is solved to obtain λ and h_0, which also permits to compute Q.
3. the pumps and tailgate are adjusted so as to obtain the normal depth just upstream the expansion ($h_0 = h_n$) in each configuration. TAB.3.2 (where Column 2 presents bottom material and Column 3 is the location of the expansion) summarizes all tested configurations done in the experiments.

As a brief, the dimensionless parameter experiment varies in the rage: Fr$\in [0.17 \sim 0.98]$, $R_b \in [0.3 \sim 0.75]$, $S \in [0.003 \sim 0.25]$, Re$\in [1.9\times 10^3 \sim 1.3\times 10^5]$, $h/d \in [0.025 \sim 0.75]$.

Table 3.2: All tested configurations .

N°	Bottom	Expansion location	B [m]	d [m]	R_b [-]	Q [l/s]	h_0 [mm]	$\overline{u}_0$ [m/s]	λ_0 [-]	S [-]	Re_0 [-]	Fr_0 [-]
1	Gray PVC		0.8	0.1	0.875	19.07	50.15	0.54	0.0201	0.005	7.28×10^{4}	0.775
2		A	0.8	0.1	0.875	8.32	29.89	0.40	0.0239	0.01	3.34×10^{4}	0.735
3			0.8	0.1	0.875	5.13	22.25	0.33	0.0267	0.015	2.10×10^{4}	0.705
4			0.8	0.1	0.875	3.64	18.1	0.29	0.029	0.02	1.51×10^{4}	0.682
5			0.8	0.1	0.875	2.09	13.01	0.23	0.0333	0.032	8.79×10^{3}	0.643
6			0.8	0.2	0.75	16.15	50.24	0.54	0.0201	0.01	7.04×10^{4}	0.764
7			0.8	0.2	0.75	9.97	37.03	0.45	0.0222	0.015	4.52×10^{4}	0.745
8			0.8	0.2	0.75	4.05	21.25	0.32	0.0272	0.032	1.92×10^{4}	0.696
9			0.8	0.2	0.75	2.39	15.48	0.26	0.031	0.05	1.16×10^{4}	0.661
10			0.8	0.2	0.75	1.05	9.57	0.18	0.0383	0.1	5.18×10^{3}	0.597
11			0.8	0.3	0.625	38.35	102.41	0.75	0.0164	0.006	1.66×10^{5}	0.748
12			0.8	0.3	0.625	21.26	68.73	0.62	0.0183	0.01	1.02×10^{5}	0.754
13			0.8	0.3	0.625	13.24	50.37	0.53	0.0201	0.015	6.73×10^{4}	0.748
14			0.8	0.3	0.625	9.43	40.54	0.47	0.0216	0.02	4.96×10^{4}	0.738
15			0.8	0.3	0.625	5.41	28.59	0.38	0.0244	0.032	2.96×10^{4}	0.715
16			0.8	0.3	0.625	3.19	20.67	0.31	0.0276	0.05	1.80×10^{4}	0.686
17			0.8	0.3	0.625	1.41	12.67	0.22	0.0338	0.1	8.20×10^{3}	0.632
18		B	0.8	0.2	0.75	4.05	21.25	0.32	0.0272	0.032	1.92×10^{4}	0.696
19		D	0.8	0.2	0.75	4.05	21.25	0.32	0.0272	0.032	1.92×10^{4}	0.696
20		C	0.8	0.2	0.75	36.51	85.65	0.71	0.0171	0.005	1.45×10^{5}	0.775
21			0.8	0.2	0.75	16.15	50.24	0.54	0.0201	0.01	7.04×10^{4}	0.764
22			0.8	0.2	0.75	9.97	37.03	0.45	0.0222	0.015	4.52×10^{4}	0.745
23			0.8	0.2	0.75	7.08	29.93	0.39	0.0239	0.02	3.28×10^{4}	0.728
24			0.8	0.2	0.75	4.05	21.25	0.32	0.0272	0.032	1.92×10^{4}	0.696
25			0.8	0.2	0.75	2.39	15.48	0.26	0.031	0.05	1.16×10^{4}	0.661
26			0.8	0.2	0.75	1.61	12.24	0.22	0.0343	0.07	7.87×10^{3}	0.633
27			0.8	0.2	0.75	1.05	9.57	0.18	0.0383	0.1	5.18×10^{3}	0.597
28			0.8	0.2	0.75	0.78	8.05	0.16	0.0419	0.13	3.87×10^{3}	0.575
29			0.8	0.2	0.75	0.48	6.05	0.13	0.0484	0.2	2.39×10^{3}	0.543
30			0.8	0.2	0.75	0.37	5.25	0.12	0.0525	0.25	1.85×10^{3}	0.518
31			0.8	0.3	0.625	38.35	102.41	0.75	0.0164	0.006	1.66×10^{5}	0.748
32			0.8	0.3	0.625	21.26	68.73	0.62	0.0183	0.01	1.02×10^{5}	0.754
33			0.8	0.3	0.625	13.24	50.37	0.53	0.0201	0.015	6.73×10^{4}	0.748
34			0.8	0.3	0.625	9.43	40.54	0.47	0.0216	0.02	4.96×10^{4}	0.738
35			0.8	0.3	0.625	5.41	28.59	0.38	0.0244	0.032	2.96×10^{4}	0.715
36			0.8	0.3	0.625	3.19	20.67	0.31	0.0276	0.05	1.80×10^{4}	0.686
37			0.8	0.3	0.625	2.14	16.26	0.26	0.0304	0.07	1.23×10^{4}	0.659
38			0.8	0.3	0.625	1.41	12.67	0.22	0.0338	0.1	8.20×10^{3}	0.632
39			0.8	0.3	0.625	1.04	10.58	0.20	0.0367	0.13	6.09×10^{3}	0.611
40			0.8	0.3	0.625	0.63	7.91	0.16	0.0422	0.2	3.73×10^{3}	0.572
41			0.8	0.3	0.625	0.49	6.83	0.14	0.0455	0.25	2.91×10^{3}	0.555
42	White PVC		0.8	0.2	0.75	20	156	0.21	0.0202	0.003	6.70×10^{4}	0.173
43			0.8	0.2	0.75	29.51	74.33	0.66	0.0178	0.006	1.20×10^{5}	0.775
44			0.8	0.2	0.75	24.62	65.99	0.62	0.0185	0.007	1.03×10^{5}	0.773
45			0.8	0.2	0.75	21.03	59.55	0.59	0.0191	0.008	8.93×10^{4}	0.770
46			0.8	0.2	0.75	16.15	50.24	0.54	0.0201	0.01	7.04×10^{4}	0.764
47			0.8	0.2	0.75	13.01	43.78	0.50	0.021	0.012	5.78×10^{4}	0.756
48			0.8	0.2	0.75	8.03	32.35	0.41	0.0233	0.018	3.69×10^{4}	0.735
49			0.8	0.2	0.75	5.43	25.42	0.36	0.0254	0.025	2.55×10^{4}	0.713
50			0.8	0.2	0.75	4.05	21.25	0.32	0.0272	0.032	1.92×10^{4}	0.696
51			0.8	0.2	0.75	3.51	19.5	0.30	0.0282	0.036	1.68×10^{4}	0.686
52			0.8	0.2	0.75	3.11	18.12	0.29	0.029	0.04	1.49×10^{4}	0.679
53			0.8	0.2	0.75	1.92	13.62	0.23	0.0327	0.06	9.35×10^{3}	0.643
54			0.8	0.2	0.75	1.37	11.17	0.20	0.0357	0.08	6.72×10^{3}	0.618
55			0.53	0.1	0.812	9.13	43.97	0.48	0.0211	0.006	5.38×10^{4}	0.736
56			0.53	0.1	0.812	5.01	30.03	0.39	0.024	0.01	3.12×10^{4}	0.715
57			0.53	0.1	0.812	3.11	22.33	0.32	0.0268	0.015	2.00×10^{4}	0.692
58			0.53	0.1	0.812	2.21	18.17	0.28	0.0291	0.02	1.45×10^{4}	0.670
59			0.53	0.1	0.812	1.28	13.05	0.23	0.0334	0.032	8.57×10^{3}	0.638
60			0.53	0.1	0.812	0.76	9.61	0.18	0.0384	0.05	5.17×10^{3}	0.599

N°	Bottom	Expansion location	B [m]	d [m]	R_b [-]	Q [l/s]	h_0 [mm]	$\overline{u}_0$ [m/s]	λ_0 [-]	S [-]	Re_0 [-]	Fr_0 [-]
61			0.53	0.2	0.625	20	150	0.40	0.0191	0.003	9.69×10^{4}	0.333
62			0.53	0.2	0.625	14.99	75.27	0.60	0.0181	0.006	9.52×10^{4}	0.703
63			0.53	0.2	0.625	8.41	50.75	0.50	0.0203	0.01	5.95×10^{4}	0.712
64			0.53	0.2	0.625	5.27	37.34	0.43	0.0224	0.015	3.98×10^{4}	0.707
65			0.53	0.2	0.625	3.77	30.14	0.38	0.0241	0.02	2.95×10^{4}	0.697
66			0.53	0.2	0.625	2.18	21.38	0.31	0.0274	0.032	1.79×10^{4}	0.675
67			0.53	0.2	0.625	1.3	15.54	0.25	0.0311	0.05	1.10×10^{4}	0.650
68			0.53	0.2	0.625	0.88	12.29	0.22	0.0344	0.07	7.58×10^{3}	0.625
69			0.53	0.2	0.625	0.58	9.62	0.18	0.0385	0.1	5.07×10^{3}	0.595
70			0.53	0.2	0.625	0.43	8.06	0.16	0.0419	0.13	3.79×10^{3}	0.575
71			0.53	0.2	0.625	0.26	6.07	0.13	0.0486	0.2	2.32×10^{3}	0.532
72			0.4	0.2	0.5	20	137	0.73	0.017	0.003	1.29×10^{5}	0.630
73			0.4	0.2	0.5	8.04	76.54	0.53	0.0184	0.006	6.95×10^{4}	0.606
74			0.4	0.2	0.5	4.63	51.45	0.45	0.0206	0.01	4.67×10^{4}	0.634
75			0.4	0.2	0.5	2.96	37.77	0.39	0.0227	0.015	3.28×10^{4}	0.644
76			0.4	0.2	0.5	2.14	30.45	0.35	0.0244	0.02	2.50×10^{4}	0.643
77			0.4	0.2	0.5	1.26	21.55	0.29	0.0276	0.032	1.58×10^{4}	0.636
78	White PVC	C	0.4	0.2	0.5	0.75	15.65	0.24	0.0313	0.05	9.90×10^{3}	0.612
79			0.4	0.2	0.5	0.51	12.35	0.21	0.0346	0.07	6.93×10^{3}	0.594
80			0.4	0.2	0.5	0.34	9.67	0.18	0.0387	0.1	4.73×10^{3}	0.571
81			0.4	0.2	0.5	0.25	5.5	0.23	0.0599	0.193	3.62×10^{3}	0.979
82			0.33	0.2	0.4	10	140	0.55	0.0206	0.004	7.45×10^{4}	0.469
83			0.33	0.2	0.4	4.74	77.96	0.47	0.0187	0.006	5.06×10^{4}	0.535
84			0.33	0.2	0.4	2.8	52.25	0.41	0.0209	0.01	3.65×10^{4}	0.576
85			0.33	0.2	0.4	1.82	38.28	0.37	0.023	0.015	2.69×10^{4}	0.597
86			0.33	0.2	0.4	1.34	30.81	0.33	0.0247	0.02	2.14×10^{4}	0.609
87			0.33	0.2	0.4	0.8	21.76	0.28	0.0279	0.032	1.41×10^{4}	0.612
88			0.33	0.2	0.4	0.48	15.77	0.23	0.032	0.05	9.07×10^{3}	0.596
89			0.33	0.2	0.4	0.33	12.44	0.20	0.035	0.07	6.51×10^{3}	0.584
90			0.33	0.2	0.4	0.22	9.72	0.17	0.039	0.1	4.50×10^{3}	0.564
91			0.29	0.2	0.3	10	145	0.77	0.0207	0.004	8.04×10^{4}	0.643
92			0.29	0.2	0.3	1.59	53.43	0.33	0.0214	0.01	2.47×10^{4}	0.457
93			0.29	0.2	0.3	1.06	39.04	0.30	0.0234	0.015	1.93×10^{4}	0.488
94			0.29	0.2	0.3	0.79	31.36	0.28	0.0251	0.02	1.58×10^{4}	0.505
95			0.29	0.2	0.3	0.48	22.09	0.24	0.0283	0.032	1.09×10^{4}	0.519
96			0.29	0.2	0.3	0.3	15.97	0.21	0.0319	0.05	7.51×10^{3}	0.528

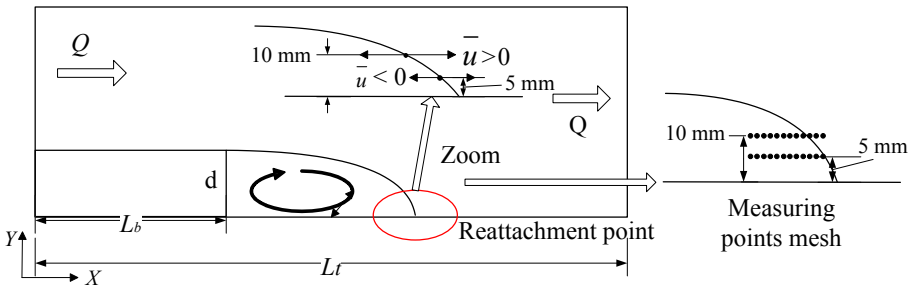

Figure 3.1: Sketch of the ADV method for detecting the reattachment point

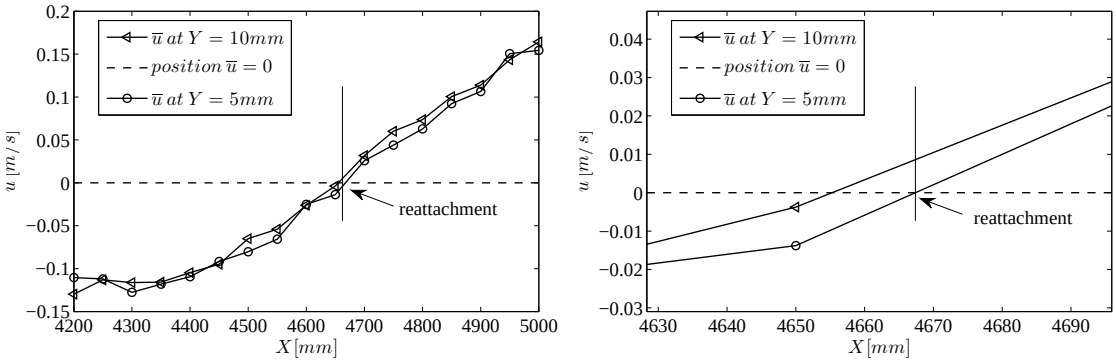

Figure 3.2: Streamwise velocity $\overline{u}$ distribution for different Y.

3.2 The methodology for detecting the reattachment point

[Riviere et al., 2011] have used long-time exposure photographs for finding the location of the reattachment (Figure 4), but this method appeared time consuming and with a bad accuracy as results depend on the time exposure chosen. Thanks to ADV, the work will be more simple and precise if the water depth is larger than 20mm. The principle is shown in FIG.3.1.

Firstly, a region which contains the reattachment point is roughly identified using floating tracers. Then a mesh grid covering a region of 80cm length in the streamwise direction is set up for the automation of ADV displacement. With the measurement of the mean velocity and the process by Matlab, the point where the time average streamwise velocity component $\overline{u}$ passes from negative to positive is found out. Another line of the mesh in the Y= 10mm to the wall is traced for confirming the measurement. The transverse point should be shorter than the point for Y = 5mm according to the physics. For the disadvantage of the ADV, the velocity at the wall (Y= 0mm) can not be measured. Thus, the near wall velocity measured by ADV is replaced with the velocity at Y=5mm. One example is exhibited in the FIG.3.2 (Condition S=0.01 with the bottom roughness).

From FIG.3.2, it is obvious that the mean velocity $\overline{u}$ passes from negative to positive along the streamwise direction. The two positions are nearly the same for the two different

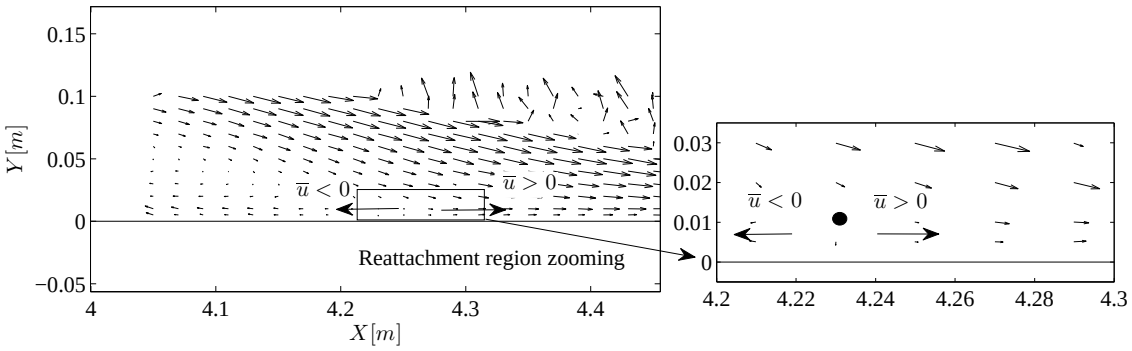

Figure 3.3: Sketch for detecting the reattaching point of LSPIV.

y distances from the wall. After zooming the local part near the reattachment, we can see that the reattachment for Y= 10mm is upstream of the one in Y= 5mm even though the difference is only about 10mm which is negligible in the experiment. So, this method is approved for our flows and will be used for detecting the reattachment point of the recirculation zone.

For LSPIV, the mean velocity field is used for detecting the reattachment point. As shown in the FIG.3.3, the point where the streamwise mean velocity changes from negative to positive is the point we define as the reattachment. For this case , the end of the recirculation is 4.24 m. The enlargement is located at 3.56m and d= 0.2m. Hence, L/d is calculated as $\frac{(4.24-3.56)}{0.2}$=3.4.

3.3 Setting experimental details

Because of the great scale of the experiment, many influences on the length of recirculation zone exist are tested below. To do so, a series of experiments were performed in order to detect the best suited parameters.

3.3.1 Preliminary tests

Firstly, two similar preliminary tests are performed in order to investigate the influence of the backwater curve on the recirculation length. For experiment N°50 and 50(a) which have similar boundary conditions, the difference is just screws added for N°50 in order to suppress a small bump on the bed, present in N°50(a). The backwater curve is illustrated in FIG.3.4 (−− is the configuration without screws fixed at X= 4m). Due to limited topographical raise at X= 4m for N°50(a) (without screws), the water depth decreases locally. The FIG.3.4 also reports that the length of the recirculation is L/d=5.45 for N°50(a), which is 6% shorter than the one for N°50. This can be explained qualitatively

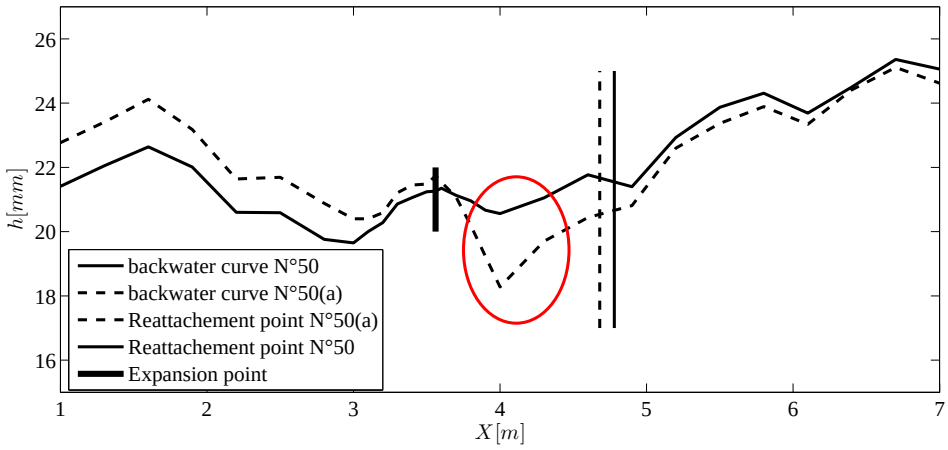

Figure 3.4: Water curves of the two configurations.

in the equation below:

$$\frac{dh}{dx} = \frac{S_{o,x} - J}{1 - Fr^2} \tag{3.7}$$

With the assumption that the loss of the energy J is negligible and the flume slope $S_{o,x}$ is constant. The streamwise mean velocity increases when the water depth decreases for No°50(a).

Hence, the backwater curve appears to play an important role in the length of the recirculation L/d. In the following experiments, we aim at finding the best configuration in our channel: to find the most stable possible backwater curve in the recirculation region: between x= 0 and $x = L$. With the following experiences, the influence on the backwater curve and on L/d is separated into 5 parts:
(1) Influence of the upstream conditions
(2) Influence of the downstream conditions
(3) Influence of the position of the expansion
(4) Influence of the detailed topography
(5) Influence of the channel and expansion widths

3.3.2 Influence of the upstream conditions

Comparing experiments N°8(a), N°8 and N°8(b)(as in TAB.3.3), the flow conditions (such as discharge and water depth) are kept constant (the bed friction number is S= 0.032 and the normal water depth is 21.25mm). The difference between the 3 cases is only the upstream boundary condition. The upstream conditions for N°8(a) is a partially blocked honeycomb which influences the upstream backwater curve from X= 1m and 2m downstream from the channel inlet as shown in FIG.3.5. However, after the expansion, the

Table 3.3: List of the parameters for three flows with different inlet condition

N°	Bottom	Condition	R_b	Q [l/s]	h_n [mm]	L/d	S	Addition condition
(8-a)	PVC	A	0.750	4.045	21.25	7.7	0.032	Partially blocked inlet
8			0.750	4.045	21.25	8.1	0.032	Clean inlet condition
(8-b)			0.750	4.045	21.25	8.2	0.032	Only honeycomb

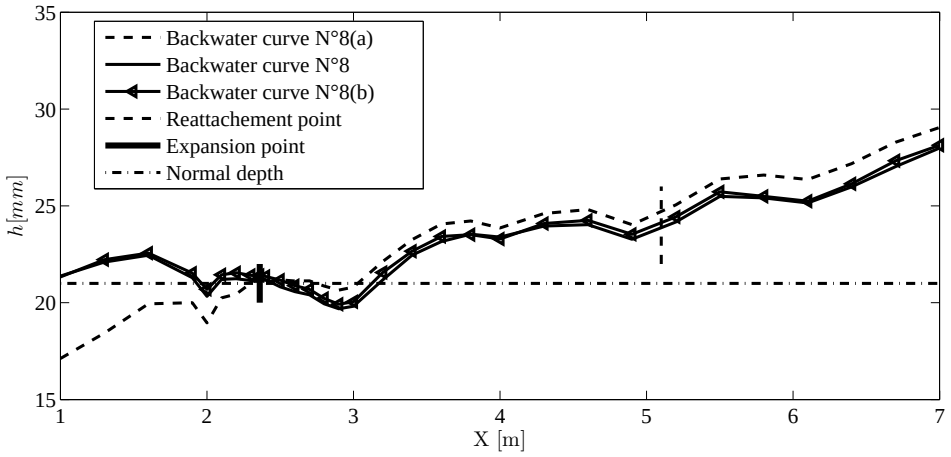

Figure 3.5: Three backwater curves in different upstream configurations.

backwater curve is not affected and remains similar. The dimensionless recirculation length is strongly reduced compared to N°8.

For N°8(b), the float board is removed and only the honeycomb is considered in the inlet boundary. The change in the length of the recirculation is negligible. To conclude, the inlet boundary does not influence much the flow as long as the honeycomb remains clean and correctly positioned (N°8). During the final experiments, the honeycomb was then regularly removed for cleaning up.

3.3.3 Influence of the downstream condition

In this section, the focus is to detect how the downstream condition influences the recirculation zone and especially its length L/d. The FIG.2.7 shows the backwater for the boundary condition used, including a tailgate and a small reservoir.

First, in the experiments including experiments N°19 and N°19(a) , the difference is the location of the tailgate which is moved from X=8m (in N°19) to X=6m (in N°19a)(details are in TAB.3.4). The backwater curves are shown in FIG.3.5 and exhibit similar general patterns. L/d for N°19(a) is 6.4 which is smaller than for N°19 (equal to 6.7). The difference of L/d remains limited so that in the following, the tailgate is located at the end of the channel (X= 8m) as for N°19.

Table 3.4: List of the consistent parameters for two flows

N°	Bottom	Condition	R_b	Q [l/s]	h_n [mm]	L/d	S	Taigate condition
19	Gray PVC	D	0.750	4.045	21.25	6.7	0.032	X=8.0m
19(a)			0.750	4.045	21.25	6.4	0.032	X=6.0m

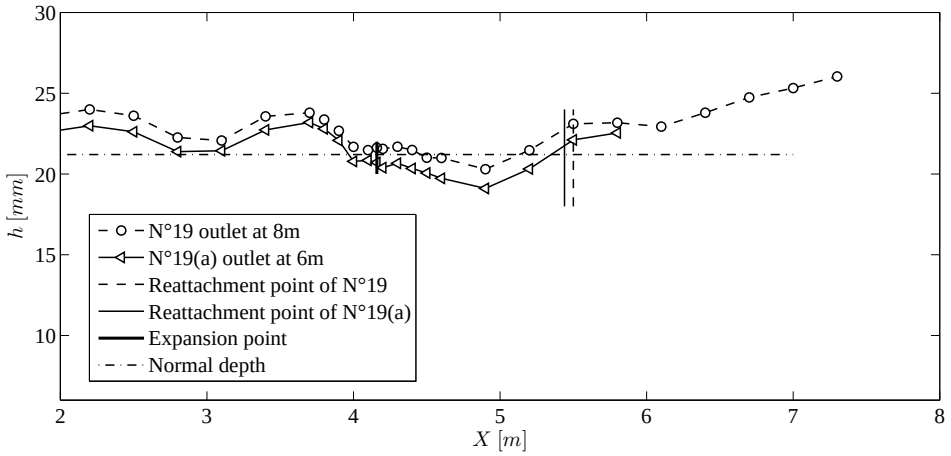

Figure 3.6: Two backwater curves in different downstream configurations.

Now, for the 3 following experiments N°8(c), 8(d) and 8(e), the height of the tailgate is slightly modified (everything else being kept similar) of +2mm (for N°8d) and -2mm (for N°8(e)) compared to N°8(c). The backward curves are shown in FIG.3.7. It is obvious that the backwater curve for N°8(d) remains higher than for N°8(c) over the whole channel and for N°8(e) it remains lower for $X >$2m (downstream from the expansion). The consequence for L/d is small but cannot be neglected : as the water depth in the expansion increases, the recirculation length increases (from L/d= 7.375 for N°8(e) to L/d= 7.6 for N°8(d). This result confirm the conclusion in section 3.3.1. For the final experiments, the water depth in the expansion region will be kept equal to h_n.

Furthermore, we tested the influence of adding gravels in the small reservoir of the downstream boundary condition for two configurations (N°5 and N°15) in order to try to reduce the slope of the backwater curve downstream. Comparing N°5 with N°5(a) and

Table 3.5: List of the consistent parameters for different h_n setting

N°	Bottom	Condition	R_b	Q [l/s]	h_n [mm]	L/d	S	Water depth
8(c)	White PVC without screws	A	0.750	4.045	21.25	7.45	0.032	h_n
8(d)			0.750	4.045	23.25	7.6	0.032	$h_n + 2$mm
8(e)			0.750	4.045	20.25	7.375	0.032	$h_n - 2$mm

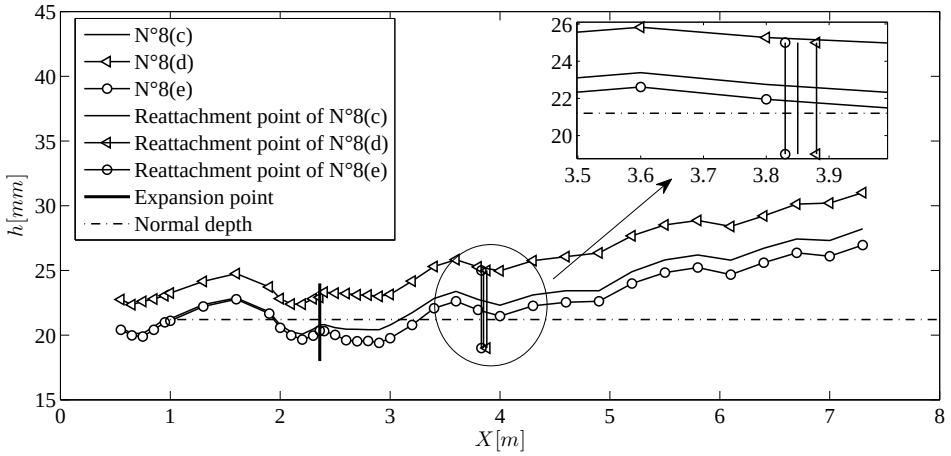

Figure 3.7: Two backwater curves in different h_n configurations.

Table 3.6: Consistent parameters with or wothout gravels

N°	Bottom	Condition	R_b	Q [l/s]	h_n [mm]	L/d	S	Tailgate condition
5	Gray	A	0.875	2.087	13.01	3.6	0.032	
5(a)			0.875	2.087	13.01	3.8	0.032	gravels
15	PVC		0.625	5.408	28.59	8.267	0.032	
15(a)			0.625	5.408	28.59	8.483	0.032	gravels

N°15 with N°15(a), the impact on the backwater curve seems limited as shown in the FIG.3.8. For case N°15, the change in L/d is 0.2, that is 2.3% of L/d (equal to 8.7). So for the final experiments, the reservoir is kept empty.

3.3.4 Influence of the expansion location

In this section, the location of the channel expansion is modified by using longer and shorter boxes and then four different positions are tested, namely A (N°8), B(N°18), C(N°24), D(N°19) as shown in FIG.3.9. For each case, the uniform depth is obviously the same and the tailgate is adjusted to obtain h_n at the expansion location, equal to x=0. In FIG.3.9, the abscise is no more X, but rather x with x=0 at the expansion.

In FIG.3.10, it is obvious that in the recirculation region (between x=0 and the reattachment line) the water depth in condition C (the black curve) varies less than the three others. The consequence for the recirculation length L/d is obvious, it varies from 6 to 8 (33% difference). So after all, condition C is chosen for the position of the expansion for the final experiments.

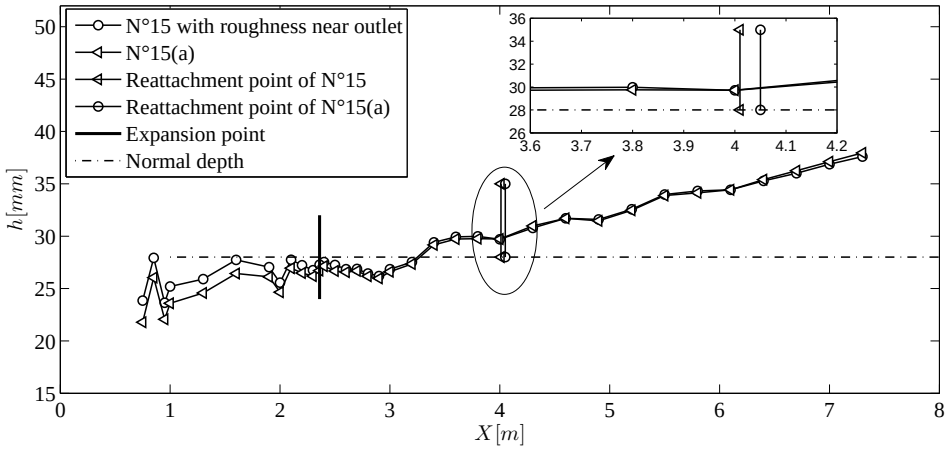

Figure 3.8: Two backwater curves with or without gravels near the tailgate.

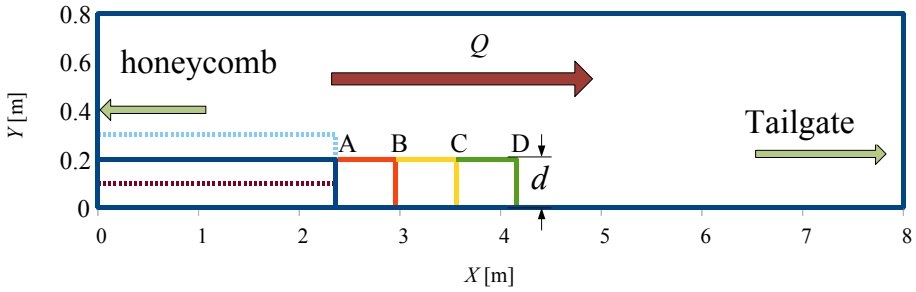

Figure 3.9: Configuration of the different positions of the expansion in experiments

Table 3.7: Consistent parameters for different expansion position

N°	Bottom	Condition	R_b	Q [l/s]	h_n [mm]	S	L/d
8	Gray	A	0.75	4.05	21.25	0.032	8.05
18		B					8.1
24	PVC	C					6.05
19		D					6.7

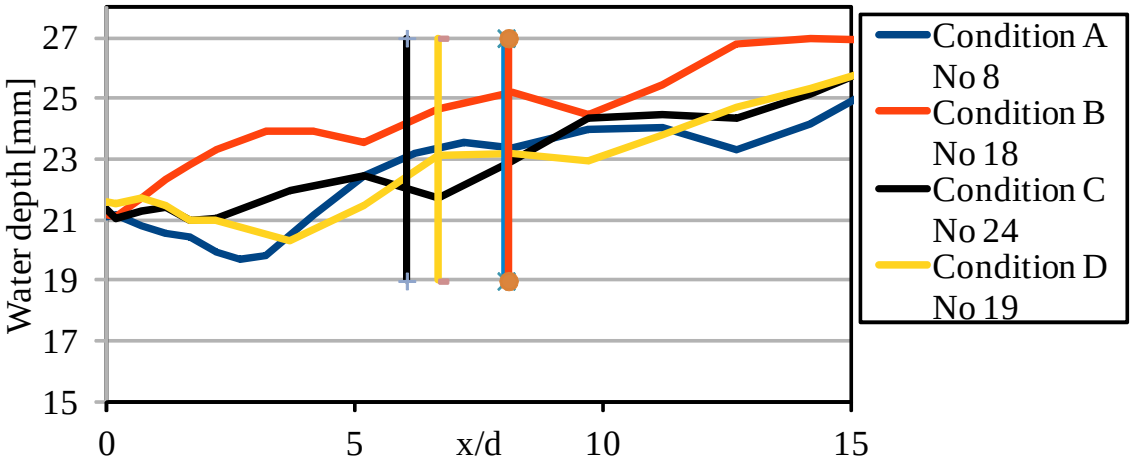

Figure 3.10: Backwater curves of 4 positions of expansion

Table 3.8: Consistent parameters for different bottom

N°	Bottom	Condition	R_b	Q [l/s]	h_n [mm]	S	L/d
24	Gray PVC	C	0.75	4.05	21.25	0.032	6.05
50	White PVC with screws						5.8
50(a)	White PVC without screws						5.45

3.3.5 Influence of the bed coverage

For the bottom of the flume, we tested two types of coverage (namely “gray PVC” and “white PVC”) for the smooth condition (ε=5$\times$10^{-5}); moreover, for the white PVC case, we added screws to smoothen even more the bed topography. The topographies are compared in FIG.3.12 for the three coverages. The three topographies exhibit some protuberances, for instance, for the gray PVC coverage some local protuberance appear at X= 2m and X= 4 m. The white PVC bottom with screws is more regular than the two other coverages in the centre region (X= 3−5 m).

The backwater curves for one flow configuration reported in TAB.3.8 are illustrated in FIG.3.12. They appear to be quite different from each other. In the recirculation region between the two vertical lines (X= 3.5 m to 4.8 m), the average water depth variation between the three coverages is 3 mm which represents 15% of the water depth. The backwater curve for the white PVC with screws is obviously less varied than the two others. It also appears that L/d varies from 5.45 in N°50(a) to L/d=6.05 in N°24, corresponding to 10% difference. Finally, the white PVC with screws is chosen as the final experiment coverage.

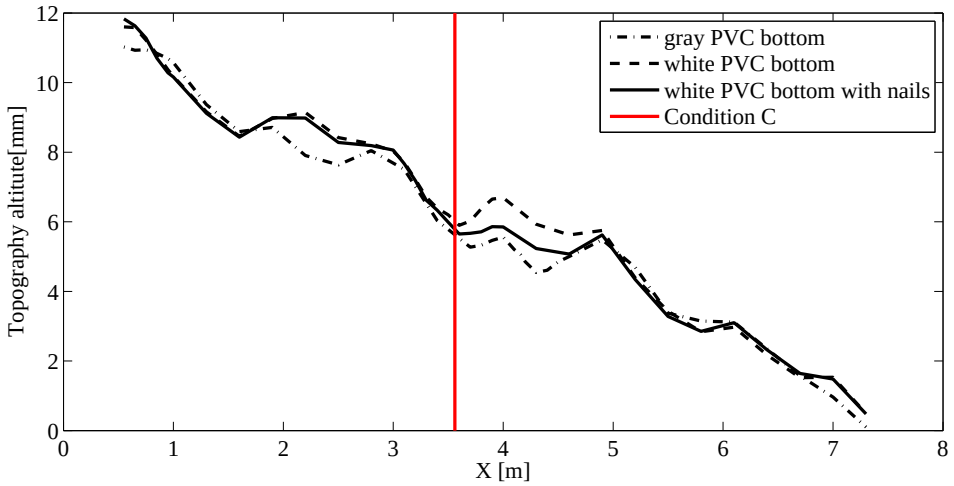

Figure 3.11: Absolute altitude of topography in different bottom condition: Y= 0.5m

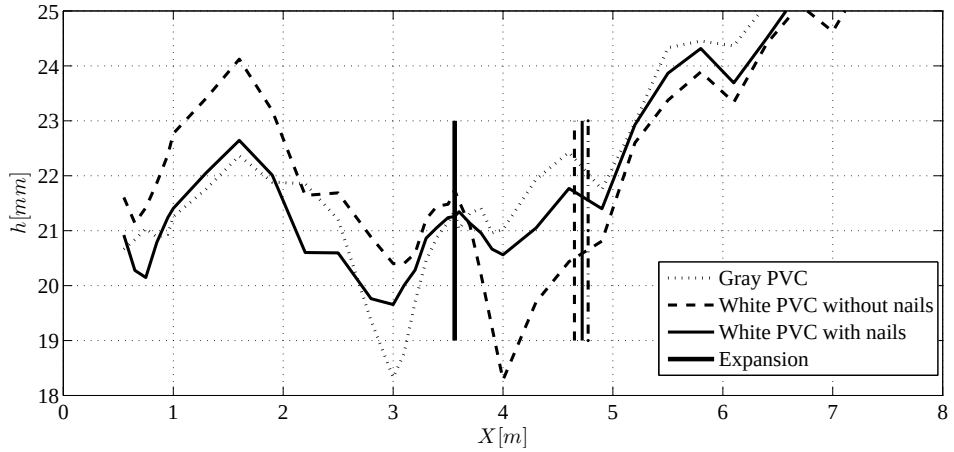

Figure 3.12: Three different water lines in different bottom condition: Y= 0.5m

Table 3.9: Consistent parameters for different configurations with same R_b

N°	Bottom	Condition	R_b	Q [l/s]	h_n [mm]	S	L/d	Additional condition
35(a)	Gray	C	0.625	8.41	50.75	0.01	12.75	B=0.533m,d=0.2m
35	PVC	C	0.625	21.26	68.73	0.01	9.333	B=0.8m,d=0.3m

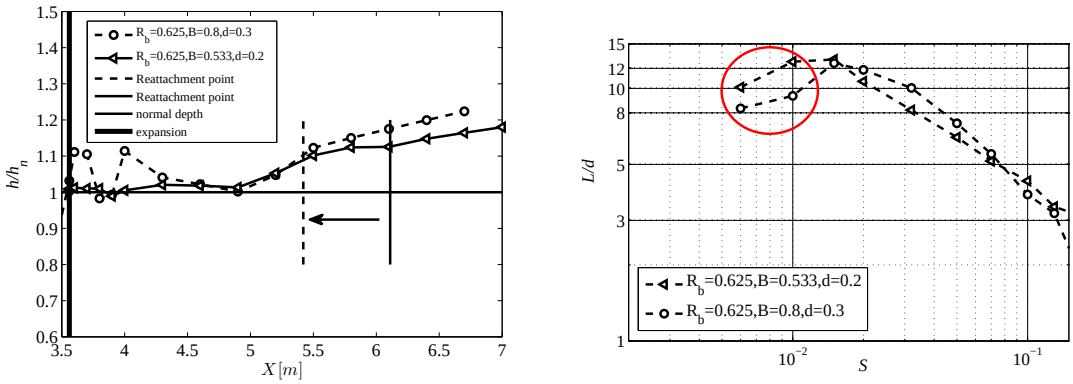

(a) Backwater curve (b) Dimensionless length L/d

Figure 3.13: Results comparison with different B and d.

3.3.6 Influence of the channel and expansion widths

To reach the same expansion ratio R_b value, it is possible to modify both B and d together. The aim of the present section is to detect the influence of such modification. In the present section, we fix R_b=0.625 with two conditions: N°35 with large B and d and N°35(a) with smaller B and d. As L/d should theoretically remain equal (no parameter change), L will be larger for N°35. The main consequence is that the reattachment point is moved towards the downstream end of the channel and may interact with the downstream boundary condition.

FIG.3.13 (a) shows that the backwater curve is higher for N°35 near the reattachment point, as the downstream condition is closer than for the other case, this can produce an adverse pressure gradient as shown as the arrow. The consequence in term of recirculation length is high, and L/d varies from 12.75 for N°35(a) to 9.33 for N°35. FIG.3.13 (b) reveals that the L/d decreases as d increases from 0.2 to 0.3m is maximum for lower S values, that is for larger L values, where the reattachment point is the closest from the downstream end of the channel. In order to limit the interaction of the recirculation zone with the downstream boundary condition, the configuration d=0.2m is selected for final experiments.

3.4 Final data-set

Following all conclusions from the tests detailed above, in section 3.3, the selected parameters for final experiments are summarized: the white PVC bottom is chosen, the condition C is chosen for the expansion position; d= 0.2m and R_b is varied by changing B; the clean honeycomb with float board is used as inlet condition, and finally the normal depth at the expansion is controlled by the tailgate at X= 8m. Finally, the data used for the final analysis in the following chapter is listed in TAB.3.9 below. It comprises 5 series corresponding to 5 different R_b values (corresponding to 5 different B values), with fixed d=0.2 m: 0.75, 0.625, 0.5, 0.4 and 0.3. For each series, about 10 to 15 data is considered with varying discharges and corresponding normal depth, leading to varying S values.

The analysis is performed by discussing the impact of each parameter from Eq.(3.2) after the other. The equation is repeated here for simplicity:

$$\frac{L}{d} = f\left(\frac{\varepsilon}{R_{h0}}, Re_0, \frac{h_0}{d}, Fr_0, \frac{B}{d}\right)$$

All the results in the TAB.3.10 are plotted in FIG.3.14. The results were also discussed in the [Chatelain et al., 2014]. Error bars are given for $R_b = 0.75$(others are similar). This is the worst case as the uncertainty on L/d implies ΔL that is fixed; the uncertainty on L does not affect significantly the vertical position on the graphs, and thus the future conclusions. The positive horizontal error bars for S is derived from the measurement uncertainty on h (ultrasonic probes); they hardly appear on FIG.3.14 and have no influence on the conclusions. Conversely, the negative error bars are not due to a measurement error but to the water depth evolution along the X axis. Indeed, during the experiments, the flow, in sub-critical regime, undergoes a drastic increase of the water depth as it passes through an expansion [Rivière et al., 2008]. This relative increase can reach 5%(several points less than 10%) of the water depth. Nevertheless, the global tendency is not affected by the experimental error and the conclusion does not change.

3.4.1 Influence of Fr and Re

The influence of Fr on L/d for fixed values of the remaining parameters is not performed in the present thesis. Indeed, [Rivière et al., 2008] showed that the Froude number Fr has a negligible effect on L/d, at least as far as the flow remains sub-critical (its range in the experiments was $0.32<\mathrm{Fr}_0<0.92$), see FIG.3.15. Moreover, influence of Re_0 is assumed ot be negligible as the flow remains turbulent ($\mathrm{Re}_0 > 10^4$ except for the largest S configurations).

3.4.2 Influence of R_b

Our results show undoubtedly that S alone does not permit to characterize the dimensionless recirculation length L/d. Indeed, five distinct curves are obtained for the five fixed R_b values. For a given S, L/d first increases as R_b decreases, reaches a maximum value for a

Table 3.10: All the tests and the results of L/d with fixing d=0.2m

N°	B [m]	d [m]	R_b	Q [l/s]	h_0 [mm]	$\overline{u}_0$ [m/s]	λ_0 [-]	S [-]	Re_0 [-]	Fr_0 [-]	L/d [-]
22	0.8	0.2	0.75	9.97	37.03	0.45	0.0222	0.015	4.52×10^4	0.745	9.05
23	0.8	0.2	0.75	7.08	29.93	0.39	0.0239	0.02	3.28×10^4	0.728	7.65
26	0.8	0.2	0.75	1.61	12.24	0.22	0.0343	0.07	7.87×10^3	0.633	4.00
27	0.8	0.2	0.75	1.05	9.57	0.18	0.0383	0.1	5.18×10^3	0.597	3.00
28	0.8	0.2	0.75	0.78	8.05	0.16	0.0419	0.13	3.87×10^3	0.575	2.75
29	0.8	0.2	0.75	0.48	6.05	0.13	0.0484	0.2	2.39×10^3	0.543	2.25
30	0.8	0.2	0.75	0.37	5.25	0.12	0.0525	0.25	1.85×10^3	0.518	1.95
42	0.8	0.2	0.75	20	156	0.21	0.0202	0.003	6.70×10^4	0.173	6.45
43	0.8	0.2	0.75	29.51	74.33	0.66	0.0178	0.006	1.20×10^5	0.775	8.95
45	0.8	0.2	0.75	21.03	59.55	0.59	0.0191	0.008	8.93×10^4	0.770	9.40
46	0.8	0.2	0.75	16.15	50.24	0.54	0.0201	0.01	7.04×10^4	0.764	10.30
50	0.8	0.2	0.75	4.05	21.25	0.32	0.0272	0.032	1.92×10^4	0.696	5.80
51	0.8	0.2	0.75	3.51	19.5	0.30	0.0282	0.036	1.68×10^4	0.686	5.70
52	0.8	0.2	0.75	3.11	18.12	0.29	0.029	0.04	1.49×10^4	0.679	5.45
53	0.8	0.2	0.75	1.92	13.62	0.23	0.0327	0.06	9.35×10^3	0.643	4.45
54	0.8	0.2	0.75	1.37	11.17	0.20	0.0357	0.08	6.72×10^3	0.618	3.75
61	0.53	0.2	0.625	20	150	0.40	0.0191	0.003	9.69×10^4	0.333	6.60
62	0.53	0.2	0.625	14.99	75.27	0.60	0.0181	0.006	9.52×10^4	0.703	10.10
63	0.53	0.2	0.625	8.41	50.75	0.50	0.0203	0.01	5.95×10^4	0.712	12.75
64	0.53	0.2	0.625	5.27	37.34	0.43	0.0224	0.015	3.98×10^4	0.707	13.00
65	0.53	0.2	0.625	3.77	30.14	0.38	0.0241	0.02	2.95×10^4	0.697	10.65
66	0.53	0.2	0.625	2.18	21.38	0.31	0.0274	0.032	1.79×10^4	0.675	8.20
67	0.53	0.2	0.625	1.3	15.54	0.25	0.0311	0.05	1.10×10^4	0.650	6.40
68	0.53	0.2	0.625	0.88	12.29	0.22	0.0344	0.07	7.58×10^3	0.625	5.15
69	0.53	0.2	0.625	0.58	9.62	0.18	0.0385	0.1	5.07×10^3	0.595	4.30
70	0.53	0.2	0.625	0.43	8.06	0.16	0.0419	0.13	3.79×10^3	0.575	3.40
71	0.53	0.2	0.625	0.26	6.07	0.13	0.0486	0.2	2.32×10^3	0.532	2.95
72	0.4	0.2	0.5	20	137	0.73	0.017	0.003	1.29×10^5	0.630	7.70
73	0.4	0.2	0.5	8.04	76.54	0.53	0.0184	0.006	6.95×10^4	0.606	9.60
74	0.4	0.2	0.5	4.63	51.45	0.45	0.0206	0.01	4.67×10^4	0.634	13.60
75	0.4	0.2	0.5	2.96	37.77	0.39	0.0227	0.015	3.28×10^4	0.644	14.15
76	0.4	0.2	0.5	2.14	30.45	0.35	0.0244	0.02	2.50×10^4	0.643	13.80
77	0.4	0.2	0.5	1.26	21.55	0.29	0.0276	0.032	1.58×10^4	0.636	10.60
78	0.4	0.2	0.5	0.75	15.65	0.24	0.0313	0.05	9.90×10^3	0.612	9.90
79	0.4	0.2	0.5	0.51	12.35	0.21	0.0346	0.07	6.93×10^3	0.594	7.10
80	0.4	0.2	0.5	0.34	9.67	0.18	0.0387	0.1	4.73×10^3	0.571	5.80
81	0.4	0.2	0.5	0.25	5.5	0.23	0.0599	0.193	3.62×10^3	0.979	4.25
82	0.33	0.2	0.4	10	140	0.55	0.0206	0.004	7.45×10^4	0.469	7.80
83	0.33	0.2	0.4	4.74	77.96	0.47	0.0187	0.006	5.06×10^4	0.535	9.03
84	0.33	0.2	0.4	2.8	52.25	0.41	0.0209	0.01	3.65×10^4	0.576	11.43
85	0.33	0.2	0.4	1.82	38.28	0.37	0.023	0.015	2.69×10^4	0.597	12.95
86	0.33	0.2	0.4	1.34	30.81	0.33	0.0247	0.02	2.14×10^4	0.609	13.05
87	0.33	0.2	0.4	0.8	21.76	0.28	0.0279	0.032	1.41×10^4	0.612	12.20
88	0.33	0.2	0.4	0.48	15.77	0.23	0.032	0.05	9.07×10^3	0.596	10.50
89	0.33	0.2	0.4	0.33	12.44	0.20	0.035	0.07	6.51×10^3	0.584	9.60
90	0.33	0.2	0.4	0.22	9.72	0.17	0.039	0.1	4.50×10^3	0.564	7.45
91	0.29	0.2	0.3	10	145	0.77	0.0207	0.004	8.04×10^4	0.643	7.80
92	0.29	0.2	0.3	1.59	53.43	0.33	0.0214	0.01	2.47×10^4	0.457	10.55
93	0.29	0.2	0.3	1.06	39.04	0.30	0.0234	0.015	1.93×10^4	0.488	11.48
94	0.29	0.2	0.3	0.79	31.36	0.28	0.0251	0.02	1.58×10^4	0.505	11.33
95	0.29	0.2	0.3	0.48	22.09	0.24	0.0283	0.032	1.09×10^4	0.519	9.35
96	0.29	0.2	0.3	0.3	15.97	0.21	0.0319	0.05	7.51×10^3	0.528	9.10

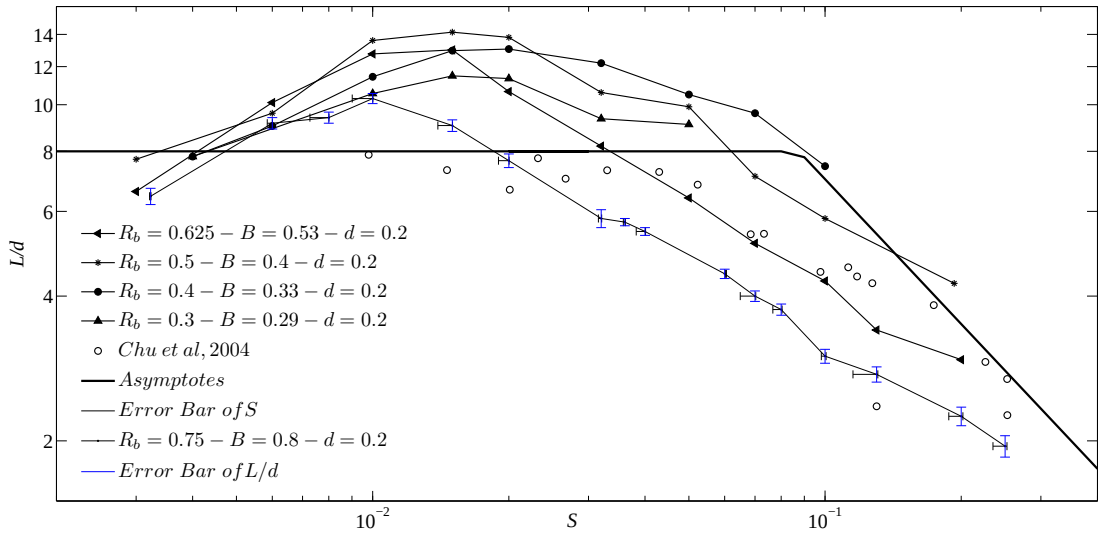

Figure 3.14: All the measured L/d in different S and R_b

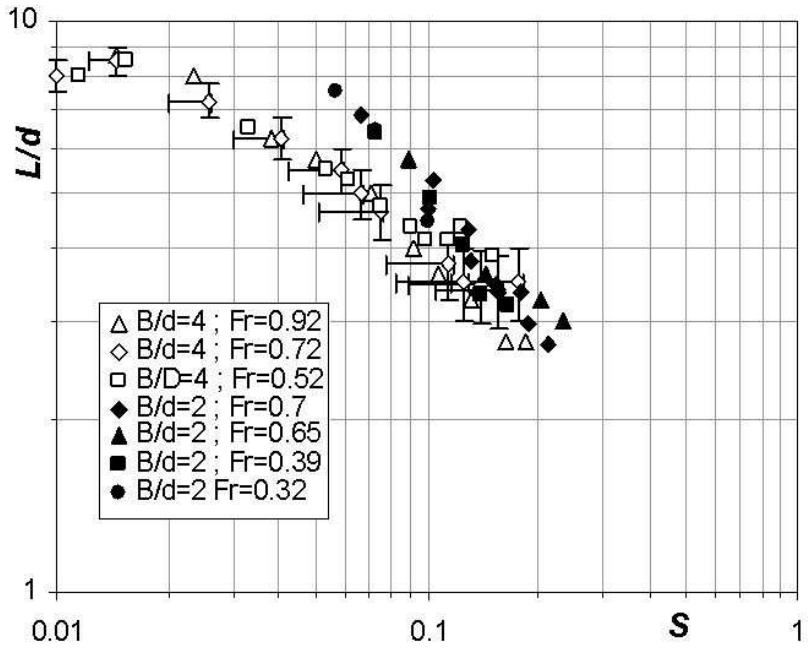

Figure 3.15: L/d in different Fr, from [Rivière et al., 2008]

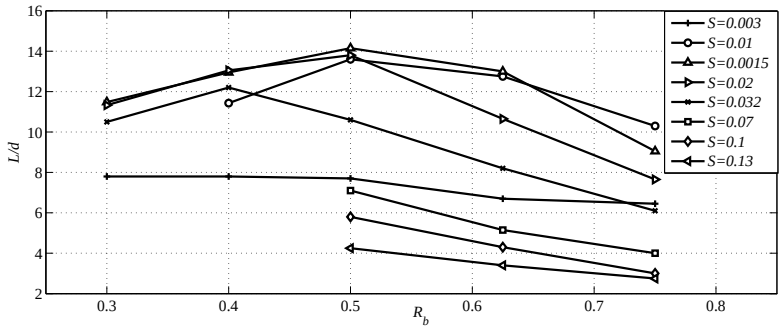

Figure 3.16: L/d in different R_b with S fixed

given R_b and then decreases as R_b decreases further. For example, FIG.3.16 shows that for S=0.02, L/d strongly increases from R_b=0.75 to R_b=0.5 (multiplied by 1.8) and then L/d decreases for R_b lower than 0.5 (divided by 1.2 from R_b=0.5 to R_b=0.3). Nevertheless, the R_b value for which L/d is maximum varies along S. For example, for S=0.032, maximum L/d is obtained for R_b=0.4. R_b is thus another parameter that rules the recirculation length, with an influence comparable to the one of S. This is corroborated by the values reported by [Babarutsi et al., 1989] (See Figure 4 in it) for recirculation downstream islands for which R_b is, from the photographs, at least R_b=0.8 and their dimensionless recirculation lengths strongly differ from their laboratory data with R_b =0.5.

3.4.3 Influence of S and h_0/d

3.4.3.1 Influence of S and h_0/d together

The experimental results are sketched on FIG.3.14 as L/d as a function of S for each of the 5 R_b series, that is using the same approach as [Chu et al., 2004] and [Rivière et al., 2008]. Note that while R_b is kept constant for each series (each curve), the other parameters are varied: S, h_0/d, Fr_0 and Re_0. While we showed above that Fr_0 and Re_0 have no influence on the data, impact of h_0/d and S independently is discussed in the following section. Moreover, experimental results from [Chu et al., 2004] and the asymptotes proposed by the same authors are also included. They deeply cast doubt on the physics of shallow recirculation downstream expansions proposed in the literature.

Indeed, present results do not exhibit any asymptotical horizontal regime for S <0.05 for a fixed R_b series, unlike data from [Chu et al., 2004]. The range of S is extended here to smaller values than [Chu et al., 2004]: 0.003< S <0.01. Instead of a plateau corresponding to L/d ∼8, a maximum dimensionless length is observed for S=0.01-0.02 with L_{max}/d=10-14, depending on R_b. L/d then decreases as S decreases to finally reach, for S <0.003, values in the range 5-8, *i.e.* comparable to the ones inventoried for 2D backward facing steps by [Adams and Johnston, 1988]. On the other hand, for the large S values, L/d decreases quite linearly with S in the log figure, as predicted by [Chu et al., 2004]. However, the rate of decrease proposed by [Chu et al., 2004] is S^{-1} while in our case it

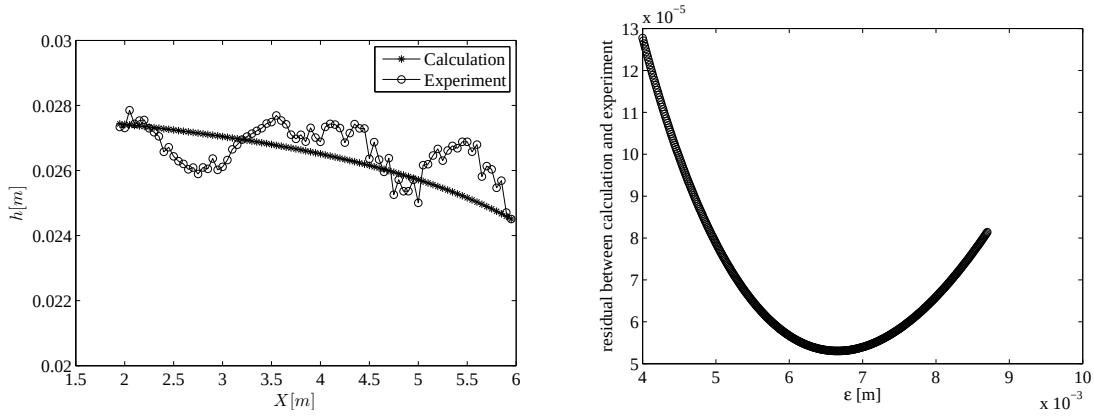

(a) Best computed and measured backwater curve

(b) Residual between the two with function of ε

Figure 3.17: Progress for obtaining the roughness ε of aluminium bottom

equals about $S^{-0.6}$ for all R_b series. Moreover, for R_b=0.5, present data and the ones from [Chu et al., 2004] differ; however, no explanation for such difference was encountered. Hence, in summary, our data shows that:
(1) In the small S region, that is deep water depth, L/d increases for increasing S values and all data tends to $L/d \approx 8$ as S tends to 0.
(2) In the intermediate region ($0.01 < S < 0.03$), L/d reaches a maximum value.
(3) In the large S region ($S > 0.03$), that is shallow flow, L/d decreases for increasing S.

The shape is referred to as "bell shape" with a maximum L/d obtained for intermediate S value. Also, it appears that for the highest $R_b(0.75)$, L/d tends to about 6, *i.e.*in the range reported for unconfined (large h_0/d), turbulent flows around small ($R_b \rightarrow 1$) backward facing steps by [Adams and Johnston, 1988].

The dimensional analysis Eq.(3.2) reveals that the dimensionless depth h_0/d can also influence L/d. Unfortunately, during experiments (the present ones and the ones from the literature), the two parameters S and h_0/d are varied simultaneously. As a consequence, the discussion presented above corresponds to variation of S and h_0/d together. Conversely, varying S without affecting h_0/d can be performed by varying continuously λ by means of modifying the roughness of the channel bed, while keeping h_0 constant.

3.4.3.2 Separated influence of S and h_0/d

In order to analyse the influence of S and h_0/d separately, the bottom roughness is increased using aluminium tear plates (see FIG.3.18).

The strategy is the following: starting from for one flow with the smooth bottom, S is kept constant by increasing λ and h_0/d by the same amount. This is done by slightly increasing the discharge. The difficulty when planning the flow conditions lies in the Darcy-Weishbach equation corrected by Colebrook-White Eq.(3.3) which includes the equivalent roughness height ε. Indeed, the topography of the board is complex, non-uniform with roughness elements of r =1.5 mm high, not aligned with the flow axis.

Figure 3.18: The channel with the aluminium roughness bottom

To identify the best ε value: i) the expansion is first removed and a uniform flow with constant width is established, ii) the backwater curve is measured for various discharge without weir leading to a critical depth at the downstream section, iii) the backwater curve is computed using the typical sub-critical approach for various values of ε, iv) the best computed/measured backwater curve fit permits to determine the most probable ε value. Results are given in FIG.3.19. It appears that for high discharges (and thus high water depths, velocity and Reynolds number), ε is constant and equals about 6mm but for low discharges, ε tends to decrease. Indeed, the limited water depth increases the ratio r/h and Colebrook-White equation is not valid any more. The relationship between r and ε becomes dependant on the water depth. In the following, we consider ε=6mm , keeping in mind that this value is doubtful for low discharges.

A serie of experiments for R_b=0.75 with the aluminium rough board is measured and detailed in TAB.3.11. These flow configurations are similar to some configurations belonging to the serie with R_b=0.75 with smooth bed in terms of S, R_b but differ in h_0/d: for the rough coverages, h_0/d exceeds that with the smooth coverage. The dimensionless recirculation lengths for these two coverage configurations are compared in FIG.3.20. It appears that the two curves bifurcate at $S \sim$0.03:
$\rightarrow$ For the shallow flows ($S >$0.03), L/d increases with increasing h_0/d (with the rough converage) but there is remains a large doubt regarding ε and thus S value.
$\rightarrow$ For the deeper configurations, ($S <$0.03), L/d decreases with increasing h_0/d (with the rough converage).

The question is whether this difference of behaviour is physical or due to the doubts regarding ε value for the shallow flows.

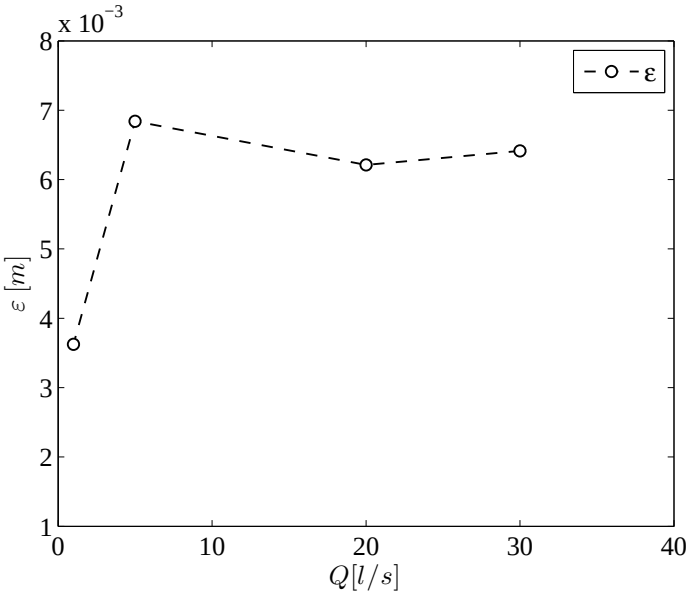

Figure 3.19: Relative roughness ε in different discharge

Table 3.11: All tested configurations with the aluminium tear plate bottom

N°	Bottom	Expansion location	B [m]	d [m]	R_b [-]	Q [l/s]	h_0 [mm]	$\overline{u}_0$ [m/s]	λ_0 [-]	S [-]	Re_0 [-]	Fr_0 [-]
97	Roughness bottom	C	0.8	0.2	0.75	31.71	109.47	0.48	0.0438	0.01	1.18×10^5	0.466
98			0.8	0.2	0.75	14.62	66.29	0.37	0.053	0.02	6.09×10^4	0.456
99			0.8	0.2	0.75	8.59	47.58	0.30	0.0609	0.032	3.77×10^4	0.441
100			0.8	0.2	0.75	3.54	27.85	0.21	0.072	0.065	1.65×10^4	0.406
101			0.8	0.2	0.75	2.36	21.98	0.18	0.078	0.089	1.12×10^4	0.386
102			0.8	0.2	0.75	1.09	14.08	0.13	0.095	0.169	5.30×10^3	0.347
103			0.8	0.2	0.75	0.7	10.96	0.11	0.108	0.246	3.44×10^3	0.325
104			0.8	0.2	0.75	0.51	9.22	0.09	0.095	0.258	2.52×10^3	0.307

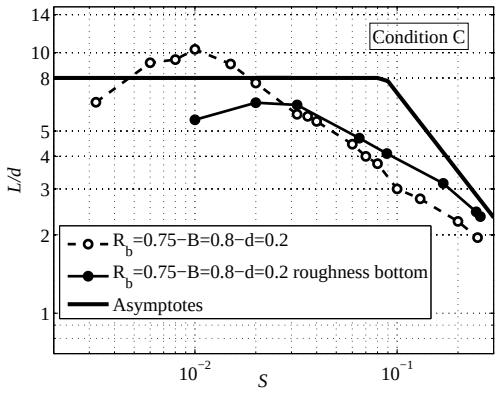

(a) The L/d obtained in the different bottoms

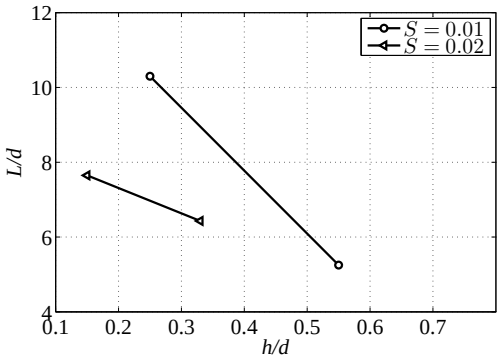

(b) The influence of h/d

Figure 3.20: Results in the roughness bottom configuration.

3.5 Chapter conclusion

This chapter was devoted to experiments. Preliminary work was a dimensional analysis which shows that 5 dimensionless parameters (Re, Fr, $S, h/d, R_b$) influence the length of the recirculation. As Re and Fr were already studied in the LMFA team ([Riviere et al., 2011]), our study focused on the 3 leading parameters: the bed friction number S, the relative water depth h/d and the expansion ratio R_b, which influences must be assessed. To obtain the appropriate database, final adjustments were performed on the experimental facility.

Results show that the expansion ratio R_b has a comparable influence as the one of S. L/d first increases as R_b decreases, reaches a maximum value for a given R_b and then decreases as R_b decreases further. Experiments also confirm the influence of the bed friction number on the recirculation length. Nevertheless, the evolution of L/d with S is at odd with the literature. There is not a plateau in the small S regime and the decreasing tendency in the high S regime differs from a S^{-1} law. This can be related to the third parameter h/d, as suggested by the results obtained with a larger roughness.

Nevertheless, in our experiments, it was impossible to vary continuously and independently the two parameters S and h/d. This is possible using numerical simulations, which are performed in the next chapter to definitely establish the influence of each of these 2 parameters.

Chapter 4

Numerical study and comparison with the experimental results

This chapter focuses on numerical calculation of the flow field in the sudden lateral expansion. The aim of this chapter is twofold:
1) A comparison of the numerical results with the experimental data and to thus evaluate the impact of the numerical simplifications (mostly the rigid-lid approach) 2) Obtain more accurate and detailed data than what could be measured for analysing the flow characteristics and understanding the detachment length behaviour.

Contents

4.1 The numerical modelling strategy

4.1.1 Equations and turbulence model

For solving the Navier-Stokes equation, the scientists have developed several methods with different degree of complexity. For this thesis, the RANS approach is selected as it is the simplest way to solve the 3D turbulent N-S equations, thus saving calculation time. RANS equations are obtained using the Reynolds decomposition, written as $u(x,y,z,t) = \overline{u(x,y,z,t)} + u'(x,y,z,t)$. Here, the Reynolds-Averaged Navier-Stokes equations are given, which comprises the momentum Eq.(4.1) and the continuity equation of the incompressible fluid Eq.(4.2), where the subscripts i and j refer to the different components along the x, y and z direction in the Cartesian coordinates:

$$\frac{\partial \overline{u_i}}{\partial t} + \overline{u_j}\frac{\partial \overline{u_i}}{\partial x_j} = -\frac{1}{\rho}\frac{\partial \overline{p}}{\partial x_i} + \nu\frac{\partial^2 \overline{u_i}}{\partial x_j \partial x_j} - \frac{\partial \overline{u_i' u_j'}}{\partial x_j} \tag{4.1}$$

$$\frac{\partial \overline{u_i}}{\partial x_i} = 0 \tag{4.2}$$

This set of equations thus includes 4 equations involving 10 unknown which are to be solved:
-The mean velocity components in three directions: $\overline{u}, \overline{v}, \overline{w}$
-The mean total pressure: $\overline{p}$
-The 6 components of the Reynolds Stress Tensor:

$$R_{uv} = -\rho \begin{pmatrix} \overline{u'^2} & \overline{u'v'} & \overline{u'w'} \\ \overline{v'u'} & \overline{v'^2} & \overline{v'w'} \\ \overline{w'u'} & \overline{w'v'} & \overline{w'^2} \end{pmatrix} \tag{4.3}$$

We thus face too few equations for solving the system. So, a turbulence model has to be introduced as a computational procedure to close the system, by estimating the Reynolds stress tensor. The most common turbulence models are in the TAB.4.1: For

Table 4.1: Different turbulent model in the numerical simulation

Classical models	Based on the (time-averaged) Reynolds equations
	1. zero-equation model, mixing length model
	2. two-equation model, $k-\varepsilon$ equation
	3. two-equation model, $k-\omega$ equation
	4. Reynolds stress equation model (RSM)
Large eddy simulation	Based on space-filtered equation
Direct numerical simulation	Navier-Stokes equations are numerically solved without any turbulence model

this thesis, the main aim is to accurately compute the length of the recirculation, so considering the accuracy and the calculation time of the available models, classical models

are preferred. The RSM approach takes too much calculating time. So, the simple $k-\varepsilon$ model is used in the thesis.

It is possible to develop transport equations for all turbulence quantities including the rate of the viscous dissipation ε and turbulent kinetic energy k [Bradshaw and Wong, 1972]. The model thus includes two additional transport equations, one for k and one for ε. Applying the same approach as in the mixing length model we specify the eddy viscosity as follows:

$$\mu_T = \rho C_\mu \frac{k^2}{\varepsilon} \tag{4.4}$$

where C_μ is a dimensionless constant. It is recommended by most previous tests as 0.09. Then, with an isotropic assumption for the eddy viscosity, the Reynolds stress tensor terms are related to the gradient of the mean flow using the standard $k-\varepsilon$ model as:

$$-\overline{\rho u_i' u_j'} = \mu_T \left(\frac{\partial \overline{u_i}}{\partial x_j} + \frac{\partial \overline{u_j}}{\partial x_i} \right) - \frac{2}{3}\rho k \delta_{ij}$$

Where δ_{ij} is the Kronecher delta (δ_{ij}=1 if $i = j$ and δ_{ij}=0 if $i \neq j$).

For this thesis, the realizable $k-\varepsilon$ model is chosen finally. It is developed from the standard $k-\varepsilon$ model. It keeps the Reynolds stresses correspond between the simulation and real phenomenon by examining the term in the calculation, for example, it checks if $\overline{u'^2} \geq 0$.

The final set of equation thus contains 7 unknown: $\overline{u}, \overline{v}, \overline{w}, p, k, \varepsilon, \mu_T$ and 7 equations : the 3 momentum Eqs.(4.1), the continuity Eq.(4.2), the equation for μ_T Eq.(4.4) and the transport equations for k and ε. The steady condition is used in the calculation, so the times term t is not included. The system can thus be solved.

4.1.2 The rigid-lid assumption

A numerical model aiming to compute the free surface location is called Volume Of Fluid (VOF), first introduced by [Noh and Woodward, 1976]. It can calculate the velocity field in the water region and the air region and also the location of the interface between the two regions. Nevertheless, this approach spends a lot of time for calculating. As the present chapter does not focus on the free surface characteristics, the VOF long calculation time is not performed. Other simplified method adapted to a rigid lid assumptions also exist [Ouillon and Dartus, 1997]. Nevertheless, consistently with experiments for which efforts were made to keep a water depth as constant as possible in the recirculation region, water depth are not considered here.

Consequently, a rigid-lid model with constant water depth is chosen: a wall with free-slip conditions parallel to the bottom is fixed at the free surface instead of using the VOF model. So, the influence of the water depth variations through the recirculation zone is neglected herein. The friction between this top wall and the flow is set to 0 using the free-slip condition.

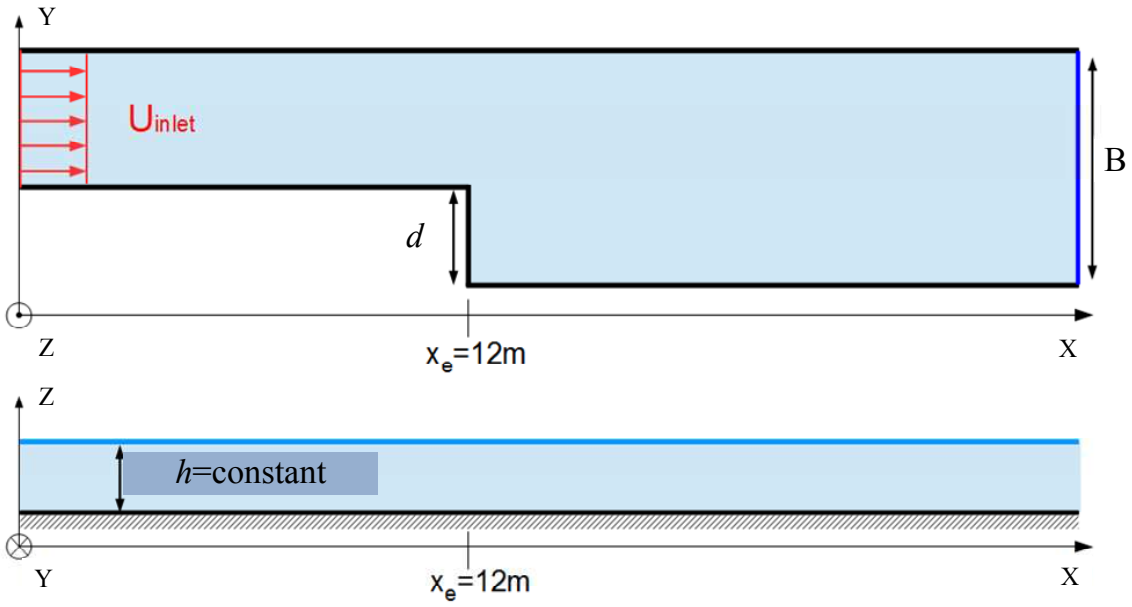

Figure 4.1: Boundary condition to solve the calculation

4.1.3 The boundary conditions

In order to solve Eqs.(4.1) to (4.4) in the fixed region, boundary conditions must be specified along the entire boundary of the domain.
$\longmapsto$ A uniform velocity profile is imposed as inlet condition, followed by a 12m long inlet channel ensuring a developed velocity profile at the expansion as shown in the FIG.4.1. The inlet velocity equals to $\overline{u} = Q/((B-d)h$.
$\longmapsto$ The outlet is controlled by a hydrostatic pressure distribution.
$\longmapsto$ The water depth is fixed along the whole channel region using the previously described rigid-lid assumption with no friction.
$\longmapsto$ All other boundaries are defined as walls with no slip conditions.

The law of the wall is introduced here to compute the flow in the near wall region. In this calculation model, we chose the treatment of the wall as "Two layers-All y^+" proposed by the software StarCCM+. This "Two layers-All y^+" function permits to choose the treatment of the wall as a function of the distance of the first cell center, noted y^+: if the first cell is located in the viscous sub-layer ($y^+ <5$) a linear velocity profile is considered and if the center is the logarithm zone of the velocity profile ($30< y^+ <500$), the empirical law of the wall is considered.

The criterion is defined by the dimensionless distance from the wall, noted as y^+:

$$y^+ = \frac{u_\tau}{\nu} y \tag{4.5}$$

Where $u_\tau = \sqrt{\frac{\tau_w}{\rho}}$ represents the local friction velocity at the level of the wall;
$\tau_w = \mu \frac{\partial \overline{u}}{\partial y}|_{y=0}$ is the local shear stress of the wall.

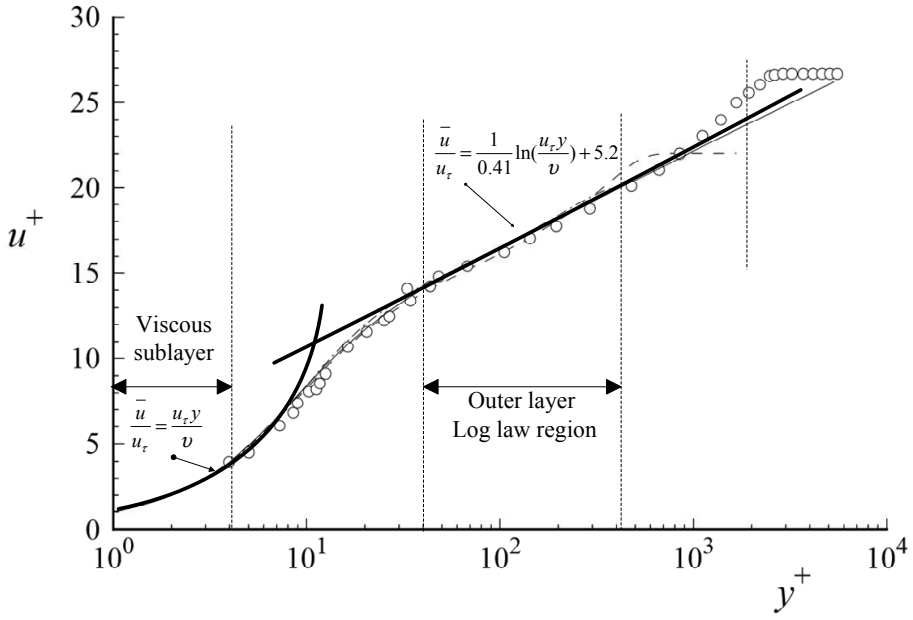

Figure 4.2: Law of the wall. [Pope, 2008]

If y^+ represents the position from the cell center closest to the wall, the empirical law of the wall can be considered effective when $30 < y^+ < 500$, that is when the center of the first cell near the wall is location within the logarithmic zone. (See FIG.4.2) The standard wall law exhibits a slope discontinuity between the viscous and logarithmic regions. In the viscosity layer ($y^+ < 5$), the velocity profile is linear:

$$u^+_{lam} = y^+ \tag{4.6}$$

In the logarithmic zone, the velocity profile is given by:

$$u^+_{turb} = \frac{1}{0.41}\ln(E' y^+) \tag{4.7}$$

where $u^+ = \overline{u}/u_\tau$ is the dimensionless velocity; and $E' = \frac{9}{f}$ with f calculated as indicated below.
Introducing the roughness parameter:

$$\varepsilon^+ = \frac{u_\tau}{\nu}\varepsilon \tag{4.8}$$

where ε is the equivalent sand-grain roughness height, the function to compute f is a slightly expanded version of the following expression given (StarCCM+):

$$f = \left\{ \begin{array}{c} 1 \\ \left[B\left(\frac{\varepsilon^+ - \varepsilon^+_{smooth}}{\varepsilon^+_{rough} - \varepsilon^+_{smooth}} \right) + C\varepsilon^+ \right]^a \\ B + C\varepsilon^+ \end{array} \right\} \qquad \begin{array}{l} for \quad \varepsilon^+ < \varepsilon^+_{smooth} \\ for \quad \varepsilon^+_{smooth} < \varepsilon^+ < \varepsilon^+_{rough} \\ for \quad \varepsilon^+ > \varepsilon^+_{rough} \end{array} \tag{4.9}$$

where the exponent a is expressed as:

$$a = \sin\left[\frac{\pi}{2}\frac{\log\left(\varepsilon^{+}/\varepsilon^{+}_{smooth}\right)}{\log\left(\varepsilon^{+}_{rough}/\varepsilon^{+}_{smooth}\right)}\right] \tag{4.10}$$

and the default values of the coefficient are: B=0, C=0.253, ε^{+}_{smooth}=2.25 and ε^{+}_{rough}=90. So, $\varepsilon^{+} < \varepsilon^{+}_{smooth}$, represents the flow which is hydraulic smooth;
$\varepsilon^{+} > \varepsilon^{+}_{rough}$ represents the flow which is hydraulic rough;
$\varepsilon^{+}_{smooth}\varepsilon^{+} < \varepsilon^{+}_{rough}$ aims the condition between the smooth and the rough.

For our calculation, the empirical wall function ($30< y^{+} <500$) is selected as often as possible. Indeed, this method:
$\longmapsto$ does not require to compute the flow characteristic on the near wall region ($y^{+} <30$). Note that the accuracy of the direct calculation of the flow in this region using the selected model is not ensured unless caring much on the time and space steps.
$\longmapsto$ permits to save calculation cells (and thus also calculation time).
The size of the cells adjacent to the walls are thus chosen in order to keep the center of the first cell within the logarithm zone of the velocity profile in the normal direction of the wall ($30< y^{+} <500$).

Initial conditions are a water region with zero velocity.

4.1.4 The mesh characteristics

Using the finite volume method for calculation, the mesh is of high importance. For our configuration, 3D rectangular cells are chosen, see FIG.4.3. The mesh is refined around the enlargement (zone 2) and even more in the recirculation zone (zone 1) in order to gain in spatial resolution of the recirculation flow structure. The m_z depends on the water depth of the flow. And also the first layer of the mesh should cover 2 times of the roughness height. It varies from 1 mm to 6 mm depending on the configurations. The typical cell sizes (along the 2 directions) in the different zones are:

1. Zone 1: m_x=3 mm and m_y=3 mm
2. Zone 2: m_x=12.5 mm and m_y=12.5 mm
3. Zone 3: m_x=50 mm and m_y=25 mm
4. Zone 4: m_x=100 mm and m_y=12.5 mm

(Note that Zone 3 includes the $0< x <$10m region and zone 4 includes 16m$< x <$20m which are only partly figured below). For checking the convergence of the results using the different meshes, 3 simulations with different meshes in zone 1 (recirculation zone) are compared in a same configuration:

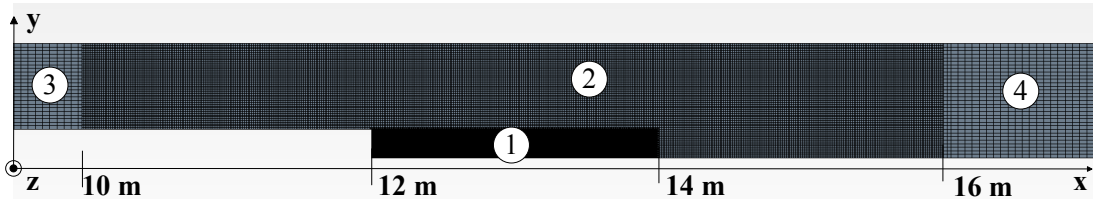

Figure 4.3: Different zone with the different size of the calculating mesh

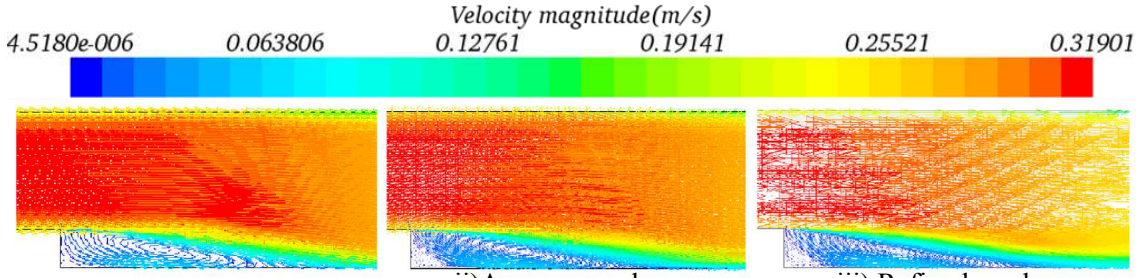

i) Coarse mesh, L/d=5.63 ii)Average mesh, L/d=5.69 iii) Refined mesh, L/d=5.50

Figure 4.4: Flow fields with different size of the calculating mesh

1. Expansion ratio : R_b=0.75 (B=0.8, d=0.2).
2. Reynolds number: Re=24000 (inlet velocity $\overline{u}$=0.326m/s).
3. Water depth: h=0.02 m.

The 3 different size of the mesh are:
a) Coarse mesh: m_x=12.5mm and m_z =12.5 mm. It obtains L/d=5.625.
b) Average size mesh: m_x=6.25 mm and m_z =6.25 mm. It obtains L/d=5.688.
c) Refined mesh: m_x=3.125mm and m_z =3.125 mm. It obtains L/d=5.5.

The relative error of the recirculation length among the three meshes is less than 5%. So the simulation method for calculating the length is considered acceptable. However, in FIG.4.1.4, the coarse mesh calculation does not exhibit all details regarding the secondary recirculation cell near the corner. Moreover, the computation time is not prohibitive. So, we keep the fine mesh as our final mesh configuration for the sequel.

4.1.5 Time convergence

As explained in CHAP.5, The advection of the turbulent cells along the mixing layer leads to a time-unsteady recirculation length and thus of the reattachment location [Riviere et al., 2011]. Nevertheless, we do not focus here on this unsteadiness; we are rather interested in the time-averaged recirculation length. In fact, the chosen turbulent model can not calculate such turbulent unsteadiness. So, here we focus on the time-averaged length of the recirculation zone L and on the global influence of every parameter on this length. To ensure the solution time-convergence in the calculation, several criterion are introduced:

Table 4.2: Flow configuration of the reference flow of the numerical simulation

$\overline{u}$ $[m/s]$	Channel width B $[m]$	Enlargement width d $[m]$	Water depth h $[m]$	Upstream Re	bottom roughness ε $[m]$	λ Darcy Coefficient
0.297	0.8	0.2	0.02	2.5×10^{-4}	3.4×10^{-5}	0.0256

1. a criterion on the magnitude of numerical residuals which should be small enough for the 7 equations solved: less than 1000 times smaller than at initial time.

2. the conservation of mass discharge between the inlet and outlet sections is also surveyed.

3. a criterion based on the time-stability of the recirculation length: the instantaneous recirculation length is estimated from the calculation every 50 iterations and compared to the previous estimations.

4. a criterion based on the stability of the qualitative recirculation topology (the number of gyres and their positions), to ensure that the flow structure in the recirculation zone is stable.

4.1.6 Additional verification

In order to ensure that the inlet and outlet boundary conditions do not impact the flow pattern in the expansion region, a long enough inlet channel (20 m) is used to obtain an established flow when reaching the recirculation region. For checking the established flow condition, the velocity profiles at different streamwise locations (upstream, middle and downstream) are plotted and compared to each other. All these criterions are illustrated in section 4.2.2 when presenting the reference configuration.

4.2 Application to a reference configuration

4.2.1 Reference configuration description

Before investigating the impact of the flow and geometrical parameters (See the dimensional analysis in CHAP.3) on the recirculation length, a reference flow configuration is selected based on the experimental configurations from CHAP.3. This reference configuration and calculation verifications are described below (TAB.4.2 and FIG.4.2.1). This procedure is the same as the one applied to all other calculations in the sequel. With the definition of the above parameters we can obtain the dimensionless parameters:
$\Rightarrow R_b$=0.75; h/d=0.1 and S=0.032.

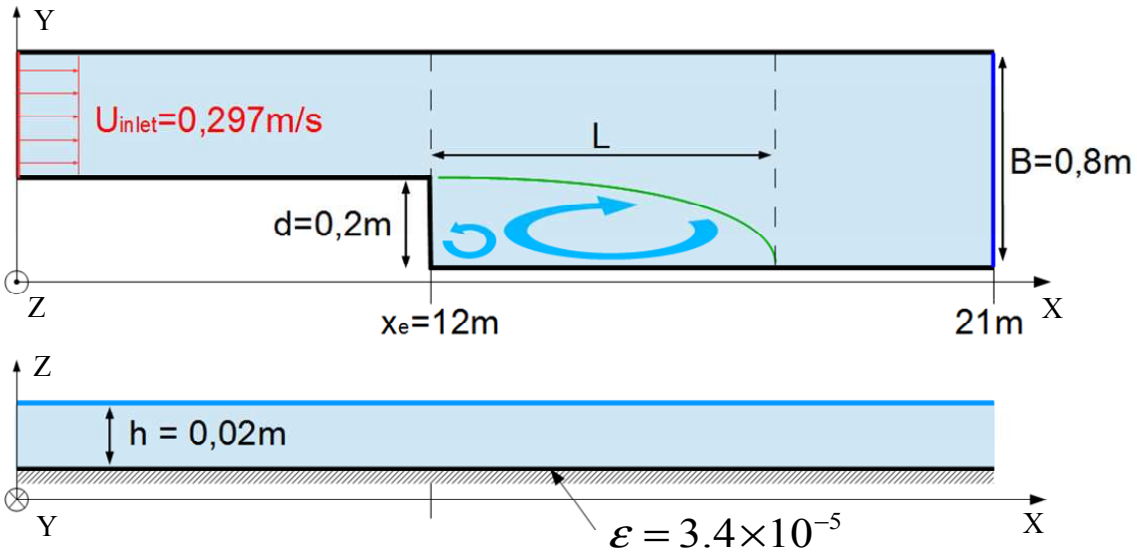

Figure 4.5: Parameter setting of the reference flow configuration

4.2.2 Verification of the convergence criterions

As discussed above, several criterions are considered for ensuring the convergence of the calculation. The first criterion is the magnitude of the residual term including:

1. "Continuity" which is the mass conservation residual.
2. "X,Y, Z momentum" which are the momentum balance residuals in three spatial directions
3. "TKE" which is the residual of the Turbulent Kinetic Energy transport equation
4. "Tdr" which is the residual of the Turbulence dissipation rate transport equation

These residuals are plotted in FIG.4.6 below. It is obvious that after 3000 iterations number, all the residuals become stable in time and are below 10^{-5}, that is 5 order if magnitude smaller than at initial time. Secondly, the discharge in the inlet section and the outlet section are calculated by integrating the velocity in the two sections, which equal:
$\rightarrow$ Inlet section: Q=3.564000$\times 10^{-3} m^3$
$\rightarrow$ Outlet section: Q=3.564002$\times 10^{-3} m^3$

The error between the two discharges is of the order of $10^{-7} m^3/s$ which is considered acceptable herein.

The third convergence criterion is based on the time stability of the recirculation length L along the calculation. The method for detecting the length L at any time step is as follows: the streamwise velocity profile along the right wall (Y=0, in FIG.4.7) (as a function of X position) is plotted as in FIG.4.8. The location where the velocity component changes sign from negative to positive is the reattachment point (here at X=13.275 m). In addition, we verify the time stability of this velocity profile with time.

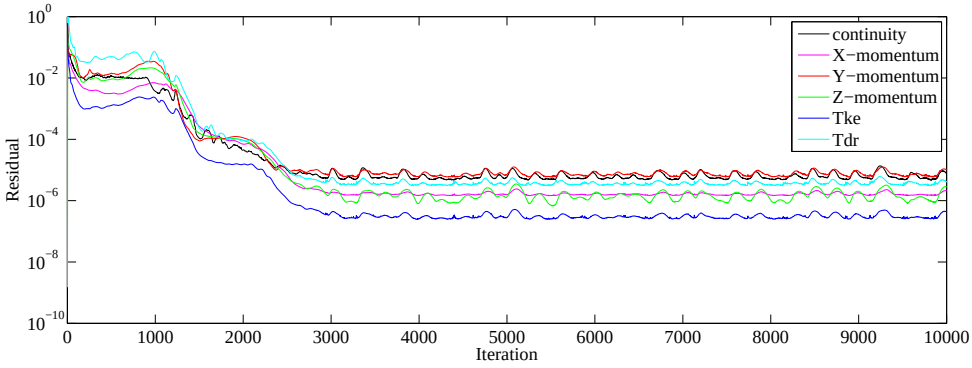

Figure 4.6: Different residual terms for the flow with 10000 iterations

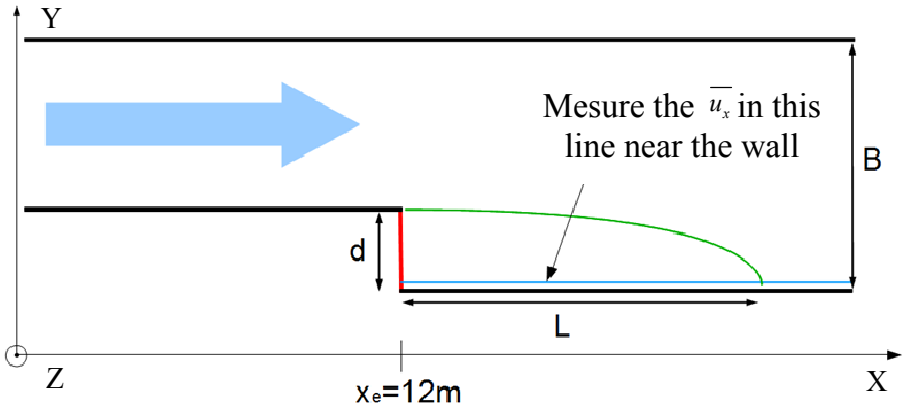

Figure 4.7: Sketch for finding the reattachment point

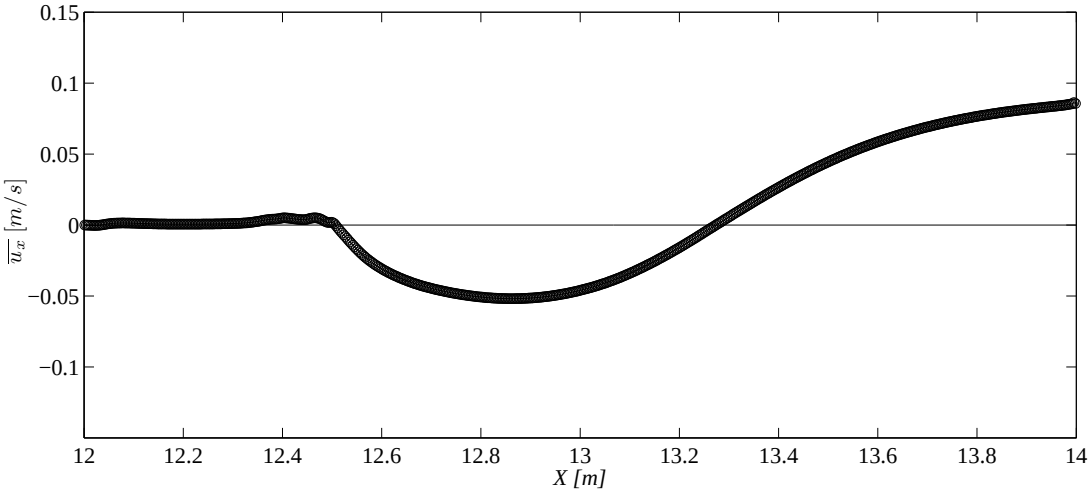

Figure 4.8: Velocity distribution for the points along the $Y = 0$

The fourth criterion is based on the qualitative pattern of the horizontal velocity field at mid-elevation ($Z = h/2$). The aim is to verify that after some time, the structure of the recirculation flow pattern becomes stable (number and the position of the cells). In FIG.4.9, the cell in the recirculation move from the expansion section to downstream and then the structure in the zone does not change after 2500 iteration, revealing that the criterion is reached. Last, the transverse profiles of streamwise velocity are plotted at different streamwise sections (x=7 m, 9 m,11 m, 16 m, 18 m and 20 m). From the FIG.4.10 we can see that clearly the flow is developed both upstream and down stream of the the recirculation zone. So the length of the channel is enough for covering the recirculation zone. To summarize, when all criterions are reached, the calculation is stopped and numerical results are exported, especially the recirculation length L obtained as indicated for the criterion.

4.3 Comparison between numerical and experimental results

Several strong hypothesis and simplifications were made regarding the numerical configuration compared to the experimental flow configuration such as:

1. a constant water depth h in the calculation while the free surface is evolving in the experiment

2. an isotropic turbulence closure ($k-\varepsilon$)

Before analysing in details the numerical data to identify the influence of each parameter on the flow pattern, two sets of experiments with R_b equal to 0.75 and 0.5 are replicated using the numerical model. For these series, it appears on FIG.4.11 that large S experiments were not replicated numerically, this is due to the very limited water depth and the too large cells required to keep a y^+ values larger than 30 in the near wall region. FIG.4.11 compares the experimental and numerical results(values are also listed in TAB.4.3). The qualitative trend is retrieved by the numerical approach:

1. for large bed friction numbers S, L/d decreases as S increases.

2. At $S \sim 0.01$, L/d reaches a maximum value

3. For small S values, L/d decreases as S decreases.

4. L/d increases as R_b decreases.

A small difference still exists in terms of quantitative recirculating length prediction, which remains limited, except for the deepest configurations, that is the smallest S values. To conclude, the numerical code appears to satisfactorily estimate the recirculating length and is in agreement with the evolution of L/d for varying S values. This numerical approach can then be used for further analysis.

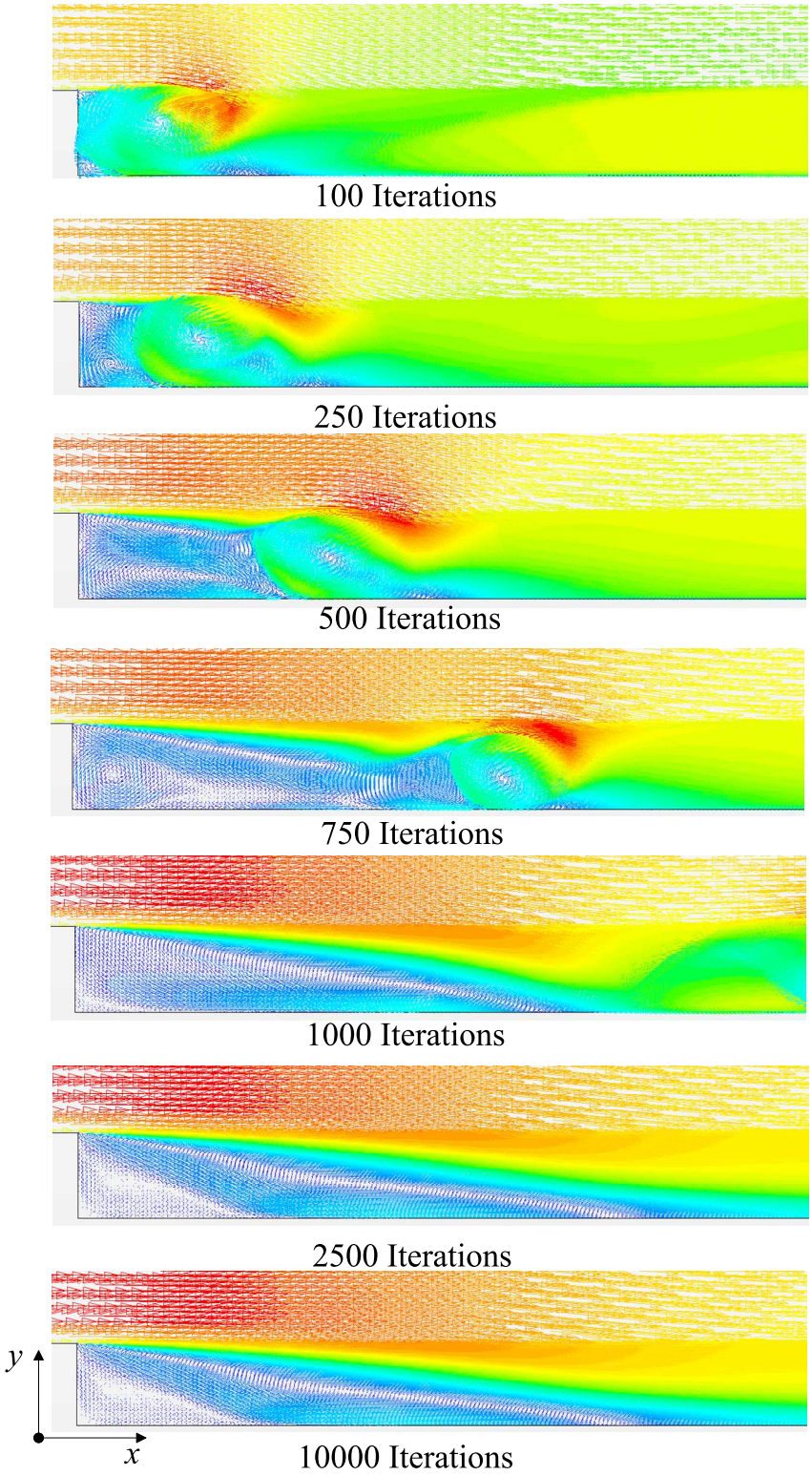

Figure 4.9: Flow dynamic structure downstream the expansion in different iterations

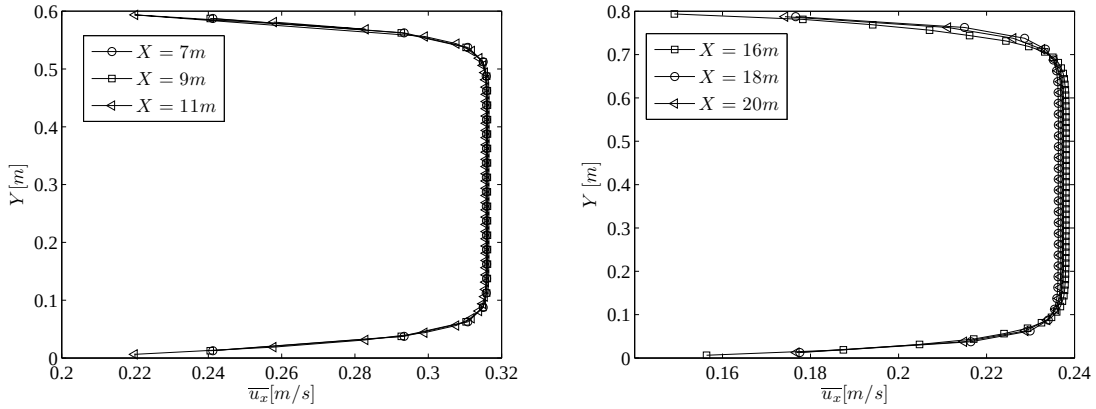

Figure 4.10: Mean velocity profiles in different sections

Table 4.3: Comparison between the experiment and simulation in different R_b

R_b=0.75				R_b=0.625				R_b=0.5			
Experiments		Simulations		Experiments		Simulations		Experiments		Simulations	
S	L/d	S	L/d	S	L/d	S	L/d	S	L/d	S	L/d
0.003	6.45	0.098	3.89	0.003	6.60	0.001	7.73	0.003	7.70	0.001	8.17
0.006	9.15	0.031	6.38	0.006	10.10	0.003	9.52	0.006	9.60	0.003	10.53
0.008	9.40	0.012	8.98	0.010	12.75	0.007	12.19	0.010	13.60	0.007	14.42
0.010	10.30	0.007	8.78	0.015	13.00	0.012	13.47	0.015	14.15	0.011	16.81
0.015	9.05	0.003	7.69	0.020	10.65	0.030	8.70	0.020	13.80	0.030	10.77
0.020	7.65	0.001	6.84	0.032	8.20			0.032	10.60		
0.032	5.80			0.050	6.40			0.050	9.90		
0.036	5.70			0.070	5.15			0.070	7.10		
0.040	5.45			0.100	4.30			0.100	5.80		
0.060	4.45			0.130	3.40			0.193	4.25		
0.070	4.00			0.200	2.95						
0.080	3.75										
0.100	3.00										
0.130	2.75										
0.200	2.25										
0.250	1.95										

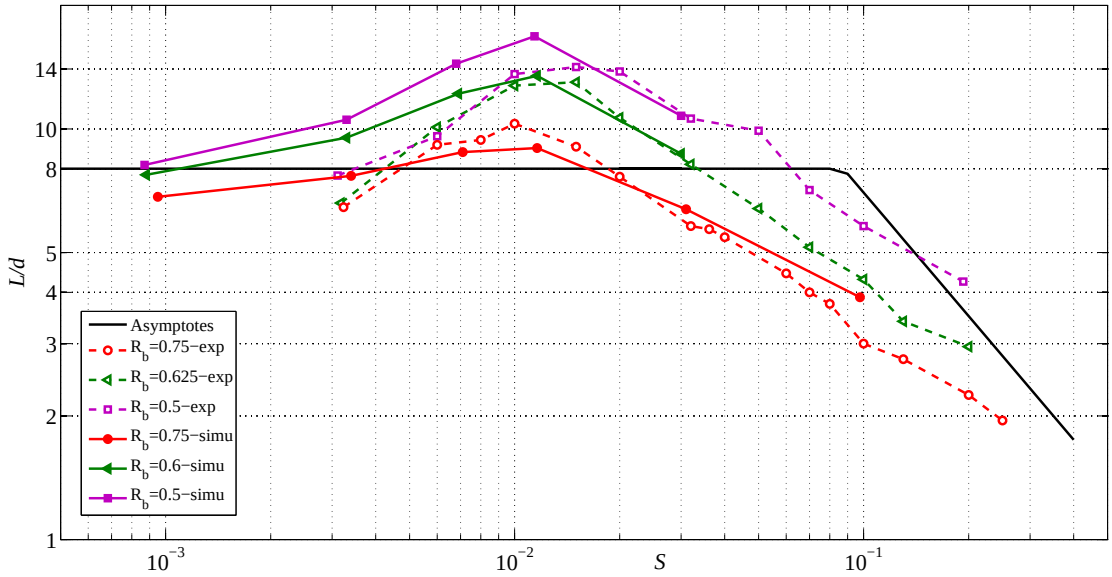

Figure 4.11: Comparison of L/d between simulations and experiments

4.4 Influence of the parameters

The dimensional analysis in CHAP.3 revealed that the parameters that could influence the dimensionless recirculation length are: 1) the Froude number of the flow Fr, 2) the expansion ratio R_b, 3) the dimensionless water depth at the expansion section h/d(in simulation h/d keeps constant), 4) the Reynolds number of the inflow Re, 5) the friction number S. Riviere et al already showed that the impact of the Froude number remains negligible; the influence of 4 parameters thus remain to be tested.

To do so, the calculations of the reference configuration (section 4.2.1) are modified by altering only one parameter in each series, keeping the other parameters constant. The strategy is detailed in TAB.4.4 the top line lists the 4 parameters to be studied, the second line lists the variable (geometry or flow characteristics) to be modified correspondingly, the 4 remaining lines represent the modification that must be made to keep the other parameters constant. For example, for studying the impact of R_b, B is modified (which directly modifies R_b,), h and d are kept constant, $\overline{u}$ is modified to keep Re constant, ε is also modified to keep S constant.

In the following subsections, the numerical results obtained for each serie are presented one by one.

Note the exact evaluation of the head loss coefficient λ. The head loss coefficient λ can be computed using the Colebrook-White law, noted λ_{th} (“th” for theoretical) using the Reynolds number and roughness height ε. However, due to the not perfect accuracy of the empirical law of the wall proposed by the code StarCCM+, this coefficient appears not to be equal to the head loss coefficient λ_{num} calculated based on the energy loss per unit length measured in the upstream channel, even though the same Re and ε are considered.

Table 4.4: The numerical simulation strategy

Parameter to be studied		R_b Section4.4.4	h/d Section4.4.3	Re Section4.4.1	S Section4.4.2
Variable to be modified		B	h	$\overline{u}$	λ
Modification to keep the other parameters constant	R_b	$-----$	fixed	fixed	fixed
	h/d	fixed	$-----$	fixed	fixed
	Re	modify $\overline{u}$	modify $\overline{u}$	$-----$	modify ε
	S	modify ε	modify ε	modify ε	$-----$

Consequently, the following procedure is used:

1. Colebrook-White law is used to roughly predict a head loss coefficient magnitude but the value used for computing the actual S coefficient is λ_{th}
2. the actual head loss coefficient λ_{num} is obtained by estimating the energy loss J_{12} equal to the pressure difference between two sections located in the upstream channel (upstream from the recirculation zone, for example between X_1=6m and X_2=11m where the water depth is uniform:

$$J_{12} = \frac{P_1 - P_2}{\rho g} = \lambda_{num} \frac{(X_2 - X_1)}{D_h} \frac{\overline{u}^2}{2g} \tag{4.11}$$

   where D_h is the hydraulic diameter in the upstream channel and p_1 and p_2 are the mean (spatial and temporal) pressure in both selected sections. Then, S is computed as

$$S_{num} = \lambda_{num} d/8h \tag{4.12}$$

3. if this value departs from the objective, one parameter (usually the roughness elevation ε) is adjusted and the procedure is repeated from the beginning.

Note that the error between S_{th} obtained using λ_{num} and S_{num} obtained using λ_{num} remains lower than 10%.

4.4.1 Influence of the Reynolds number Re

For evaluating the influence of the upstream Reynolds number Re, we define 5 flow configurations (see TAB.4.5) analogous to the reference configuration (R_b=0.75, h/d=0.1 and S=0.032) but with a varying Re from $2.5\times10^4$to 5×10^5. The configuration named Re-1 is the reference configuration detailed in section 4.2.1. For changing Re, the streamwise inlet velocity $\overline{u}$ is modified while h remains constant. In the same time, the Darcy friction coefficient λ, which depends on Re, is kept constant by altering the roughness elevation ε of the flume bottom. Consequently, as h and ε remains fixed, the bed friction S is not altered.

The FIG.4.12 illustrates the streamwise velocity profiles along the reattachment wall which are used for determining the recirculation length. The velocity is normalized by

Table 4.5: Configurations for flows with different Reynold number

N°	Re	S_{th}	$\overline{u}$ (m/s)	ε (m)	L/d	y^+	ε^+	S_{num}
Re-1	2.5×10^4	0.032	0.297	3.40×10^{-5}	6.375	59	0.57	0.0311
Re-2	5.0×10^4	0.032	0.594	3.00×10^{-4}	6.328	57	9.82	0.0291
Re-3	1.0×10^5	0.032	1.188	4.20×10^{-4}	6.094	61	20.71	0.0320
Re-4	2.5×10^5	0.032	2.970	4.75×10^{-4}	6.234	145	78.70	0.0306
Re-5	5.0×10^5	0.032	5.939	4.50×10^{-4}	5.750	151	155.43	0.0317

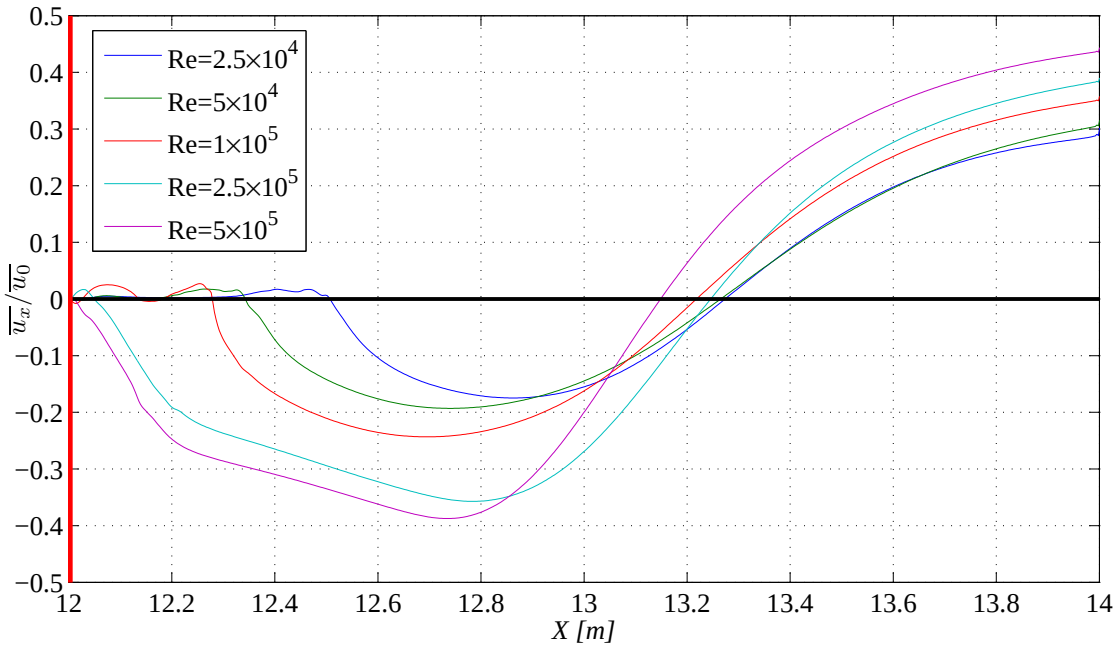

Figure 4.12: Reattachment point of the recirculation zone for 5 different values for Reynolds number Re.

the mean velocity upstream: $\overline{u}$. It is obvious that the point where the sign of the velocity changes from negative to positive ($\overline{u}_x/\overline{u}$ =0) equals about 13.2 m for the five configurations (except for the largest Reynolds case $Re-5$). We conclude that the impact of Re on the length of the recirculation remains limited. On the other hand, FIG.4.12 reveals that Re influences the flow pattern in the recirculation zone: the length of the secondary recirculation decreases as Re increases and the secondary recirculation disappears when Re becomes larger than 2.5×10^5(See FIG.4.13).

4.4.2 Influence of the bed friction number S

TAB.4.6 represents the chosen configurations for studying the influence of S magnitude on the recirculation length L/d. The configuration S-7 is the reference configuration (the same as *Re*-1, detailed in section 4.2.1). In section 4.3, 3 flow regimes as introduced,

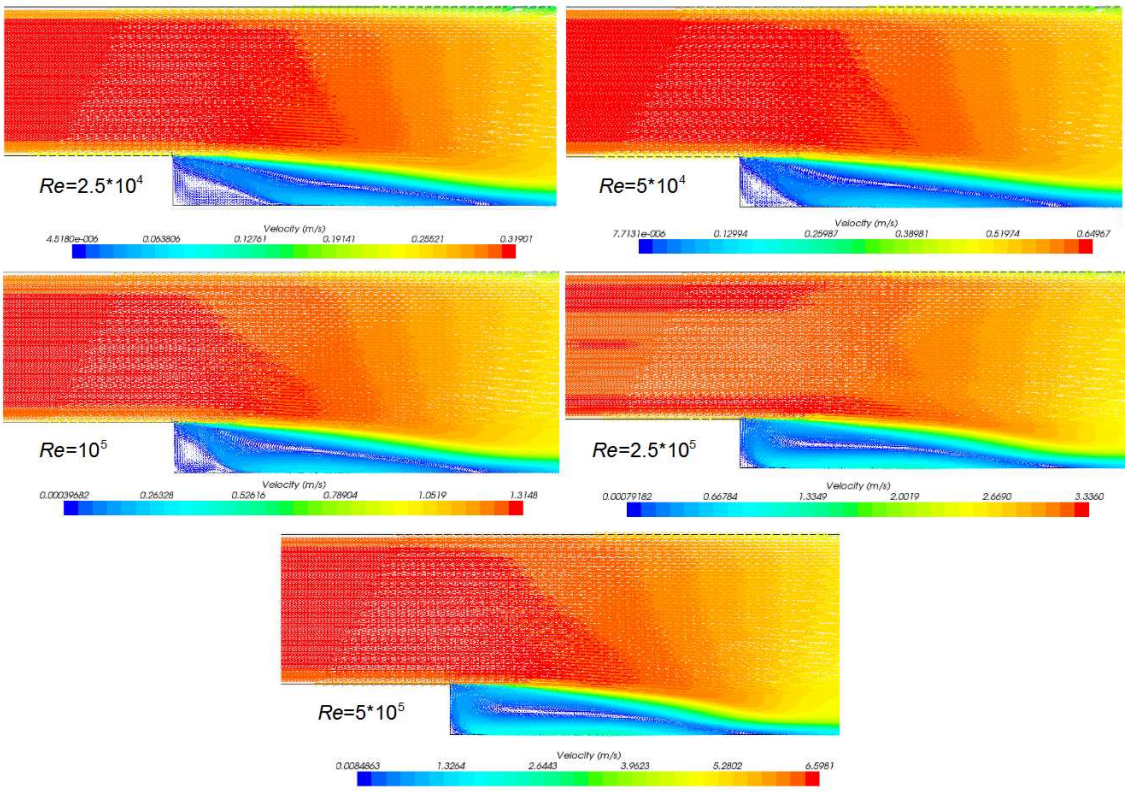

Figure 4.13: Countours of the velocity field in different Re

including the friction regime, no-friction regime and the transition regime. For studying the whole region, S varies here from 0.003 to 0.2. In theory, S should be simply modified by changing the roughness height ε and thus the λ parameter. But when ε exceeds the distance between the wall and the center of the first cell, the calculation can not be proceed. Thus, S cannot be varied in a large extent with a constant h/d magnitude. Hence:

1. for the first 3 configurations (S-1 to S-6, S-7 to S-12 and S-13 to S-18), h/d is modified for changing S (h/d=0.01, h/d=0.1, h/d=0.15), permitting to vary S between 0.0202 and 0.11.

2. in order to reach lower values of S parameter, Re number also has to be changed (2.5×10^5 instead of 2.5×10^4) in the following 4 series (S-19 to S-41) with h/d varying from 0.1 to 0.5. As discussed in section 4.2.1, we suppose that the modification of Re number does not influence the length of the recirculation.

In FIG.4.14, it appears that:

1. as S increases, L/d decreases linearly (in logarithmic representation) for each h/d tested parameters.

2. unlike predicted by the literature, and especially by [Chu et al., 2004], the impact of S on L/d is high even for low values of S (smaller than 0.01).

3. the red and violet symbols (h/d=0.1 with 2 Reynolds number values) and on the other hand the green and light blue symbols (h/d=0.15 with 2 Reynolds number values) are fairly aligned, confirming that the Reynolds number has a limited impact on the recirculation length.

4. the normalized water depth has a strong impact on the recirculation length : as h/d increases, L/d decreases (see for instance the green and dark blue series or the light blue and violet series with same Re magnitude).

Note that for a fixed h/d magnitude, the impact of S remains monotonic: as S increases, L/d decreases. This differs from the experimental shape seen on FIG.3.14 in FIG.3 where a “bell” was obtained by changing both h/d and S parameters.

4.4.3 Influence of the water depth h/d

To further study the influence of the relative depth, h/d is modified by changing the depth h (remember that is the present calculations, h is kept constant over the whole domain), keeping S constant (by modifying the wall roughness height ε), and keeping the Reynolds number constant by modifying the inlet velocity $\overline{u}$. The TAB.4.7 details the two configurations series (with two different Reynolds numbers, see previous section for explanation). FIG.4.15 plots the evolution of L/d as a function of h/d. It appears that: L/d decreases

Table 4.6: Configurations for studying the influence of S

N°	h/d	Re	S_{th}	h (m)	$\overline{u}$ (m/s)	ε (m)	L/d	y^+	ε^+	S_{num}
S-1	0.05	2.5×10^4	0.066	0.01	0.575	3.40×10^{-5}	4.891	57	1.10	0.0634
S-2	0.05	2.5×10^4	0.082	0.01	0.575	1.67×10^{-4}	4.797	58	5.51	0.0661
S-3	0.05	2.5×10^4	0.098	0.01	0.575	3.56×10^{-4}	4.359	63	12.84	0.0792
S-4	0.05	2.5×10^4	0.115	0.01	0.575	6.07×10^{-4}	3.891	70	24.31	0.0976
S-5	0.05	2.5×10^4	0.134	0.01	0.575	9.27×10^{-4}	3.547	75	39.51	0.1105
S-6	0.05	2.5×10^4	0.157	0.01	0.575	1.40×10^{-3}	3.531	75	59.75	0.1108
S-7	0.1	2.5×10^4	0.032	0.02	0.297	3.40×10^{-5}	6.375	59	0.57	0.0311
S-8	0.1	2.5×10^4	0.037	0.02	0.297	1.67×10^{-4}	6.375	59	2.80	0.0311
S-9	0.1	2.5×10^4	0.042	0.02	0.297	3.56×10^{-4}	6.203	61	6.15	0.0330
S-10	0.1	2.5×10^4	0.047	0.02	0.297	6.07×10^{-4}	5.828	64	11.14	0.0373
S-11	0.1	2.5×10^4	0.053	0.02	0.297	9.27×10^{-4}	5.406	69	18.31	0.0431
S-12	0.1	2.5×10^4	0.067	0.02	0.297	1.79×10^{-3}	4.719	77	39.47	0.0537
S-13	0.15	2.5×10^4	0.022	0.03	0.204	8.84×10^{-5}	6.641	40	1.02	0.0202
S-14	0.15	2.5×10^4	0.024	0.03	0.204	9.27×10^{-4}	6.219	44	11.70	0.0240
S-15	0.15	2.5×10^4	0.026	0.03	0.204	1.25×10^{-3}	6.000	46	16.56	0.0265
S-16	0.15	2.5×10^4	0.028	0.03	0.204	1.50×10^{-3}	5.828	48	20.57	0.0283
S-17	0.15	2.5×10^4	0.030	0.03	0.204	1.75×10^{-3}	5.672	50	24.77	0.0301
S-18	0.15	2.5×10^4	0.032	0.03	0.204	2.00×10^{-3}	5.547	51	29.12	0.0319
S-19	0.1	2.5×10^5	0.020	0.02	2.970	8.91×10^{-6}	8.516	57	1.15	0.0179
S-20	0.1	2.5×10^5	0.022	0.02	2.970	1.10×10^{-4}	7.516	63	15.80	0.0220
S-21	0.1	2.5×10^5	0.024	0.02	2.970	1.50×10^{-4}	7.125	66	22.49	0.0240
S-22	0.1	2.5×10^5	0.026	0.02	2.970	1.91×10^{-4}	6.813	68	29.66	0.0258
S-23	0.1	2.5×10^5	0.028	0.02	2.970	3.75×10^{-4}	6.484	141	60.29	0.0277
S-24	0.1	2.5×10^5	0.030	0.02	2.970	4.75×10^{-4}	6.234	145	78.70	0.0306
S-25	0.15	2.5×10^5	0.013	0.03	2.042	7.62×10^{-6}	8.984	39	0.68	0.0118
S-26	0.15	2.5×10^5	0.014	0.03	2.042	1.00×10^{-4}	8.563	41	9.33	0.0129
S-27	0.15	2.5×10^5	0.016	0.03	2.042	2.00×10^{-4}	7.922	44	20.25	0.0151
S-28	0.15	2.5×10^5	0.018	0.03	2.042	3.00×10^{-4}	7.438	47	32.28	0.0170
S-29	0.15	2.5×10^5	0.020	0.03	2.042	4.00×10^{-4}	7.328	48	43.35	0.0173
S-30	0.25	2.5×10^5	0.0075	0.05	1.299	4.60×10^{-7}	8.781	50	0.03	0.0071
S-31	0.25	2.5×10^5	0.008	0.05	1.299	2.00×10^{-4}	8.406	54	12.26	0.0081
S-32	0.25	2.5×10^5	0.009	0.05	1.299	3.00×10^{-4}	8.109	57	19.36	0.0089
S-33	0.25	2.5×10^5	0.010	0.05	1.299	4.00×10^{-4}	7.891	59	26.92	0.0096
S-34	0.25	2.5×10^5	0.011	0.05	1.299	5.00×10^{-4}	7.703	61	34.68	0.0101
S-35	0.25	2.5×10^5	0.012	0.05	1.299	7.00×10^{-4}	7.672	61	48.60	0.0102
S-36	0.5	2.5×10^5	0.0038	0.1	0.742	8.06×10^{-7}	7.688	57	0.03	0.0034
S-37	0.5	2.5×10^5	0.0045	0.1	0.742	1.25×10^{-4}	7.688	57	4.05	0.0034
S-38	0.5	2.5×10^5	0.0050	0.1	0.742	2.45×10^{-4}	7.594	59	8.25	0.0036
S-39	0.5	2.5×10^5	0.0055	0.1	0.742	3.97×10^{-4}	7.484	62	14.13	0.0039
S-40	0.5	2.5×10^5	0.0060	0.1	0.742	5.85×10^{-4}	7.375	66	21.99	0.0042
S-41	0.5	2.5×10^5	0.0065	0.1	0.742	8.11×10^{-4}	7.250	69	32.05	0.0046

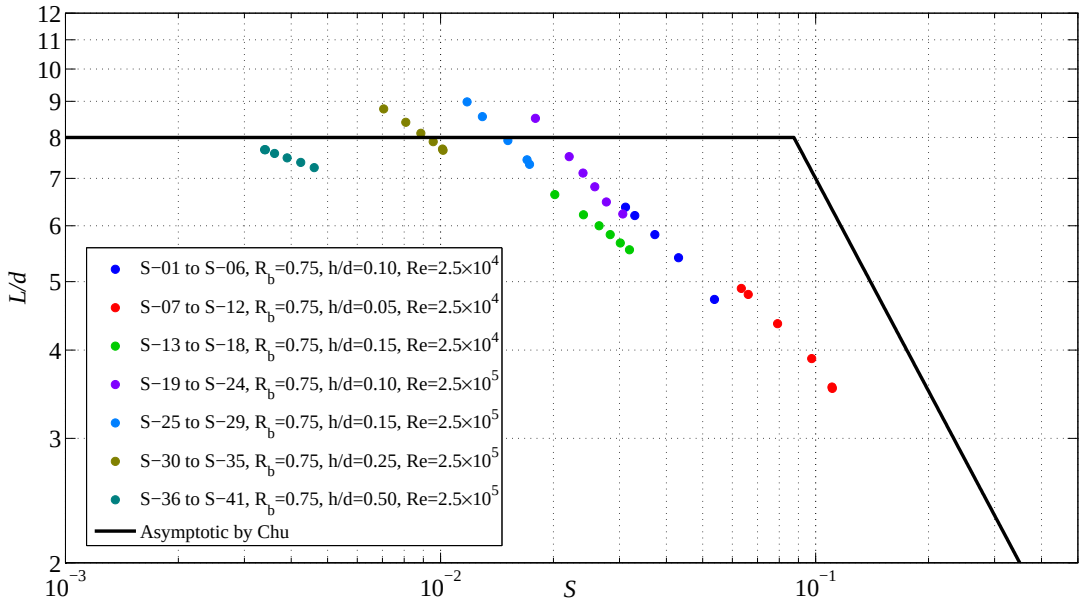

Figure 4.14: L/d with influence of S

Table 4.7: Configurations for studying the influence of h/d

N°	Re	h/d	S_{th}	h (m)	$\overline{u}$ (m/s)	ε (m)	L/d	y^+	ε^+	S_{num}
h-1	2.5×10^4	0.100	0.032	0.0200	0.297	3.40×10^{-5}	6.375	59	0.57	0.0311
h-2	2.5×10^4	0.113	0.032	0.0225	0.266	4.20×10^{-4}	6.328	54	6.51	0.0293
h-3	2.5×10^4	0.125	0.032	0.0250	0.241	9.00×10^{-4}	5.969	54	13.73	0.0308
h-4	2.5×10^4	0.138	0.032	0.0275	0.221	1.52×10^{-3}	5.656	53	22.97	0.0325
h-5	2.5×10^4	0.150	0.032	0.0300	0.204	2.00×10^{-3}	5.547	51	29.12	0.0319
h-6	2.5×10^4	0.175	0.032	0.0350	0.178	3.50×10^{-3}	5.516	46	45.54	0.0282
h-7	2.5×10^5	0.060	0.032	0.0120	4.826	1.94×10^{-6}	7.266	93	0.41	0.0308
h-8	2.5×10^5	0.070	0.032	0.0140	4.163	5.40×10^{-5}	7.078	85	10.48	0.0297
h-9	2.5×10^5	0.080	0.032	0.0160	3.666	1.41×10^{-4}	6.547	82	26.27	0.0308
h-10	2.5×10^5	0.090	0.032	0.0180	3.279	2.78×10^{-4}	6.344	77	48.58	0.0299
h-11	2.5×10^5	0.100	0.032	0.0200	2.970	4.75×10^{-4}	6.234	145	78.70	0.0306
h-12	2.5×10^5	0.113	0.032	0.0225	2.660	5.50×10^{-4}	6.266	143	89.76	0.0312

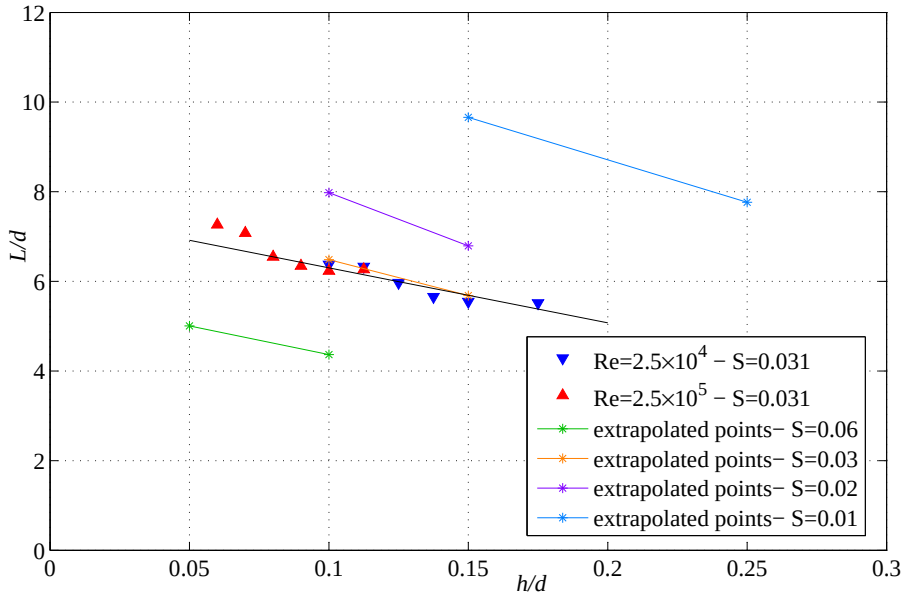

Figure 4.15: L/d with influence of h/d

as h/d increases. This evolution is quite linear (in logarithmic representation). The black line is a linear interpolation of the computed points.

We can additionally extrapolate the data plotted in FIG.4.15 to each four different S values in order to obtain additional relations between h/d and L/d. It appears that as for all tested S (from 0.01 to 0.06), L/d always decreases as h/d increases, this tendency is thus consistent. Moreover, the decrease of L/d from one series to another for increasing S values (from 0.01 to 0.06) confirms the previous conclusions.

4.4.4 Influence of the expansion ratio R_b

The last parameter to consider is the expansion ratio R_b, which is modified by changing the channel width B whilst keeping the expansion width d constant. When modifying B, R_h is affected and it is necessary to modify at the same time $\overline{u}$ and ε to keep the Reynolds number, the Darcy coefficient, and thus S constant. TAB.4.8 details the 5 series (in series 1 Re=2.5×10^4 and in the other series Re=2.5×10^5). With the same consideration as before, the influence of Re is neglected here.

Additional data is included for the analysis of the influence of R_b, they concern 2D calculations. These calculations exclude the vertical confinement between the bottom and the free surface, that means h is infinite and S tends to 0. These data are included in TAB.4.9. The results are sketched on FIG.4.16, they reveal that:

1. For high R_b values (R_b >0.3), as R_b increases, L/d decreases. Oppositely, for low R_b (R_b <0.3), as R_b increases, L/d increases. This behaviour is in fair agreement with experimental data plotted in FIG.3.14 in CHAP.3.

Table 4.8: Configurations for studying the influence of R_b

N°	R_b	S_{th}	h/d	B (m)	$\overline{u}$ (m/s)	ε (m)	L/d	y^+	ε^+	S_{num}
B-1	0.20	0.032	0.1	0.25	0.501	2.01×10^{-5}	18.688	100	0.575	0.029
B-2	0.35	0.032	0.1	0.308	0.382	2.64×10^{-5}	14.609	78	0.591	0.028
B-3	0.50	0.032	0.1	0.4	0.334	3.02×10^{-5}	10.766	68	0.588	0.030
B-4	0.60	0.032	0.1	0.5	0.316	3.20×10^{-5}	8.703	63	0.579	0.030
B-5	0.75	0.032	0.1	0.8	0.297	3.40×10^{-5}	6.375	59	0.570	0.031
B-6	0.80	0.032	0.1	1.0	0.292	3.45×10^{-5}	5.844	58	0.566	0.031
B-7	0.90	0.032	0.1	2.0	0.285	3.54×10^{-5}	5.250	56	0.562	0.031
B-8	0.92	0.032	0.1	2.5	0.283	3.56×10^{-5}	5.172	55	0.561	0.031
B-9	0.94	0.032	0.1	3.333	0.282	3.58×10^{-5}	5.172	55	0.559	0.031
B-10	0.96	0.032	0.1	5.0	0.281	3.59×10^{-5}	5.086	55	0.559	0.032
B-11	0.35	0.013	0.15	0.308	2.890	5.38×10^{-6}	22.047	56	0.69	0.0113
B-12	0.50	0.013	0.15	0.4	2.413	6.45×10^{-6}	16.813	47	0.70	0.0114
B-13	0.60	0.013	0.15	0.5	2.227	6.99×10^{-6}	13.469	43	0.69	0.0116
B-14	0.75	0.013	0.15	0.8	2.042	7.62×10^{-6}	8.984	39	0.68	0.0118
B-15	0.80	0.013	0.15	1.0	1.995	7.80×10^{-6}	7.844	38	0.67	0.0118
B-16	0.90	0.013	0.15	2.0	1.918	8.11×10^{-6}	6.531	36	0.67	0.0119
B-17	0.20	0.008	0.25	0.25	3.341	1.79×10^{-7}	16.188	123	0.03	0.0071
B-18	0.35	0.008	0.25	0.308	2.148	2.79×10^{-7}	16.828	83	0.03	0.0069
B-19	0.50	0.008	0.25	0.4	1.670	3.58×10^{-7}	14.422	64	0.03	0.0068
B-20	0.60	0.008	0.25	0.5	1.485	4.03×10^{-7}	12.188	58	0.03	0.0069
B-21	0.75	0.008	0.25	0.8	1.299	4.60×10^{-7}	8.781	50	0.03	0.0071
B-22	0.80	0.008	0.25	1.0	1.253	4.78×10^{-7}	7.781	48	0.03	0.0071
B-23	0.90	0.008	0.25	2.0	1.175	5.09×10^{-7}	6.547	44	0.03	0.0071
B-24	0.20	0.0038	0.5	0.25	2.784	2.15×10^{-7}	10.281	96	0.02	0.0036
B-25	0.35	0.0038	0.5	0.308	1.591	3.76×10^{-7}	11.641	59	0.03	0.0035
B-26	0.50	0.0038	0.5	0.4	1.114	5.37×10^{-7}	10.531	84	0.03	0.0033
B-27	0.60	0.0038	0.5	0.5	0.928	6.45×10^{-7}	9.523	72	0.03	0.0033
B-28	0.75	0.0038	0.5	0.8	0.742	8.06×10^{-7}	7.688	57	0.03	0.0034
B-29	0.80	0.0038	0.5	1.0	0.696	8.60×10^{-7}	7.062	53	0.03	0.0034
B-30	0.90	0.0038	0.5	2.0	0.619	9.67×10^{-7}	6.172	47	0.03	0.0033
B-31	0.35	0.001	2	0.308	1.173	2.25×10^{-5}	8.375	82	1.05	$0.91 * 10^{-3}$
B-32	0.50	0.001	2	0.4	0.696	3.80×10^{-5}	8.172	51	1.10	$0.87 * 10^{-3}$
B-33	0.60	0.001	2	0.5	0.510	5.18×10^{-5}	7.734	77	1.13	$0.88 * 10^{-3}$
B-34	0.75	0.001	2	0.8	0.325	8.14×10^{-5}	6.836	49	1.13	$0.95 * 10^{-3}$
B-35	0.80	0.001	2	1.0	0.278	9.50×10^{-5}	6.500	84	1.13	$0.96 * 10^{-3}$
B-36	0.90	0.001	2	2.0	0.201	1.32×10^{-4}	6.023	61	1.14	$0.99 * 10^{-3}$

Table 4.9: Configurations for the 2D simulations

N°	R_b	Re	h/d	S	B (m)	$\overline{u}$ (m/s)	L/d
B-2D-1	0.20	2.50×10^4	∞	0	0.25	2.500	7.578
B-2D-2	0.35	2.53×10^4	∞	0	0.308	1.173	8.281
B-2D-3	0.50	2.78×10^4	∞	0	0.4	0.696	8.141
B-2D-4	0.60	3.06×10^4	∞	0	0.5	0.510	7.734
B-2D-5	0.75	3.90×10^4	∞	0	0.8	0.325	6.859
B-2D-6	0.80	4.45×10^4	∞	0	1.0	0.278	6.547
B-2D-7	0.90	7.24×10^4	∞	0	2.0	0.201	6.086
B-2D-8	0.92	8.63×10^4	∞	0	2.5	0.188	6.016
B-2D-9	0.94	1.10×10^5	∞	0	3.333	0.175	6.000
B-2D-10	0.96	1.56×10^5	∞	0	5.0	0.162	5.938

2. as $R_b \to 1$ (that is $d \to 0$ or $B \to \infty$), L/d tends to an asymptotic value: about 6, *i.e.* in the range reported for unconfined, turbulent flows around small ($R_b \to 1$) backward facing steps by [Adams and Johnston, 1988]. This is also the recirculation length value obtained using 2D simulations (equivalent to $h/d \to \infty$, that is an unconfined geometry). This asymptotic behaviour can be explained using to a momentum balance: when $R_b \to 1$, *i.e.* when $B \to \infty$, the upstream and downstream sections tend to the same width, and so do the mean velocities; the specific momentums upstream and downstream the expansion tend to be equal so that the resisting forces (wall friction and shear at the recirculation boundary) tend to their minimum magnitude, and so do the recirculation length.

3. as $R_b \to 0$, (that is $d \to B$,), the dimensionless recirculation length L/d decreases. Again, this can be explained by a momentum balance: when $R_b \to 0$, the upstream discharge and specific momentum tend to zero. The resisting forces logically tend to zero, and so L/d decreases.

4. R_b value corresponding to the maximum of L/d is influenced by the other parameters. All curves on FIG.4.16 are obtained for different values or h/d and S; for some of them, the maximum was not observed.

4.4.5 The relative influence of the parameters

The influence of the three parameters S, h/d and R_b being established (Re impact was shown to be negligible), it is worth comparing their relative impacts on L/d values. This is the aim of FIG.4.17 where, within each constant R_b series, S and h/d are modified simultaneously. The figure illustrates the competition between impact of S and h/d:

1. For high bed friction numbers S, corresponding to small values of h/d (right part of the graph) the dimensionless recirculation length "obey" to S (see FIG.4.14): L/d decreases as S increases but does not "obey" to h/d as L/d increases as h/d

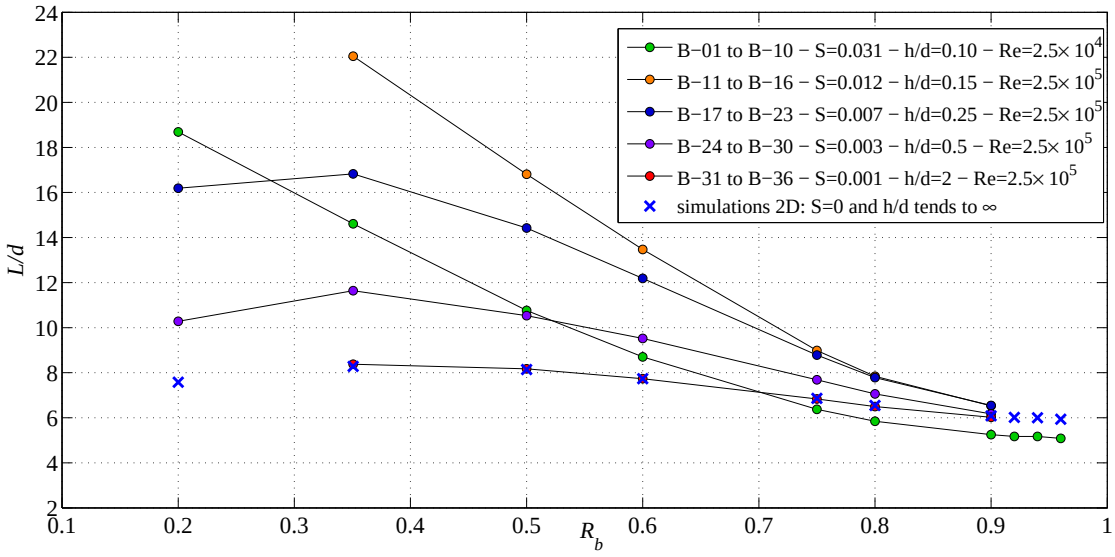

Figure 4.16: Computed L/d as a function of the expansion ratio R_b

increases. Thus the impact of S exceeds that of h/d: the dimensionless recirculation length is governed by S.

2. For low bed friction number S, corresponding to higher values of h/d, (left part of the graph), the dimensionless length "obeys" to h/d: L/d decreases as h/d increases, but not "obeys" to S as L/d increases as S increases. Thus the impact of h/d exceeds that of S: the dimensionless recirculation length is now governed by h/d.

3. Also, FIG.4.17 shows that the expansion ratio R_b strongly influences L/d values but does not affect the tendency described above regarding the evolution of L/d as a function of S or h/d.

4.5 Chapter conclusion

In this chapter, numerical simulations were undertaken to vary independently S and h/d, and then to observe their respective influences. Simulations were performed using 3D RANS Equations, with a constant water depth and a rigid-lid assumption.

Firstly, numerical results confirm the tendencies , namely the "bell shape" curve, observed during the experiments (CHAP.3). The increasing left branch of $L/d(S)$ curve instead of a plateau as proposed in the literature cannot attributed to experimental problems, as the same tendencies are retrieved in numerical simulations with neither backwater effect nor topography defaults.

Secondly, our results permit to conclude that:

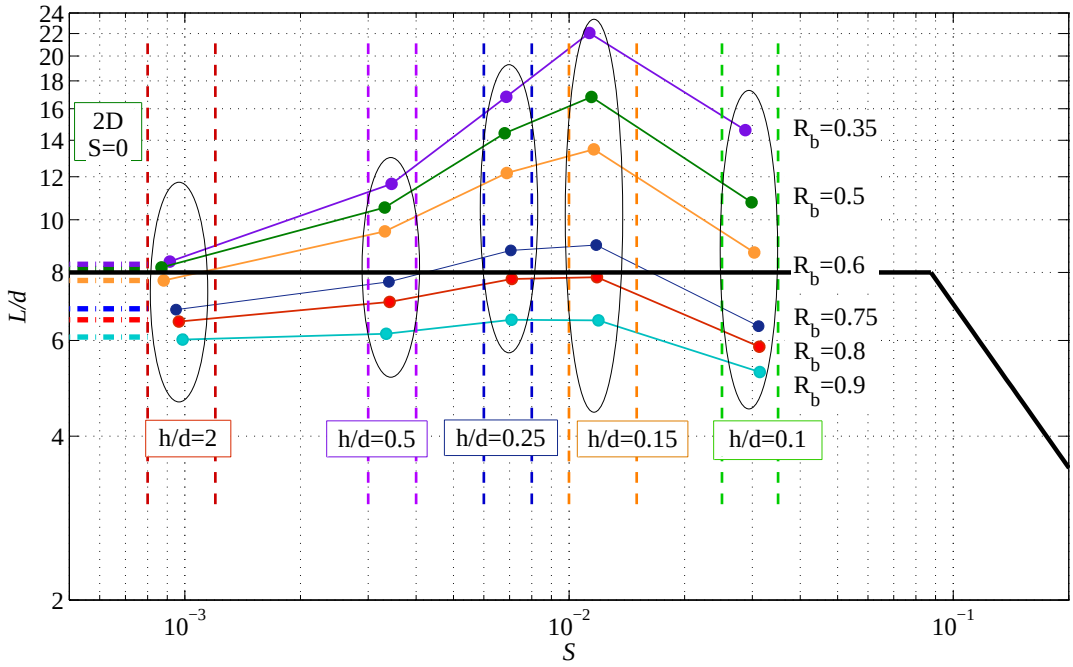

Figure 4.17: Computed L/d as a function of S.

1. the Reynolds number of the inflow Re does not affect the sudden expansion recirculation length, at least in the moderate range investigated

2. the increase of the friction number S tends to decrease the dimensionless recirculation length

3. the increase of the dimensionless water depth h/d tends to decrease the dimensionless recirculation length

Thirdly, the numerical simulations allow understanding the behaviour observed in the experiments and referred to a "bell shape" in FIG.3.14. In the experimental procedure, 2 parameters from the dimensional analysis were modified at the same time: as S was increased, h/d was simultaneously decreased. We showed, based on the numerical analysis performed in the present chapter, that increasing S and decreasing h/d have opposite effect on the recirculation length: increasing S tends to decrease L/d while decreasing h/d tends to increase L/d. The "bell shape" is observed as:
$\rightarrow$ for low S values, L/d obeys to h/d: as h/d decreases (and though S increases), L/d increases.
$\rightarrow$ for high S values, L/d obeys to S: as S increases (and though h/d decreases), L/d decreases.

These tendencies are in perfect agreement with the experimental measurements where, for a fixed R_b geometry, we faced a maximum L/d value for an intermediate S and decreasing L/d values for higher and lower S values. Note that explanation of the "bell

shape" using only an experimental approach would have been a very difficult task, as it would require to vary S and h/d separately that is adjusting the roughness height (done in one configuration) for various configurations. This gives credit to our analysis, combining experimental and numerical investigations.

The respective influences of the three parameters being established, it is now necessary to find out the physical mechanisms explaining them. Literature suggests that the phenomena ruling the flow are located within the mixing layer. Thus, next chapter is devoted to a detailed, experimental study of this mixing layer.

Chapter 5

Mixing layer downstream the expansion flow

The aim of the present section is to measure the characteristics of the mixing layer at the interface between the main flow and the recirculation zone. A specific attention was paid on the impact of shallowness on these characteristics and on the coherent structures. Four configurations with identical geometry and varying shallowness were thus selected. Precise and exhaustive velocity field measurements were performed for them and the analysis of their mixing layers permitted to sort all their characteristics.

Contents

5.1 Experimental description

5.1.1 Experimental parameters

From the experiments of CHAP.3, FIG.5.2 plots a series of 16 non-dimensional recirculation lengths configurations with increasing S values, with R_b=0.75. The axis system is set as depicted on Fig.5.1 with the center located at the expansion section along the side wall, x the streamwise axis and y the transverse axis. Note that here the point (0,0) locates at the section of expansion, that differs from the X,Y whose (0,0) locates at the beginning of the channel. The recirculation length L is defined as the distance from the expansion where the mean streamwise velocity along the side wall changes sign from negative (towards upstream) in the recirculation to positive (towards downstream) further downstream. Four configurations, F1 to F4, are specifically selected for the detailed analysis of the mixing layer characteristics in this chapter. They are located on both sides of the "bell" with comparable recirculation lengths: F1 is a deep configuration (S <0.01) and F3 a shallow configuration (S >0.01). F2 located on the "bell" is refereed as a transitional flow. F4 is an additional shallow configuration obtained with a bottom roughness (addition of aluminium tear plates) larger than in the other three configurations.

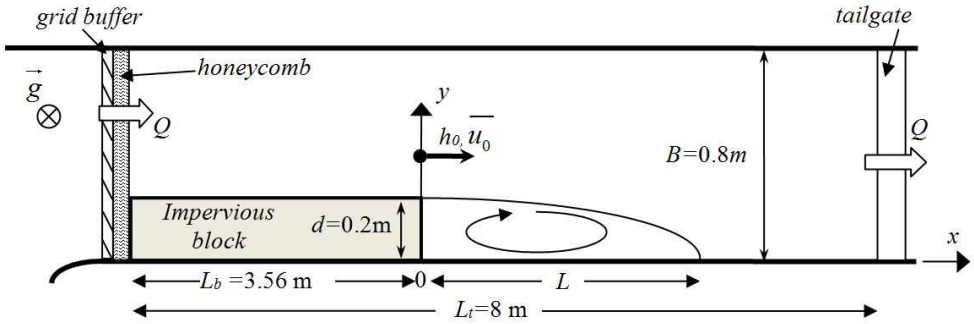

Figure 5.1: Plan view of the experimental set-up

Table 5.1: Flow characteristics for all studied configurations

Test	Q(l/s)	$\overline{u}_0$(m/s)	h_0(m)	c_{f0}	S	L(m)	L/d
F1 (deep)	20	0.23	0.156	0.0049	0.0032	1.29	6.45
F2 (transitional)	16.15	0.55	0.050	0.0050	0.01	1.99	9.95
F3 (shallow)	4.05	0.36	0.021	0.0068	0.032	1.16	5.80
F4 (shallow)	2.363	0.20	0.022	0.0195	0.089	0.86	4.3

All parameters for the 4 experiments are given in TAB.5.1. Let us recall that:
$\rightarrow$ x is the streamwise axis with $x = 0$ located at the enlargement; y is the transverse axis

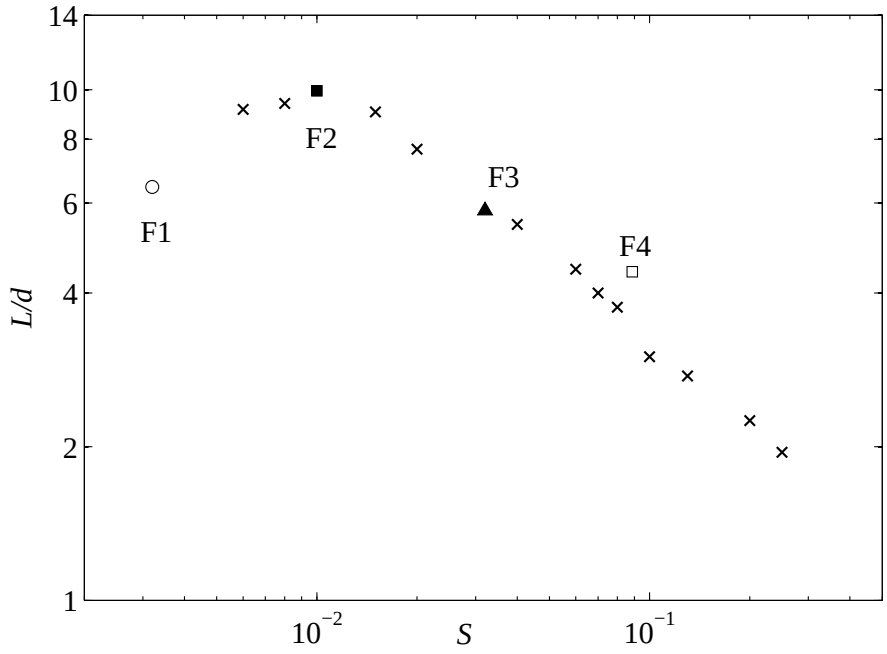

Figure 5.2: Selected configurations (○, ▲, ■ and □) for measuring mixing layer

with y=0 located at the side wall (see FIG.5.1).
→ B is the channel width.
→ d is the expansion width.
→ Q is the total discharge.
→ $\overline{u}_0$ is the mean velocity in the center of the canal at x=0 and y=0.3m.
→ h_0 is the water depth in the center of the channel at x=0 and y=0.3m.
→ c_{f0} is the friction coefficient at x=0 and y=0.3m.
→ S is the bed-friction number.
→ L_b is the upstream flow development length, from the honeycomb to the enlargement.
→ L is the recirculation length, from the enlargement (x=0) to the reattachment point.

5.1.2 Measurement conditions

As the ADV measurement is automatic (performed using the LabVIEW software), the measurement grid must be defined beforehand. About one thousand points are selected in the region downstream from the enlargement as shown in FIG.5.3 for F2. This region covers the whole recirculation area, plus the center of the channel up to $y >$0.6m, and it finishes slightly further downstream. For each grid point, a 180 seconds ADV acquisition is performed with sample frequency of 30 Hz. The ADV permits to measure the 2 horizontal velocity components u (along x axis) and v (along y axis). For the deepest conditions (F1 and F2), the vertical components are also measured. No data is available

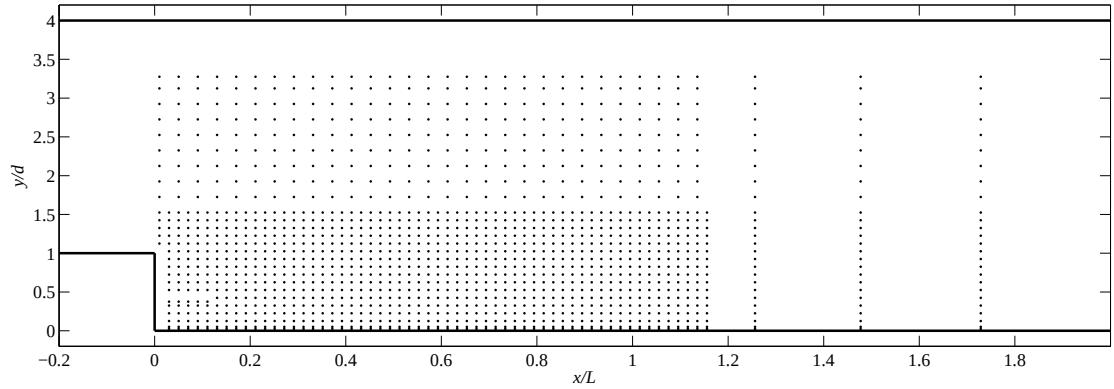

Figure 5.3: ADV measurement grid for F2

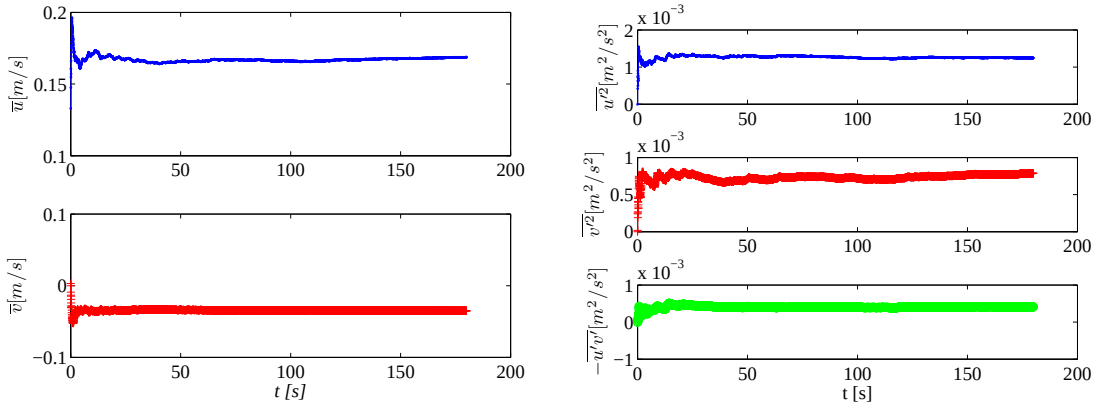

(a) Streamwise and transverse velocity u and v

(b) The Reynolds stress $\overline{u'^2}$, $\overline{v'^2}$ and $\overline{-u'v'}$

Figure 5.4: Time convergence for the velocity and the Reynolds stress.

near the left bank (y/d >0.6m, *i.e.* y/d >3.3) due to ADV positioning.

5.1.3 Time-convergence verification

The 180 seconds measurements ensure a convergence of most components as shown below. The point is selected from configuration F3, x/L=0.5, y/d=0.7 which is the the center of the mixing layer. For the mean velocity $\overline{u}$ and $\overline{v}$, 180 seconds are enough for the convergence. Even after 100 s, the convergence show less fluctuations. The Reynolds stress are also converged after 100 s as shown in the FIG.5.4, which validates the choice of 180s during measurements. For the water depth, the fluctuation change very little (<1%), so 120 s measurement is considered herein for for obtaining the convergence well as in the FIG.5.5.

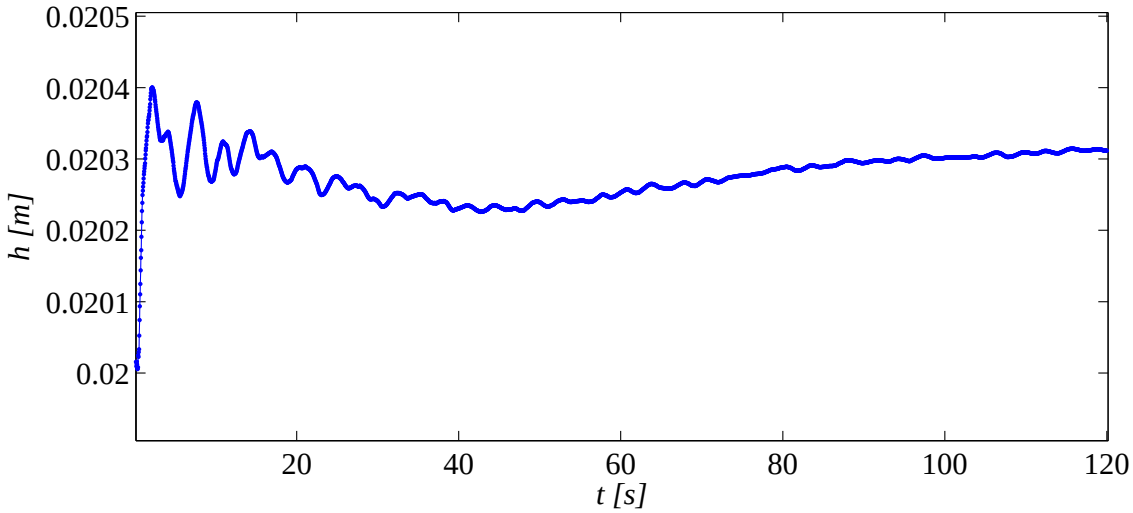

Figure 5.5: Time convergence for the water depth h

Note: F3, x/L=0.5, y/d=0.7 and R_b=0.75.

5.2 Mean flow description

5.2.1 Upstream flow development

Before performing the measurements, it should be verified that L_b is sufficient to reach an established inflow before reaching the enlargement. This development condition is verified for the following flow parameters, measured along x axis at y=0.5m, that is at the center of the upstream channel (y=$d+(B-d)/2$):
$\rightarrow$ the streamwise and transverse mean velocity components $\overline{u}$ and $\overline{v}$ at z/h=0.4
$\rightarrow$ water depth h
$\rightarrow$ the approximate discharge per unit width $h\times\overline{u}$
$\rightarrow$ the 3 measured Reynolds stress components: $\overline{u'v'}$, $\overline{u'^2}$, $\overline{v'^2}$.
In FIG.5.6, these data are plotted for F3 (S=0.032). It can be seen that after x/L=-1, all values become quite constant. So establishment condition when reaching the enlargement is satisfactory. All curves show a satisfactory established flow before reaching x=0. After the enlargement ($x/L>0$), the same figure is also obtained at the same position of y=0.5 m. Because they are in the outer region of the mixing layer, all the parameters remain constant as upstream except those:
$\rightarrow$ the term $\overline{u}$ which decreases as the flow section increases
$\rightarrow$ $h\overline{u}$ which decreases due to mass conservation ($h\overline{u}=Q/(B-d)$ at x/L=0 and tends toward $h\overline{u}=Q/B$ at $x/L>1$).

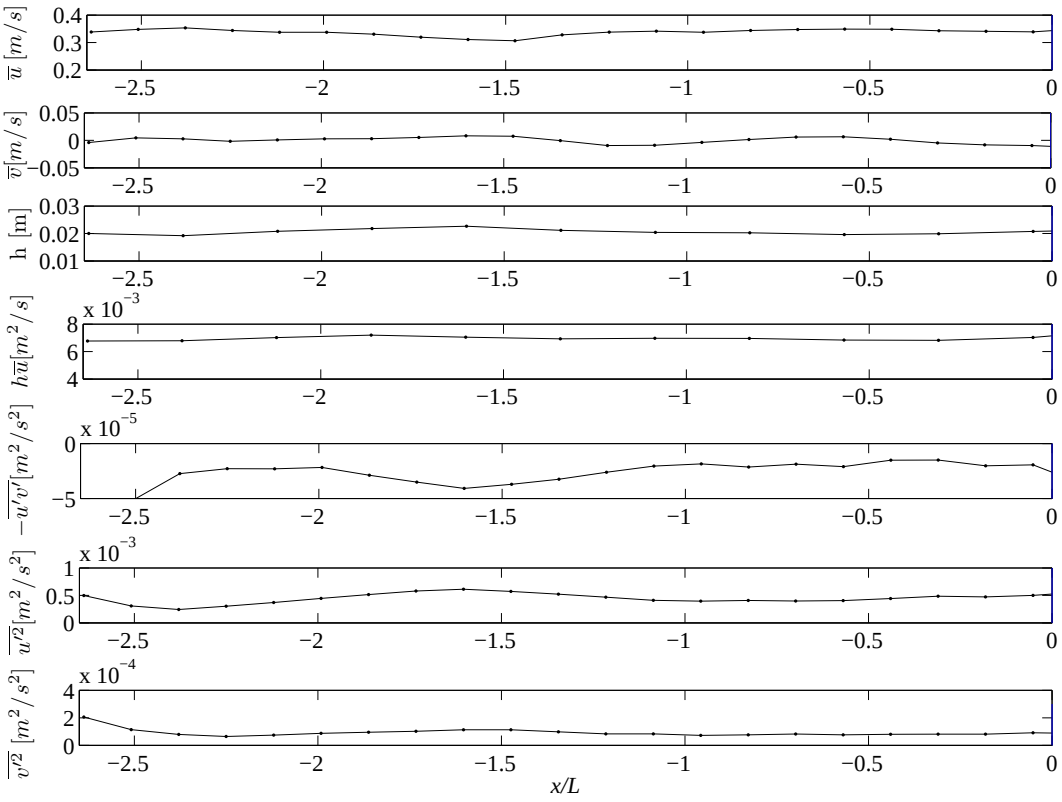

(a) upstream the expansion $x/L < 0$

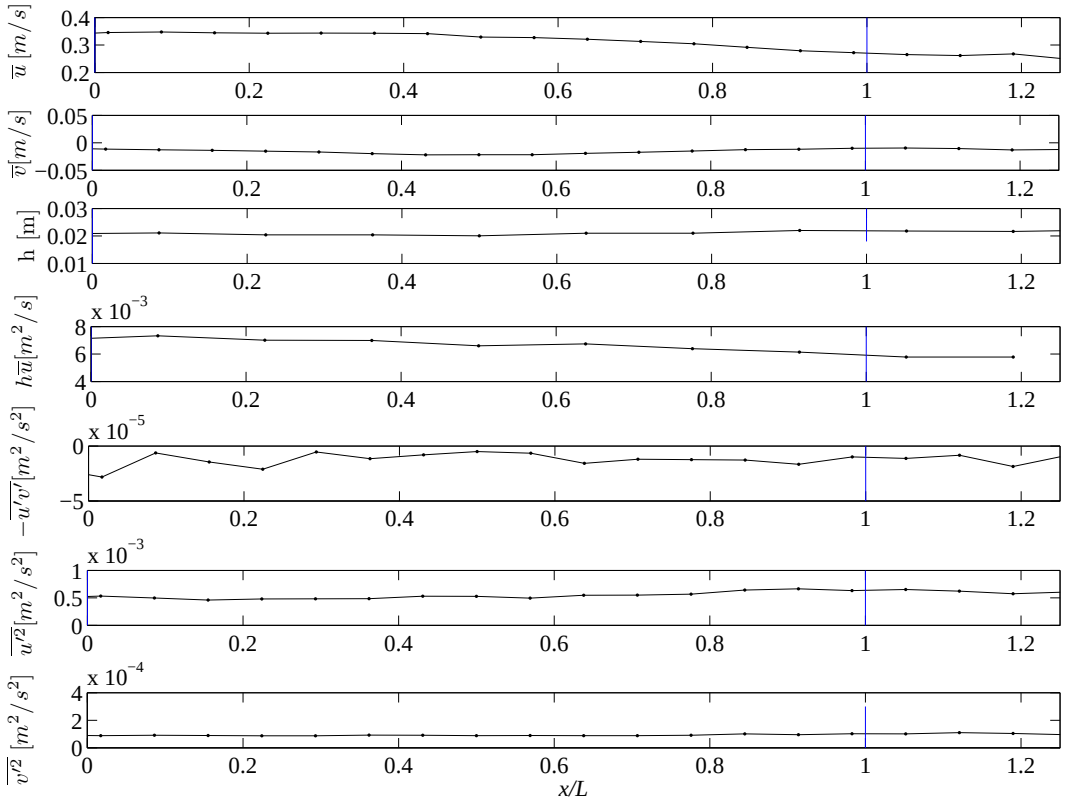

(b) downstream the expansion $x/L > 0$

Figure 5.6: Longitudinal variations of different measurement at y/d=0.5 along the streamwise direction, used to gauge the the flow development

Table 5.2: Location of the center of the recirculation zones

Test N°	x/L	y/d
F1	0.57	0.52
F2	0.41	0.42
F3	0.47	0.42
F4	0.36	0.42

5.2.2 Mean flow field

After despiking the velocity signals (see CHAP.2) and applying the rotation correction, each velocity signal is time-averaged. The mean velocity field is then plotted as shown in FIG.5.7 to FIG.5.10. The enlargement begins at section $x/L = 0$ and ends at x/L=1. It appears that:

1. The flow separates at x/L=0 and y/d=1, with a velocity vector almost parallel to x axis ($v \sim$0).
2. A recirculation zone is observed for $y/d <$1 and $x/L <$1. The center of this recirculation cell is located at about x/L=0.5 and y/d=0.4, which are shown in TAB.5.2. The velocity along the side wall (y/d=0) is oriented towards upstream ($\overline{u} <$0).
3. The velocity field outside the recirculation region ($y/d >$1) is oriented towards the side wall ($\overline{v} <$0) as the flow section increases.
4. In the outer region ($y/d >$1.5), the velocity field is nearly uniform along y axis but decreases along the x axis (see FIG.5.6)
5. In the region downstream from reattachment ($x/L >$1), recovery towards a uniform velocity profile along the transverse direction begins but it is not reached in the measurement region (x/L=2) (see FIG.5.11(b), for F3 with S=0.032).
6. A secondary gyre exists near the corner x/L=y/d=0, but it is fairly measured only in F2 flow (S=0.01) which has the greatest velocity $\overline{u}_0$. This gyre can be seen in FIG.5.11(a), in the zoom around the corner of the enlargement.

When comparing the four average velocity fields, it can be seen that the four mean flow patterns are very similar one to the other (in which selected streamlines (plain lines $-$), the bottom plot is a zoom of the top plot in the recirculation zone where $y/d <$1). The main difference is the location of the center of the main gyre which is given in TAB.5.2.

5.2.3 Mean streamwise velocity profiles

5.2.3.1 Comparison among 4 flow cases

From the mean velocity field, transverse profiles are presented for the 4 cases from x/L=0.01 to x/L=1.2. The mean velocity profiles are all normalized by the mean velocity

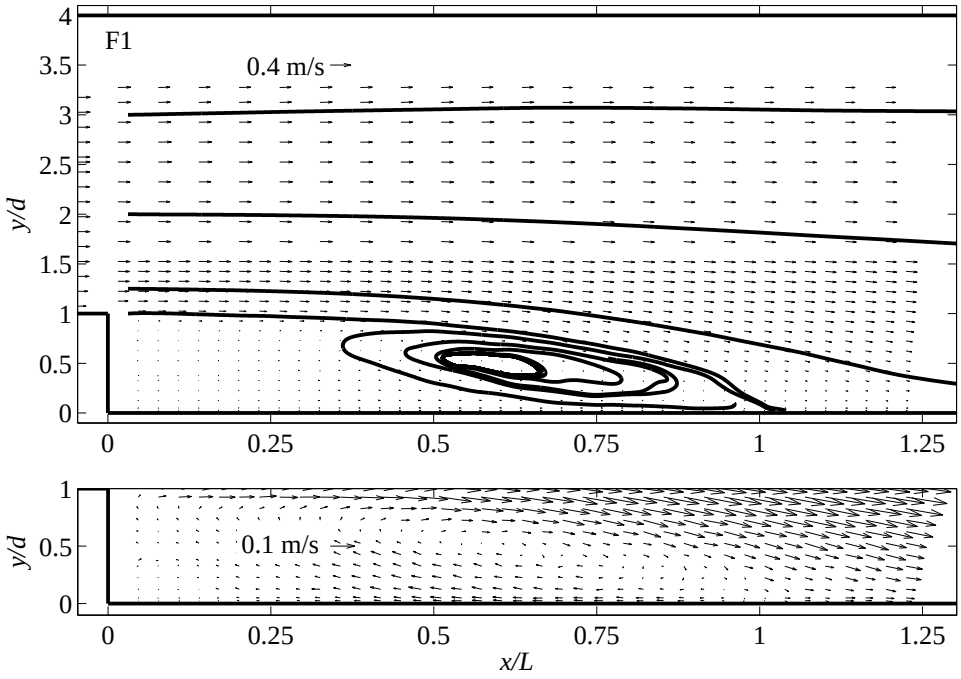

Figure 5.7: Time-averaged velocity field (F1).

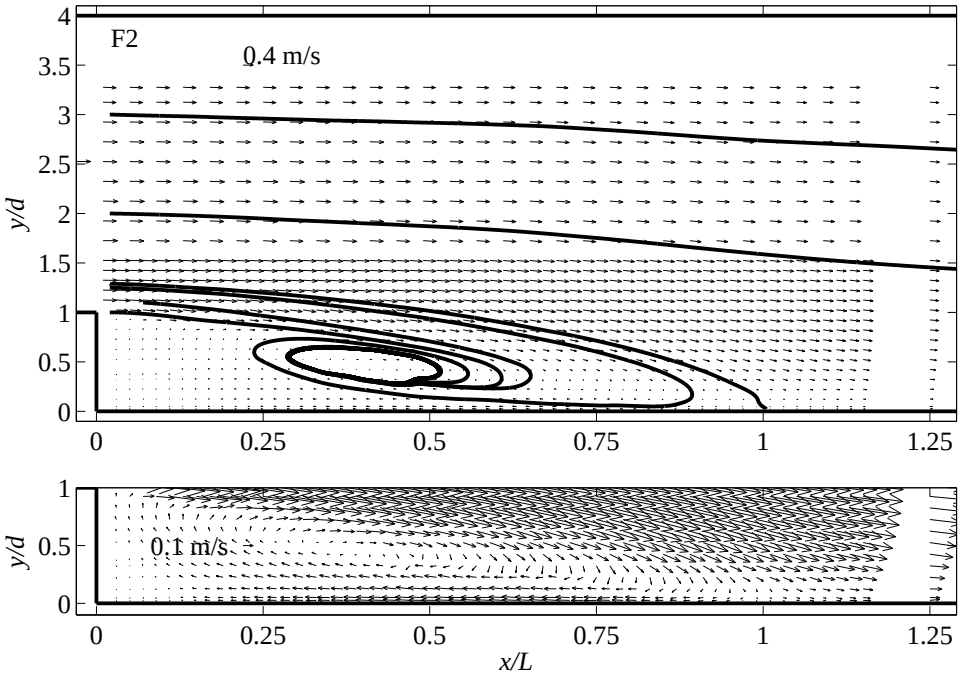

Figure 5.8: Time-averaged velocity field (F2).

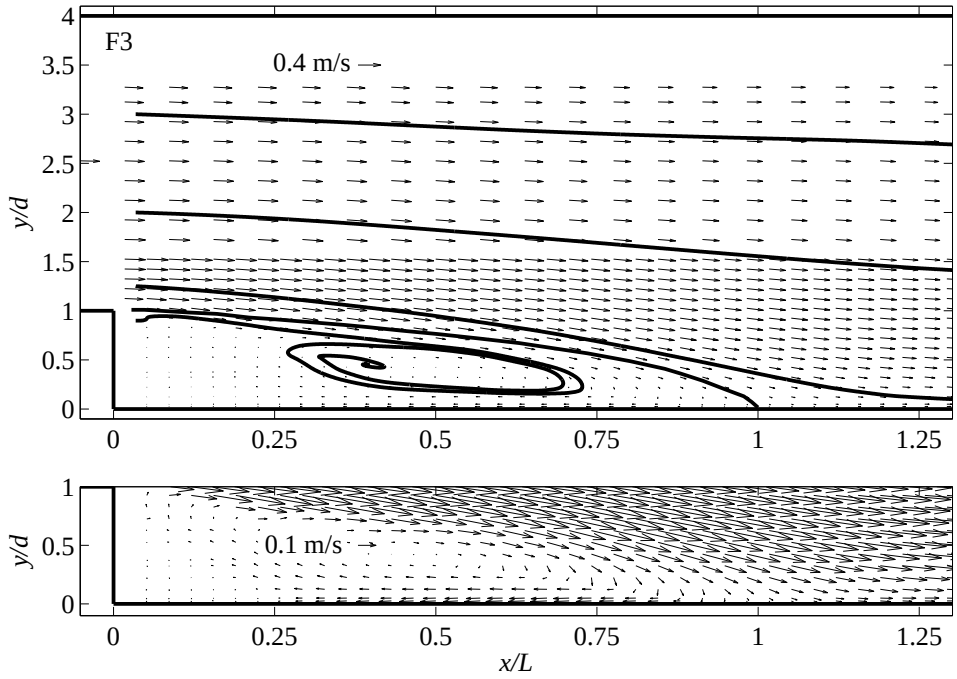

Figure 5.9: Time-averaged velocity field (F3).

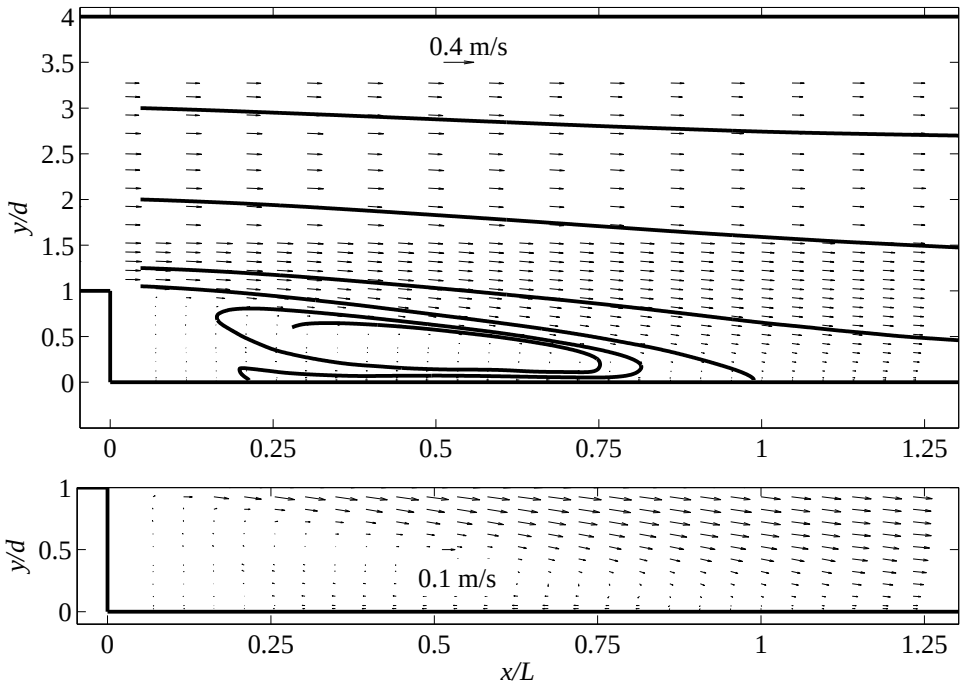

Figure 5.10: Time-averaged velocity field (F4).

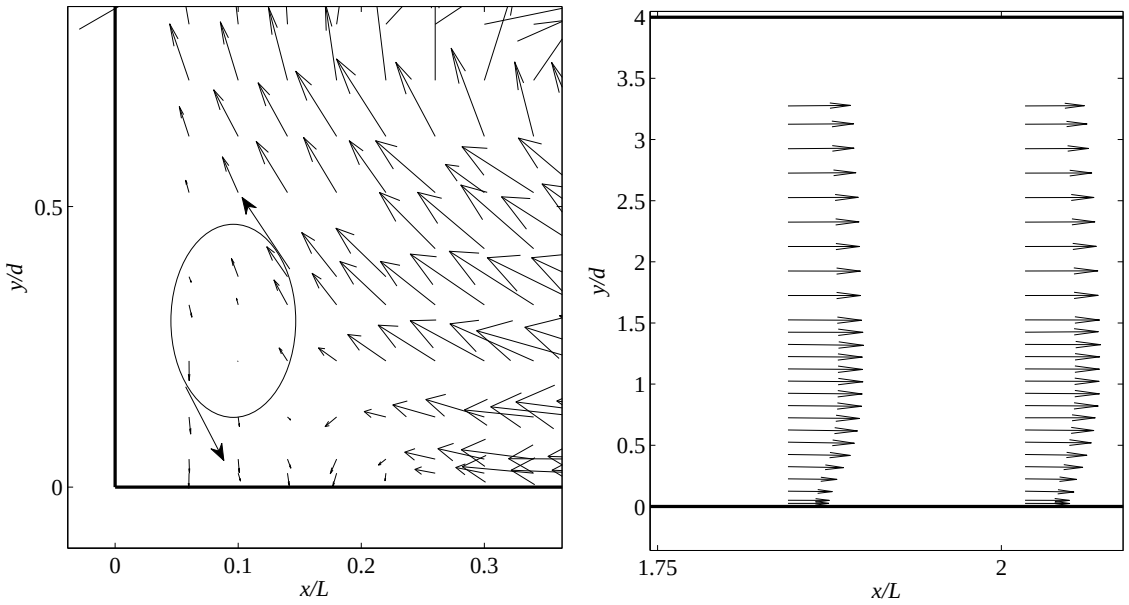

(a)The secondary gyre obtained for F2 S=0.01 (b)The downstream velocity recovery for F3 S=0.032

Figure 5.11: Some characteristics of F2 and F3

$\overline{u}_0$ (which is measured at the beginning of the recirculation: x/L=0, y=0.3 m). Those profiles are plotted in FIG.5.12. It can be seen that:
(1) Near the enlargement (x/L=0.01), the profiles are almost uniform equal to $\overline{u}/\overline{u}_0$ =1.
(2) In the most upstream section of the recirculation zone (x/L=0.1), the profiles exhibit a maximum velocity gradient at y/d=1: $\overline{u} \sim 0$ for $y/d < 1$ and $\overline{u} \sim \overline{u}_0$ for $y/d > 1$). There is not much difference among the 4 cases.
(3) From section x/L=0.2 to x/L=1, the outer velocity (at $y/d > 2$) decreases. The velocity near the side wall ($y/d < 0.5$) first becomes negative and increases in magnitude ($0.2 < x/L < 0.5$ and tends towards zero for $x/L > 0.6$. The velocity gradient around $y/d = 1$ decreases as x/L increases. The differences appear among the 4 cases are analysed in section 5.2.4 hereafter.
(4) After the end of the recirculation ($x/L > 1.2$), the recovery region occurs and the profiles tend towards uniformity. However, the constant velocity profile at x/L=2 is not equal to $\overline{u} = \overline{u}_0(B-d)/B = 0.75\overline{u}_0$ as the water depth increases towards downstream (see FIG.5.13) so that $h(x/L$=1.2)$> h_0$. It should be noted that for F1 the velocity profile remains non uniform with a maximum velocity at the center of the channel (y/d=2, y/B=0.5). But there exits a symmetry in the direction y. We will now compare the velocity profiles with the ones from [Babarutsi et al., 1989].

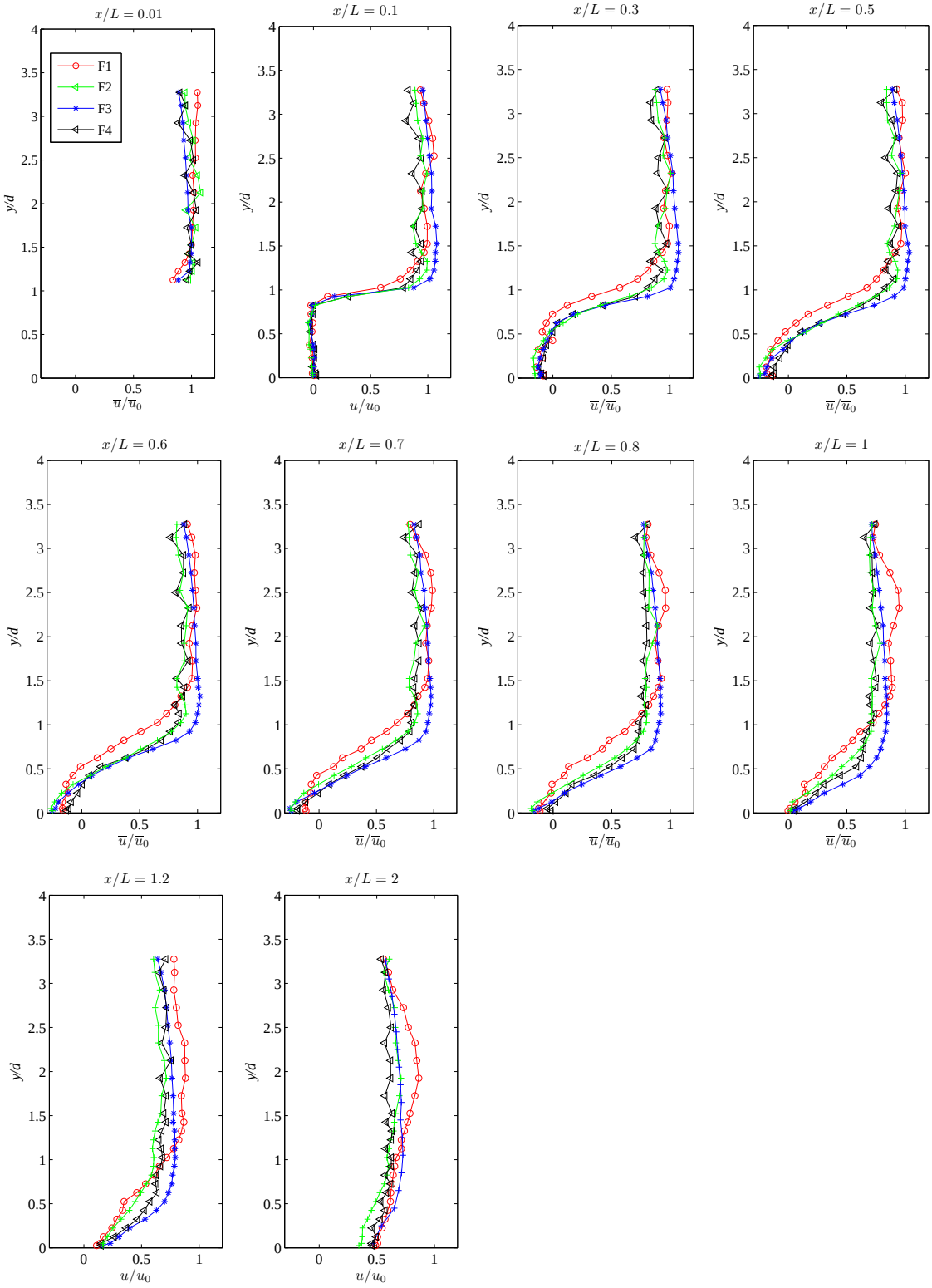

Figure 5.12: Streamwise velocity profiles dimensionless by $\overline{u}_0$ for four cases

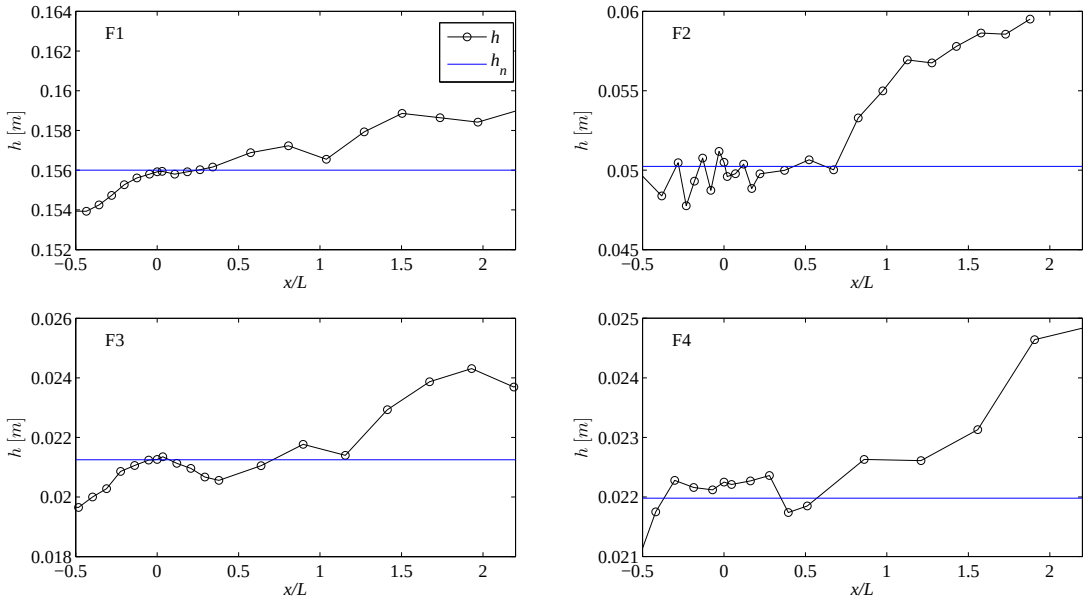

Figure 5.13: Water depth at y=0.5 m along the streamwise direction for four cases

5.2.3.2 Comparison with literature data

In the literature, similar data is available in the study from [Babarutsi et al., 1989]. These authors considered 5 configurations with S=**0.0098, 0.0232, 0.043, 0.0977, 0.2529**. In the present section and in FIG.5.15, we compare the mean velocity profiles with $S \sim$0.01 (S=0.0098 from [Babarutsi et al., 1989] and present for F2 (S=0.01). The green lines are for the profiles of [Babarutsi et al., 1989] and the red lines for the present configuration F2. However, a main difference exists between present and [Babarutsi et al., 1989] configurations: the dimensionless channel width R_b equals 0.5 for [Babarutsi et al., 1989] (at the line black dash $--$), and equals 0.75 in the present case. This explains the different shape near the left wall for [Babarutsi et al., 1989]. Where the data ($y/d > 1$) cannot be compared especially in the downstream region. Moreover, neglecting the evolution in water depth, the homogeneous velocity far downstream tends towards $\overline{u}_0/2$ for [Babarutsi et al., 1989] configuration and $3/4\overline{u}_0$ for our case.

Due to these 2 reasons, comparison is limited to the upstream region of the recirculation in FIG.5.15. When comparing the two profiles of streamwise mean velocity, a fair agreement is observed.

5.2.4 Transverse gradient of mean streamwise velocity

The transverse gradient of mean streamwise velocity is defined as $\partial\overline{u}/\partial y$, and made normalization with $d/\overline{u}_0$. The contours of this gradient are presented for the 4 cases FIG.5.16. Further more, the profiles of the same term is plotted in FIG.5.17. The 4 cases show very similar behaviour:

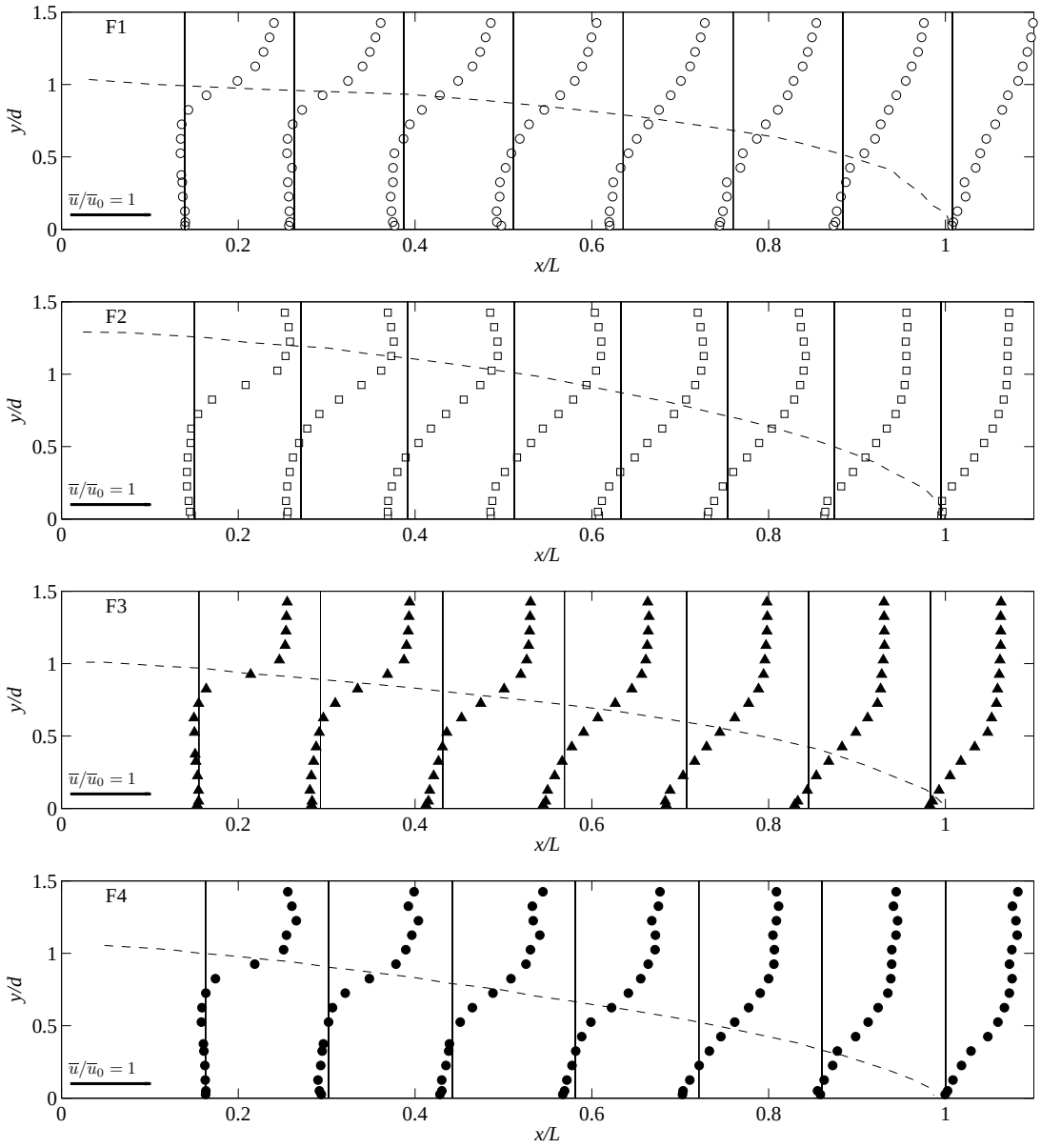

Figure 5.14: Streamwise velocity profiles dimensionless by $\overline{u}_0$ for each case

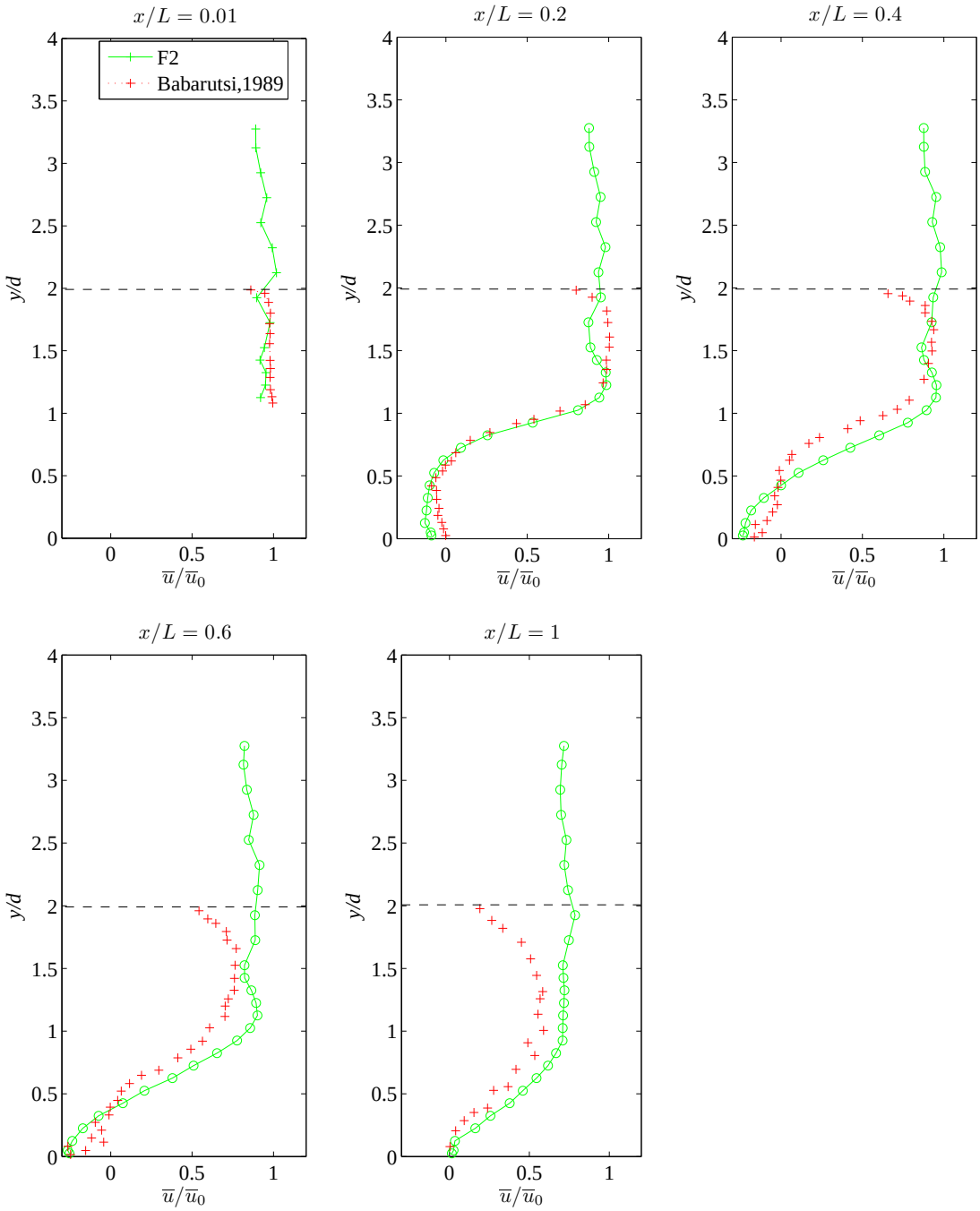

Figure 5.15: Streamwise velocity profiles of F2 with comparison with the literature

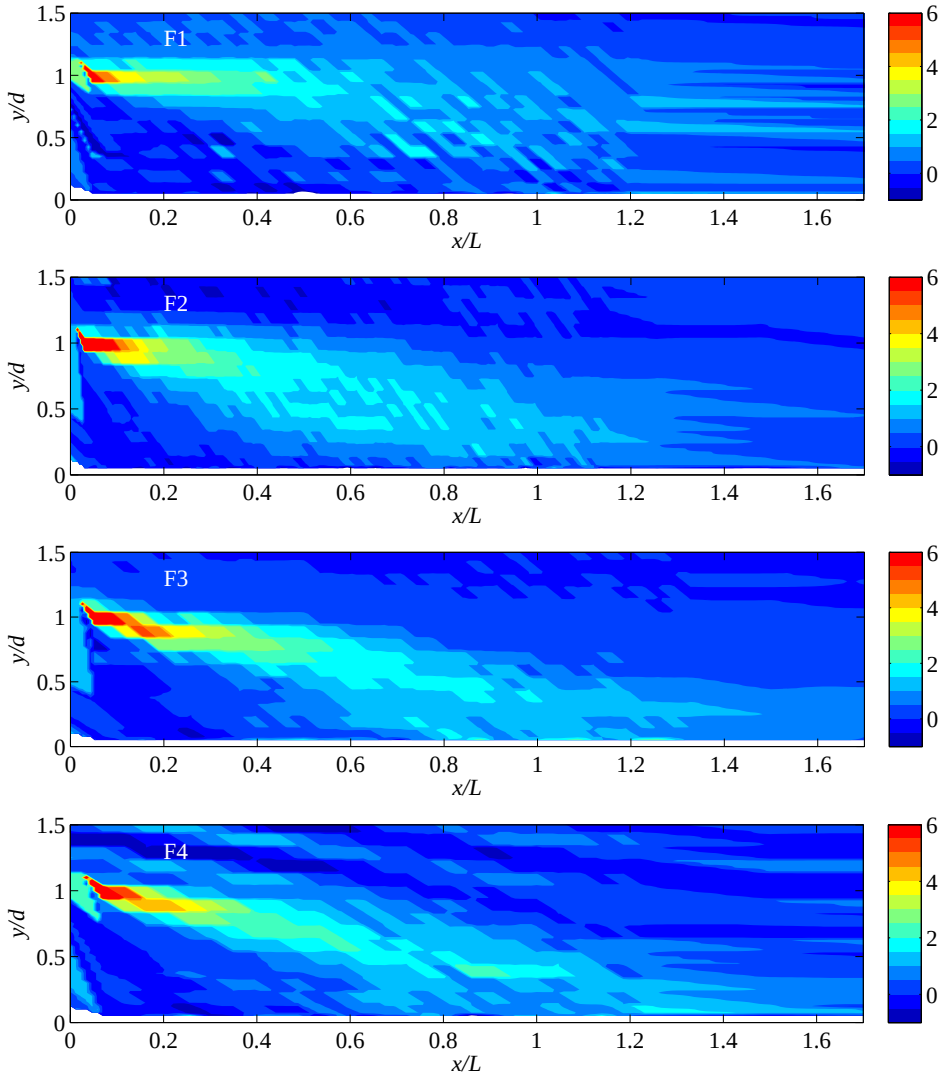

Figure 5.16: Contours of the mean velocity Gradient $d\overline{u}/dy \times d/\overline{u}_0$

1. Outside of the mixing layer (which will be defined in the sequel), that is far from the recirculation frontier, the gradient is close to 0.

2. In the mixing layer, the gradient increases and reaches its maximum near the center of the layer (see below). Moreover, the maximum gradient is obtained in the upstream part of the recirculation ($x/L \sim 0.1$) and this gradient decreases along the flow axis and reaches small values (below 1) after x/L=1.

3. Finally, near the right wall ($y/d \sim 0$), just downstream from the enlargement ($0 < x/L < 0.5$), a negative gradient region is obtained, in agreement with the velocity profiles presented above.

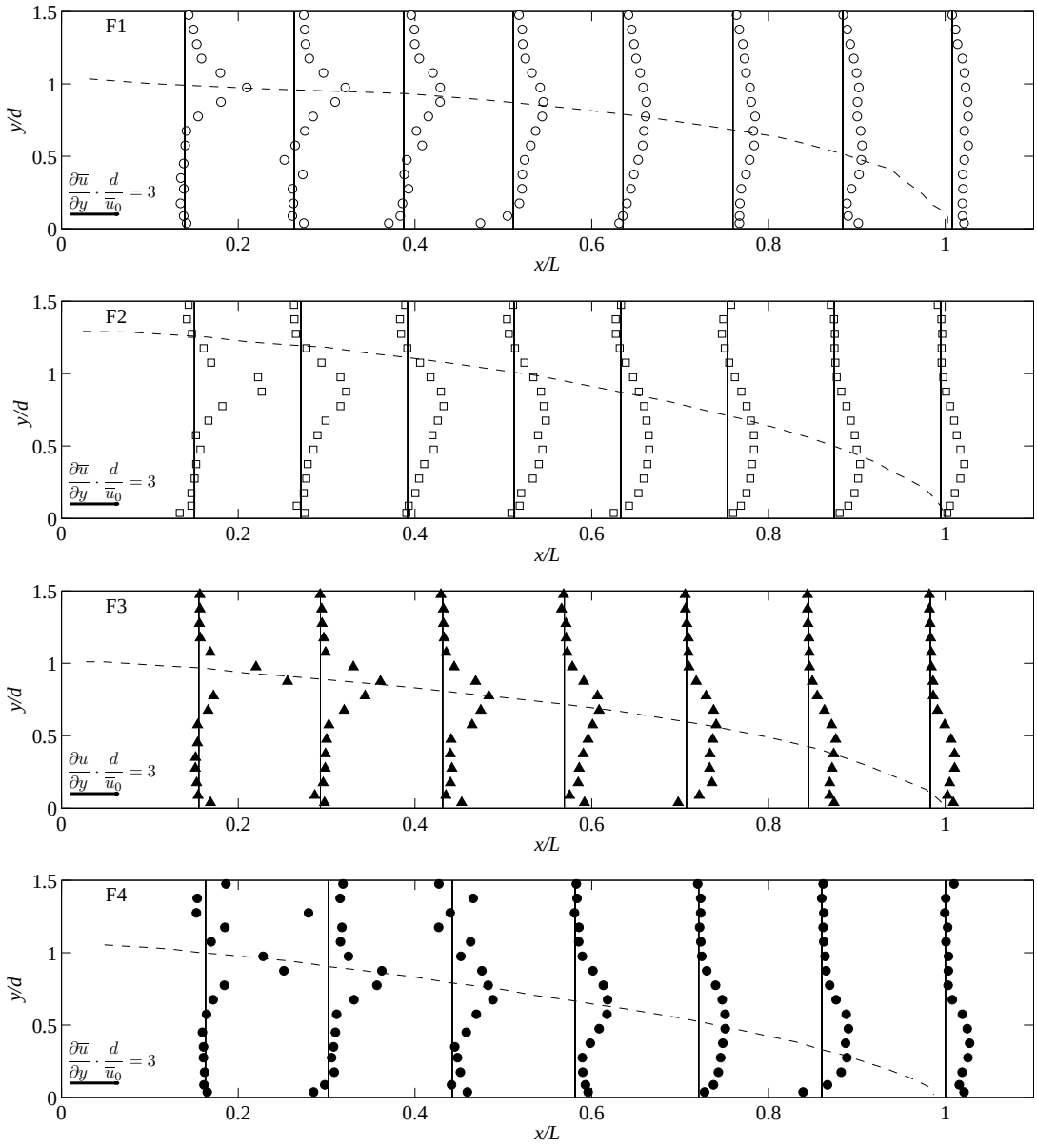

Figure 5.17: Profiles of the mean velocity Gradient $d\overline{u}/dy \times d/\overline{u}_0$

FIG.5.17 shows transverse profiles of this gradient. Due to perturbations of the measurements in the experiments, the profiles near the end of the recirculation are not smooth. So a Savitzky-Golay filtering method [Chen et al., 2004] is introduced to obtained smoother profiles indicated in black in FIG.5.18. The smooth profiles (in black −) will be used in the sequel.

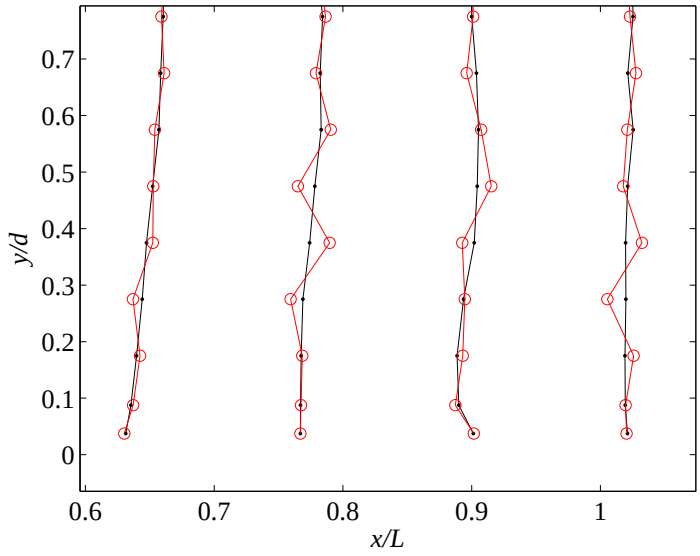

Figure 5.18: The Savitzky-Golay filtering for the gradient (•) zooming from F1

5.3 Characteristics of the mixing layer

All previous figures and flow descriptions reveal the presence of a slow recirculation region for $y/d < 1$ and a rapid mean flow which width expands slowly from $(B-d)$ to B on the side of this recirculation ($x/L < 1$). At the frontier between these 2 zones, we reported a region with high velocity gradient, named mixing layer in the literature. Present section aims at detailing this mixing layer characteristics. In the present case, the mixing layer is confined transversally (mostly due to the reattachment wall) and is confined vertically (due to the shallowness of the flow and the bed friction).

5.3.1 Definitions

The mixing layer is characterized considering:
→ $\overline{u}_1(x)$ is the outer velocity magnitude in the free stream, measured at y/d=1.5 for each section.
→ $\overline{u}_2(x)$ is the outer velocity on the recirculation side. In their study around a square cylinder, [Lyn and Rodi, 1994] define $\overline{u}_2$ as the minimum velocity (negative) along the

profile measured within the recirculation region. In a sudden expansion, [Talstra, 2011] consider $\overline{u}_2$=0, *i.e.* the mean streamwise velocity in the zero-discharge recirculation region. This definition is used in the present paper.
$\rightarrow \Delta\overline{u}(x)$ is the outer velocity difference $\Delta\overline{u}(x) = \overline{u}_1(x) - \overline{u}_2(x) = \overline{u}_1(x)$
$\rightarrow \overline{u}_c(x)$ is the mean outer velocity $\overline{u}_c(x) = (\overline{u}_1(x) + \overline{u}_2(x))/2 = \overline{u}_1(x)/2$
$\rightarrow$ at each section x/L, the center of the mixing layer is defined as the point with the maximum transverse gradient of streamwise velocity, $\partial\overline{u}/\partial y$ (see FIG.5.20)), as proposed by [Mignot et al., 2014b] and [Mignot et al., 2014a].
$\rightarrow$ the width of the mixing layer is defined as:

$$\delta(x) = \frac{\Delta\overline{u}(x)}{|\frac{\partial\overline{u}(x)}{\partial y}|_{max}} \tag{5.1}$$

The local bed friction number $S(x)$ was defined by [Chu et al., 1983] as below:

$$S(x) = \frac{c_f\overline{u}_c}{2h|\frac{\partial\overline{u}(x)}{\partial y}|_{max}} = \frac{c_f\delta(\overline{u}_1+\overline{u}_2)/2}{2h(\overline{u}_1-\overline{u}_2)}$$

Including the assumption that $\overline{u}_2$=0, this parameter becomes $S(x) = \delta c_f/4h$. Now, assuming that the friction coefficient does not evolve noticeably and that the water is perfectly constant along the mixing layer, the final expression used herein reads:

$$S(x) = \frac{\delta(x)c_{f0}}{4h_0} \tag{5.2}$$

5.3.2 Outer velocity

The streamwise evolution of the velocity difference, equal to the free stream outer velocity $\Delta\overline{u}(x) = \overline{u}_1(x)$, is plotted for 4 flows in FIG.5.19 together and the FIG.5.22) separately. It appears that:
(1) for the deep F1 configuration, the velocity difference remains almost constant along x axis, with a very limited decrease from the expansion to the reattachment section, in agreement with the literature (see discussion by [Sukhodolov et al., 2010])
(2) for the F2 and F3 configurations, the velocity difference decrease is much stronger, from $\Delta\overline{u}/\overline{u}_0$=1 at the expansion to 0.8 at the reattachment section. This behavior was already observed in a shallow mixing layer: in Fig.4 by [Van Prooijen and Uijttewaal, 2002]. However, the shape of the decreasing velocity difference in the unbounded shallow mixing layers in the literature are: i) an exponential curve for [Van Prooijen and Uijttewaal, 2002] and [Booij and Tukker, 2001] (cases A and D) or ii) a linear curve for [Sukhodolov et al., 2010] and [Booij and Tukker, 2001](cases B and C). In our shallow and bounded F2 and F3 configuration, these two types of curve do not fit the data, a better-fit is obtained using a parabolic curve. (see FIG.5.20).
(3) For the F4 configuration , the $\Delta\overline{u}(x)$ increases in the beginning of the recirculation zone and then decreases following a linear tendency.

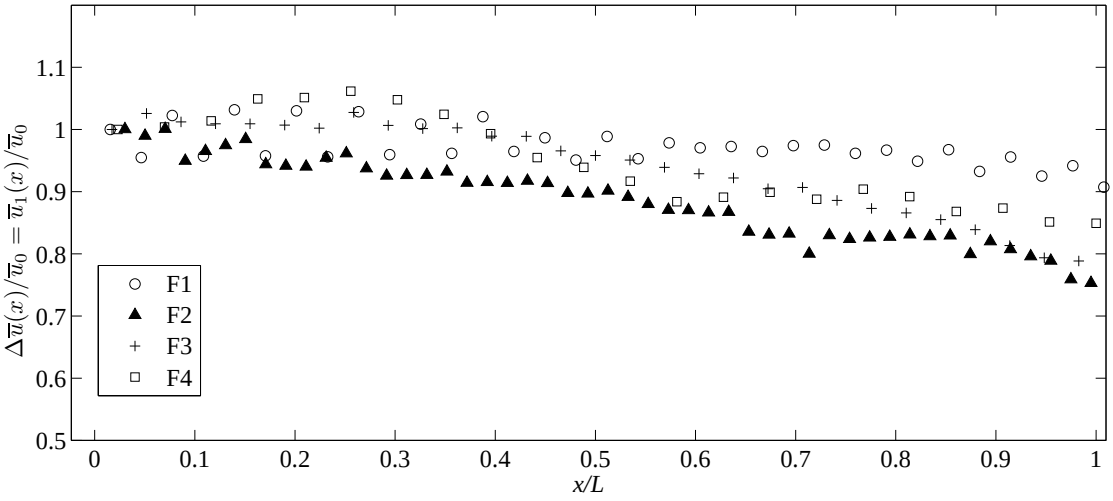

Figure 5.19: Streamwise evolution of the outer velocity difference $\Delta\overline{u}$

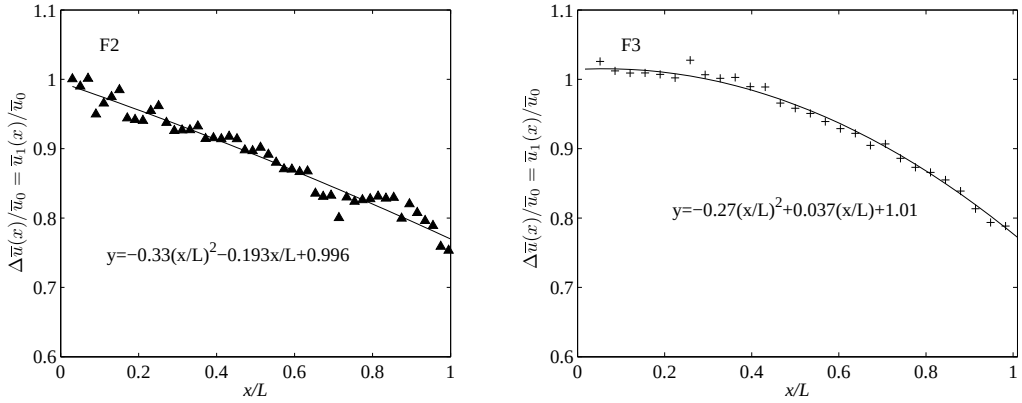

Figure 5.20: $\Delta\overline{u}$ with the best fit line −−

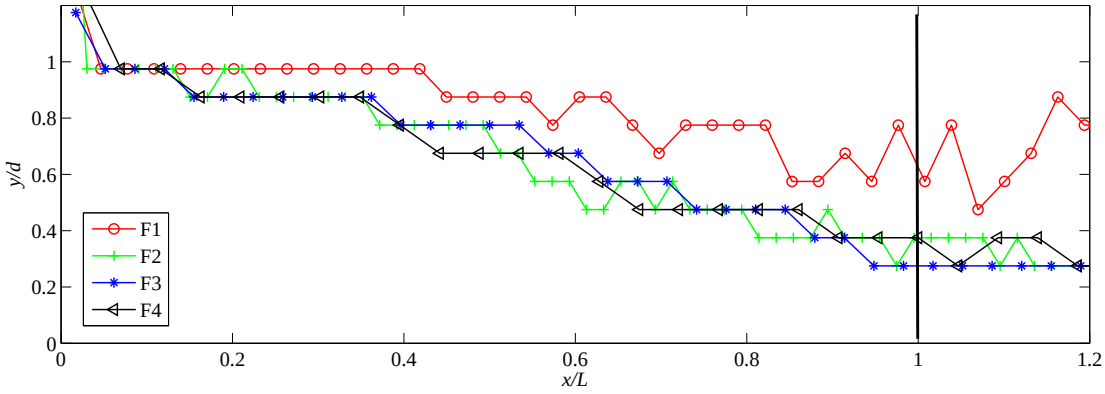

Figure 5.21: Position of the maximum transverse gradient of the streamwise velocity for the four cases

5.3.3 "Center" of the mixing layer

Based on the gradient profiles in FIG.5.17, the transverse position of the maximum gradient is obtained. The values decay from y/d=1 at x/L=0 to 0.2 at x/L=1 except for F1 as shown in FIG.5.22. Comparing the 4 cases together, the tendency are very similar among F2, F3 and F4. The influence of the reattachment wall is that the maximum gradient location does not reach the side wall (y=0). The location of the maximum gradient at x/L=1 equals $y/d \sim$0.2 and is about constant further downstream. For F1, the shape of the maximum gradient location differs : it remains far from the reattachment wall. Reason for that may be that this case contains the largest vortices (see section 5.6), so that their interactions with the side wall takes place very early in the mixing layer development. In the following, these curves constitute the evolution of the center of the mixing layer. Another definition for the center of the mixing layer could be the location of the maximum Reynolds Stresses $-\overline{u'v'}$, even though we could not find any reference in the literature using this definition. In FIG.5.22, the two lines corresponding to the two definitions are plotted and appear to be in fair agreement with each other (except for some points in F4).

5.3.4 Width of the mixing layer

The streamwise evolution of the measured mixing layer widths δ is plotted in FIG.5.23. When comparing the cases, the mixing layer widths appear to be similar at the expansion, $\delta_0 = \delta(x = 0) \approx 0.02$m, but they increase quite differently:
i) For the deep configuration F1, δ increases linearly with a first increasing rate up to $x/L = 0.7$ and further downstream the linear increase rate strongly reduces, as demonstrated by the two linear tendencies on FIG.5.23.
ii) For the shallow case F2, δ also increases linearly up to $x/L = 0.7$, with a smaller slope than F1, but experiences a plateau for $x/L >$0.7 corresponding to a local bed friction number $S(x)$=0.009.

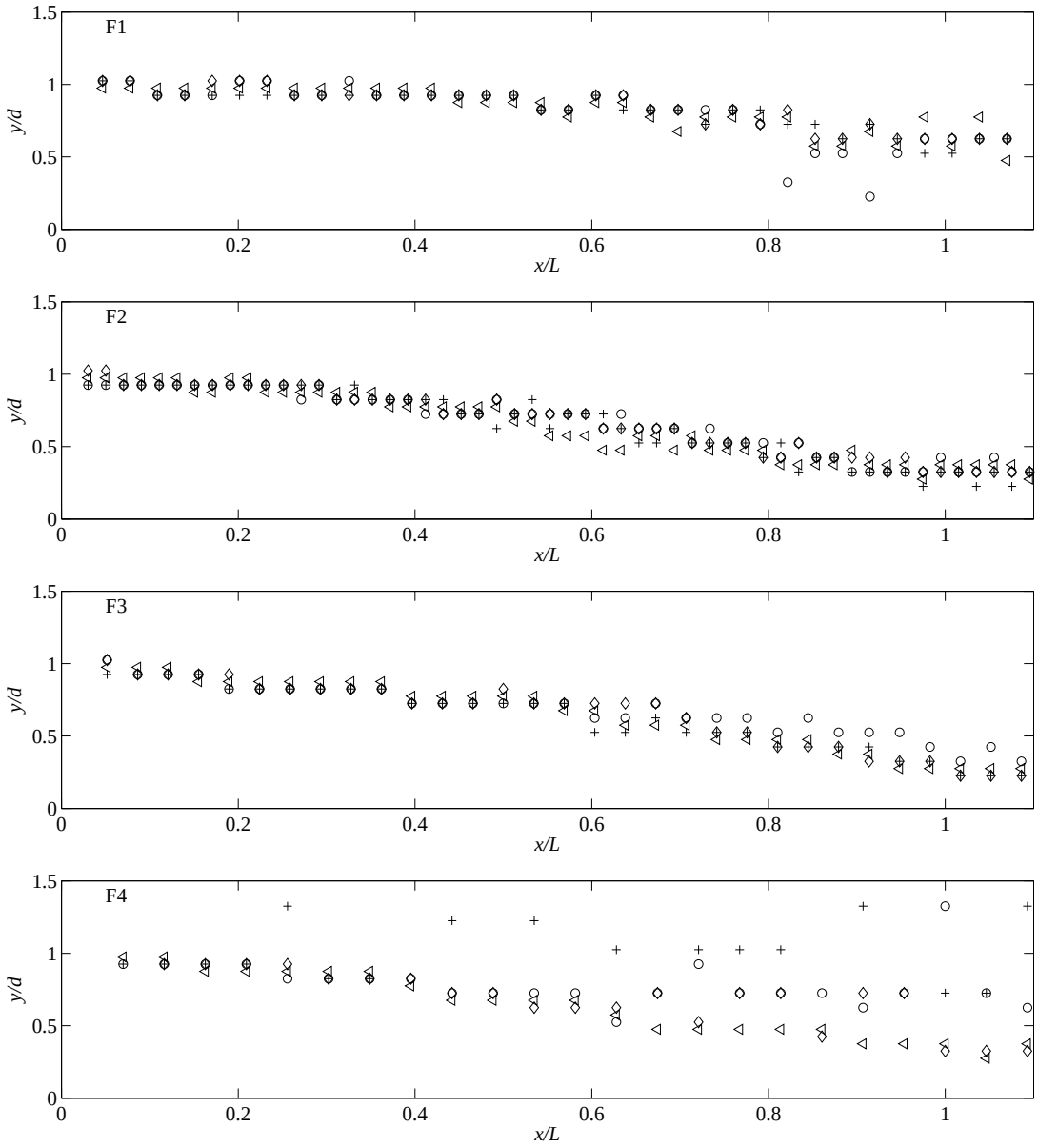

Figure 5.22: Location of maximum velocity gradient (◁), $\overline{u\prime^2}$ (○), $\overline{v\prime^2}$ (+) and $-\overline{u\prime v\prime}$ (◇)

iii) F3 and F4 configurations also exhibit a linear spreading, which slope is minimum for the shallower cases (F2 and F4) and maximum for the deeper cases (F1 and F3). Further downstream F3 and F4 exhibit a plateau, as for F2, for respectively x/L >0.55 and 0.65 and $S(x)$=0.003 and 0.025. These trends are compared with results from the literature. The streamwise growth of the mixing-layer width can be estimated as a function of the ratio between the velocity difference and the center velocity as:

$$\frac{d\delta}{dx} = \alpha \frac{\Delta\overline{u}(x)}{\overline{u}_c(x)} \tag{5.3}$$

which reads alternatively, when considering $\overline{u}_2$=0 in the present problem:

$$\frac{d\delta}{dx} = 2\alpha \tag{5.4}$$

A linear trend, *i.e.* a constant spreading rate coefficient α, is frequently reported in the literature for unbounded free mixing layers due to constant $\Delta\overline{u}$ and $\overline{u}_c$ (see [Bell and Mehta, 1990]). Considering the fitting slopes of FIG.5.23, the values of the spreading rate for both deep and shallow regimes in the upstream region of the mixing layer are α=0.07 for F1, α=0.08 for F2, α=0.06 for F3 and α=0.075 for F4 in agreement with values reported for free unbounded mixing layers: α=0.03-0.11 from [Pope, 2008] or α=0.085 from [Lesieur, 1997]. Note that $\frac{d\delta}{d(x/L)} = 2\alpha L$ where L is the length of the recirculation.

On the other hand, as reminded in the introduction, all published papers for shallow unbounded mixing layers agree that the shallowness affects the $\Delta\overline{u}/\overline{u}_c$ ratio and limits the mixing layer spreading (see [Booij and Tukker, 2001] or [Chandrsuda and Bradshaw, 1981]). Thus the vertical confinement effect could be the cause for the plateaus in configurations F2, F3 and F4. In the literature this spreading decreases along the flow: [Van Prooijen and Uijttewaal, 2002] report that $\delta(x)$ increases following a $-e^{-x}$ curve, while [Sukhodolov et al., 2010] report a parabolic $a + bx - cx^2$ curve,both considering a constant spreading rate α of 0.085 and 0.11 respectively. Regarding the the impact of shallowness on the spreading rate coefficient α, [Chu and Babarutsi, 1988] expressed it as:

$$\begin{cases} \alpha = \alpha_0(1 - \dfrac{S(x)}{S_c}) & \text{for} \quad S(x) < S_c \\ \alpha = 0 & \text{for} \quad S(x) > S_c \end{cases} \tag{5.5}$$

where α_0 is constant, $S(x)$ is the local bed friction number and S_c a critical bed friction number. Hence, in deep conditions, $\lim_{S(x)\to 0} \alpha = \alpha_0$. Based on a stability analysis, [Chu et al., 1983] propose S_c=0.12 while [Alavian and Chu, 1985] obtain S_c=0.06 and [Chu et al., 1991] obtain S_c=0.12-0.145. Through measurements, [Chu and Babarutsi, 1988] propose α_0=0.18 and S_c=0.09 while [Uijttewaal and Booij, 2000] propose α_0=0.11 and S_c=0.08. However, these trends

Table 5.3: S_{max} for the four configurations

Test	S_{max}
F1 (deep)	-
F2 (transitional)	0.003
F3 (shallow)	0.009
F4 (shallow)	0.025

do not match present observations. Firstly, α is constant in the deep case (F1) so as in the transitional (F3) and shallow cases (F2 and F4) before the plateaus, at odd with Eq.(5.5). Secondly, the appearance of the plateau ($\alpha = 0$) occurs for quite variable values of $S(x)$ (refereed to as S_{max} in TAB.5.3), all significantly smaller than the critical values proposed in the literature (S_c=0.08-0.09). Thus, though the macroscopic behaviour (recirculation length) so as the global bed friction numbers define F1 as a deep, F3 as a transitional and F2 and F4 as shallow recirculations, it appears that the vertical confinement is not the parameter responsible for the specific shape of the mixing layer width evolution (linear increase followed by a plateau or a reduced linear increase). Indeed, vertical confinement has an influence only if the mixing layer is sufficiently developed *i.e.* if the term $S(x)/S_c$ in Eq. (5.5) is high enough.

Yet, the mixing layer development is indicated by dimensionless streamwise distance $x^* = xc_{f0}/(2h_0)$. Experiments by [Chu and Babarutsi, 1988] (see their Fig.6) show that Eq.(5.5) does not depart from a linear increase as long as x^* remains smaller than 0.5. In the present experiments, the maximum values of x^* obtained at x/L=1 are always smaller than 0.45 for the four configurations; and thus even smaller at the initiation of the plateau for F2, F3 and F4. This additionally gives credit to the fact that vertical confinement does not affect the mixing layer development in our experiments.

The plateaus (F2, F3, F4) or the slope shortage (F1), marking a rupture in the mixing layer spreading, are attributed to the interaction of the mixing layer with the side wall ($y = 0$). In Fig.5.25, the centerline of the mixing layer (location of maximum velocity gradient) is plotted along with the half width $\delta/2$ extension on both sides, assuming a symmetrical extension distribution. It shows that the downstream end of the recirculation corresponds to the intersection of the mixing layer boundary with the side wall: $(y_c - \delta/2) \sim 0$ at x/L=1 both for shallow and deep cases. This tendency is in agreement with [Biancafiore et al., 2011] and [Biancofiore, 2014] who reveal through DNS calculations for a laminar transversally-confined mixing layer that the increasing width of the mixing layer suddenly stops at a given streamwise axis due to the lateral confinement. When the effective of the confinement in z direction (which corresponds to our $z(h)$ direction) increases, the rate of the δ increasing becomes bigger, as seen in FIG.5.24. In FIG.5.23, the phenomenon is observed for F1 and the F2. Although the experiments of [Biancafiore et al., 2011] are performed in the laminar flow, the results show great agreement with us in some degree.

From FIG.5.23, it can be seen that for the deep case F1, the centerline remains far from

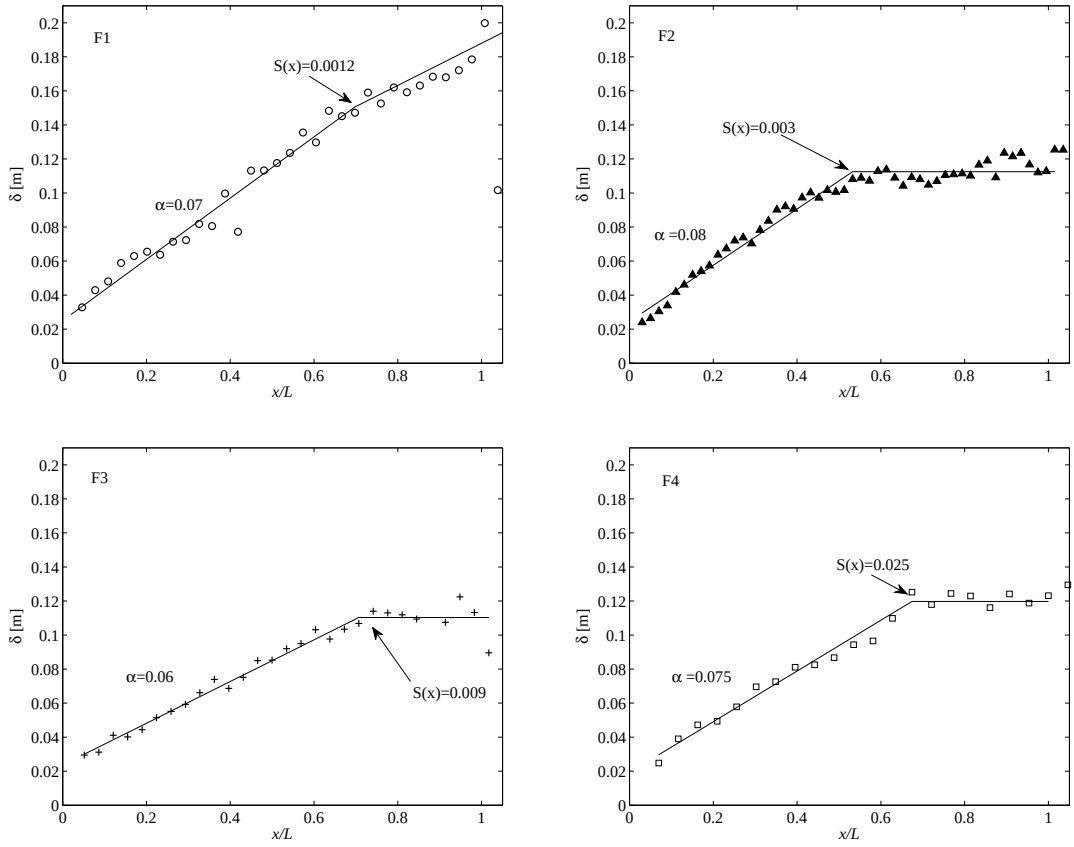

Figure 5.23: Width of the mixing layer and $S(x)$. Note: slopes of curves are $\frac{d\delta}{d(x/L)}$

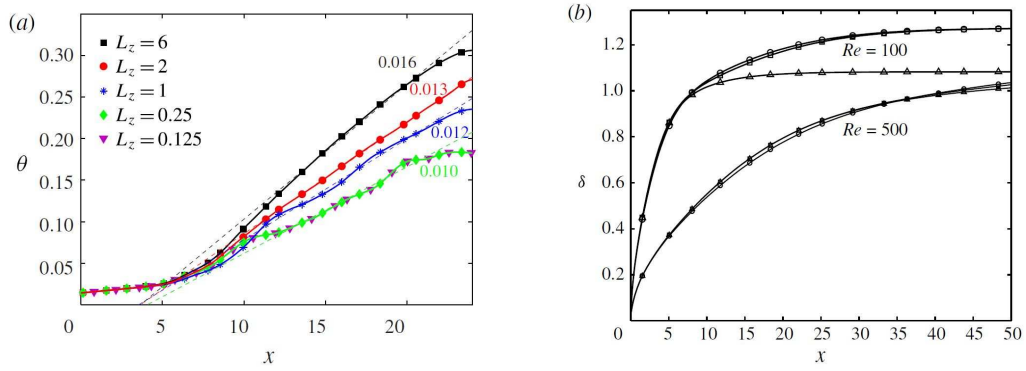

(a)Growth of the momentum thickness δ along the streamwise direction *x*. [Biancofiore, 2014]

(b)Evolution of the shear layer thickness δ along the domain. [Biancafiore et al., 2011]

Figure 5.24: Streamwise evolution of the mixing layer. from [Biancafiore et al., 2011] and [Biancofiore, 2014]

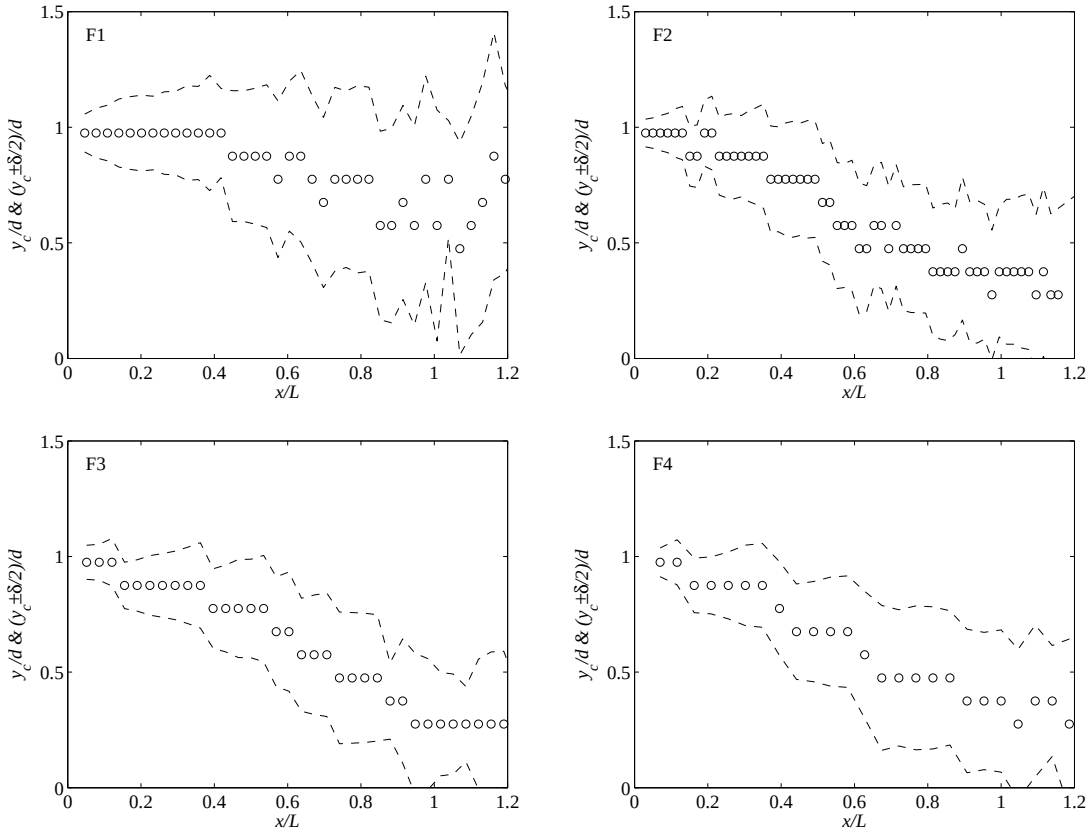

Figure 5.25: Evolution of the mixing layer centerline (○) and boundaries (−−) for $0 < x/L < 1.2$.

the side wall but the mixing layer half-width is high. Conversely, for the shallow cases F2, F3 and F4, the centerline approaches the side wall and the mixing layer half-width is smaller. This can explain the different modifications of the mixing layer development (plateau or slope rupture) observed in FIG.5.23 as a function of the shallowness.

Secondly, as shown in FIG.5.26, the position line with $y_{0.9} = y_{\overline{u}=0.9\times\overline{u}_1}$ (*i.e.* y position where the streamwise velocity is $0.9\overline{u_1}$), $y_{0.5} = y_{\overline{u}=0.5\times\overline{u}_1}$, and $y_{0.1} = y_{\overline{u}=0.1\times\overline{u}_1}$, are added up with the red lines (using the definition from [Pope, 2008], page 140). The position $y = 1/2(y_{\overline{u}=0.1\times\overline{u}_1} + y_{\overline{u}=0.9\times\overline{u}_1})$ is also plotted in black points [Champagne et al., 1976]. The centres provided using the 3 definitions are fairly in the same position and the same tendency. The outer boundary ($y_{0.9}$) and the inner boundary ($y_{0.1}$) are a little farther than $y_{maxgradient} \pm \delta/2$. But they show the same tendency of the growth of the width. However, for F3, it is fairly observed that the two regions defined by δ and the velocity are quite similar.

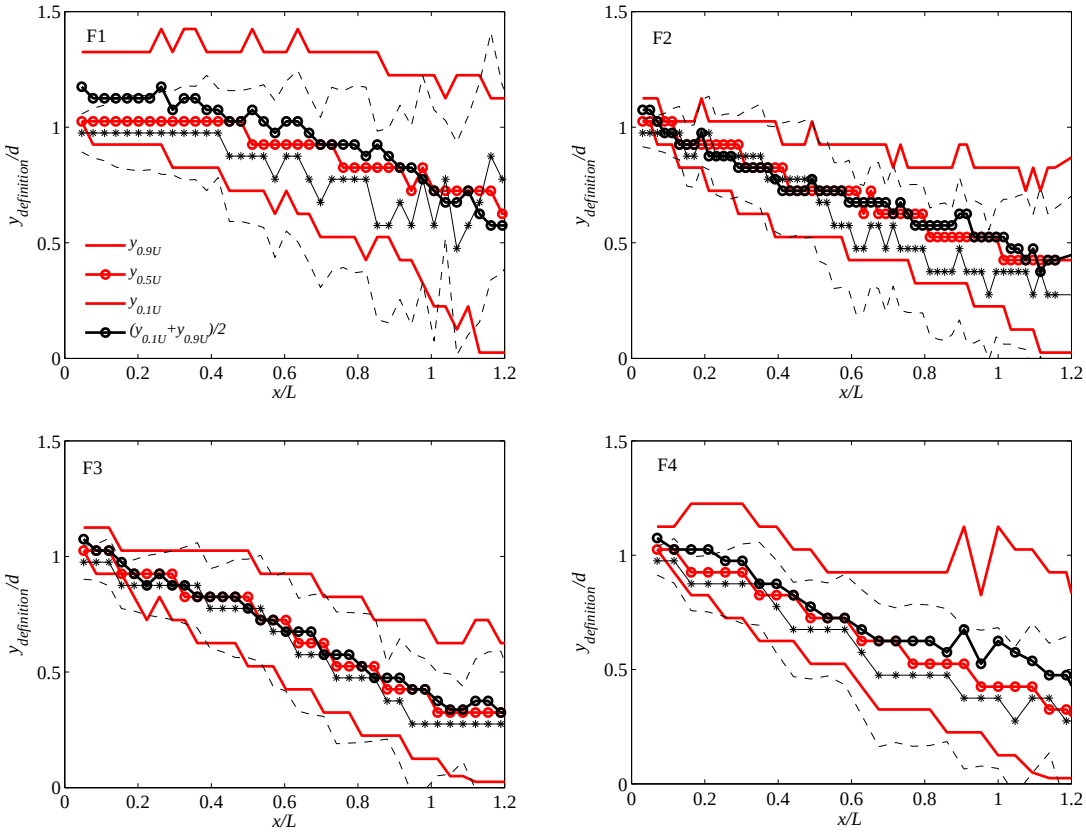

Figure 5.26: Evolution of the mixing layer centerline (○) and boundaries (−−) for $0 < x/L < 1.2$

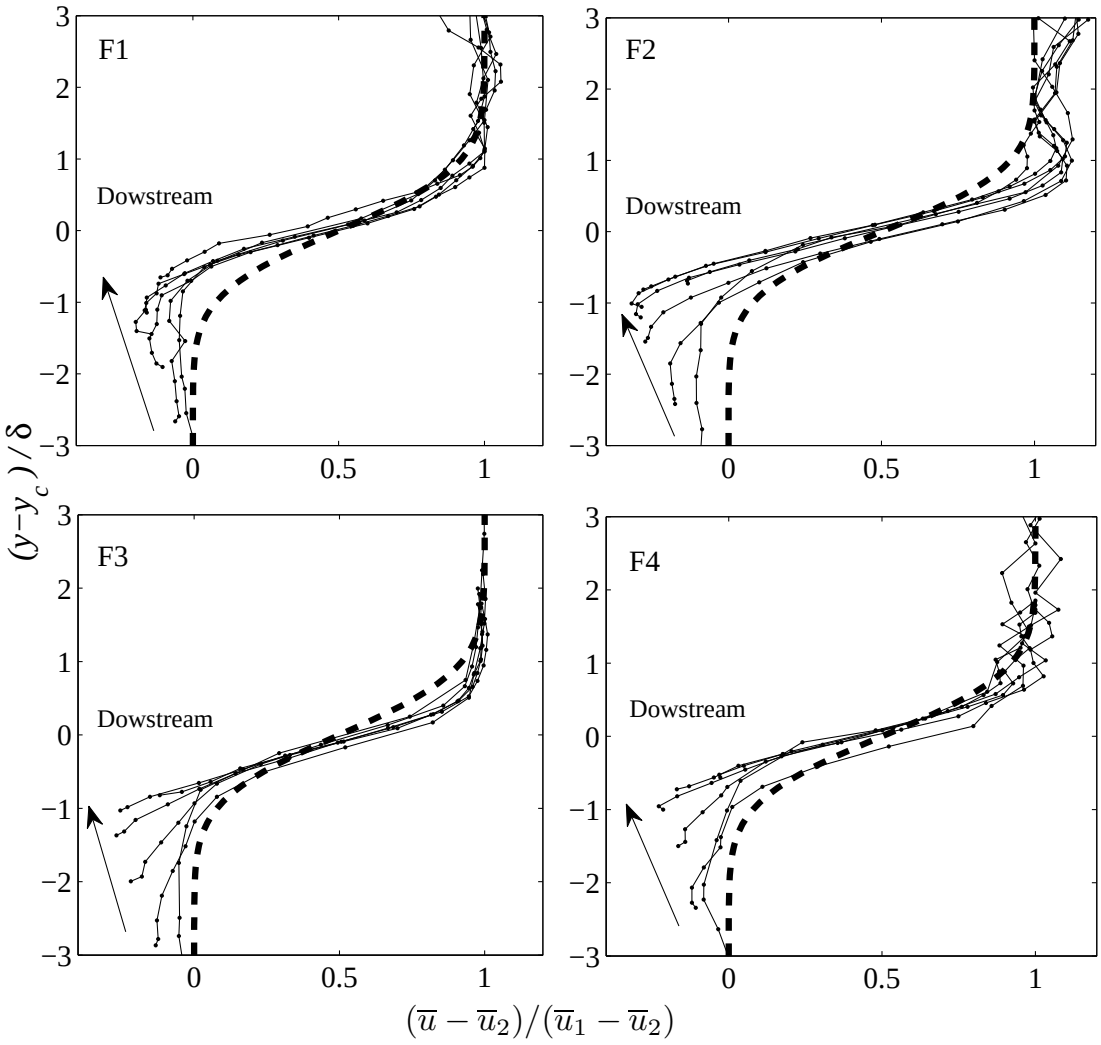

Figure 5.27: Mean streamwise velocity profiles of in similarity coordinates

5.3.5 Similarity of the mean velocity profile

Now that the mixing layer width is defined and measured, the present section aims at verifying the similarity of transverse profiles of mean streamwise velocities $\overline{u}(y)$. Many studies in the literature showed that the transverse profiles of mean streamwise velocity are self-similar (see for instance, [Bell and Mehta, 1990] for a free unbounded mixing layer, [Mignot et al., 2014b] for a junction, or [Lyn and Rodi, 1994] for the flow over an obstacle). This behaviour is also retrieved in our flows with $(\overline{u}-\overline{u}_2)/(\Delta\overline{u})$ plotted (black points) as a function of $(y-y_c)/\delta$ in Fig.5.27. The tendency is fair over about two mixing layer widths ($y-y_c=\pm\delta$). The dash lines in the figures are the Gaussian curve plus a constant, as proposed by [Lyn and Rodi, 1994]. The curve fit well in the outer side of the mixing layer and produces a small error in the region of the recirculation. Along the

streamwise direction x, the measurements separate from the Gaussian curve for the four configurations where $(y-y_c)/\delta$ <-1.

5.3.6 Wake downstream the recirculation

As a rest of the FIG.5.25 along the streamwise direction, the wake region for the four cases are shown in FIG.5.28. Note that F2 is the case with the longest recirculation, the end of the flow terminates at x/L=2. The four wakes are similar and can be considered as transition toward a 1D channel flow.

5.3.7 Conclusion

This section shows the necessity to distinguish two definitions of the bed friction number: a local bed friction number $S(x)$ derived using the mixing layer width δ as horizontal length scale and a global bed friction number derived using the expansion width d as horizontal length scale. Indeed, in our experiments, the local $S(x)$ is always smaller than the critical value S_c but a abrupt stop of the widening of the mixing layer is still observed. It is due to the lateral right wall, which effect, as other characteristic of the flows such as L/d, *etc*., is connected to the value of the global bed friction number S. The results were explained also in the article submitted [Han et al., a].

5.4 Turbulent characteristics of the mixing layer

5.4.1 Reynolds stress tensor analysis

5.4.1.1 Characteristics of the Reynolds stress

In this section, the three terms of the 2D Reynolds stress tensor are measured and compared to each other. These are the longitudinal Reynolds stress $\overline{u'^2}$, transverse Reynolds stress $\overline{v'^2}$,and Reynolds shear stress $-\overline{u'v'}$. For comparing the 4 cases with different initial velocities, $1/\overline{u}_0^2$ is used for normalizing. The contour and the profiles of the dimensionless:
$\rightarrow$ Longitudinal Reynolds Stress $\overline{u'^2}/\overline{u}_0^2$ is given in FIG.5.29,
$\rightarrow$ Transverse Reynolds Stress $\overline{v'^2}/\overline{u}_0^2$ is given in FIG.5.30,
$\rightarrow$ Reynolds shear Stress $-\overline{u'v'}/\overline{u}_0^2$ is given in FIG.5.31. We obtain the following results.

1. For the 3 terms of the Reynolds tensor, the distribution pattern is quite similar:
$\rightarrow$Outside of the mixing layer (in the recirculation zone and for y/d >1.2), the Reynolds stress is weak compared with the mixing-layer region. The maximum Reynolds stresses are obtained along the centerline of the mixing layers. The maximum stress magnitude can be easily found in each transverse profile: there is only one maximum in each profile and the magnitudes decrease on the both sides towards the wall which y/d=0 and y/d=4.
$\rightarrow$ The maximum magnitudes are obtained in the upstream region of the mixing layer

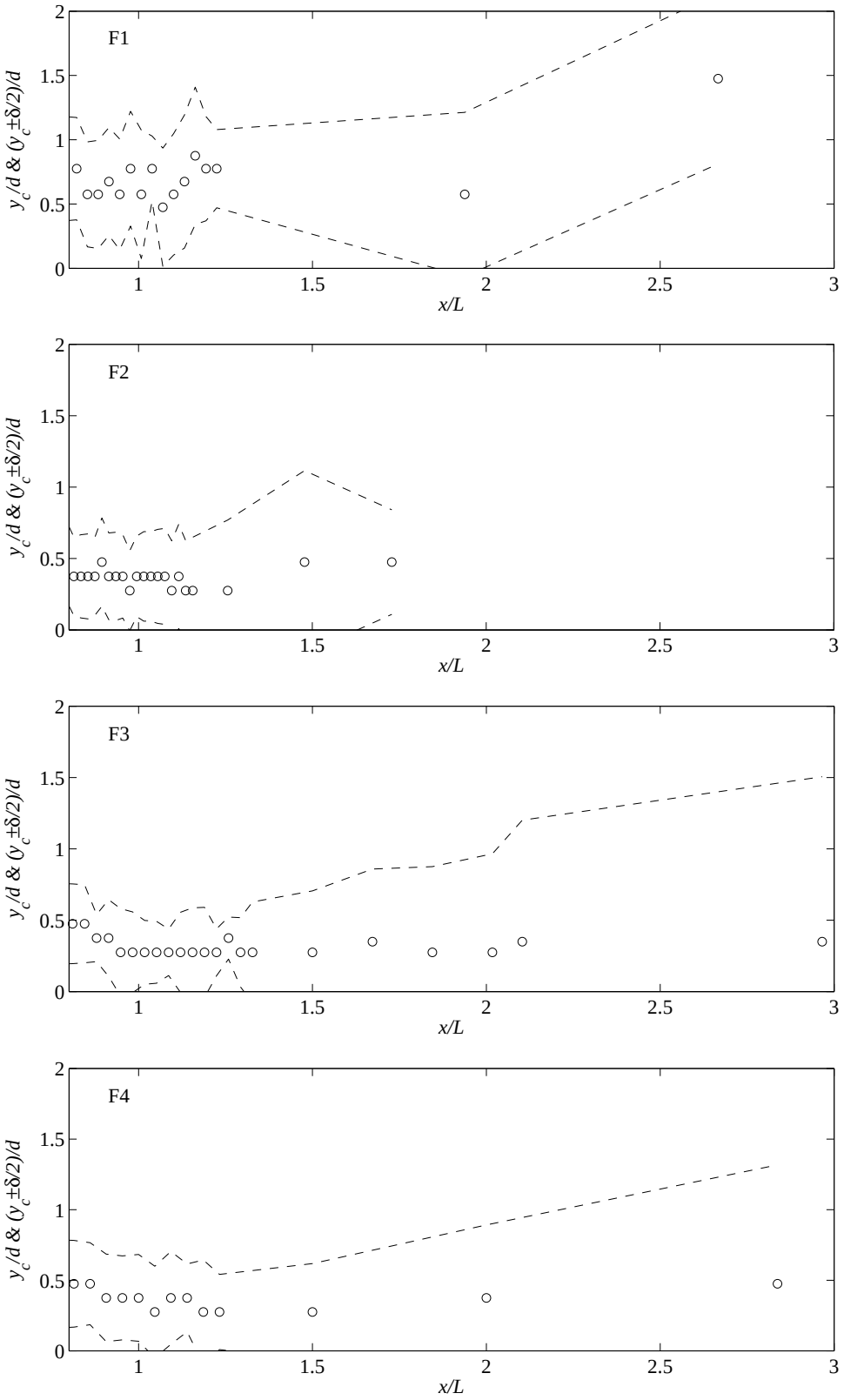

Figure 5.28: Wake downstream the recirculation for the 4 cases.

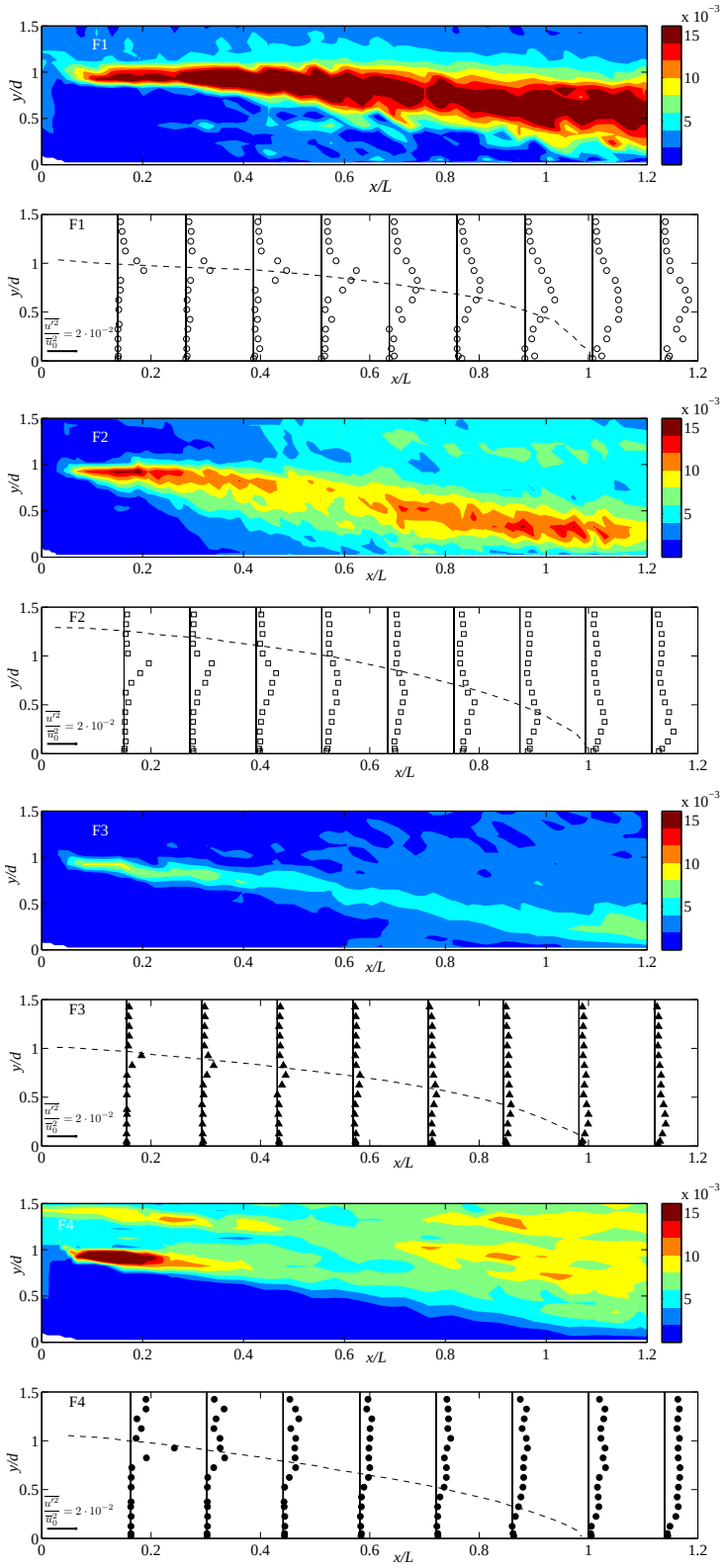

Figure 5.29: Streamwise Reynolds Stress $\overline{u'^2}$

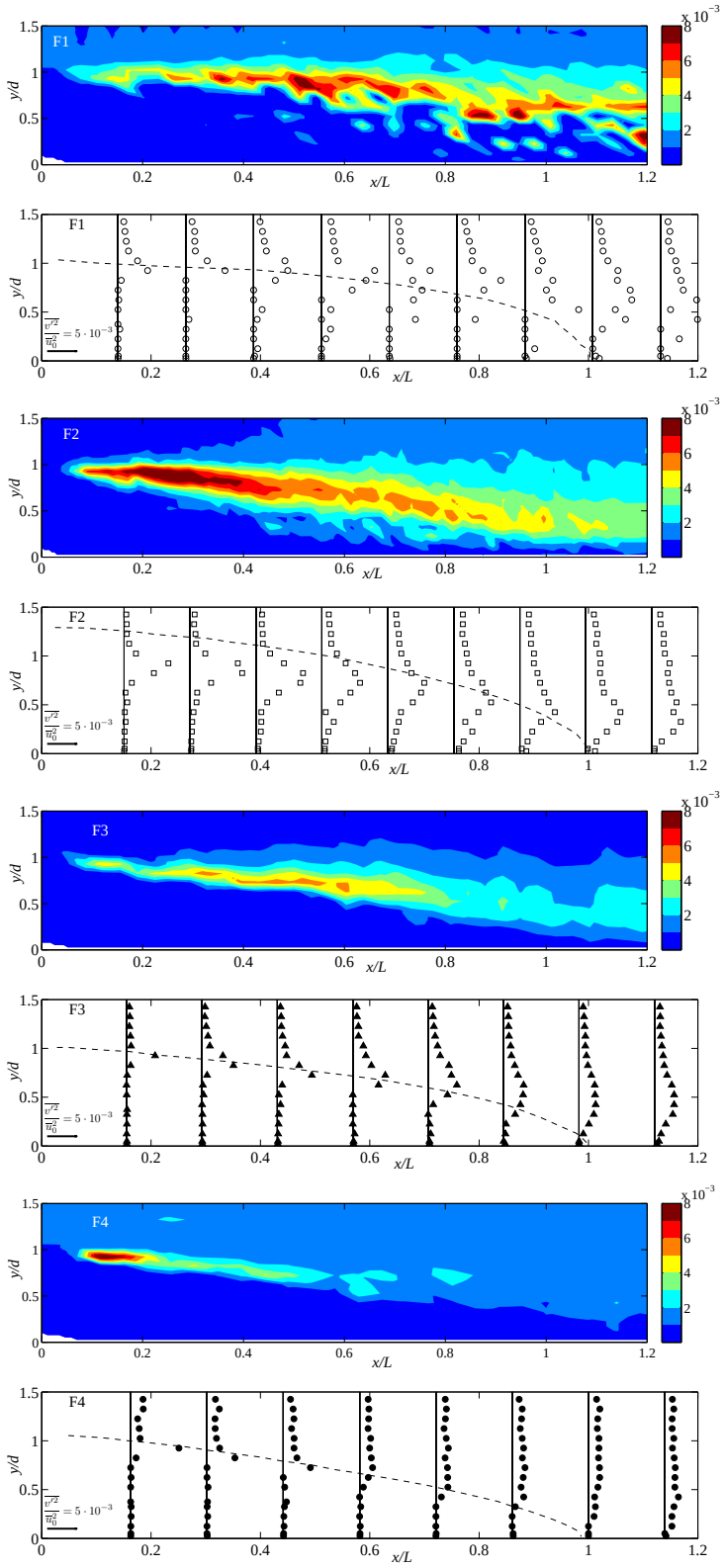

Figure 5.30: Transverse Reynolds Stress $\overline{v'^2}$

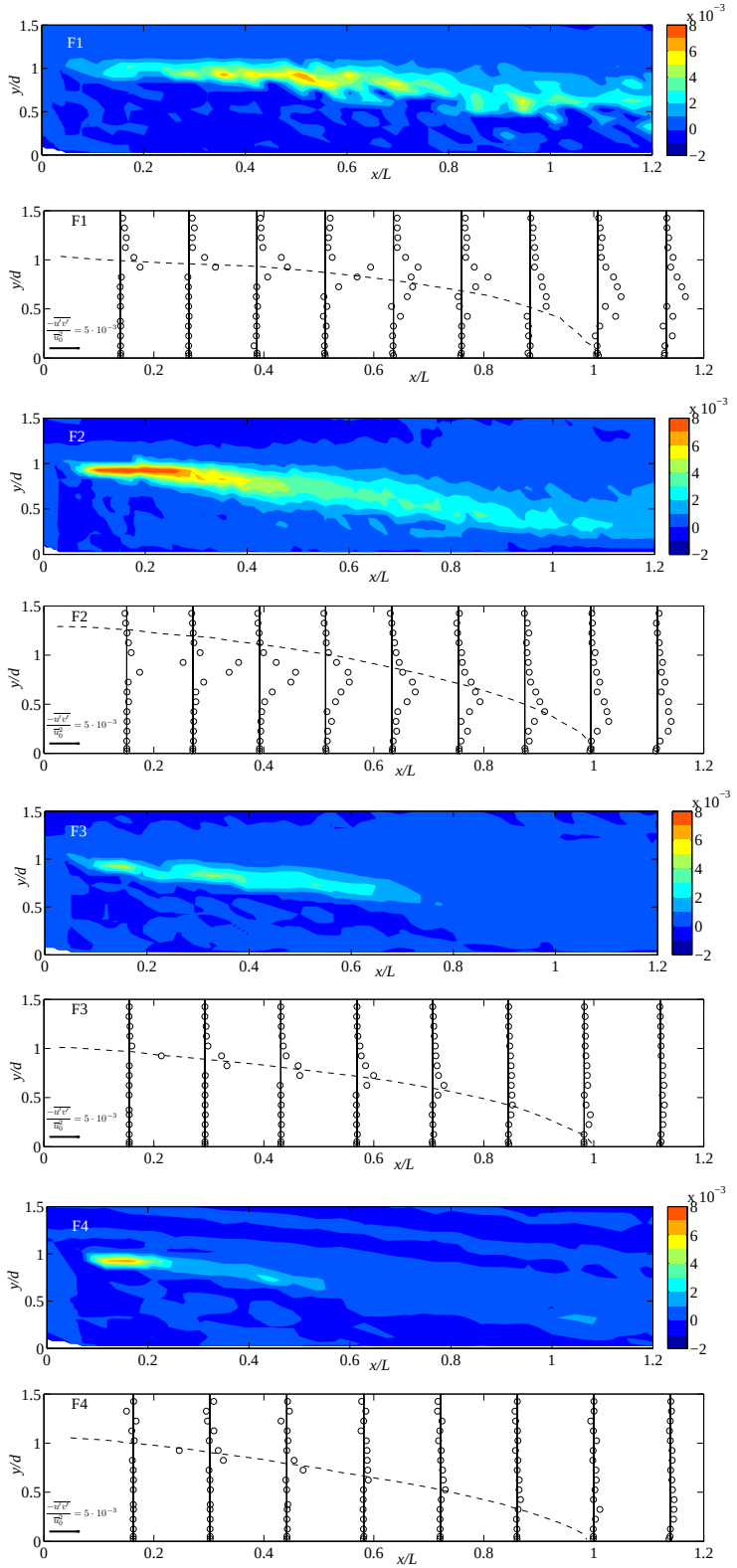

Figure 5.31: Reynolds shear Stress $-\overline{u'v'}$

Table 5.4: Maximum measured Reynolds stresses compared with literature data. (Note: FML means free mixing layer [White and Nepf, 2007], BFS means backward facing step [Chandrsuda and Bradshaw, 1981], SUM means shallow unbounded mixing layer [Uijttewaal and Booij, 2000] and SSE means shallow sudden expansion [Babarutsi et al., 1989].

	FML	BFS	SUM	SSE		SSE	
				S=0.0098	S=0.098	F1	F2
$\overline{u\prime^2}/\Delta\overline{u}_0^2(\%)$	3.1	2.7	2.97	5.4	2.25	2.38	1.2
$\overline{v\prime^2}/\Delta\overline{u}_0^2(\%)$	1.9	1.5	1.36	-	-	0.88	0.6
$-\overline{u\prime v\prime}/\Delta\overline{u}_0^2(\%)$	0.925	1	1.04	-	-	0.74	0.5
$\overline{v\prime^2}/\overline{u\prime^2}(\%)$	61	56	46	-	-	37	50
$-\overline{u\prime v\prime}/\overline{u\prime^2}(\%)$	30	37	35	-	-	31	42

(x/L=0.2∼0.4) and all Reynolds stresses decrease along the mixing layer towards downstream.

2. For each term of the Reynolds tensor, the evolution with the bed friction number S is similar:
→ As S increases from 0.0032 to 0.089, the region with high Reynolds stress magnitude decreases.
→ As S increases, the maximum magnitude of Reynolds stress decreases. These tendencies are also found by [Babarutsi et al., 1989]: $\overline{u'^2}$ are measured and figured out. The maximum dimensionless longitudinal Reynolds Stress is between 0.01∼0.03. Here, the maximum dimensionless longitudinal Reynolds Stress is 0.016. Note that for the $\overline{u'^2}$ term for F4, some points at the upstream region of the recirculation have a high magnitude.

5.4.1.2 Comparison between the three terms of the Reynolds stress tensor

For the 4 cases, the dimensionless magnitudes and the ratio between each term in the literature and present work are given in TAB.5.4.
(1) The dimensionless magnitudes of the three terms of the 2D Reynolds tensor are comparable to the literature data: the longitudinal Reynolds stress is the strongest term among the three.
(2) The ratio between the transverse Reynolds stress and the longitudinal Reynolds stress is 0.4∼0.5. The ratio between the transverse Reynolds stress and the longitudinal Reynolds stress is 0.4∼0.6 which is a little higher than the literatures.

5.4.1.3 Perturbations in the measurements

In FIG.5.29, the profiles are not similar for flow F4 than for other flows. This is due to the influence of the bottom roughness that creates additional turbulence in the wake of the

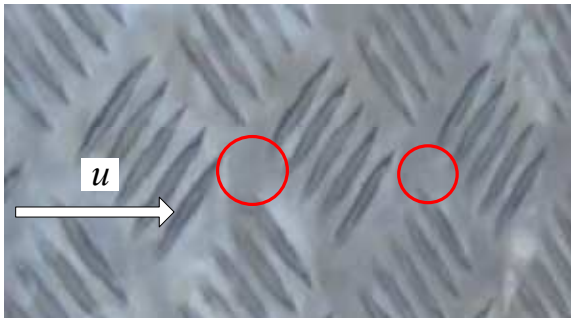

Figure 5.32: Sketch of the perturbation produced by the roughness tears

roughness elements (See sketch FIG.5.32). However the amplitude of the fluctuation of the perturbation is smaller then the region of the Reynolds concentration.

5.4.2 Turbulent kinetic energy analysis

The aim of the present section is to gain information on the turbulent activity in the mixing layer and the recirculation zone by estimating some of the terms from the Turbulent Kinetic Energy equation.

5.4.2.1 TKE Equation

From the Reynolds-Averaged Navier-Stokes equation (CHAP.4), the turbulent kinetic energy equation is obtained as follows:

$$-\overline{u_i' u_j'}\frac{\partial \overline{u_i}}{\partial x_j} - \overline{u_j}\frac{\partial k}{\partial x_j} = \varepsilon + \frac{\partial}{\partial x_j}(\overline{k' u_j'} + \frac{1}{\rho}\overline{p' u_j'}) - \nu\nabla^2 k \tag{5.6}$$

where ε is the viscous dissipation term and $k\prime$ and k the fluctuate and mean turbulent kinetic energy, p is the pressure. Introducing the 2D assumption (horizontal flow): $\partial\phi/\partial z = 0$and $\overline{\phi_z}$ for any ϕ parameter linked to the velocity field (not the pressure) we obtain:

$$\begin{aligned} &-\overline{u'v'}\frac{\partial \overline{u}}{\partial y} - \overline{u'v'}\frac{\partial \overline{v}}{\partial x} - \overline{u'^2}\frac{\partial \overline{u}}{\partial x} - \overline{v'^2}\frac{\partial \overline{v}}{\partial y} - \overline{u}\frac{\partial k}{\partial x} - \overline{v}\frac{\partial k}{\partial y} \\ =&\varepsilon + \frac{\partial}{\partial x}(\overline{k'u'} + \frac{1}{\rho}\overline{p'u'}) + \frac{\partial}{\partial y}(\overline{k'v'} + \frac{1}{\rho}\overline{p'v'}) - \nu(\frac{\partial^2 k}{\partial x^2} + \frac{\partial^2 k}{\partial y^2}) \end{aligned} \tag{5.7}$$

Here, due to experimental limitations to 2D measurement, another assumption is introduced:

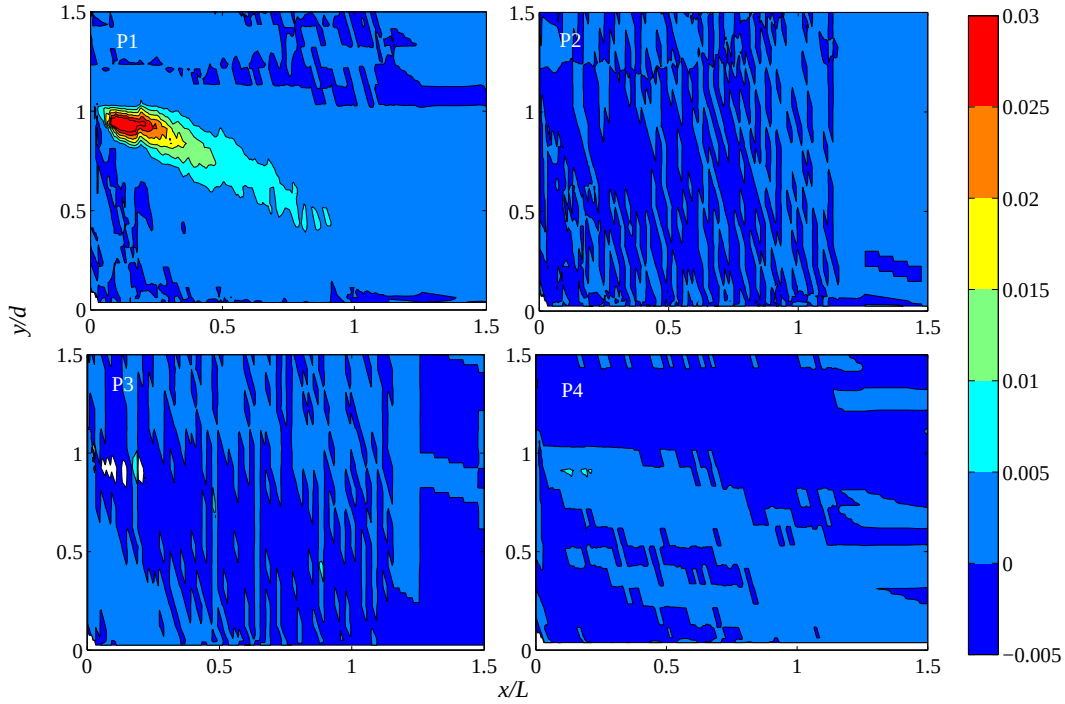

Figure 5.33: 4 productions (P_1 to P_4) terms normalized using $\overline{u}_0^3/d$ for F2

$$w'^2 = \frac{1}{2}(u'^2 + v'^2) \tag{5.8}$$

So, $k' = \frac{1}{2}(u'^2 + v'^2 + w'^2) \Longrightarrow k' = \frac{3}{4}(u'^2 + v'^2)$ and $k = \frac{3}{4}(\overline{u'^2} + \overline{v'^2})$

5.4.2.2 Turbulent production term

In the 2D TKE Eqs.(5.7), four production terms appear : P1=$-\overline{u'v'}\frac{\partial \overline{u}}{\partial y}$, P2=$-\overline{u'v'}\frac{\partial \overline{v}}{\partial x}$, P3=$-\overline{u'^2}\frac{\partial \overline{u}}{\partial x}$ and P4=$-\overline{v'^2}\frac{\partial \overline{v}}{\partial y}$. FIG.5.33 shows for F2 that P1 magnitude strongly exceeds the three other terms. Consequently, in the following, only discussion regarding P1 in detailed. The production terms are responsible for dissipating energy from the mean flow and transferring it to the fluctuating flow. FIG.5.34 presents the first production terms for the 4 Cases are reveals that:
→ The TKE production is maximum in the mixing layer and decreases from upstream to downstream (as for the Reynolds shear stress and the velocity gradient, see FIG.5.31 and FIG.5.17).
→The same order of magnitude is retrieved for the four cases.

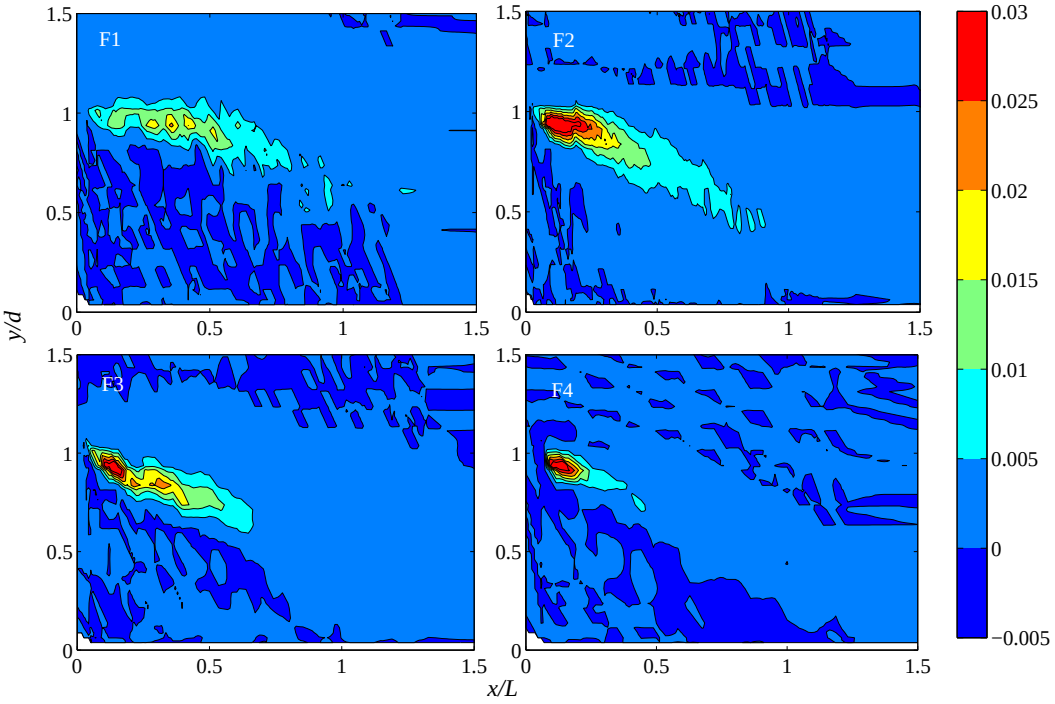

Figure 5.34: P1 dimensionless with $\overline{u}_0^3/d$ for four cases

5.4.2.3 Turbulent kinetic energy term

The TKE term k for the 4 cases is normalized by the upstream bulk velocity as $k/\overline{u}_0^2$ and is plotted in FIG.5.34. It appears that (as for the normal Reynolds stresses):
1. The distribution pattern is quite similar for the 4 cases and similar to Reynolds stress terms $\overline{u'^2}$ and $\overline{v'^2}$:
$\rightarrow$ Outside of the mixing layer (in the recirculation zone and for y/d >1.2), the TKE is weak compared with the mixing-layer region. The maximum magnitude is obtained along the centerline of the mixing layer.
$\rightarrow$ The maximum magnitude is obtained in the upstream region of the mixing layer ($x/L = 0.2 \sim 0.4$) and it decreases along the mixing layer towards downstream.
2. The evolution with the bed-friction number S is similar for the 4 cases and similar to $\overline{u'^2}$ and $\overline{v'^2}$:
$\rightarrow$ As S increases from 0.0032 to 0.089, the region with high k magnitude decreases.
$\rightarrow$ As S increases, the maximum magnitude of k decreases. The region of maximum TKE is thus the same as the region of maximum turbulent production.

We saw above that the maximum turbulent production and turbulent kinetic energy is located along the centerline of the mixing layer.

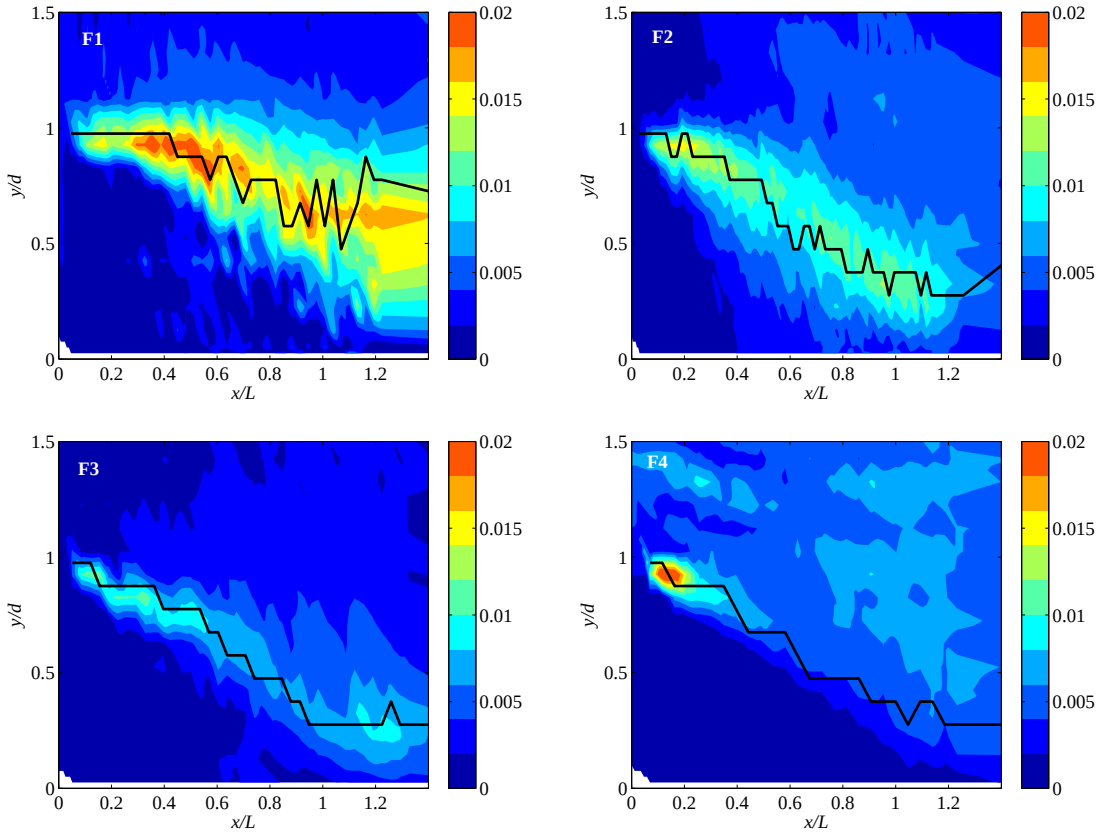

Figure 5.35: Evolution of the TKE for the four cases.

5.4.2.4 TKE fluxes

Definition of the two flux terms, along the two directions is: $F_{ku} = \overline{k'u'}$ and $F_{kv} = \overline{k'v'}$ as in Eq.(5.7). In FIG.5.36 (a) both fluxes are made dimensionless using $\frac{F_k}{\overline{u}_0^3}$. It appears that:
$\rightarrow$ Both fluxes are negligible in the region far from the mixing layer.
$\rightarrow$ F_{kv} is negative below (lower y value) the centerline and positive above (higher y value) the centerline of the mixing layer. This behaviour is in fair agreement with the results of [Mignot et al., 2009] and [Mignot et al., 2011]. This reveals that F_{kv} transports turbulent kinetic energy from the maximum production location (the centerline) towards the less energetic regions. This confirms that the TKE flux is directed "from the energy-rich zones to the energy-want zones".
$\rightarrow$ F_{ku} is positive below (lower y value) the centerline and negative above (higher y value) the centerline of the mixing layer. This behaviour is in agreement with data from [Dey and Nath, 2009] and [Mignot et al., 2011]: F_{ku} is positive is the slowest region (the recirculation zone) and negative is the most rapid region (the outer region away from the recirculation).
$\rightarrow$ The contours for the four cases show the same tendency for both flux terms. Nevertheless, the magnitudes are not equal.

5.4.2.5 Advection term

Advection terms correspond to the transport of turbulent kinetic energy by the mean flow. Two terms appear in the 2D TKE Eqs.(5.7): $Adv_x = -\overline{u}\frac{\partial k}{\partial x}$ and $Adv_y = -\overline{v}\frac{\partial k}{\partial v}$. In FIG.5.36 (b) both advection terms are made dimensionless as $\frac{d}{\overline{u}_0^3}$. It appears that:
$\rightarrow$ both advection terms are negligible in the region far from the mixing layer.
$\rightarrow$ Adv_x distribution is complex as $\frac{\partial k}{\partial x}$ is weak in the mixing layer.
$\rightarrow$ Adv_y distribution is much more evident: $\overline{v}$ is negative in the mixing layer and $\frac{\partial k}{\partial y}$ is positive below (lower y value) the centerline of the mixing layer and negative above (larger y values).
Consequently, $Adv_y = -\overline{v}\frac{\partial k}{\partial v}$ is positive below and negative above the centerline of the mixing layer.

5.5 Gradient model and eddy viscosity

5.5.1 Definition of the ν_T

Gradient model is based in the eddy viscosity conception following the results of Boussinesq in 1877 [Schmitt, 2007]. It relates the Reynolds stress tensor to the mean rate of strain tensor:

$$-\overline{u_i'u_j'} + \frac{2}{3}k\delta_{ij} = \nu_T(\partial\overline{u_i}/\partial x_j + \partial\overline{u_j}/\partial x_i) = 2\nu_T S_{ij} \tag{5.9}$$

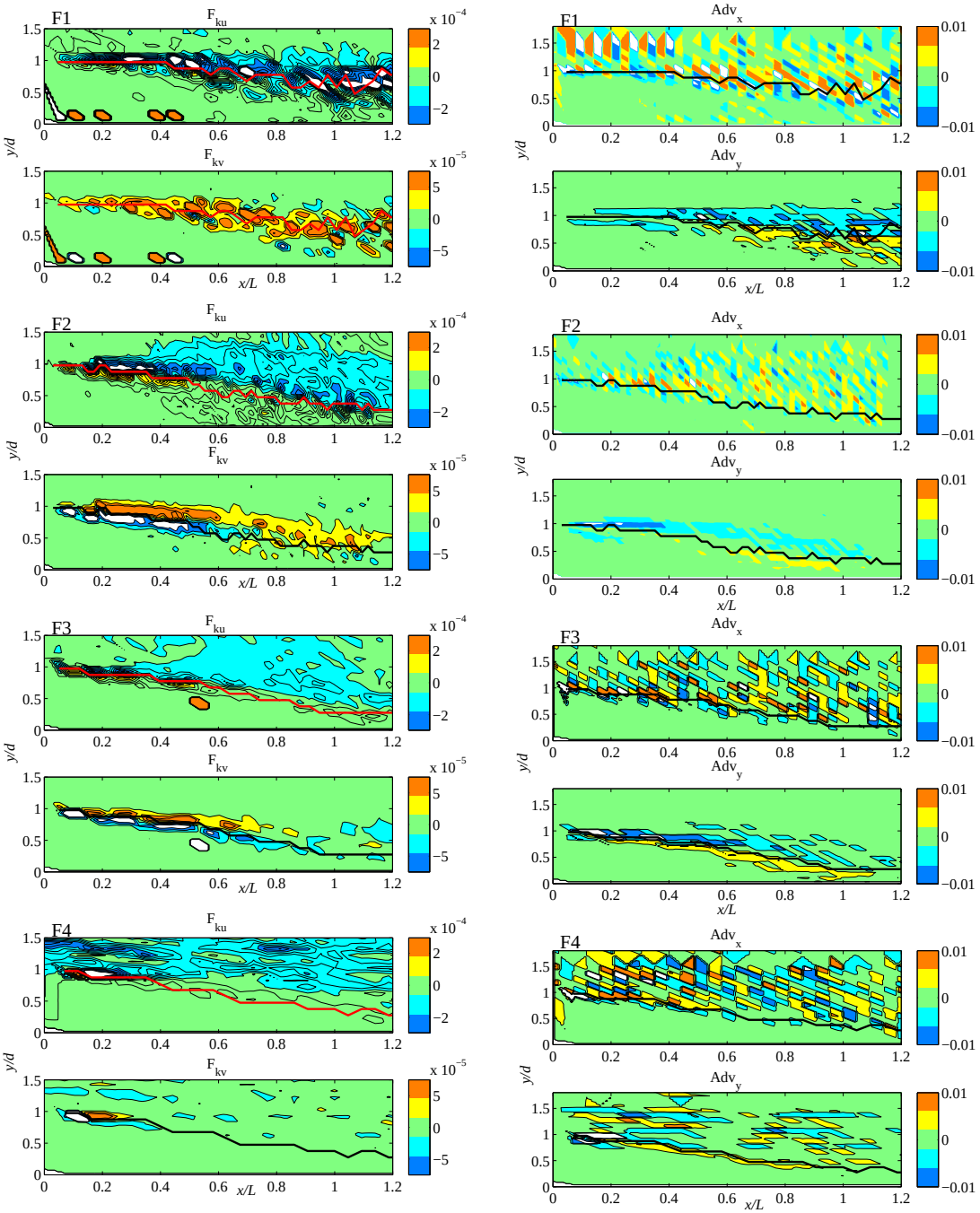

(a)Evolution of the TKE flux for the four cases.

(b)Evolution of the advection for the four cases

Figure 5.36: TKE flux and TKE advection

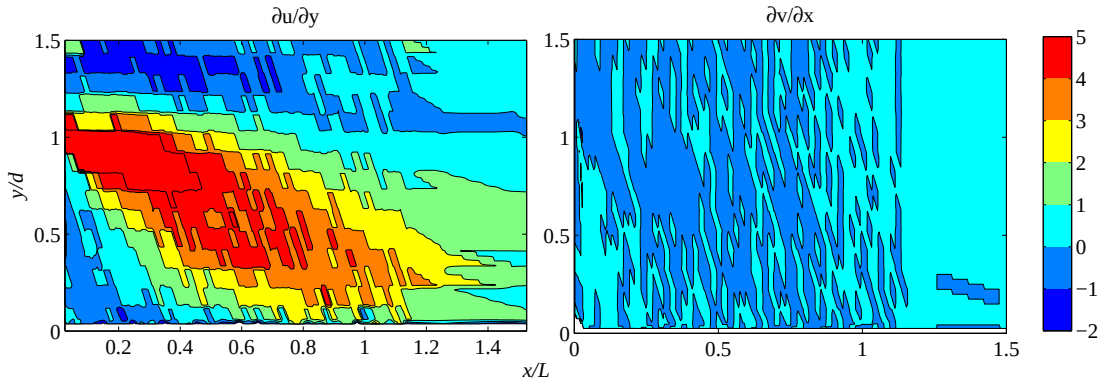

Figure 5.37: Magnitude comparison between the $\frac{\partial \overline{u}}{\partial y}$ and $\frac{\partial \overline{v}}{\partial x}$ for F2

with ν_T the so-called "turbulent viscosity" or "eddy viscosity" coefficient, k the turbulent kinetic energy. δ_{ij} the Kronecker symbol which equals to 1 when $i = j$ and 0 if $i \neq j$ and finally S_{ij} the mean rate of strain tensor.

Here, as well known, ν_T is hypothesized isotropic as it does not depend on i and j, and it is not satisfied in many configurations(See [Pope, 2008]). So it is not expected to be valid in the present flow configuration, and no discussion regarding the validity of the isotropic turbulent viscosity assumption is made here. This paper is based on a two-dimensional (2D) analysis, application of Eq.5.9 to the nondiagonal term becomes as below:

$$-\overline{u'v'} = \nu_T(\frac{\partial \overline{u}}{\partial y} + \frac{\partial \overline{v}}{\partial x}) = 2\nu_T S_{xy} \tag{5.10}$$

with x and y the streamwise and transverse axes, respectively; u and v are instantaneous velocity components along x and y; and S_{xy} is mean shear rate. Note that in our flows, $\frac{\partial \overline{u}}{\partial y} >> \frac{\partial \overline{v}}{\partial x}$(FIG.5.37), Eq.5.10 thus simplifies as below:

$$-\overline{u'v'} = \nu_T(\frac{\partial \overline{u}}{\partial y}) \tag{5.11}$$

The aim of the next sections is to discuss the turbulent viscosity values.

5.5.2 Estimation of ν_T coefficient

In order to gain precision, this section aims at identifying the longitudinal evolution of turbulent viscosity coefficient $\nu_T(x)$ used in the Gradient model. Example is given in FIG.5.38 for F2 including:

→ the transverse profiles of Reynolds shear stress $-\overline{u'v'}$.

→ the transverse profiles of Gradient model term $\nu_T \partial \overline{u}/\partial y$ using the best fit turbulent viscosity coefficient $\nu_T(x)$, fitted for each transverse profile.

→ the transverse profiles of Gradient model term $\nu_T \partial \overline{u}/\partial y$ using a global constant noted

Table 5.5: $\nu_T(x)$ for each case

F1		F2		F3		F4	
x/L	ν_T $(10^{-4}m^2\cdot s^{-1})$	x/L	ν_T $(10^{-4}m^2\cdot s^{-1})$	x/L	ν_T $(10^{-4}m^2\cdot s^{-1})$	x/L	ν_T $(10^{-4}m^2\cdot s^{-1})$
0.15	0.5	0.1	2	0.2	0.3	0.25	0.18
0.3	0.5	0.2	2	0.3	0.8	0.4	0.2
0.4	1	0.35	2	0.45	0.7	0.55	0.2
0.55	1	0.45	2	0.6	0.6	0.7	0.15
0.65	1	0.6	1.5	0.75	0.3	0.8	0.1
0.8	0.7	0.7	1.5	0.9	0.4	0.95	0.1
0.9	0.7	0.8	1.5	1	0.4		
1	1	0.95	1.5				

$\nu_{T-Global}$ value indicated in TAB.5.5, which is obtained as the average value of the ν_T(see the next section and TAB.5.5). It appears that $\nu_T\partial\overline{u}/\partial y$ using $\nu_T(x)$ fairly fits the Reynolds stress profiles except for some high values near the mixing layer centerline $y/d \sim$0.8. The profiles obtained using $\nu_{T-Global}$ are quite similar as $\nu_T(x)$ does not evolve too much (see TAB.5.5). Using the same methodology, the $\nu_T(x)$ and $\nu_{T-Global}$ for the 3 other cases are given in the TAB.5.5 and FIG.5.40 (Note $\circ$ is $\nu_T\frac{\partial\overline{u}}{\partial y}$ and $*$ is $-\overline{u'v'}$).

TAB.5.5 and FIG.5.39 confirm that $\nu_T(x)$ does not varies much and $\nu_{T-Global}$ is defined as the averaged value from x/L=0 to 1. Values for $\nu_{T-Global}$ are given in TAB.5.6. Data from the literature in mixing layers (shallow or not) are also included and appear to be of comparable magnitude as the present results. Moreover, it appears that $\nu_{T-Global}$ for F2 exceeds those for the other cases. This result may be related to the fact that $\overline{u}_0$ for F2 is much higher than for the other cases (see TAB.5.6). We thus propose to introduce a dimensionless $\nu_{T-Global}$ coefficient ε_0. For further studying the bed friction influence on the turbulent viscosity, the dimensionless turbulent eddy viscosity coefficient ε_0 is introduced here. [Tennekes and Lumley, 1972] and [Wygnanski and Fiedler, 1970] defined it as $\varepsilon_0 = \Delta U\delta$. In the recirculation flow, the selected characteristic scales for normalising are d and $\overline{u}_0$. ε_0 is then defined as:

$$\varepsilon_0 = \frac{\nu_{T-Global}}{\delta(x)\overline{u}_0} \tag{5.12}$$

Fig.5.41 reveals that as S increases , ε_0 decreases. Regarding the measurements, the tendency is quite linear for the deep cases with the mathematical expression indicated on Fig.5.41 and for shallower cases, the decrease rate becomes smaller. Moreover, the simulation results correspond the experimental results except when the small S. This maybe related to the fact that the rigid lid hypothesis for the calculating impacts the turbulent viscosity turbulent coefficient.

[Wygnanski and Fiedler, 1970] obtained $\varepsilon_0 = 0.06$ in the mixing layer. For [Alavian and Chu, 1985], ε_0 ranges 0.05 to 0.11, as seen in TAB.5.7. For this paper, the

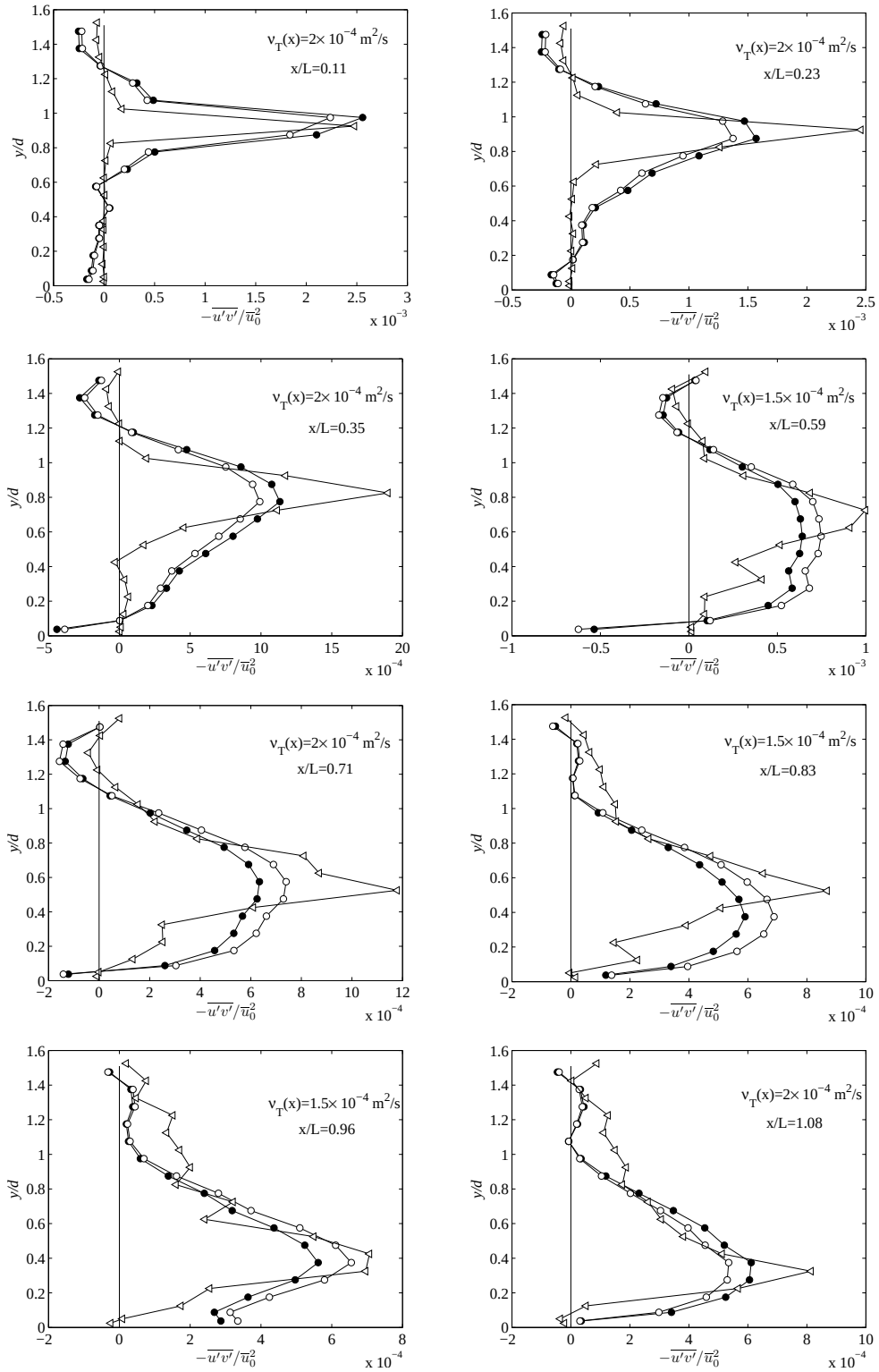

Figure 5.38: Profiles with different ν_T comparing with shear stress $-\overline{u'v'}$ (◁) for F2. ○ presents the Eq.(5.11) with $\nu_{T-Global}$. ● presents the Eq.(5.11) with $\nu_T(x)$.

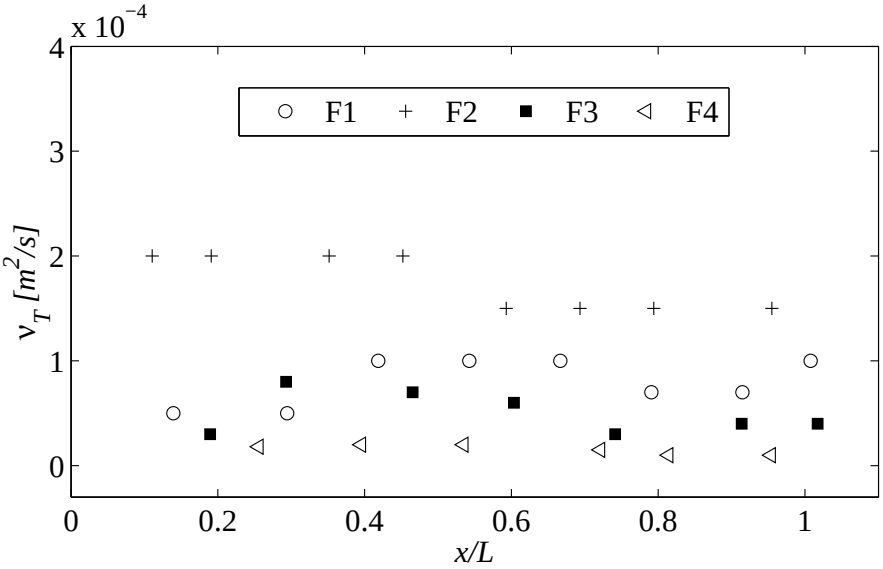

Figure 5.39: Turbulent viscosity magnitude $\nu_T(x)$ along the streamwise for 4 cases

Table 5.6: $\nu_{T-Global}$ of the four cases with comparison of the litterature.

Case	S	$\nu_{T-Global}$ $(10^{-4}m^2/s)$
F1	0.0032	0.8
F2	0.01	1.75
F3	0.032	0.5
F4	0.089	0.155
[Mignot et al., 2014a]	deep	0.5
[Peltier, 2011]	deep	3
[Alavian and Chu, 1985]	deep	1∼3

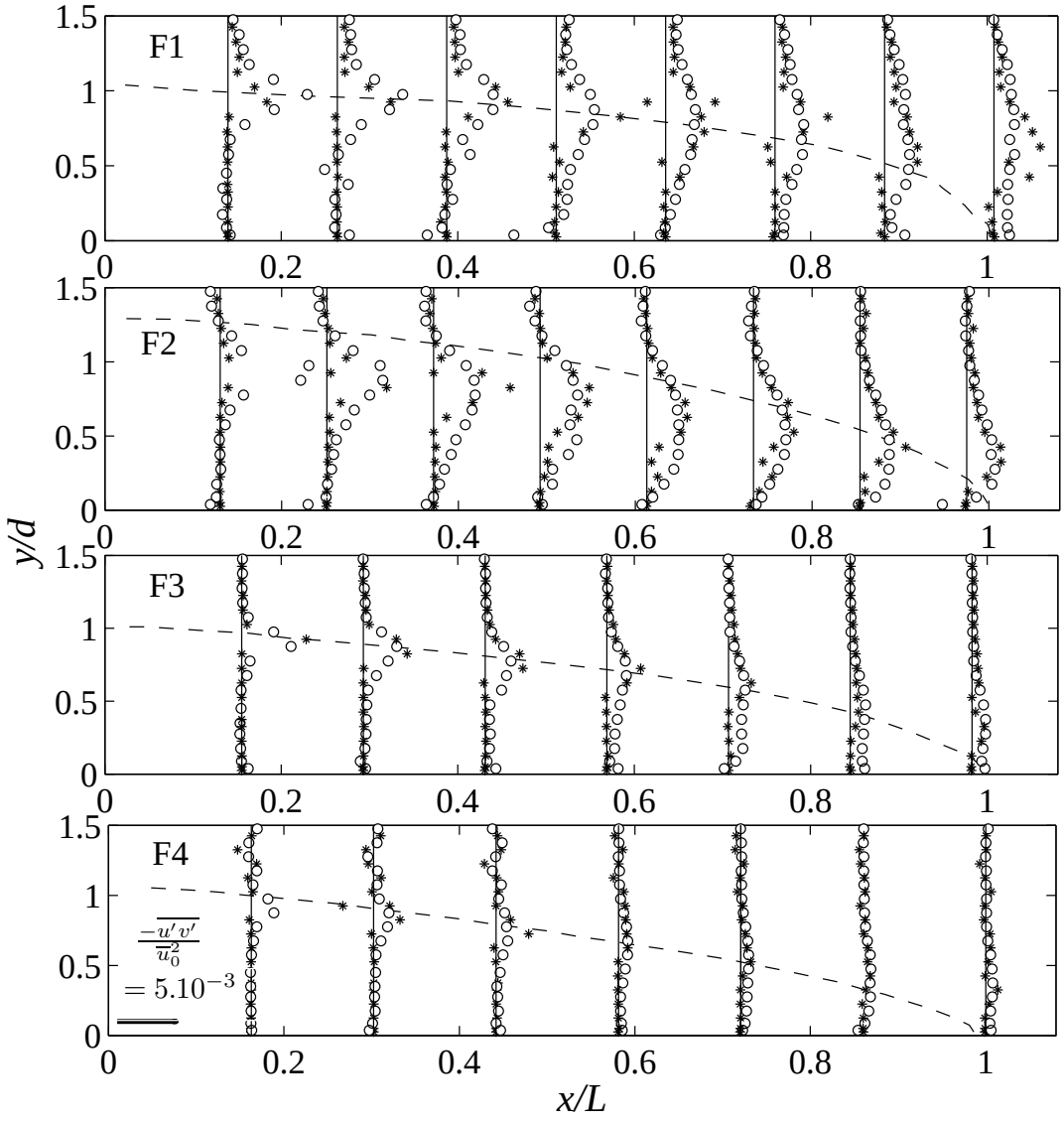

Figure 5.40: Evolution of the Eq.5.11 in each profiles normalized with $\overline{u}_0^2$.

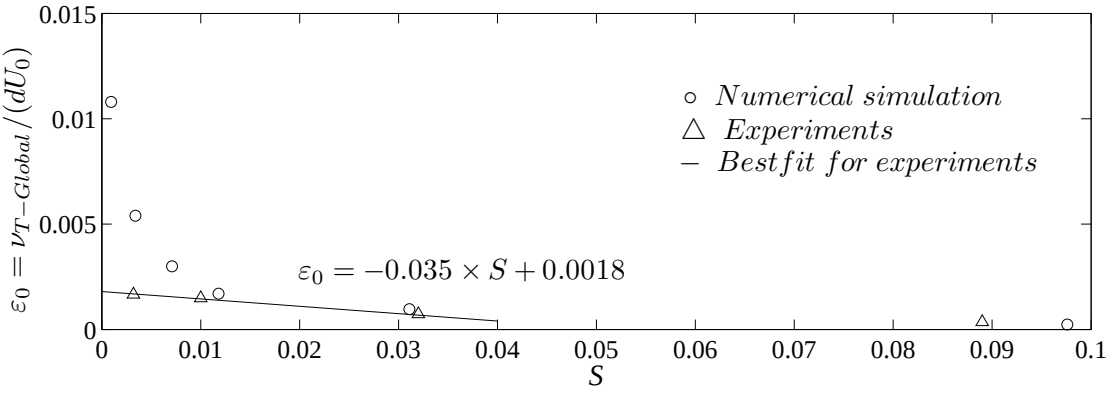

Figure 5.41: The dimensionless turbulent eddy viscosity ε_0

Table 5.7: Dimensionless turbulent viscosity ε_0 with comparison of the literature

	ε_0
[Wygnanski and Fiedler, 1970]	0.06
[Alavian and Chu, 1985]	0.05-0.11
Present results	0.003-0.03

value ranges from 0.003 to 0.03 that is lightly smaller than in the literature. The different configuration could influence the turbulence development. For the present sudden expansion configuration, the side wall makes the mixing layer different from the free mixing layer [Talstra, 2011]. This part was prepared to be submitted on line [Han et al., b]

5.5.3 Prandtl mixing length

The Prandtl mixing length assumption writes:

$$\nu_{T-Prandtl} = {l_m}^2 \left| \frac{\partial \overline{u}}{\partial y} + \frac{\partial \overline{v}}{\partial x} \right|_{max} \tag{5.13}$$

With:
$\rightarrow \nu_{T-Prandtl}$ is the Prandtl horizontal eddy viscosity.
$\rightarrow l_m$ is the Prandtl mixing length (in meter).
$\rightarrow \left| \frac{\partial \overline{v}}{\partial x} \right|_{max}$ is the maximum velocity gradient along the transverse y direction for each streamwise section x.
In the present flow pattern,

$$\frac{\partial \overline{u}}{\partial y} \gg \frac{\partial \overline{v}}{\partial x}$$

(see FIG.5.37), so that Prandtl turbulent viscosity coefficient reads:

$$\nu_{T-Prandtl} = {l_m}^2 \left| \frac{\partial \overline{u}}{\partial y} \right|_{max} \tag{5.14}$$

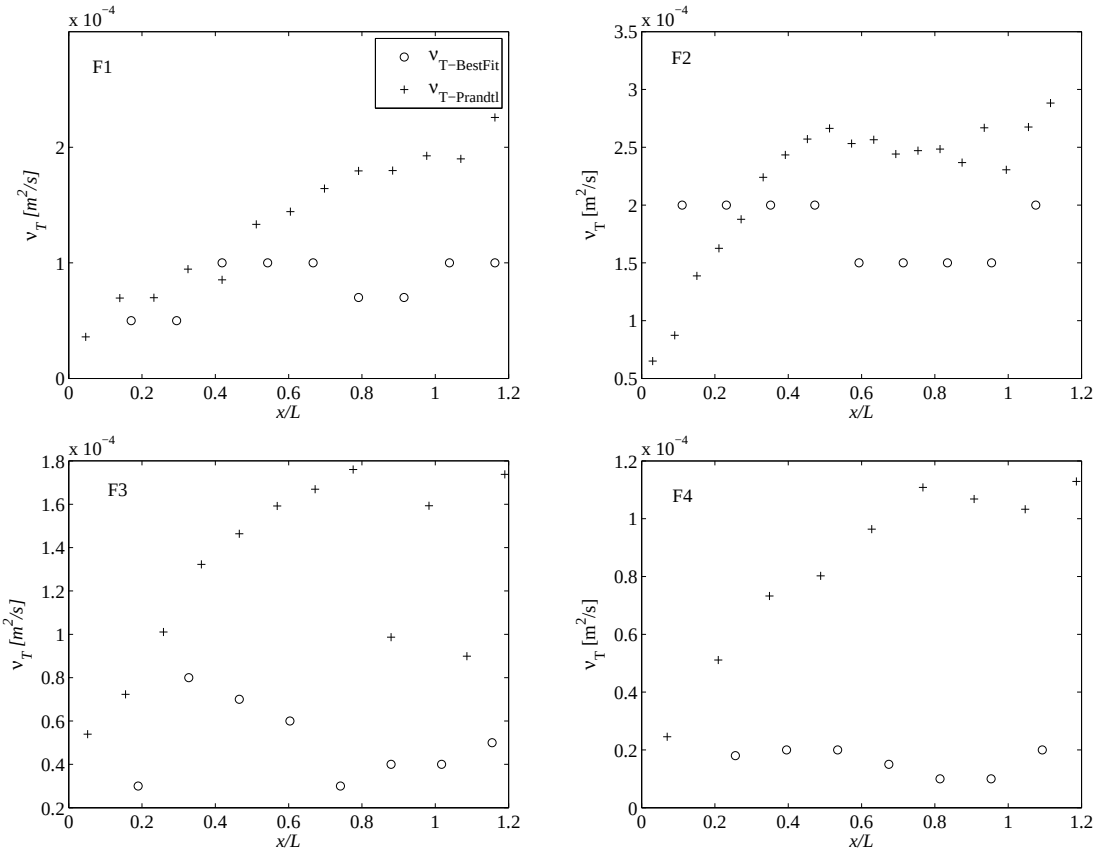

Figure 5.42: Evolution along x/L of eddy viscosity coefficient $\nu_{T-Prandtl}$ and $\nu_{T-Global}$

Based on numerous experiments from the literature, [Pope, 2008] proposes the magnitude of the mixing length, $l_{m(x)} = 0.07 \times \delta_x$ so that:

$$\nu_{T-Prandtl}(x) = 0.07^2 {\delta_x}^2 \left| \frac{\partial \overline{u}}{\partial y} \right|_{max} \tag{5.15}$$

With Eq.(5.10), we obtain $-\overline{u'v'}(x,y) = \nu_{T-Prandtl}(x) \frac{\partial \overline{u}}{\partial y}(x,y)$.
Streamwise evolution of best-fit $\nu_T(x)$ from FIG.5.38 and Prandtl turbulent viscosity from Eq. (5.15) are plotted for the 4 cases in FIG.5.42. It appears that Prandtl assumption of mixing length equal to 0.07 does not compare well with the experimental data for the four cases.

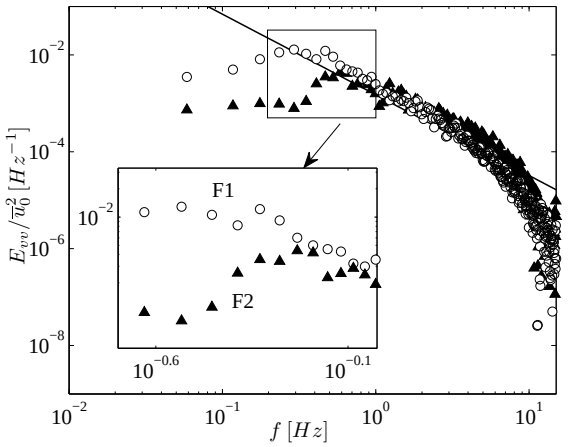

Figure 5.43: Energy spectrum of v along the centerline at $x = 0.2L$ of F3.

5.6 Role of the detached eddies in the mixing layer

5.6.1 One dimensional spectra

The aim of the present section is to estimate the frequency of the coherent cells advected along the mixing layer. FIG.5.43 plots the energy spectrum of the transverse velocity component v in the mixing layer at x/L=0.2 and $y = y_c$ while FIG.5.44 plots similar spectra every $x = L/13$ distance, in a similar manner as [Hertzberg and Ho, 1995] or [White and Nepf, 2007] for other mixing layer configurations, with the peak indicated by a symbol for each spectrum (Note: the symbols presents the peak value of each x/L section.). It appears that:
$\rightarrow$ For averaged frequencies (f=0.7 to 7 Hz), the main inertial range characterized by the -5/3 cascade is observed.
$\rightarrow$ In the low frequency range, the peak frequency f_p corresponding to the dominating vortex passing frequency appears to differ between the two cases: at x/L=0.2, $f_p \sim$0.6Hz for the shallow F3 case, while $f_p \sim$0.3Hz for the deep F1 case (see FIG.5.44). For F1, this peak frequency decreases towards downstream from f_p=0.3Hz to f_p=0.1Hz at x/L=0.5 and an even lower frequency at the reattachment section (x/L=1). For F3, the peak frequency decreases less rapidly from f_p=0.6Hz to f_p=0.4Hz at x/L=0.5 and f_p=0.2Hz at x/L=1. The decreasing peak frequency behaviours along the streamwise axis are in agreement with observations from [Uijttewaal and Booij, 2000].

The vortex passing frequency decreases less rapidly for the shallow case than for the deep case and this can be connected to the dynamic of large eddies addressed in the next section.

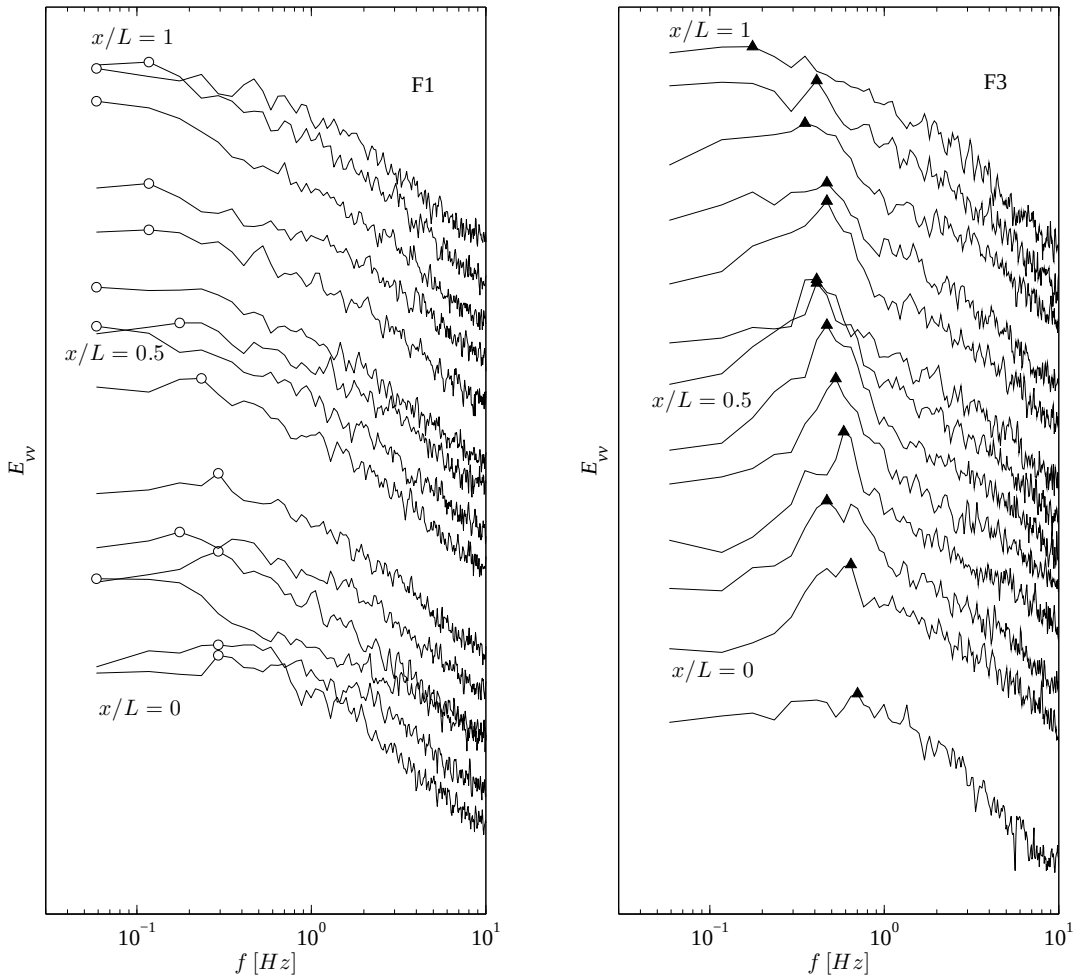

Figure 5.44: Energy spectrum of crosswise velocity component v along the centerline in recirculation zone for different x/L streamwise distance values.

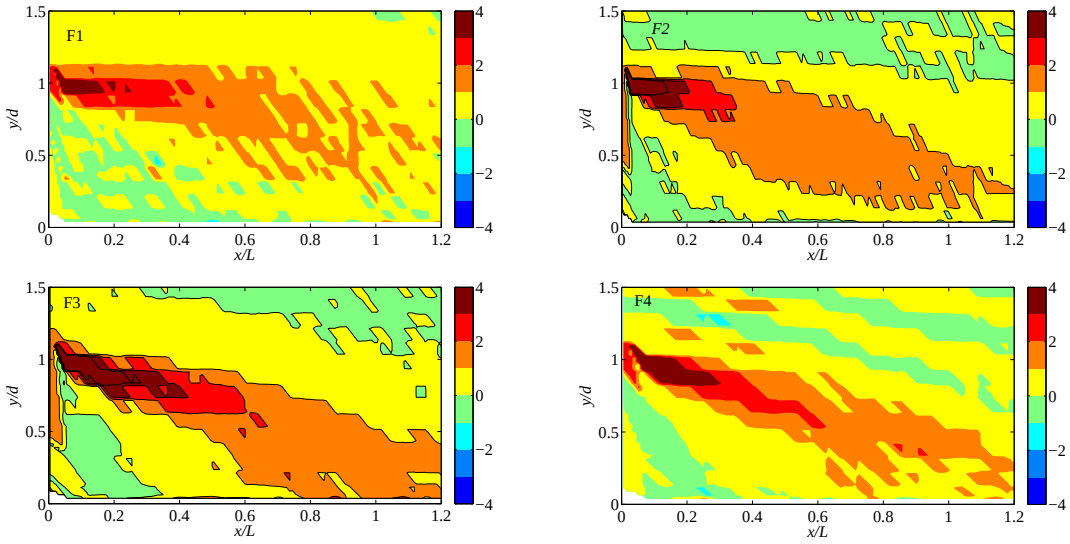

Figure 5.45: Amplitude of the vorticity for 4 Cases

5.6.2 Vorticity characteristics

The dimensionless vorticity $\omega = (\frac{\partial \overline{u}}{\partial y} - \frac{\partial \overline{v}}{\partial x})/\frac{d}{\overline{u}_0}$ is plotted in FIG.5.45. In the upstream region of the recirculation, the magnitude is maximum value, and then decreases along the streamwise axis. It appears that:
$\rightarrow$ The flow can be separated into 3 regions with different vorticity sign (rotation direction): in the recirculation $\omega < 0$ (zone A), in the mixing layer region, $\omega > 0$ (zone B), in the outer region $\omega < 0$ (zone C). In the figure of the sketch of vorticity, these regions are marked using three circles with the rotating directions.
$\rightarrow$ The magnitude of the positive vorticity in the mixing layer region is higher than the magnitude in both negative vorticity regions
$\rightarrow$ In the mixing layer the magnitude of the vorticity is maximum near the upstream corner and decreases towards downstream.
$\rightarrow$ The four cases show similar qualitative and quantitative vorticity maps.

5.6.3 Photography

The end of the recirculation corresponds to the reattachment of the flow to the wall, *i.e.* to a stagnation point. This one is located through trajectories of sawdust particles floating on the free surface, which are visualized thanks to long time-exposure photographs [Riviere et al., 2011]. The random passing of vortices – frequency $O(0.1\text{Hz})$ – strongly affects the location of the reattachment point that significantly varies from one photograph to another. This is sketched on FIG.5.46 representing four successive photographies with a 2s time exposure. All the trends observed within the mixing layer are connected to the large eddies detached from the upstream corner of the expansion and

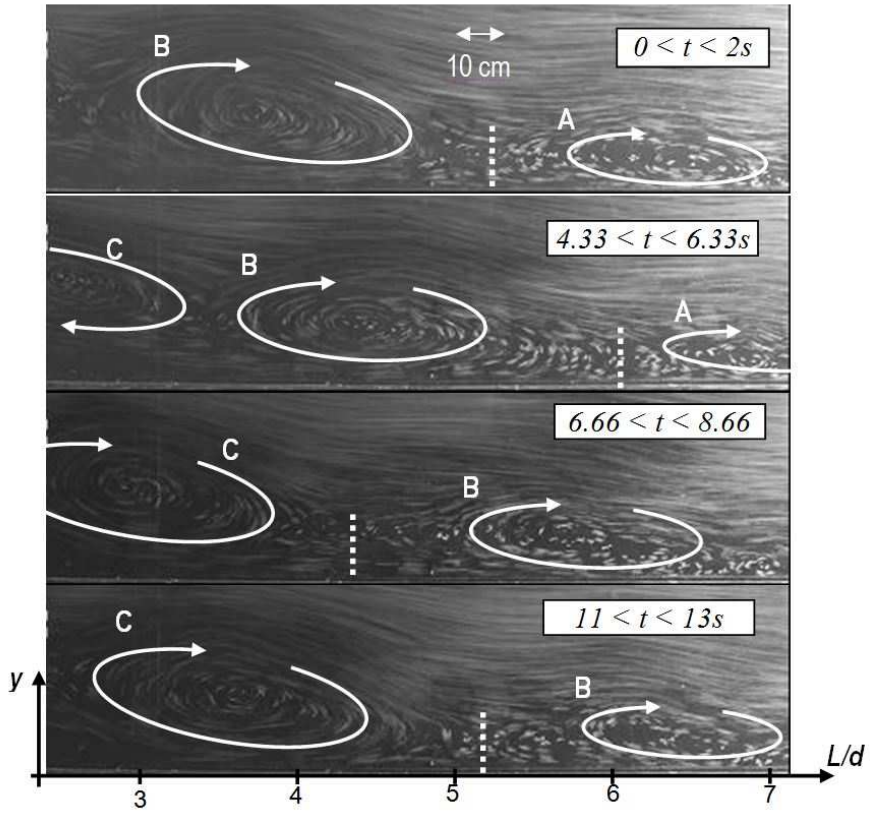

Figure 5.46: Successive 2 s long time exposure photographs. From [Riviere et al., 2011]

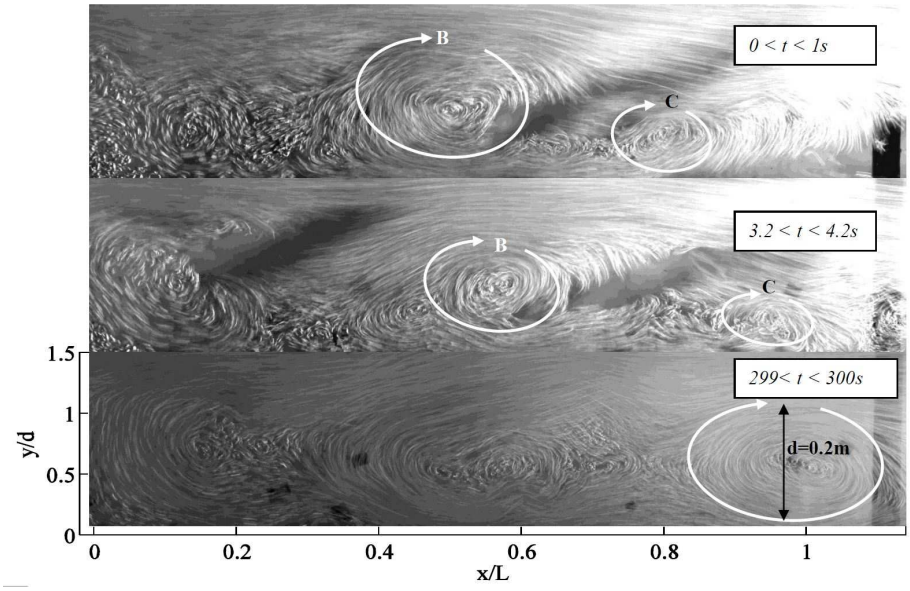

Figure 5.47: Successive 1s exposure photograph for case F1

advected towards downstream. Such eddies can be observed using time-exposure photography of floating sawdust (see [Riviere et al., 2011]). Due to the different flow velocities, the time exposure are 1s and 0.5s for cases F1 and F3 in FIG.5.47 (Dotted line ⋮ marks the location of the instantaneous reattachment) and FIG.5.48, respectively. Photographs for the shallow case F3 are given in Fig.5.48 where vortices of vertical axis are clearly visible, with an increasing size during their advection. The behaviour appears quite reproducible from one vortex to another. The reattachment location can be identified, and varies from one photograph to another around the $x/L = 1$ location, depending on the position of the vortices. On Fig.5.47, the deep case F1 appears more complex: again, vortices of vertical axis are clearly visible, with bigger sizes, but with less reproducible trajectories and sizes. The flow reattachment cannot be located as easily as for the shallow case F3. The pattern of eddies varies significantly with time (*e.g.* from t=0 to t=300s, Fig.5.48).

5.6.4 Autocorrelation

In order to obtain more quantitative vortices characteristics, the autocorrelation function of the transverse velocity fluctuation *Rvv* is computed along the centerline of the mixing layer, at x/L=0.2, 0.5, 0.8 and 1. The characteristic time scale of the large scale coherent structures is considered as the time shift between two successive peaks defined by [Constantinescu, 2013]. The signal is more complex for the deep case F1, confirming that eddies are less reproducible as shown by the photographs, but the two cases exhibit similar trends (see FIG.5.49). Firstly, FIG.5.49 shows that that the time shift τ between two successive eddies increases as x/L increases, indicating that the 2D eddies grow in the streamwise direction. Secondly, the coherence of the signal is worse for x/L=0.2,

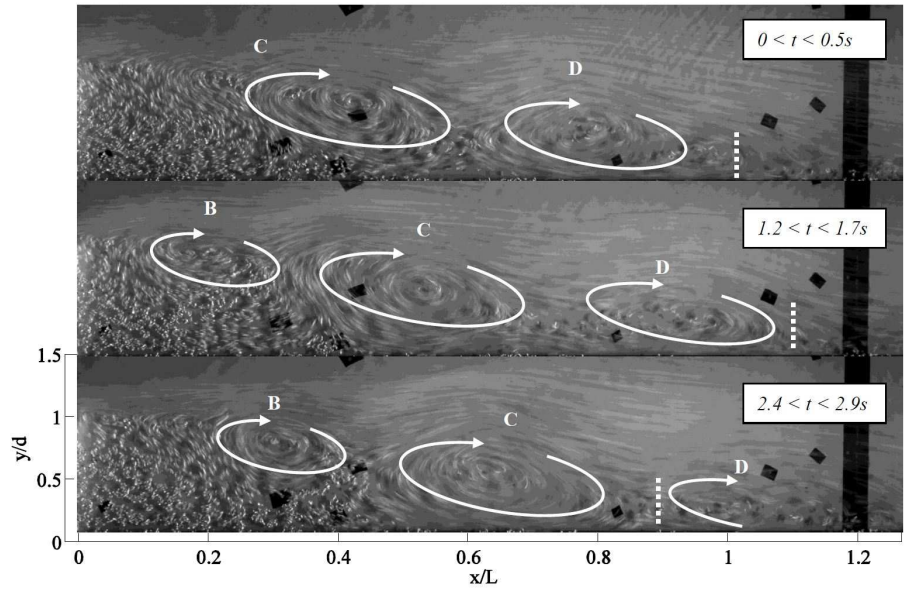

Figure 5.48: Successive 0.5s exposure photograph for case F3.

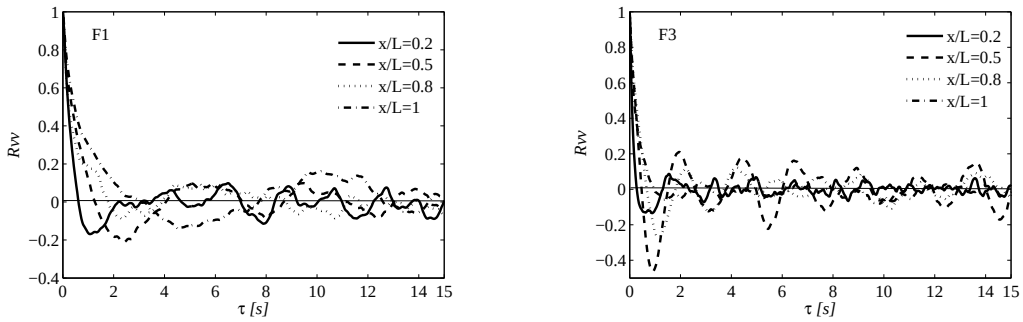

Figure 5.49: Autocorrelation function *Rvv* in different x/L section along the centerline

corresponding to the initial development of eddies. Thirdly, the time shift for the shallow case F3 is much shorter than for the deep condition F1, corroborating the frequencies observed through the spectrum analysis. TAB.5.8 compares the results from the different techniques, for two x/L values, for the shallower case F3. Estimates of the transverse length scale of vortices from photographs compare well with the mixing layer width derived from the mean velocity profiles. Estimates of the convection velocity by locating the vortex center displacement between two successive photographs compare well with the measured local mean velocity. For the letter, two values are provided, measured on both sides of the maximum gradient location. Estimate of the passing frequencies from photographs compare well with the spectra frequencies at the same location. Finally, estimates of the longitudinal length of vortices from photographs compare well with the integral length Λ obtained by multiplying the local mean velocity with the characteristic times from the autocorrelation *Rvv* on both sides of the maximum gradient loca-

Table 5.8: Characteristics of vortices and the mixing layer for F3 at two locations

	$x/L \sim 0.4$		$x/L \sim 0.7$	
	Photograph	ADV	Photograph	ADV
Transverse size (m)	0.09	δ=0.07	0.12	δ=0.11
$\overline{u}_{advection}$ (m/s)	0.25	0.14-0.24	0.2	0.13-0.2
Frequency (Hz)	0.59	0.6	0.44	0.47
Streamwise size (m)	0.3	Λ=0.24-0.36	0.36	Λ=0.31-0.42

Table 5.9: Characteristics of the vortex passing along the mixing layer for F1

	$x/L \sim 0.5$	
	Photograph	ADV
Thickness (m)	0.2	δ=0.13
$\overline{u}_{advection}$ (m/s)	0.06	0.08-0.12
Frequency (Hz)	0.13	0.18
Streamwise size (m)	0.25-0.44	Λ=0.35-0.61

tion [Uijttewaal and Booij, 2000]. The same comparison is performed for the deep case F1 in TAB.5.9, at x/L=0.5. The agreement is worse than for case F2. This is clearly due to the difficulty in estimating accurate values, without an averaging process, from the photographs.

To correlate further the role of vortices on the behavior of the mixing layer and on the flow reattachment, the dimensionless mixing layer width δ/d is plotted in FIG.5.50 (autocorrelation evolution is right axis with symbols • and ▲) and definition of Eq.(5.1) is left axis with symbols ○ and △) along the mixing layer centerline from x/L=0 to x/L=1) as a function of x/L, along with the integral longitudinal length scale Λ of vortices. The behaviours of δ/d and of Λ are similar: linear increase for the deep case F1 and linear increase followed by a plateau for the shallow case F3. Considering the two different vertical axis, the mixing layer width is about 3 times smaller than the longitudinal integral length scale. This corresponds to the longitudinal/transverse diameters ratio observed in the photographs (FIG.5.48) and to the one obtained by [Cheng and Constantinescu, 2014] for an unbounded shallow mixing layer of larger scale.

5.7 Chapter conclusion

This chapter was devoted to the mixing layer separating the free-stream and the recirculation.

Detailed experimental characterisations were undertaken for different flow configurations, corresponding to different values of the dimensionless parameters, S and h/d. As for shallow, plane mixing-layers, the present mixing layer is the location of high velocity gradient, Reynolds stresses, turbulent production and turbulent kinetic energy. A self-similarity was reported for these quantities, with a maximum magnitude at the cen-

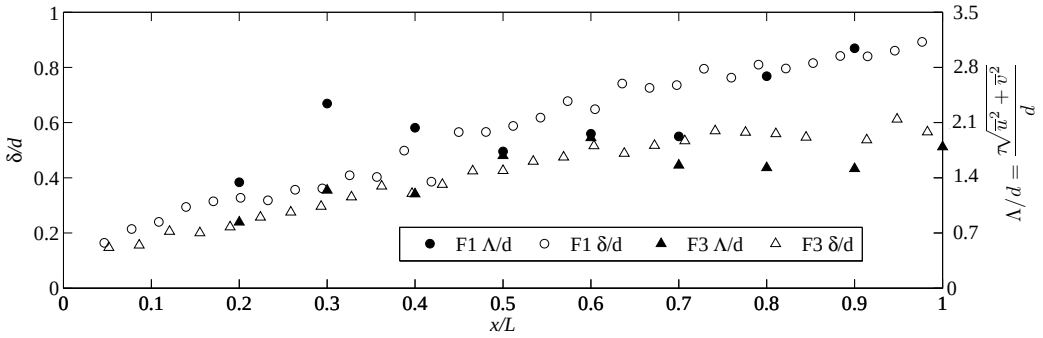

Figure 5.50: Comparison between autocorrelation evolution and the photography

treline of the mixing layer and a rapidly decreasing magnitude on both sides as previously reported in the literature.

Then, the influence of the shallowness could be examined. Surprisingly, due to the moderate flow dimensions, the local bed friction number $S(x)$ derived using the mixing layer width was always smaller that the critical value S_c (0.09∼0.12) above which the confinement effect stops the growing of the mixing layer. Such a growing stop was nevertheless observed, but it is due to the influence of the lateral wall and not to the vertical confinement. This lateral wall effect increases when S extends. This explains the relevance of a flow shallowness quantified by the global bed friction number S based on the expansion width as length scale [Babarutsi et al., 1989], independently of the mixing layer shallowness, quantified by the local bed friction number $S(x)$ based on the local mixing layer width as length scale.

However, the differences are limited to the downstream end of the mixing layer, close to the flow reattachment location and they cannot explain the non-monotonic dependency of L/d on S. This local approach at the mixing layer scale being unable to explain the experimental and numerical results, an integral approach at the whole flow scale is undertaken in next chapter, using momentum and energy balances.

Chapter 6

Analysis and understanding of the results

Both experimental and numerical results show behaviours of the recirculation length at odd with the ones reported in the literature. Notably, we obtained a bell shaped curve with (i)a left increasing branch for the non-frictional regime, where the recirculation zone length L/d increases with bed friction number S instead of a plateau and (ii) a right decreasing branch for the frictional regime, where L/d decreases with increasing S but with an exponent different from "S^{-1}" proposed in the literature. The objective of this chapter is to explain these tendencies, using momentum and head balance, with additional numerical simulations devoted to the frictional regime.

Contents

6.1 Introduction

As described in the CHAP.3 and CHAP.5, the experimental and numerical results show behaviours of the recirculation length at odd with the ones reported in the literature. As seen in the FIG.6.1, we obtained two regimes: the non-frictional regime and the frictional regime. In the next section, the analysis starts with the momentum balance.

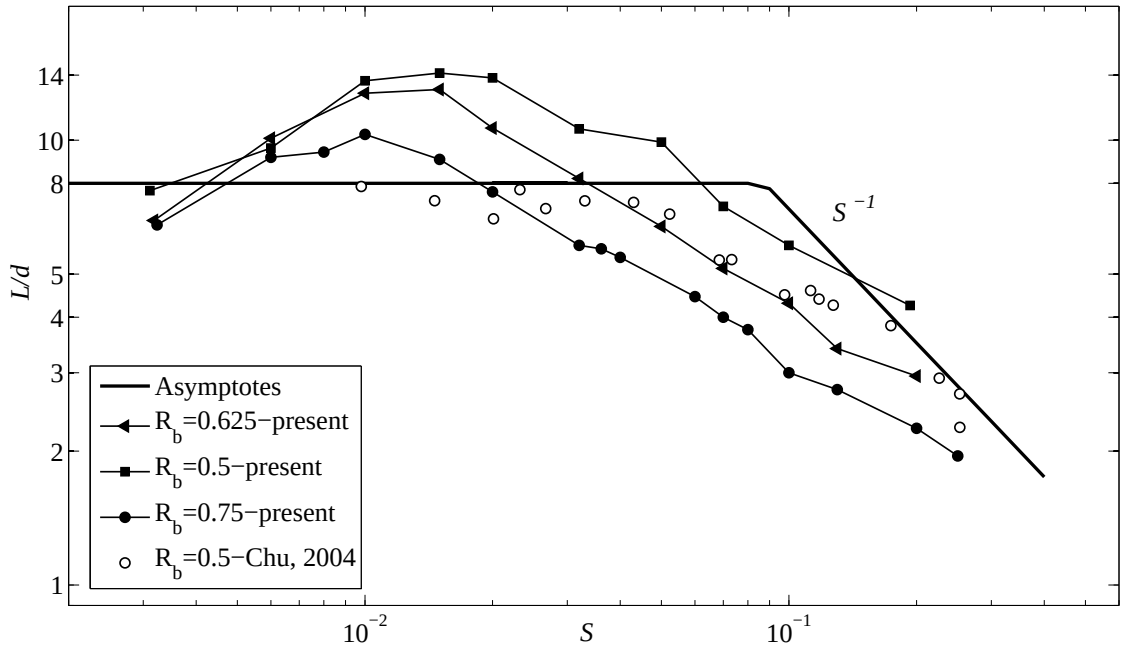

Figure 6.1: Dimensionless length of the recirculation zone L/d.

6.2 Momentum Balance

6.2.1 Control volume and forces

For deriving the momentum balance of our computed flows, the region covering the entire recirculation zone is chosen as the control volume "I-M-K-J" as in FIG.6.2 with the separation point, K the reattachment point and I and J the corresponding left-bank points. We thus define:

→ the inlet section S_1 (mean velocity $\overline{u}_1$ and pressure p_1)
→ the outlet section S_2 (mean velocity $\overline{u}_2$ and pressure p_2)
→ the bottom wall S_w with a resisting wall shear stress τ_w and where the pressure forces act perpendicularly to x
→ the side wall S_s (vertical plane from I to J) with a resisting wall shear stress and with pressure forces exerted perpendicularly to x. The shear stress is however negligible on this

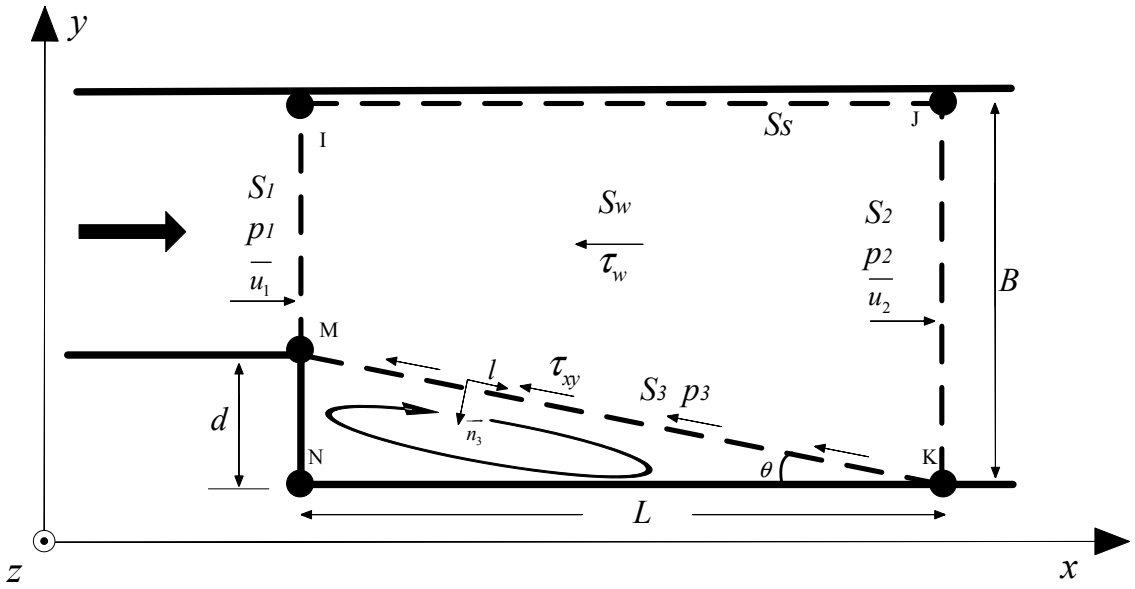

Figure 6.2: Control volume used for the momentum balance.

Note that the recirculation boundary is approximated by an inclined plane.

section, as checked in our numerical results. This is explained by the transverse velocities caused by the expansion, which tend to promote a flow separation on this wall.
$\rightarrow$ the interface S_3 between the recirculation and the main flow. There, the pressure is p_3 and the interface shear stress τ_{xy} acts against the flow. S_3 should be the limit of the recirculation zone; due to the difficulty of defining precisely this limit for numerous test cases, it is approximated by a plane (Assumption H6-1)
$\rightarrow$ the upper surface S_4 (rigid lid with free slip conditions) where the pressure forces are perpendicular to x and where the shear stress is by definition nil. This section does not participate to the momentum balance.

The momentum balance is applied and projected on the x-axis. It reads as the equation below:

$$M_x = F_{px} + F_{xy} + F_{wx} \tag{6.1}$$

Where M_x is the variation of $x-$momentum flux across the control volume, F_{px} is the sum of all pressure forces projected along x, F_{xy} is the shear force along the mixing layer projected along x and F_{wx} is the bottom friction force projected along x.

6.2.1.1 Variation of momentum flux across the control volume M_x

$M_x = M_{2x} + M_{1x}$, which are the inlet and outlet momentum derived by integrating the corresponding momentum on the S_1 and S_2 sections, respectively, as:

$$\begin{aligned} M_{1x} &= -\beta_1 \rho \overline{u}_1^2 h(B-d) \\ M_{2x} &= \beta_2 \rho \overline{u}_2^2 hB \\ &= \beta_2 \rho \overline{u}_1^2 R_b h(B-d) \end{aligned} \tag{6.2}$$

where β is the Boussinesq momentum coefficient, defined as $\beta_1 = \frac{\int_d^B \overline{u}^2 dy}{\overline{u}^2(B-d)}$ and $\beta_2 = \frac{\int_0^B \overline{u}^2 dy}{\overline{u}^2 B}$.

Then the momentum balance reads:

$$M_x = \rho \overline{u}_1^2 h(B-d)(\beta_1 - \beta_2 R_b) \tag{6.3}$$

6.2.1.2 Pressure forces

The total pressure force projected along x is:
$F_{px} = F_{p1} + F_{p2} + F_{p3}$ where F_{p1} and F_{p2} are the pressure forces obtained by integrating the pressure over S_1 and S_2. They can be expressed as :

$$\begin{aligned} F_{p1} &= p_1(B-d)h \\ F_{p2} &= -p_2 Bh \end{aligned} \tag{6.4}$$

F_{p3} is the pressure force along S_3, computed as:

$$\begin{aligned} F_{p3} = \int_M^K (-p(l)\overrightarrow{n_3}) \cdot \overrightarrow{l_x} dlh &= h\sin\theta \int_M^K p(l)dl \\ &= h\sin\theta p_3 \frac{L}{\cos\theta} = hL\tan\theta p_3 = p_3 hd \end{aligned} \tag{6.5}$$

where p_3 is the average pressure on S_3 in the sense of pressure forces, l is unit length along S_3 direction. In order to allow simplifications, a second assumption (H6-2) considers $p_3 = (p_1 + p_2)/2$. It is considered as satisfactory as FIG.6.6 shows that the associated error is less than 0.5%. Therefore, the pressure force on section S_3 projected along x is:

$$p_3 dh = \frac{p_1 + p_2}{2} dh \tag{6.6}$$

Finally, the total pressure force exerted on the control volume and projected on x is:

$$F_{px} = (p_1 - p_2)h(B - \frac{d}{2}) \tag{6.7}$$

6.2.1.3 Bottom friction

The bottom friction can be related to the skin friction coefficient c_f, which is considered as a constant (assumption H6-3) on the whole bottom, at least between S_1 and S_2.

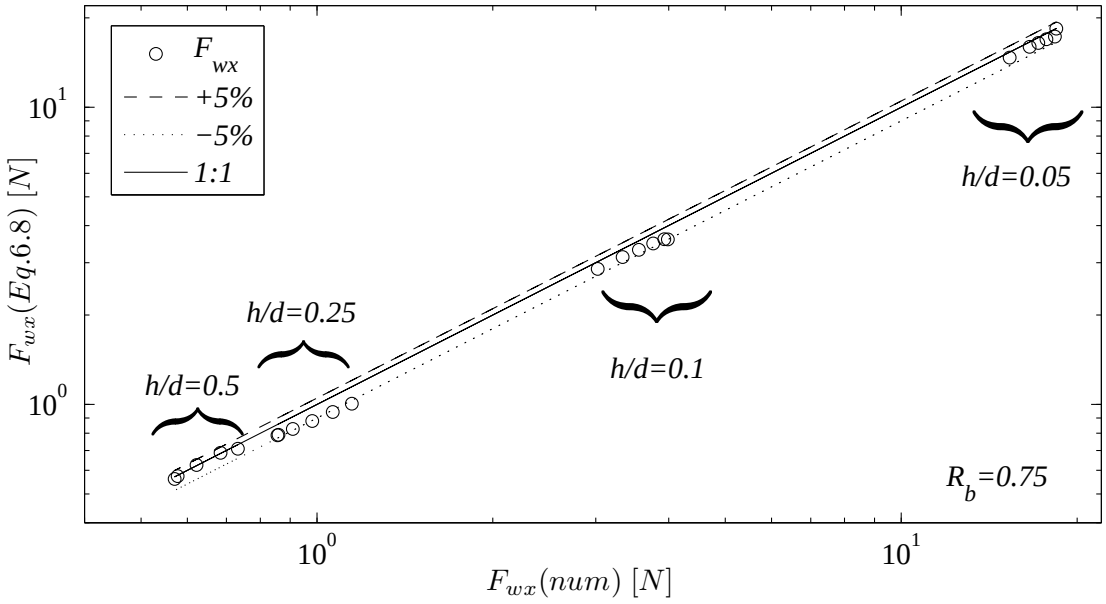

Figure 6.3: Comparison between the F_{wx}(Eq.(6.8)) and from simulation results

$$\begin{aligned} F_{wx} = \iint_{S_w} \tau_w dS \approx c_f \frac{1}{2}\rho\frac{\overline{u}_1^2+\overline{u}_2^2}{2}L(B-\frac{d}{2}) &= \rho\overline{u}_1^2 L\frac{c_f}{4}(1+R_b^2)(B-\frac{d}{2}) \\ &= \rho\overline{u}_1^2 L\frac{2hS}{d}(1+R_b^2)(B-\frac{d}{2}) \end{aligned} \tag{6.8}$$

F_{wx} from Eq.(6.8) is plotted as a function of F_{wx} from numerical computations in FIG.6.3, which shows that assumption H6-3 is satisfactory.

6.2.1.4 Shear stress in the mixing layer

The force due to shear stress in the mixing layer is

$$F_{xy} = \int_0^L |\tau_{xy}(hd\overrightarrow{l_x})| = |\overline{\tau_{xy}}|\, Lh \tag{6.9}$$

and we checked on numerical results that this term is satisfactorily approximated by:

$$\tau_{xy} \approx \mu_t \frac{\partial \overline{u}}{\partial y} \tag{6.10}$$

Where the gradient is the center of the mixing layer. Then assume both (H6-4) that an estimate of the gradient is

$$\frac{\partial \overline{u}}{\partial y} \approx \frac{\overline{u}_1 - 0}{d} = \frac{\overline{u}_1}{d} \tag{6.11}$$

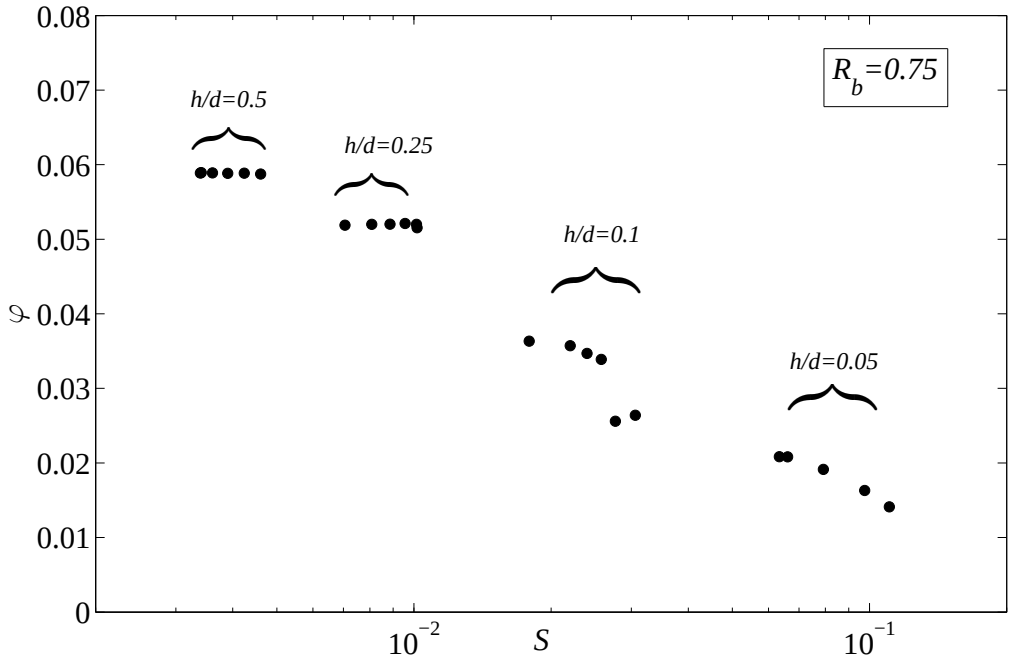

Figure 6.4: Evolution of φ with S from numerical calculations of CHAP.4

and that the eddy viscosity μ_t can be derived through a mixing length model, *i.e.* :

$$\mu_T = \rho(\varphi d)^2 \frac{\overline{u}_1}{d} \tag{6.12}$$

where $(\varphi d)$is the mixing length associated to the shear in the mixing layer and defined as a fraction φ of the enlargement width d. The space averaged shear is :

$$\mid \tau_{xy} \mid = \rho\varphi^2 \overline{u}_1^2 \tag{6.13}$$

and the associated force:

$$F_{xy} = \rho\overline{u}_1^2\varphi^2 Lh \tag{6.14}$$

Based on the numerical database, φ decreases from 0.06 to 0.02 as S increases(See FIG.6.4). However, as F_{xy} is very small and negligible compared with the other forces, the form used in Eq.(6.14) is retained as it can be easily normalized.

All the forces rewritten as in Eqs (6.3), (6.7), (6.8) and (6.14), the momentum balance finally reads,once normalized:

$$\begin{aligned} \frac{L}{d}\left[S + \frac{4(1-R_b)}{(1+R_b)(1+R_b^2)}\varphi^2\right] = & \frac{p_1 - p_2}{\frac{1}{2}\rho\overline{u}_1^2}\frac{1}{(1+R_b^2)} \\ & + \frac{4R_b}{(1+R_b)(1+R_b^2)}(\beta_1 - \beta_2 R_b) \end{aligned} \tag{6.15}$$

The terms of this equation are explicitly function of L/d, S, R_b but also implicitly of S, R_b, h/d through φ, β_1, β_2 and the pressure force term.

6.2.2 The different terms in the momentum analyse

Eq.(6.15) is composed of four terms which influence L/d. FIG.6.5 sketches their dependency on S for different h/d in fixed $R_b = 0.75$.
$\rightarrow M_2 = \frac{L}{d}\frac{4(1-R_b)}{(1+R_b)(1+R_b^2)}\varphi^2$ implies L/d and accounts for the shear force in the mixing layer. In FIG.6.5, M_2 is clearly negligible compared to the other terms, whether values from numerical simulations or from Eq.(6.15) are used.
$\rightarrow M_3 = \frac{p_1-p_2}{\frac{1}{2}\rho\overline{u}_1^2}\frac{1}{(1+R_b^2)}$ accounts for the pressure forces exerted on S_1, S_2 and S_3. It strongly depends on the bed friction number S but also on h/d (see the shifts in the M_3 curve) and on R_b (not shown here). In the frictional regime, M_3 can be considered approximately as evolving as $S^{0.4}$.
$\rightarrow M_4 = \frac{4R_b}{(1+R_b)(1+R_b^2)}(\beta_1 - \beta_2 R_b)$ accounts for the momentum variation across the control volume. It depends on R_b obviously, but also on other parameters, through the influence of the Boussinesq momentum coefficients β_1 and β_2 which evolution as a function of S and h/d is depicted on FIG.6.7. β_1 appears as constant, $\beta_1 \approx 1$, as the incoming flow is fully developed and turbulent. Conversely, β_2 depends mainly on h/d. Indeed, h/d gives an estimate of the size of the large scale, vertical axis, coherent structures([Uijttewaal and Booij, 2000]). These structures develop in the mixing layer, participate to the momentum exchange, and thus influence β_2. In the frictional regime, where both h/d and these structures are small, β_2 and M_4 are almost constant (for $S >$0.06, see FIG.6.7 and FIG.6.5); conversely, in the non-frictional regime, M_4 decreases when S decreases under the influence of h/d.
$\rightarrow M_1 = \frac{L}{d}S$ implies L/d and accounts for the forces due to bottom friction; it experiences dependencies to the different flow parameters, following the evolutions of M_2, M_3 and M_4. L/d depends mainly on S in the frictional regime, but also on h/d in the non-frictional regime.

From these observations, we can say that the momentum balance analysis provides the following information:

1. M_2 is clearly negligible compared to the other terms: the shear force in the mixing layer does not influence L/d.

2. in the frictional regime, ($M_1 = L/d \times S$) follows the increase of the pressure term (M_3) with S. Hence, L/d evolves as the sum of M_4/S ($\propto$ to S^{-1}) and of M_3/S ($\propto S^{-0.6}$).

3. the different behaviour in the non-frictional regime is due to the M_4 term, *i.e.* to the momentum coefficient β_2 which depends on h/d and thus makes L/d decrease when h/d decreases.

In other words, the bell shaped curve $L/d(S)$, observed both in the experimental and numerical results, is caused on the left side (non-frictional regime) by the modification

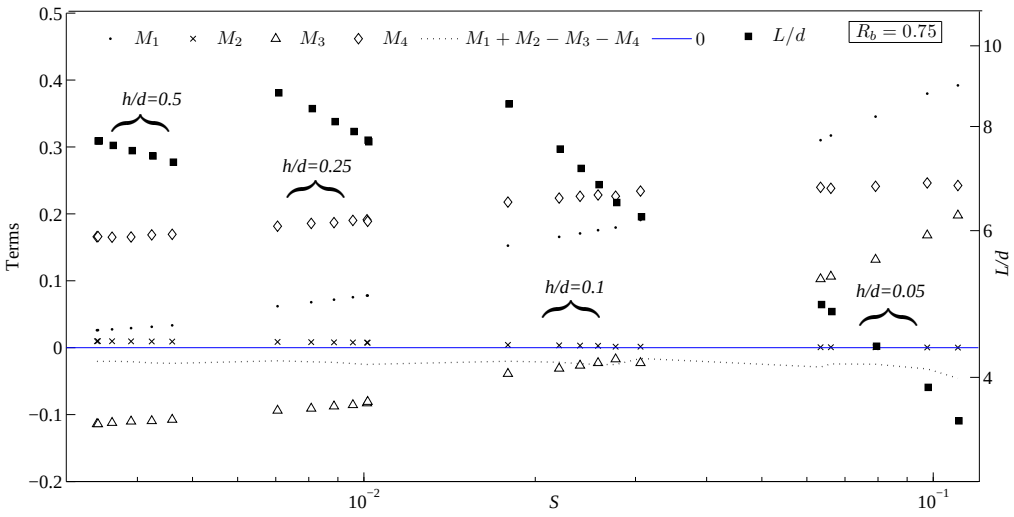

Figure 6.5: Evolution of four different terms of Eq.(6.15) in different S

of the momentum distribution by h/d and on the right side by the increase of the bottom friction with S.

Hence, the momentum balance provides significant information, notably that the shear force exerted along the mixing layer is negligible compared to other forces. Nevertheless, with the assumptions made to re-write the different terms, the balance is not perfectly ensured, as shown on FIG.6.5 where the sum $(M_1+M_2-M_3-M_4)$ is always negative. This is mainly due to the pressure term M_3. The assumption $p_3 = (p_1+p_2)/2$ is quite satisfactory to estimate the pressure force F_3, but leads to a significant relative error when used to estimate the total force $(F_1+F_2+F_3+F_w+F_{xy})$, as depicted by FIG.6.6. Additionally, Eq.(6.15) includes two terms involving L/d which complicates the evolutions that have to be considered. For these reasons, a head balance is performed in the next section, 6.3.

6.3 Head balance

6.3.1 Control volume and head losses

The control volume "I-N-K-J" is sketched in FIG.6.8. It is bigger than the control volume used for the momentum balance, as it includes the whole recirculation region. Pressure p_3 along the mixing layer will thus not appear explicitly in the derivations.

Head loss includes two parts as in FIG.6.8: The first part J_f is due to the bottom friction, and the second part J_r is the head loss in the recirculation zone.

6.3.1.1 Dissipation due to bottom friction

The term J_f concerns the dissipation due to the wall friction on the bottom, excluding the bottom within the recirculation zone (see J_r) and the vertical wall ("IJ"). On this vertical

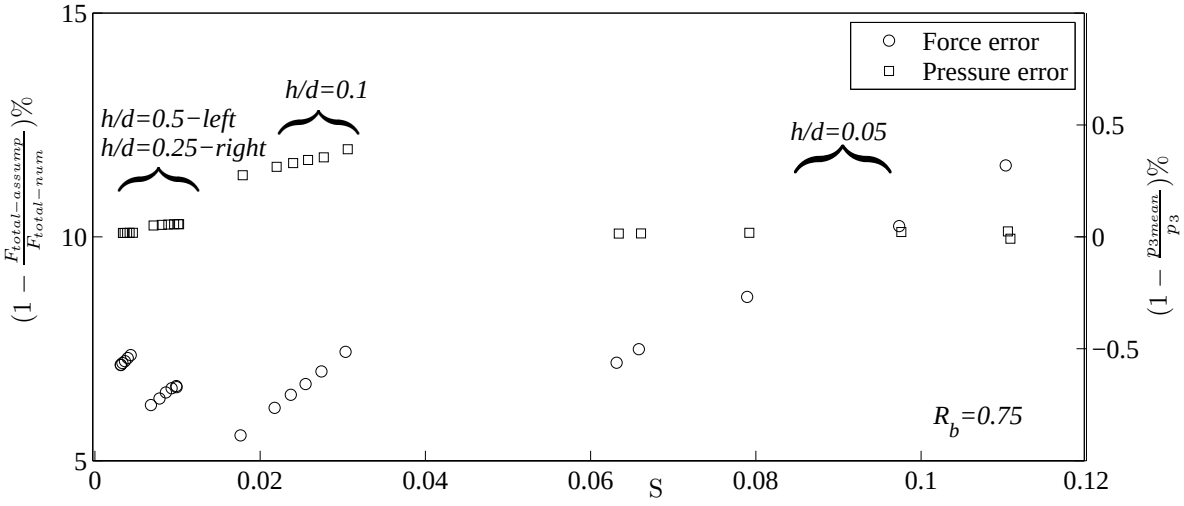

Figure 6.6: Relative error on the pressure with different definition of p_3

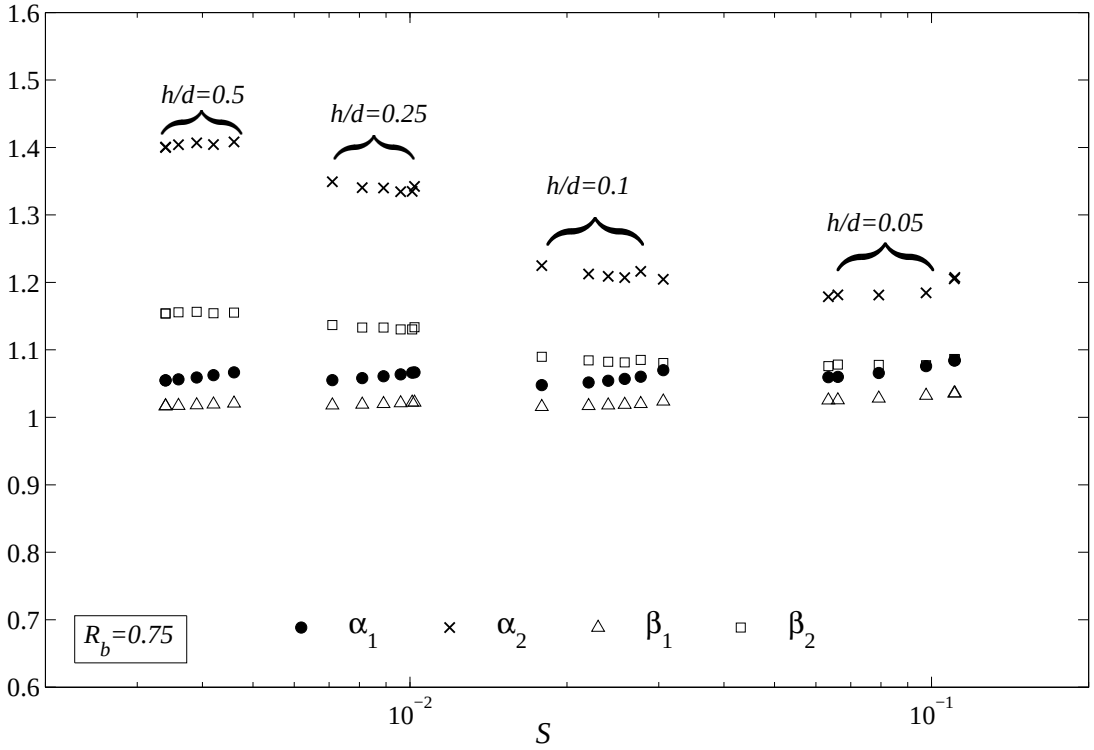

Figure 6.7: Coriolis kinetic energy coefficient and Boussinesq momentum coefficient

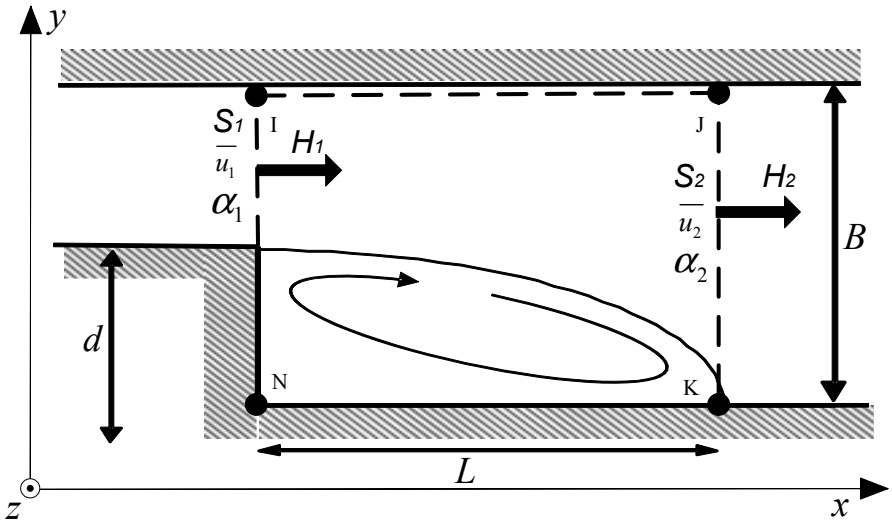

Figure 6.8: Sketch of the head balance which covers the whole recirculation zone

wall, the wall shear stress is negligible, as mentioned in section 6.2, and does not promote significant dissipation in the flow. In the simulation results, as mentioned in section 6.2, the friction force exerted by the side wall "IJ" is less than 1% of the bottom friction, so the friction force on the side wall ($y = B$) is assumed to promote no significant dissipation in the flow. Excluding this side wall ($y = B$), the hydraulic diameter D_h in the inlet and outlet sections, S_1 and S_2, writes as below:

$$D_{h1} = \frac{4(B-d)h}{B-d} = 4h = \frac{4Bh}{B} = D_{h2} \tag{6.16}$$

In fact, when excluding the vertical wall ("IJ"), the hydraulic diameter is constant along the whole control volume. Hence, the classic 1D linear head loss equation is used for this term and reads:

$$\begin{aligned} J_f \approx \lambda \frac{L}{D_h} \frac{1}{2} \rho \left(\frac{\overline{u}_1^2 + \overline{u}_2^2}{2} \right) &= \frac{1}{2} \rho \overline{u}_1^2 \lambda \frac{L}{8h} (1 + R_b^2) \\ &= \frac{1}{2} \rho \overline{u}_1^2 \frac{LS}{d} (1 + R_b^2) \end{aligned} \tag{6.17}$$

where we consider (Assumption H6-4) an average square velocity $(\overline{u}_1^2 + \overline{u}_2^2)/2$, which proved to close the head balance equation far better than an average velocity leading to the term $((\overline{u}_1 + \overline{u}_2)/2)^2$.

6.3.1.2 Dissipation in the recirculation

The second term J_r focuses on the head loss in the recirculation which corresponds to a sudden expansion and should be well estimated using Borda-Carnot equation, leading to:

$$J_r = \frac{1}{2}\rho\overline{u}_1^2\left[(1-\frac{S_1}{S_2})^2\right] = \frac{1}{2}\rho\overline{u}_1^2(1-R_b)^2 \tag{6.18}$$

6.3.1.3 Head in the inlet and outlet sections

The total head in section 1 and 2 read as below:

$$\begin{aligned} H_1 &= \alpha_1\frac{1}{2}\rho\overline{u}_1^2 + p_1 \\ H_2 &= \alpha_2\frac{1}{2}\rho\overline{u}_2^2 + p_2 \end{aligned} \tag{6.19}$$

Where α is the Coriolis kinetic energy coefficient.

Bernoulli's energy equation expresses the head balance:

$$H_1 - H_2 = (J_f + J_r) \tag{6.20}$$

Then, with the 4 equations derived above, the Eq. (6.20) can be rearranged as:

$$\underbrace{\frac{L}{d}S}_{T_1} = \underbrace{\frac{p_1-p_2}{\frac{1}{2}\rho\overline{u}_1^2}\frac{1}{(1+R_b^2)}}_{T_2} + \underbrace{\frac{(\alpha_1-\alpha_2R_b^2)}{(1+{R_b}^2)}}_{T_3} - \underbrace{\frac{(1-R_b)^2}{(1+{R_b}^2)}}_{T_4} \tag{6.21}$$

$\rightarrow T_1 = \frac{L}{d}S$ expresses the bottom friction; it is influenced directly by the bed friction number S;
$\rightarrow T_2 = \frac{p_1-p_2}{\frac{1}{2}\rho\overline{u}_1^2}\frac{1}{(1+R_b^2)}$ expresses the variation of (potential energy of) pressure from section 1 to section 2.
$\rightarrow T_3 = \frac{(\alpha_1-\alpha_2R_b^2)}{(1+{R_b}^2)}$ expresses the variation of kinetic energy from section 1 to section 2, which depends on the coefficient α_1 and α_2;
$\rightarrow T_4 = \frac{(1-R_b)^2}{(1+{R_b}^2)}$ expresses the Borda-Carnot head loss and depends directly only on R_b.

Eq.(6.21) involves explicitly the dimensionless recirculation length L/d, influenced by the bed friction number and by the three other terms. Next section examines the evolution of these 4 terms depending on the dimensionless parameters R_b, h/d and S stemming from the dimensional analysis, and also compares their relative weights in the different flow regimes.

6.3.2 Head balance analysis

6.3.2.1 Influence of the R_b

In order to analyse the influence of the expansion ratio, the four terms are plotted as a function of R_b, for three groups of computations, one with $h/d = 0.25$ and $S \sim 0.01$ (FIG.6.9 (a)), the other with $h/d = 0.1$, $S \sim 0.03$ (FIG.6.9 (b)) and the third one is $h/d = 0.5$, $S \sim 0.003$ (FIG.6.9 (c)).

$\rightarrow T_1 = \frac{L}{d}S$ increases as R_b decreases. It means that for a given S, when R_b becomes smaller, L/d turns bigger. R_b tending to 1 corresponds to an expansion d becoming drastically smaller than the channel width B (d/B tends to zero). Hence, T_1 tends asymptotically to the (dimensionless) head loss in a flow of constant width B.

$\rightarrow T_3$, which expresses the variation of kinetic energy through the control volume, has the greatest magnitude among the four terms. It decreases as R_b increases, following a quasi-linear tendency. These variations are connected to the evolution of the Coriolis kinetic energy coefficient α_2 in section 2. Indeed, T_3 tends to zero when R_b tends to 1: this correspond to α_1=α_2 when the channel becomes a square duct.

$\rightarrow T_4$, related to Borda-Carnot head loss, depends explicitly on R_b, and decreases as R_b increases, tending to zero for vanishing expansions (R_b tending to 1 or d/B tending to zero).

$\rightarrow T_2$ is a complex term as it includes the pressure evolution from section 1 to 2. Hence, T_2 depends on R_b not only trough $\frac{1}{(1+R_b^2)}$ but also through (p_1-p_2) which depends also on R_b. T_2 is the only term that has negative values, depending on R_b. This is connected to the evolution of the three other terms. On the one hand, the expansion increases the section and thus decreases the mean velocity and so the kinetic energy ($T_3 >$0). With no head losses, this results in $p_2 > p_1$ (repressuring through an expansion) and thus ($T_2 <$0). On the other hand, the head losses due to the expansion (Borda-Carnot) and to bottom friction decreases the head in section 2 and so the (potential energy) pressure p_2. If head losses are strong enough, then $p_2 < p_1$ and $T_2 >$0. The sign of T_2 results from a balance between head losses and expansion repressuring: for small R_b values, repressuring is stronger and $T_2 <$0 while friction more influences the flow above a threshold value of R_b that depends on the other parameters (please compare FIG.6.9 (a) and FIG.6.9 (b)). When R_b tends to 1, d/B tends to zero: both the expansion repressuring and the Borda-Carnot head loss vanishes ; T_2 logically tends to T_1 as the pressure gradient is due to the bottom friction alone.

The sum (T_2+T_3-T_1-T_4), should be zero according to Eq.(6.21). Its values are plotted on FIG.6.9 as a dashed line ($--$), which indicates that for $h/d = 0.25$ and $S \sim 0.01$ and $h/d = 0.5$ and $S \sim 0.003$, Eq.(6.21) is well closed. This is more questionable for $h/d = 0.1$ and $S \sim 0.03$, but similar with $R_b >$0.6. This validates the different assumptions concerning the head losses.

As a result, analysis of these different terms showed that the expansion ratio R_b influences the energy balance and then the relative length L/d.

6.3.2.2 Influence of h/d

To study the influence of the relative flow depth h/d, the four terms are plotted as a function of S on FIG.6.10, with fixed S=0.03 and R_b=0.75. h/d varies from 0.1 to 0.175, which is the maximum possible range whilst keeping S constant. Eq.(6.21) is satisfactorily closed, the sum of the four terms being almost zero on the whole h/d range. The observed tendencies on the different terms are:

$\rightarrow T_4$ exhibits explicitly no variations with h/d, as it depends only on R_b.

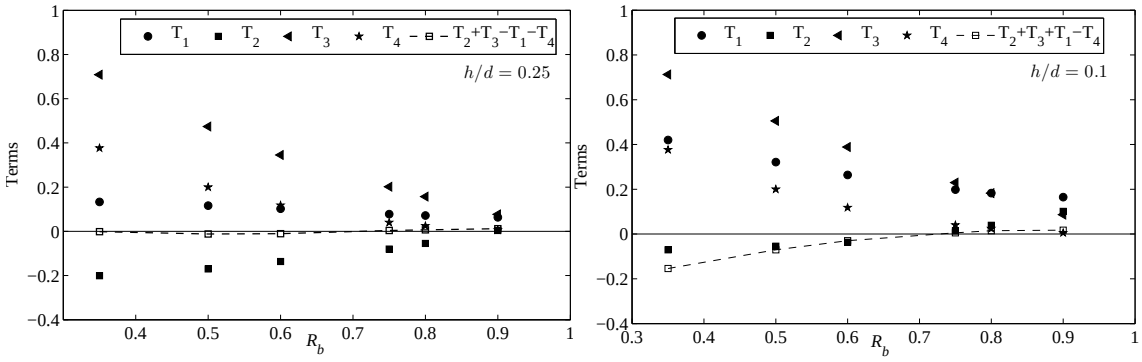

(a) $h/d = 0.25$ and $S \sim 0.01$

(b) $h/d = 0.1$ and $S \sim 0.03$

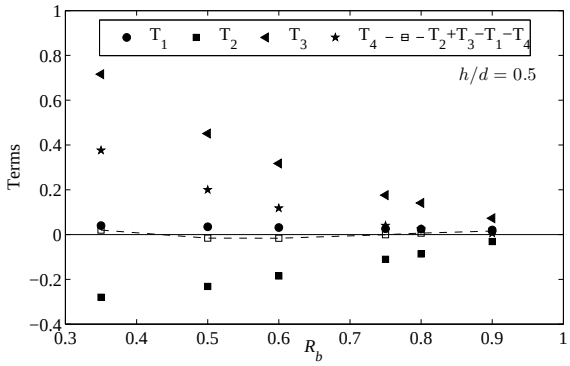

(c) $h/d = 0.5$ and $S \sim 0.003$

Figure 6.9: Evolution of each term of Eq.6.21 for different R_b.

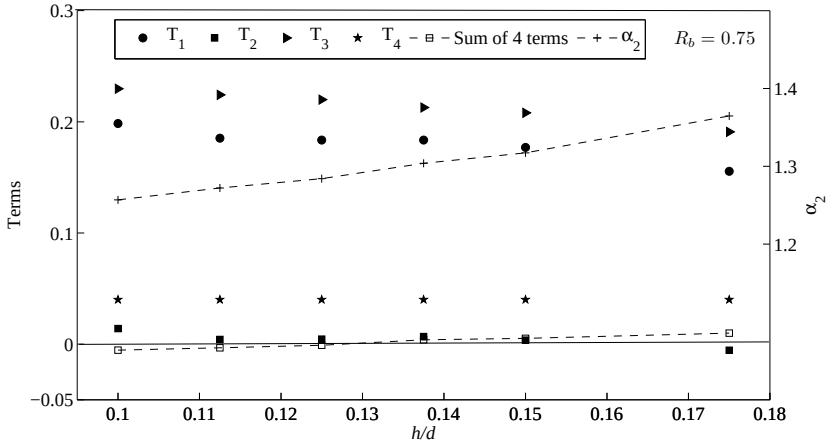

Figure 6.10: The four terms with fixed S=0.03 and R_b=0.75.

$\rightarrow$ T_3 decreases when h/d increases. This decrease is connected to the redistribution of the kinetic energy, and hence related to the evolution of the Coriolis kinetic energy coefficients with h/d. In our configuration, the upstream channel is long enough to ensure a uniform flow at the inlet condition and α_1 is constant (α_1=1.066). T_3 is therefore influenced by α_2: as observed in FIG.6.10, α_2 increases as h/d increases. According to Eq.6.21, this decreases T_3 when h/d increases.

$\rightarrow$ T_2 exhibits almost no variations with h/d, at least in the present range of numerical simulations.

$\rightarrow$ as a result, T_1 exhibits the same variations as T_3, which are also the variations of L/d as S is constant here. Hence, h/d is able to decrease the relative length of the recirculation L/d, by means of a modification of the Coriolis kinetic energy coefficient α_2.

6.3.2.3 Influence of bed friction number S

The bed friction number S is the most important parameter in our research. It influences the length of the recirculation directly through T_1=$\frac{L}{d}S$, but also through its influence on the other terms, which is detailed hereafter. For studying this, the 4 terms of 23 configurations with different S are plotted in the FIG.6.11, for different values of h/d and with R_b=0.75. Eq.(6.21) is satisfactorily closed, the sum of the four terms being almost zero on the whole S range.

The four terms exhibits different dependencies on S:

$\rightarrow$ again, T_4, related to Borda-Carnot, is constant as it depends only on R_b.

$\rightarrow$ T_3, related to the kinetic energy variation through the control volume, exhibits two different behaviours: for S <0.3, T_3 increases continuously with S and then reaches a plateau. This behaviour follows the one of α_2, depicted on the same figure. It is related to the large eddies behaviour that changes with S, as it will be discussed hereafter

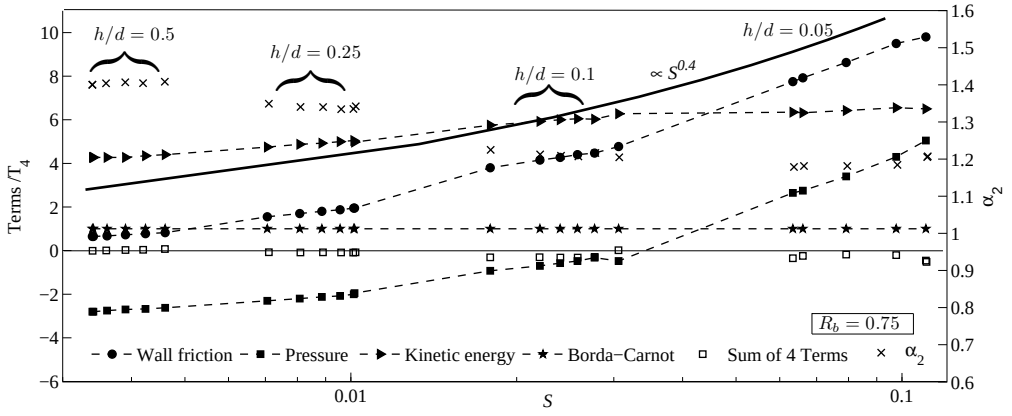

Figure 6.11: Evolution of each term of Eq.6.21 in different S.

$\rightarrow$ T_1 globally behaves as $S^{0.4}$ except for the small S values ($S < 0.005$) or high h/d values ($h/d = 0.5$)

$\rightarrow$ as a result, T_2, which expresses the pressure variation through the control volume, also exhibits three different behaviours.
(i) For S <0.01, both T_1 and T_4 are small compared to the two other terms. T_2 varies as a function of S similarly as T_3. The variations of S induce variations of the kinetic energy redistribution (α_2 and T_3) which impose the pressure gradient (T_2).
(ii) For S >0.03, as T_3 experiences a plateau and as T_4 is smaller than the other terms, T_2 experiences the same variations with S as T_1. With constant kinetic energy distribution in the upstream and downstream sections, an increase of the bed friction (T_1) causes an equivalent increase of the pressure drop.
(iii) For 0.01< S <0.03, the four terms have comparable magnitudes: this is a transition from the two preceding regimes, and the flow is influenced by bottom friction, dissipation in the recirculation and kinetic energy distribution.

6.3.2.4 Frictional and non-frictional regimes

From the preceding observations, we can define two asymptotic flow regimes: non-frictional for S <0.01 and frictional for S >0.03.

In the non-frictional regime(S <0.01), the kinetic energy distribution in the downstream section has the lead role. It imposes the pressure gradient along the recirculation and then the recirculation length L/d. This kinetic energy distribution is expressed by α_2 and, with a constant R_b, depends only on h/d (see FIG.6.12). Indeed, α_2 is influenced by large eddies (vortices of vertical axis due to vortex shedding) advected along the mixing layer, which participate to the redistribution of the kinetic energy within section 2, by injecting small velocity water in high velocity regions and *vice et versa*.

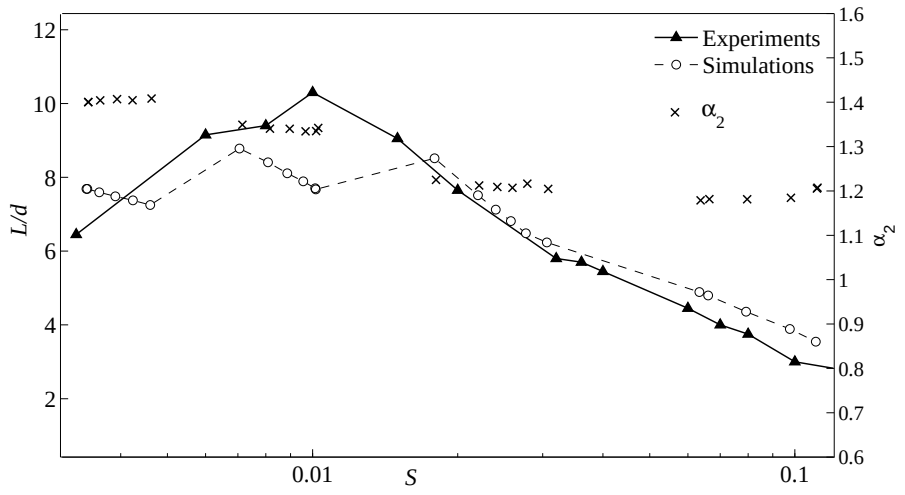

Figure 6.12: L/d with comparison of the α_2 with function of S

h/d provides an estimate of the size of these structure ([Uijttewaal and Booij, 2000] and [Sukhodolov et al., 2010]). For large h/d (h/d=0.75; FIG.6.13(a)), the flow is unconfined, the eddies have a size comparable to d (please refer to the study of the mixing layer, in the CHAP.5) and promote kinetic energy transfers throughout the whole section. This results in a smooth streamwise velocity profile, with no constant velocity region. The more α_2 is different from 1, the more this effect is important. As h/d decreases, the flow is vertically confined as the large eddies diameter evolves as h/d, leading to higher L/d value.

In the frictional regime, the bottom friction has the lead role. With a smaller h/d (h/d=0.1; FIG.6.13(b)), the eddies diameter remains small compared to d (please again refer to the study of the mixing layer, as CHAP.5). They do not participate to the kinetic energy transfers in the free-flow, where the velocity profiles exhibits a plateau. This plateau imposes $\alpha_2 \approx 1.2$, with no more kinetic energy modifications in section 2 when extending S. The flow and the recirculation length are driven by the equilibrium between the dissipation, proportional both to S and L/d, and the pressure gradient along the flow. This results in $L/d \propto S^{-0.6}$, as detailed in next section.

To conclude, the bell shaped curves $L/d = f(S)$ obtained experimentally are explained by the roles of two parameters stemming from the dimensional analysis:

$\rightarrow S$, the bed friction number, accounts for the bottom friction, at the control volume scale. Its extension always decreases the recirculation length L/d to ensure the equilibrium between the dissipation ($\propto \frac{L}{d}S$) and the pressure drop.

$\rightarrow h/d$, the relative water depth, accounts for the size of the vortices of vertical axis advected along the mixing layer and thus of their capacity to influence the kinetic energy distribution in the main flow. An extend of h/d decreases L/d. This decrease remains however limited as when h/d becomes, say, larger than one, vortices diameter becomes independent of h/d. This situation corresponds to the backward-facing step. Hence, as observed in CHAP.4 , L/d experiences a plateau when h/d (and so S) tends to 0.

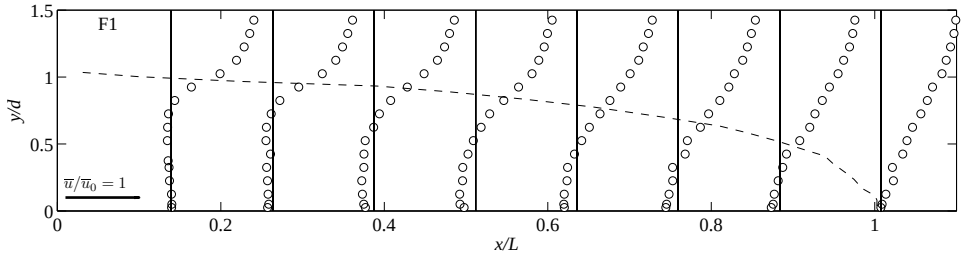

(a) $S = 0.0032$; $h/d = 0.75$; L/d=5.8

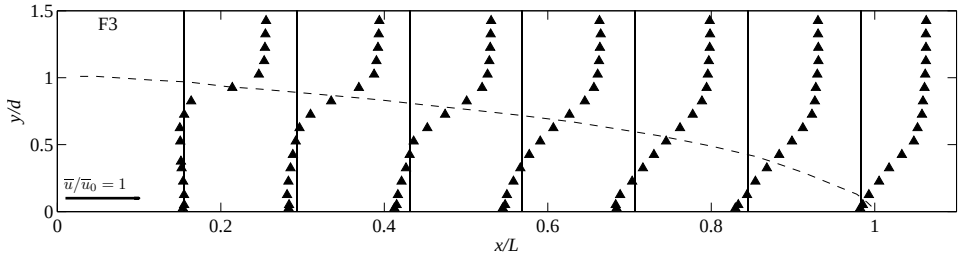

(b) S=0.032; $h/d = 0.1$; L/d=6.45

Figure 6.13: The transverse profiles of streamwise velocity $\overline{u}(x)/\overline{u}_0$.

This explanation must be completed by two additional observations:

$\rightarrow$ R_b, the third parameter, also influences L/d, although without changing the respective roles of S and h/d. When R_b decreases, the Borda-Carnot head losses become non-negligible and intervene in the pressure drop-bottom friction equilibrium. For high values of S, this shifts vertically $L/d = f(S)$ curves, as observed in the experiments. Different values of R_b expresses different ratio of the inlet and outlet sections of the control volume: as seen previously, α_2 is function of R_b. However, R_b influences also the kinetic energy distribution, and so L/d, in the non-frictional regime.

$\rightarrow$ the impossibility to modify independently h/d and S over high ranges also complicates the problem. This is illustrated by (FIG.6.12) with R_b=0.75. Let us examine first the numerical results. For fixed values of h/d, α_2 is constant with S. The bottom friction increase (with S) acts alone on L/d which decreases. $L/d = f(S)$ curve is thus a discontinuous succession of decreasing segments corresponding to different h/d values. This is quite different for the experimental results. As S and h/d evolve simultaneously, $L/d = f(S)$ curve is uninterrupted : the increasing left branch is due to the dominating effect of h/d *i.e.* of the large eddies which modify the kinetic energy distribution; the decreasing right branch is due to the the dominating effect of the bottom friction (through S). Experiments using different roughnesses may lead to a different S values for the transition between these two regimes, and should modify also the increasing branch: indeed, with different roughnesses, a given value of S corresponds to different values of the relative water depth h/d. This is consistent with the experimental results obtained with aluminium tear plates see FIG.3.20.

6.4 Empirical correlation $L/d = f(S, R_b, h/d)$

6.4.1 Correlation for numerical simulations

The different terms (T_1, T_2, T_3, T_4) exhibits different dependencies on the three parameters stemming from the dimensional analysis (S, R_b, h/d), studied in the previous section. From FIG.6.9 to FIG.6.11 (complete information concerning each influence are detailed in Appendix A), these dependencies can be expressed as follow.

$\rightarrow$ The term T_4 accounting for the "Borda-Carnot" dissipation in the recirculation depends explicitly only on R_b.

$$T_4 = \frac{(1-R_b)^2}{(1+Rb^2)} \tag{6.22}$$

$\rightarrow$ The term T_3 expresses the influence of the kinetic energy distribution. It thus depends on h/d, through an exponential function which expresses a strong influence of h/d in the non-frictional regime (in fact for high h/d values) and no more effect once the velocity profile in the free-flow is a plateau (small h/d values):

$$T_3 = \frac{[\alpha 1 - R_b^2 \cdot (k_{31} + k_{32} e^{(k_{33}(h/d) + k_{34} R_b)})]}{(1+R_b^2)} \tag{6.23}$$

$\rightarrow$ The term T_2 accounts for the pressure gradient through the control volume. It depends on the three parameters S ,h/d and R_b. Its expression is in the form:

$$T_2 = S^{0.4} + [(k_{21} {R_b}^2 + k_{22} R_b + k_{23}) \frac{h}{d} + (k_{24} {R_b}^2 + k_{25} R_b + k_{26})] \tag{6.24}$$

Finally, the term T_1 expresses the bottom friction in the free-flow outside of the recirculation. In the frictional regime, its dependency on S is the same as the one of T_2. The obtained correlation reads:

$$T_1 = S^{0.4} \cdot \{[k_{11}(1-R_b)^{k_{12}} + k_{13}] \ln(h/d) + [k_{14}(1-R_b)^{k_{15}} + k_{16}]\} \tag{6.25}$$

For each term, a least square method is used for identifying all the parameters, using all the numerical simulation database. The object is to find the minimum value of the $\Sigma_1^n (T_{num} - T_{reg})^2$ for each term. The parameters obtained for Eqs. (6.22) to (6.25) are listed in TAB.6.1.

The accuracy of these correlations is illustrated by figures FIG.6.14, FIG.6.15 and FIG.6.16 where the values from the correlations are plotted as a function of the numerical values in the same flow conditions.

The three figures exhibit a satisfactory agreement between numerical and correlation results, notably for T_1 and T_3, as most of the points are located in the $\pm 5\%$ error lines. The regression process was more tedious and less accurate for T_2. This is due to the possible change of sign of this pressure gradient when the bottom friction excesses the pressure increase due to the section expansion.

The correlation providing the dimensionless recirculation length L/d can be obtained from Eq.(6.25) as $T_1 = S \times L/d$. Hence, $L/d \propto S^{-0.6}$.

Table 6.1: List of the regressed parameters for the 4 energy terms

	T_1		T_2		T_3
k_{11}	-1.876	k_{21}	0.914	k_{31}	-0.095
k_{12}	2.412	k_{22}	1.571	k_{32}	3.198
k_{13}	-0.219	k_{23}	0.620	k_{33}	1.191
k_{14}	-2.887	k_{24}	0.707	k_{34}	0.291
k_{15}	4.531	k_{25}	0.646		
k_{16}	0.114	k_{26}	0.157		

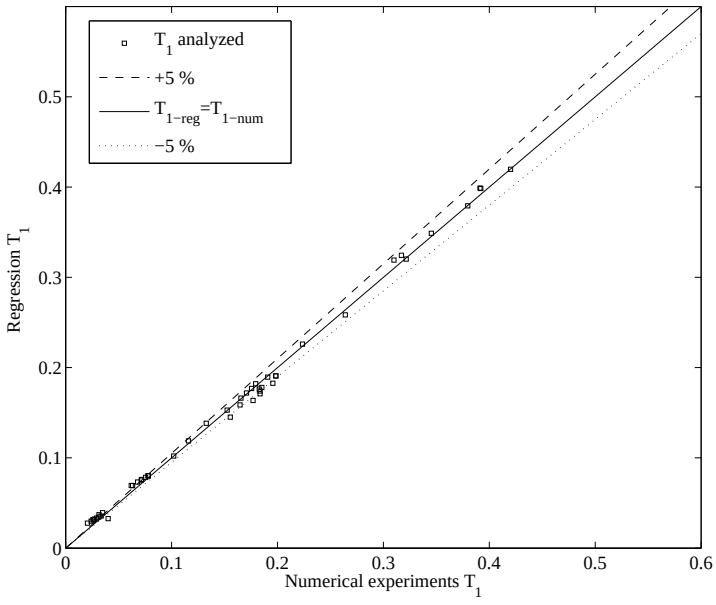

Figure 6.14: Calculated T_1 versus the assumpted T_1

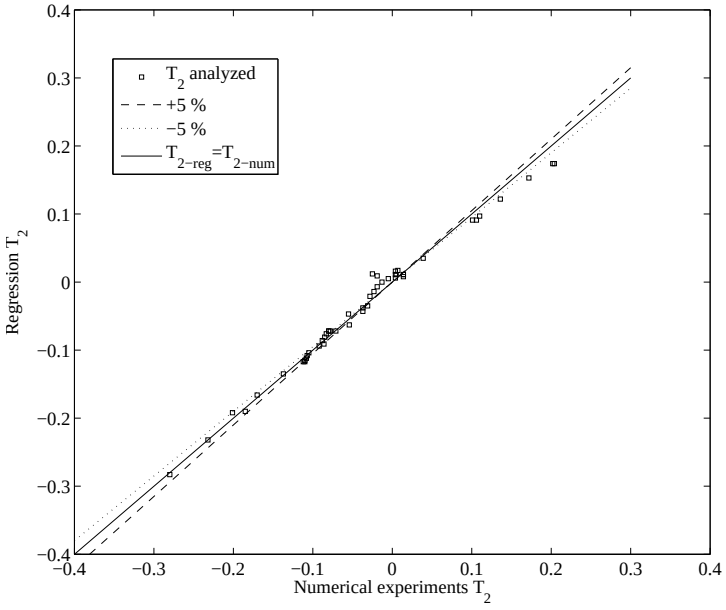

Figure 6.15: Calculated T_2 versus the assumpted T_2

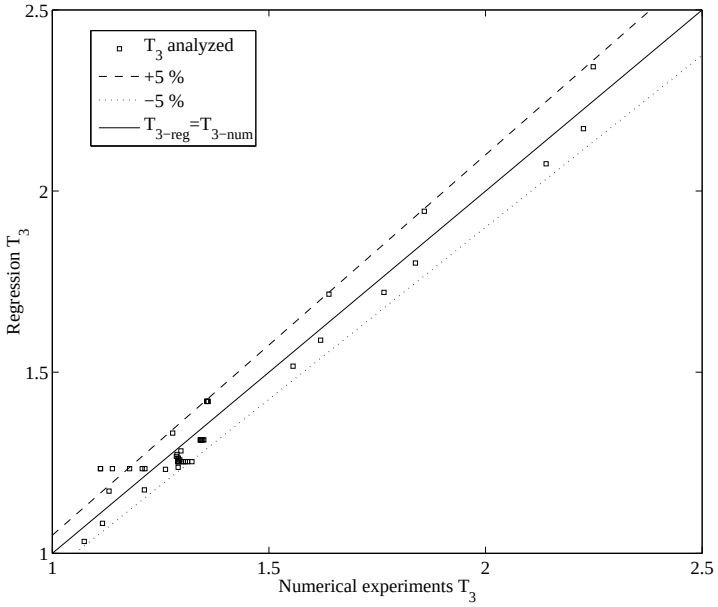

Figure 6.16: Calculated T_3 versus the assumpted T_3

6.4.2 Final correlation for experiments

Previous section confirmed the dependencies observed on the different parameters. However, to cope with the assumptions made in the numerical simulations, it is necessary to seek a correlation based on the experimental data. For each value of R_b, a least square method is again used to obtain an empirical correlation, as illustrated by FIG.6.17. These correlations are of the form:

$$L/d = S^{-0.6} \cdot [k_1 + (k_2 - k_1) \cdot e^{-k_3 (h/d)^2}] \tag{6.26}$$

where h/d acts on L/d through a Gauss function, which expresses its influence related in the previous sections. When $h/d \to 0$, $e^{-k_3(h/d)^2} \to 1$ and $L/d \to k_2 S^{-0.6}$: this is the frictional regime. When h/d is sufficiently high, it counterbalance the influence of S and has the lead influence on L/d. L/d values from both the empirical correlation and from experiments are plotted in FIG.6.17, and exhibit a fair agreement.

Coefficients k_1, k_2 and k_3 used in Eq.(6.26) depend on R_b. They can be obtained using a cubic-polynomial fitting with R_b:

$\to k_1 = 6.5255 R_b^3 - 10.259 R_b^2 + 4.8917 R_b - 0.4524$
$\to k_2 = 47.741 R_b^3 - 83.246 R_b^2 + 44.059 R_b - 5.5163$
$\to k_3 = 483.4 R_b^3 - 766.06 R_b^2 + 360.34 R_b - 36.07$

The accuracy of this final correlation is illustrated by FIG.6.18 where the values from the correlation are plotted as a function of the experimental values of the dimensionless recirculation length in the same flow conditions. The result is satisfactory, as most of the values computed from the correlation are within $\pm 10\%$ around the experimental ones. Due to a lack of time, a more efficient regression method, leading to more accurate results, was not undertaken.

The final correlation is now evaluated with experimental results from the two studies available in the literature. FIG.6.19 sketches data from [Chu et al., 2004]. In FIG.6.19 (a), the values from correlation are plotted as a function of the experimental ones. The agreement is admissible in the frictional regime ($S > 0.03$), not in the non-frictional one. FIG.6.19 (b) shows that, conversely to our correlation, experimental results from [Chu et al., 2004] are not affected by h/d. As our experimental observations were confirmed by numerical simulations, we attribute these differences to possible backwater effects (please refer to CHAP.3) in [Chu et al., 2004]'s experiments. FIG.6.20 sketches data from [Wang et al., 2011] for muddy water (CHAP.1 presented their results for clean water for which, unfortunately, the water depth is not provided). Beware of the the water depth h, that is measured by the authors in the downstream part of the channel, very downstream of the reattachment location. FIG.6.20 shows puzzling results, as some data match well while some others are at odd with our correlation. In fact, the different data series (group of four or five points) correspond to different discharges. Such a dependency on a dimensional parameter (the discharge) is questionable. We attribute this to the location of the water depth measurement, leading to non relevant values of S or h/d, and this can explain the observed results. Unfortunately, no backwater curves are provided by the authors and this makes impossible to emit any definite conclusion.

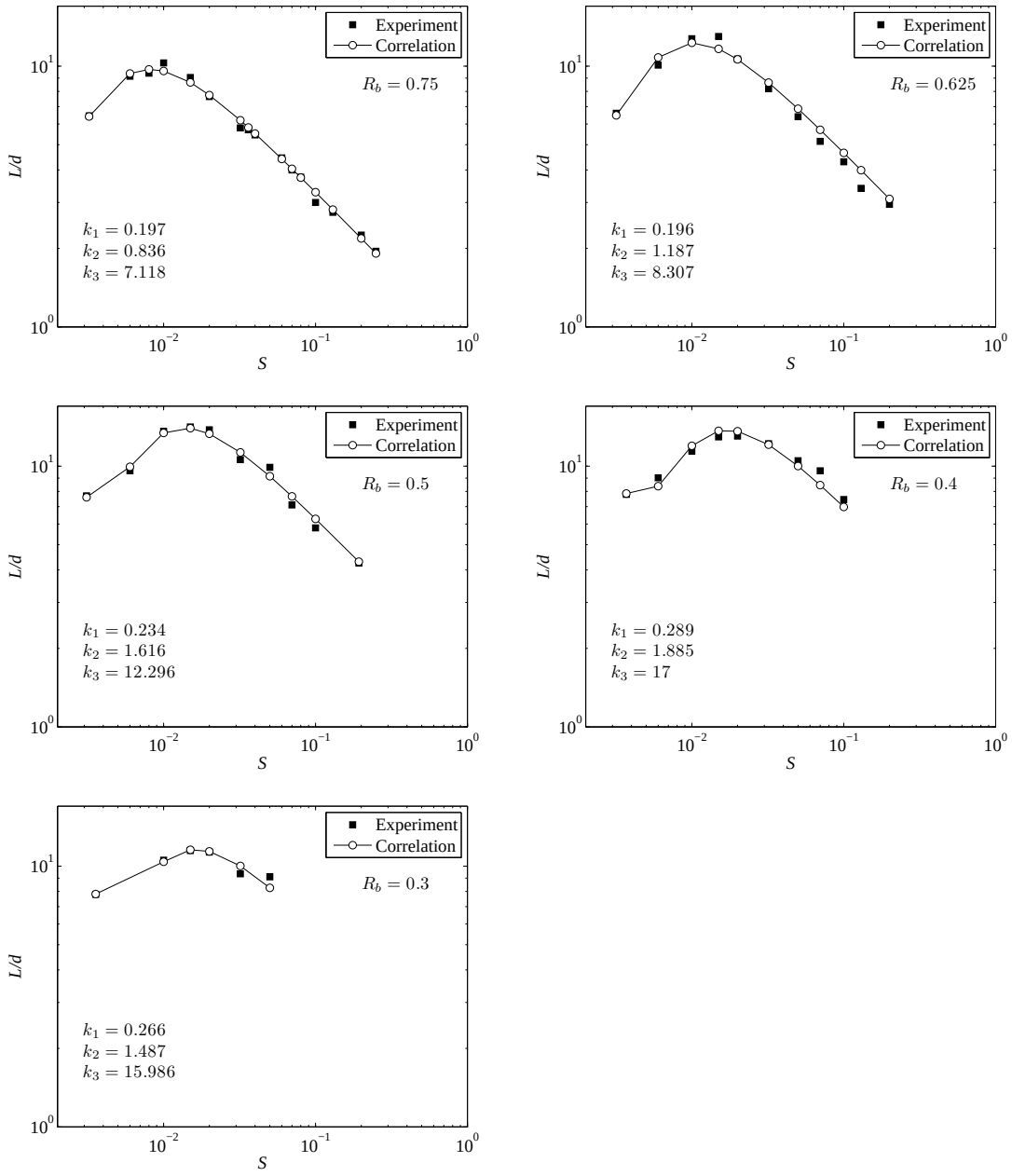

Figure 6.17: Comparison of L/d from experiments and correlation (Eq.(6.26)), for different R_b

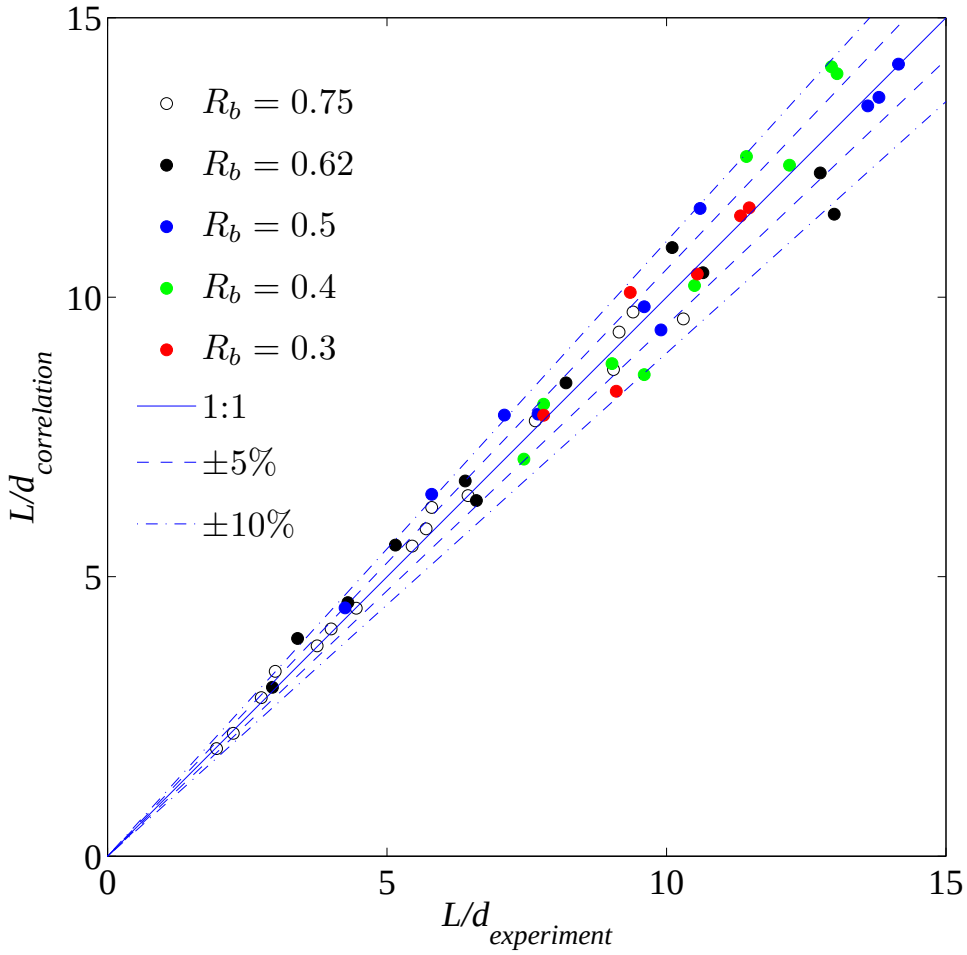

Figure 6.18: Comparison of L/d from experiments and correlation (Eq.(6.26))

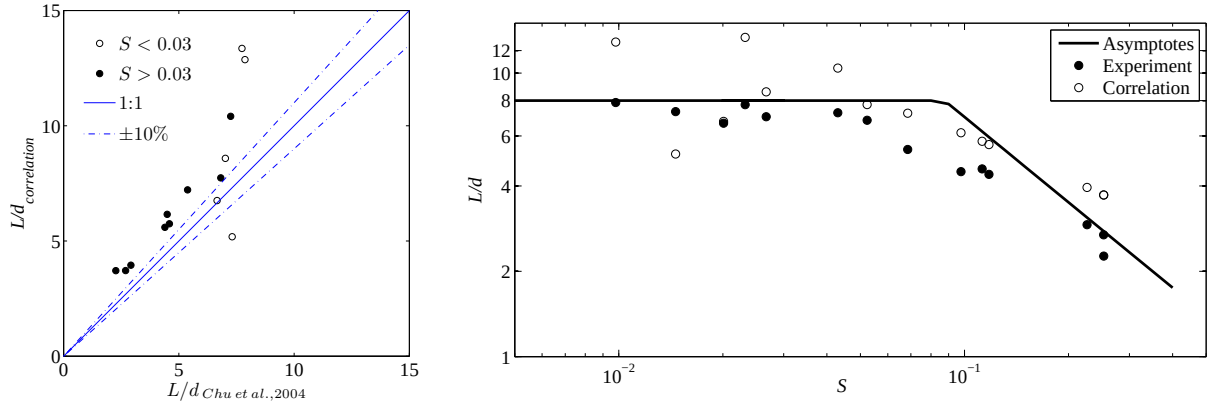

(a) (b)

Figure 6.19: The correlation for the data of [Chu et al., 2004]

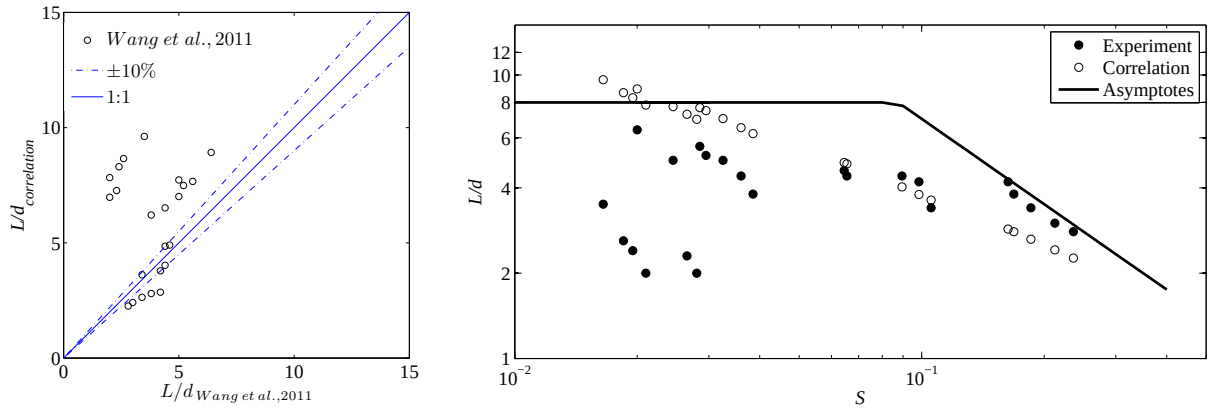

(a) (b)

Figure 6.20: The correlation for the data of [Wang et al., 2011]

Note that our correlation Eq.(6.26) is valid only for $S > 0.003$ that corresponds to the present experimental range of parameters. For smaller S or higher h/d values, the diameter of the large scale vortices of vertical axis becomes independent of both h/d and S. Yet, our correlation is dominated, for very small S values, again by $S^{-0.6}$ when $S \to 0$, as $S^{-0.6} \to \infty$. A form suitable for the whole range of parameters would be:

$$L/d = [k_1 e^{-k_4 S^2} + (1 - e^{-k_4 S^2}) S^{-0.6}][1 + (k_2 - 1) e^{-k_3 (h/d)^2}] \tag{6.27}$$

When $h/d \to 0$, $L/d \to k_2 S^{-0.6}$: this is the frictional regime. When h/d is high and thus $S \to 0$, $L/d \to k_1$: this corresponds to the backward facing step. The intermediate region is the non-frictional regime where the vertical confinement affects the large scale vortices but where the bottom friction effect has a weaker influence compared with the kinetic energy redistribution. Nevertheless, the identification of the four coefficients (k_1, k_2, k_3, k_4) could not be undertaken as, without experiments corresponding to the backward-facing step, no values are available to identify k_1.

The influence of the different dimensionless parameters is now understood and corroborated by the empirical correlation (6.26). In the frictional regime, a dependency such as $L/d \propto S^{-0.6}$ was observed in our experiments, consistently with [Wang et al., 2011] but at odd with [Chu et al., 2004]. The reason for this $L/d \propto S^{-0.6}$ dependency is still to be established. This is the aim of the next section.

6.5 L/d dependency on S in the frictional regime

In the frictional regime, the dependency of L/d on S we obtained is $L/d \propto S^{-0.6}$. This is at odd with the literature where the tendency, proposed from experimental data, is $L/d = a/S$ (where a=0.6 for [Babarutsi et al., 1989] and $a = 0.7$ for [Chu et al., 2004]).

We showed that the dependency of L/d on S must not be considered through considerations on the flow at the scale of the mixing layer, but through a balance (namely of

head) at the whole flow scale. We have shown that the $S^{-0.6}$ dependency in the frictional regime stems from the equilibrium between bottom friction and the streamwise pressure gradient. Nevertheless, in the head balance equation, neither the pressure gradient nor the recirculation length are known *a priori*. Hence, willing to obtain theoretically the $S^{-0.6}$ dependency, a closure law is required. To our knowledge, no such a closure law being available, we use local equations to complete our integral approach at the control volume scale.

6.5.1 Local differential flow equations

The same flow conditions as in the numerical simulations (CHAP.4) are considered here. The water depth h is constant and the upper wall with a slip condition. A depth average of the Navier-Stokes equations is operated, over h. As only the frictional regime is considered, an additional assumption (H6-5) is used. In this regime, the large scale vortices of vertical axis have no influence on the crosswise kinetic energy transfers. Moreover, the dissipation in the free-flow is well estimated by a bottom friction induced head loss. Hence, the effects of both molecular viscosity and turbulence are discarded in the equations. They are considered as accounted for by the bottom friction.

Under this assumption, the depth averaged equations read:

$$\begin{aligned} \frac{\partial \overline{u}}{\partial x}+\frac{\partial \overline{v}}{\partial y} &= 0 \\ \overline{u}\frac{\partial \overline{u}}{\partial x}+\overline{v}\frac{\partial \overline{u}}{\partial y} &= -\frac{1}{\rho}\frac{\partial p}{\partial x}-\frac{\tau_{wx}}{\rho h} \\ \overline{u}\frac{\partial \overline{v}}{\partial x}+\overline{v}\frac{\partial \overline{v}}{\partial y} &= -\frac{1}{\rho}\frac{\partial p}{\partial y}-\frac{\tau_{wy}}{\rho h} \end{aligned} \tag{6.28}$$

In which p is the depth averaged pressure, h is the constant water depth, ρ is the fluid density. $\overline{u}$ and $\overline{v}$ are the depth-average velocity components in the x and y directions, respectively. These equations are different from Saint-Venant's shallow water equations as the water depth is constant and as they involve the pressure. The bed friction term is derived as follows:

$$\begin{aligned} \tau_{wx}/\rho &= \frac{1}{2}c_f\overline{u}\cdot\left|\overline{u}^2+\overline{v}^2\right|^{\frac{1}{2}} \\ \tau_{wy}/\rho &= \frac{1}{2}c_f\overline{v}\cdot\left|\overline{u}^2+\overline{v}^2\right|^{\frac{1}{2}} \end{aligned} \tag{6.29}$$

where c_f is the bottom friction coefficient, assumed to be constant in the whole flow, consistently with the assumption validated in the momentum balance section. It is related to S as $S=\frac{c_f d}{2h}$. The Eq.6.28 thus explicitly contains the bed friction number becomes and

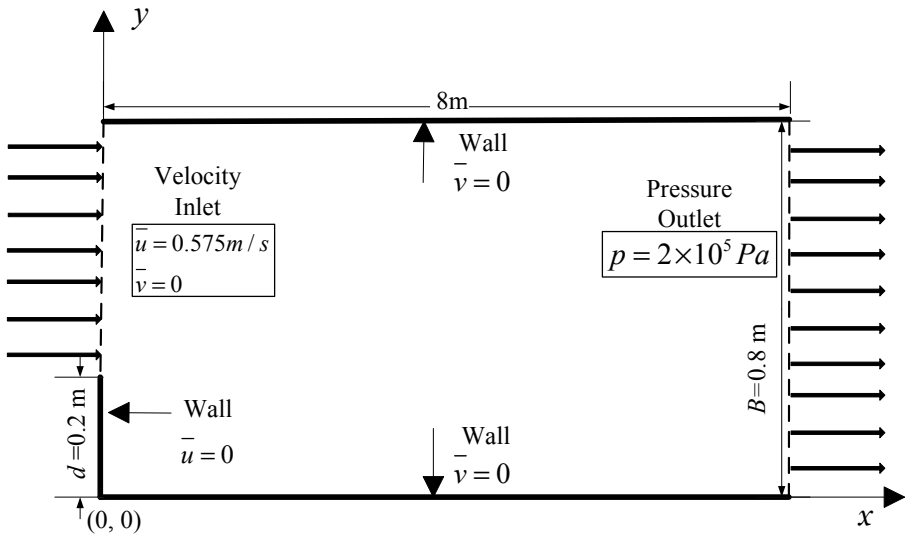

Figure 6.21: Boundary conditions for the numerical simulations

writes:

$$\begin{aligned}
\frac{\partial \overline{u}}{\partial x}+\frac{\partial \overline{v}}{\partial y}&=0\\
\overline{u}\frac{\partial \overline{u}}{\partial x}+\overline{v}\frac{\partial \overline{u}}{\partial y}&=-\frac{1}{\rho}\frac{\partial p}{\partial x}+S\frac{\overline{u}}{d}\sqrt{\overline{u}^2+\overline{v}^2}\\
\overline{u}\frac{\partial \overline{v}}{\partial x}+\overline{v}\frac{\partial \overline{v}}{\partial y}&=-\frac{1}{\rho}\frac{\partial p}{\partial y}+S\frac{\overline{v}}{d}\sqrt{\overline{u}^2+\overline{v}^2}
\end{aligned} \tag{6.30}$$

6.5.2 Solver used for these equations

These equations are solved using the code StarCCM+. They correspond to 2D inviscid Euler's equations, in which two source terms, corresponding to the bed friction, must be added. This is performed simply by using UDF (User Defined Functions).

The computational domain is a rectangle of variable width B and length 8 m, which is thus much longer than the recirculation zone, as seen in FIG.6.22. FIG.6.21 describes the boundary conditions. The left side of the domain corresponds to the expansion. The boundary condition is hence splitted in a wall (length d, lower part) featuring the expansion and in a velocity inlet (upper part). The right boundary condition is a pressure outlet, the pressure being always fixed as $p = 2\times10^5$ Pa in the computations. B is adjustable to obtain the different R_b.

The geometry is very simple and a rectangular mesh is chosen. Cells dimensions are 30mm $\times$7mm. They are refined in the vicinity of the expansion ($0< x <$ 3m and $0< y <$0.3m) with 3mm $\times$3mm cells. The dependency of the results on the mesh was checked as shown in the TAB.6.2.

For solving the Eqs.(6.30), an implicit unsteady solver is chosen, notably as divergence problems were encountered with a steady solver for $S <$0.3. When the steady and

Table 6.2: The dependency of the mesh size

	L	L/d	Difference
Coarse	0.3	0.15	16%
Refine	0.33	0.165	Reference
Very refine	0.33	0.165	0%

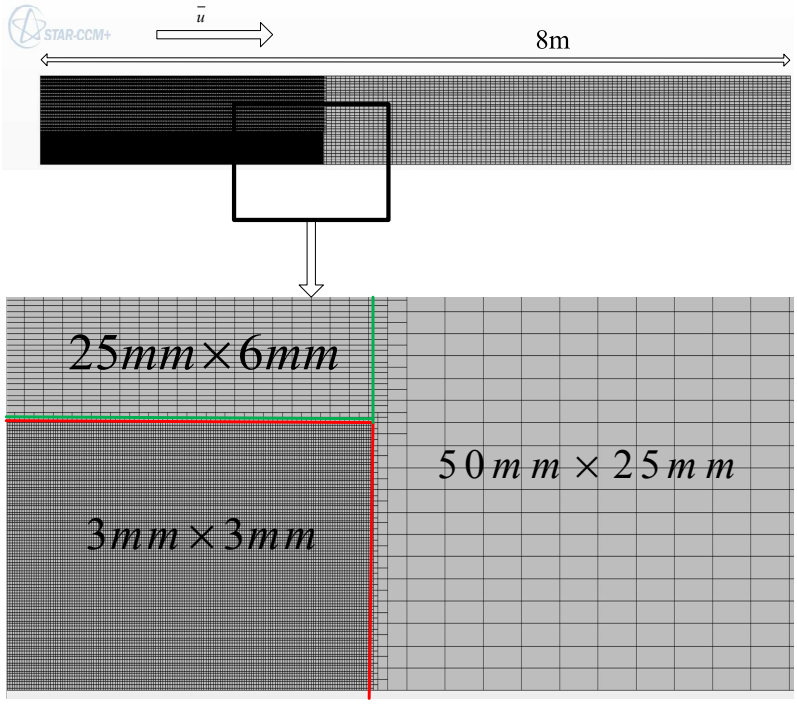

Figure 6.22: 3 different mesh zones. Note: this is the configuration of R_b=0.75.

unsteady computations were possible, they led to the same results. The time step was defined it as $\frac{L_{mesh}}{\overline{u}_0}$=0.01 s. The precision chosen is second order. The maximum inner iteration number is chosen as 100, which ensures a reasonable convergence in each 0.01 s time step. The initial condition includes the inlet velocity ($\overline{u}$ =0.001 m/s) and the pressure (2×10^5 Pa).

The computation convergence is first checked through the residuals. For our configurations, all the residuals of continuity, momentum in x and y direction are in the magnitude of 10^{-6} and keep constant and steady, as in FIG.6.23. The peak is the initial value at the beginning of each time step. The convergence is confirmed by checking the stabilization with time of the streamwise velocity, in different positions near the side wall from x=0 to x=1.8, as in the FIG.6.24(R_b=0.625, S=0.1). We can see that although the residuals experience a plateau at 15 s, the x-velocity at x=0.6 still decreases until 30 s.

Table 6.3: The dependency of inlet velocity. Note: S=0.4, R_b=0.75

Inlet velocity(m/s)	L	L/d	Difference
0.1	0.33	0.165	0%
0.575	0.33	0.165	reference
1	0.33	0.165	0%

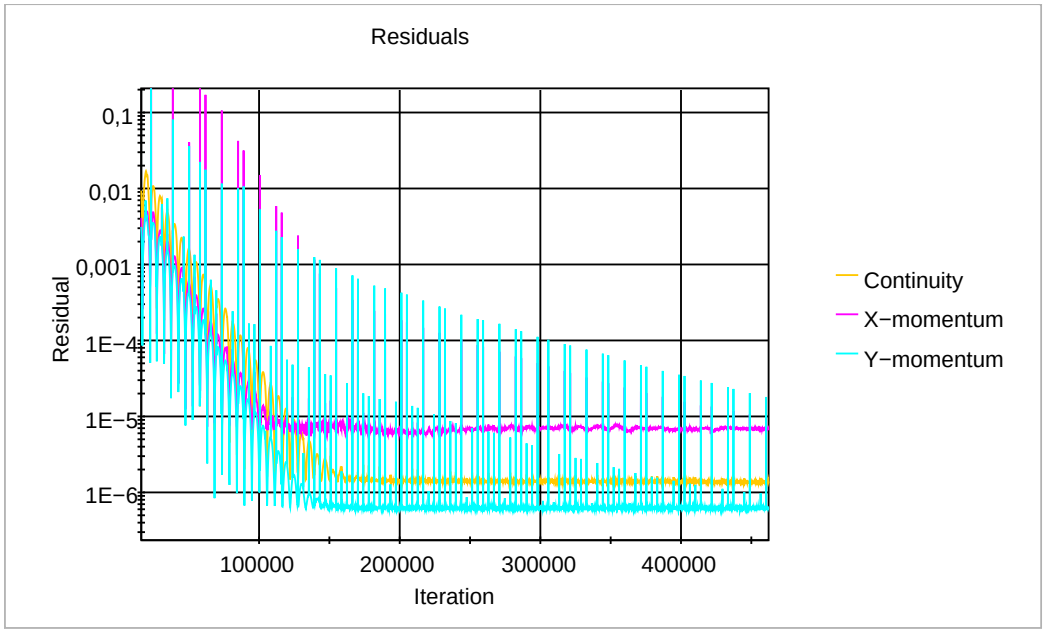

Figure 6.23: 3 residuals with the iteration. Note:Config. R_b=0.625, S=0.1

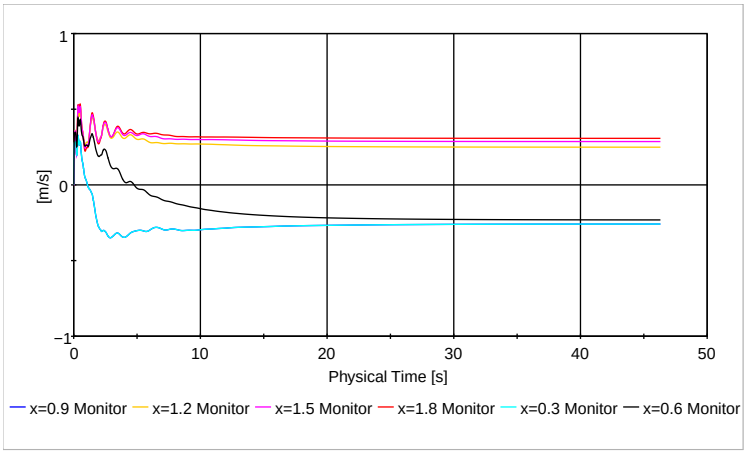

Figure 6.24: Time evolution of the velocity $\overline{u}$ in different positions near the side wall.

6.5.3 Results of the simulation

Figure 6.25 gives an example of velocity fields obtained for different values of S and R_b. Note that no velocity gradient is imposed near the walls due to the inviscid fluid assumption. It is worth noting that, despite Eq.(6.30) does not contain any dissipation term, two main features are retrieved in the velocity field : (i) a momentum transfer from the free-stream to the recirculation, extending the positive x-velocity to the walls and (ii) a "mixing layer", characterized by a strong crosswise velocity gradient, between the free stream and the recirculation. In fact, dissipation is ensured by the two source terms in x and y momentum equations: local bottom friction in the high velocity zone promotes pressure gradient and then crosswise velocities. Crosswise momentum transfers are ensured by this velocity component, with no need of momentum transfers due to turbulence. They explain why both the streamwise velocity profile and the Coriolis kinetic energy coefficient α_2 do not evolve any more with h/d in the frictional regime.

The recirculation length is obtained by locating the zero velocity on the right wall. The results are plotted in FIG.6.26. The three different series, corresponding to different values of R_b, show the same tendency: L/d decreases as S increases, with an asymptotic behaviour $S^{-0.6}$, consistently with the experiments of CHAP.3 and the simulations of CHAP.5. Note that the velocity does not influence the result of L/d as shown in the TAB.6.3, consistently with the dimensional analysis.

The comparison of these numerical results with experimental results is emphasized by FIG.6.27. For the highest S values, the dependency on S fairly matches the experimental one. More, the frictional region where $S > 0.2$, that cannot be investigated during the experiments, was extended to S=1 and keeps a similar tendency. Quantitative agreement is satisfactory for R_b=0.75, more questionable for R_b=0.625 and 0.5. The fact that the influence of R_b is not reproduced by the 2D, simplified equations is not surprising. Indeed, in the frictional regime, as the kinetic energy distribution (or α_2) is almost fixed, R_b acts mainly through the Borda-Carnot recirculation head loss. The more R_b is small, the more this recirculation is huge, which causes the parallel shift observed from one experimental curve to another in the frictional regime. "Borda-Carnot" head losses are mainly caused by the strong velocity gradients and the associated turbulence in the recirculation. With no turbulence model nor molecular viscosity, the 2D simplified equations cannot reproduced such head losses; only the bottom friction and slight difference on α_2 causes the "slight" differences between the three numerical inside the recirculation.

6.6 Chapter conclusion

Previous chapters showed that the relative recirculation length, plotted as a function of the bed friction number S, follows a bell-shaped curve, instead of a plateau followed by a decrease as proposed in the literature. They showed that the bed friction number S is not the only parameter ruling the dimensionless recirculation length, and that the expansion ratio R_b and the relative water depth h/d have comparable influences. This chapter explained these results.

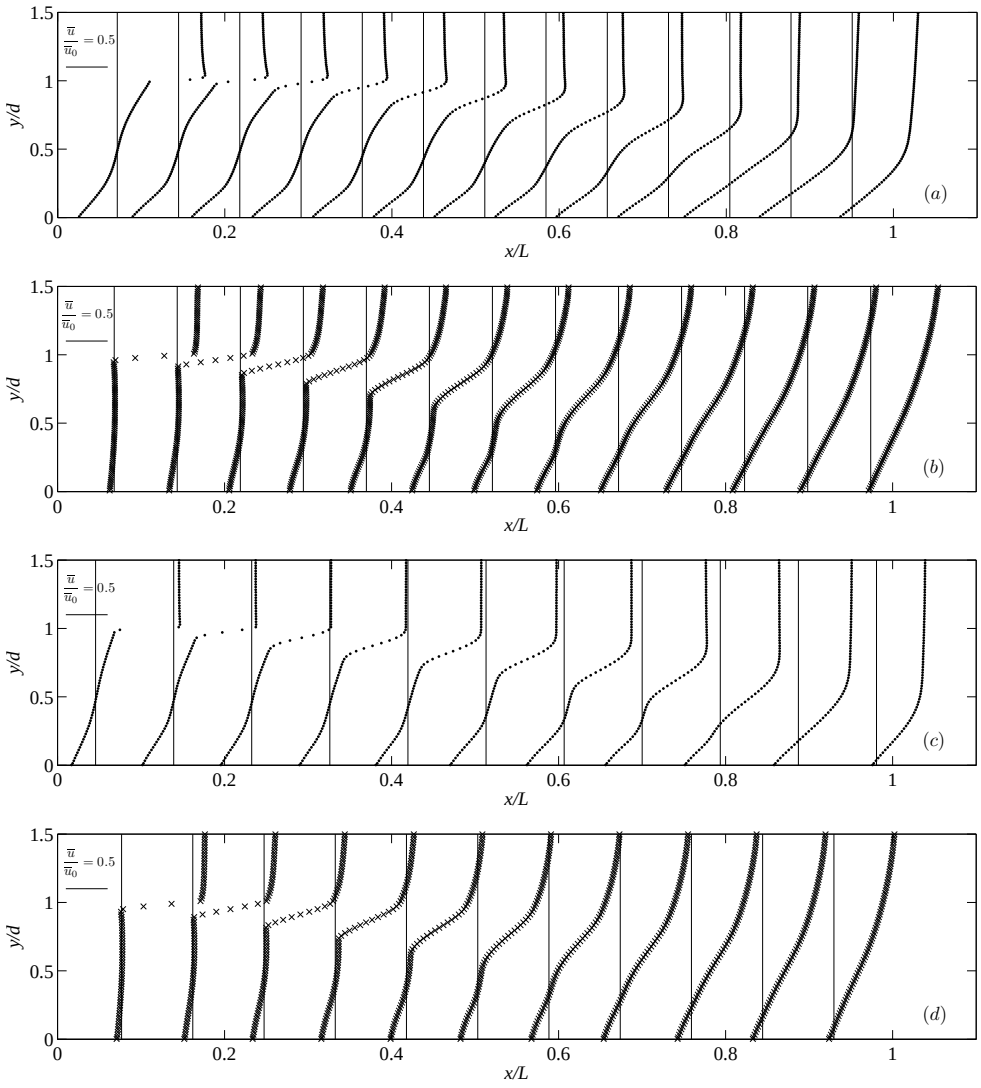

Figure 6.25: Velocity fields obtained from Eq.(6.30)
(a) $R_b = 0.75$; $S = 0.05$
(b) $R_b = 0.75$; $S = 0.8$
(c) $R_b = 0.5$; $S = 0.05$
(d) $R_b = 0.5$; $S = 0.8$

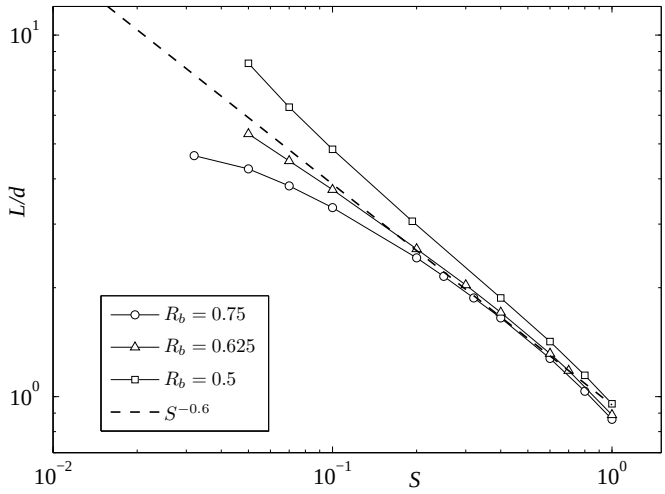

Figure 6.26: Calculated L/d in three different R_b in the friction region where $S > 0.01$.

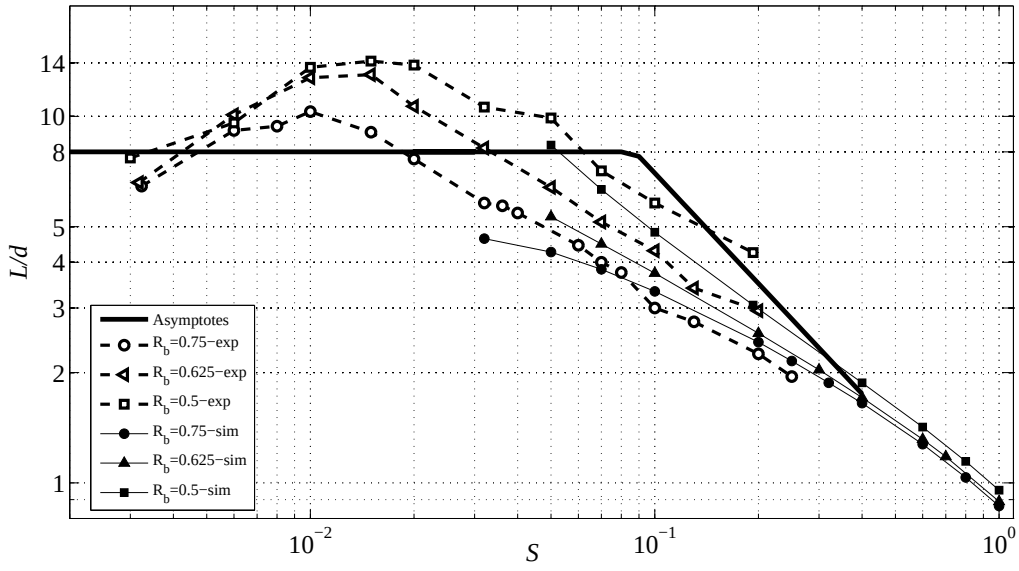

Figure 6.27: Comparison between experiments and the simulations of 2D equation.

Firstly, we confirmed that S has a strong influence, but through the bottom friction, at the whole flow scale, and not through a stabilizing effect on the vortices within the mixing layer. The water depth h/d has a comparable influence. In fact, h/d accounts for the diameter of vortices of vertical axis due to vortex shedding. When this diameter is comparable to the expansion width d, the vortices influence the kinetic energy distribution in the free-stream. This decreases L/d when increasing h/d.

Secondly, in experiments, S and h/d cannot be modified independently, as S is increased notably by decreasing h/d. This causes the obtained, characteristic, bell-shaped curves $L/d=f(S)$. These curves can be described from the left ($S \to 0$) to the right.
$\to$ Very small S values correspond to quite high h/d values: the flow is not affected by the bottom friction and the vortices are not affected by the vertical confinement. The flow is unconfined and non-frictional. L/d is constant and the expansion is in fact a (horizontal) backward facing step.
$\to$ When S increases and so h/d decreases, the bottom friction remains negligible but the vertical confinement limits the size of the large scale vortices in the mixing layer, and thus their influence on the kinetic energy distribution. L/d increases as h/d decreases (corresponding to increasing S values). The regime is confined vertically but non-frictional.
$\to$ When S increases further more, both the bottom friction and the vertical confinement organise the flow. The flow is both frictional and confined. L/d evolves as $S^{-0.6}$ instead of S^{-1} as reported in the literature. This was explained thanks to our local equations: in absence of any turbulent or viscous diffusion, the bottom friction creates crosswise velocities and then momentum/kinetic energy exchanges.

Finally, the expansion ratio R_b adds its influence on the preceding results, as it modifies both the "Borda-Carnot" head loss in the recirculation and the kinetic energy distribution downstream of the recirculation.

Conclusion

In this work, we have investigated a sudden, lateral expansion of an open-channel flow. Such flow expansions could be considered as similar to a horizontal backward facing step, but the vertical confinement effect and the associated bottom friction considerably affect the flow.

Dimensional analysis suggested that two dimensionless parameters are necessary to account for this confinement: the bed friction number S already proposed in the literature but also the dimensionless water depth h/d. A third dimensionless parameter accounts for the intensity of the expansion: the expansion ratio R_b.

The influence of these parameters was studied first through experiments in a 8m long open channel that was modified in order to allow adjusting the expansion ratio on demand. A specific care was devoted to obtain results without backwater influences. Measurements of water depth, velocity and associated turbulent characteristics, characterized the flow. The experimental finding casted doubt on the results available in the literature: instead of a plateau followed by a decrease, our curves $L/d = f(S)$ exhibited a bell-shape with a right branch following a $S^{-0.6}$ decrease.

Numerical simulations, performed using 3D RANS equations with the code Star-CCM+, confirmed these results. More, they allow separating the influence of each parameter, which was not possible in the experiments where the roughness modification is highly difficult. They showed that both the increase of the bed friction number S and the decrease of the relative water depth h/d decrease the recirculation length. This proves that the "bell shape" (for increasing S values) is in fact the result of the double and opposite influence of the increase of S and the decrease of h/d.

To understand these influences, a local approach, at the mixing layer scale was adopted first. Velocities, velocity gradient, turbulent characteristics such as Reynolds stresses, showed that the mixing layer behaves almost as a plane, shallow mixing layer. No connexion was found between the mixing layer stability and the behaviour of the recirculation length. Indeed, the "local" bed friction number derived using the mixing layer width was always below its critical value. And yet, a sudden stop in the mixing layer widening was observed, which is in fact due to a lateral wall effect, accounted for by the "global" bed friction number derived using the expansion width.

Hence, an integral approach was adopted, using balances at the whole flow scale.

1. Momentum balance showed that the shear force exerted along the mixing layer is negligible compared to the other forces.
2. Energy (head) balance explained the influence of the dimensionless parameters.

When the water depth is high enough, the large scale vortices of vertical axis are big enough to take on a share of the kinetic energy distribution throughout flow sections. This results in smooth bumped velocity profiles in the free-stream. This effect disappears when h/d is too small, *i.e.* when the vertical confinement is strong. When the bottom friction is strong enough, corresponding to strong bed friction numbers S, it ensures the kinetic energy redistribution by creating pressure gradients and transverse velocities, as shown by simplified equations. This results in characteristics flat velocity profiles (plug flow) in the free-stream. The expansion ratio participates both to kinetic energy redistribution − adding its influence to the one of h/d − and to the pressure gradients by modifying the head losses in the recirculation − adding its influence to the one of S. The combined effects of S and h/d explain the bell-shape curves obtained experimentally, that could be reproduced by an empirical correlation involving S, h/d and R_b.

To conclude for the present work, the present results bring significant new knowledge compared to the literature. They cast doubts on the two asymptotic regimes considered so far and show that the bed friction number cannot by itself account for the recirculation behaviour. Nevertheless, apart from these two deep re-assessments, our work should be considered as a complement and as a clarification of existing works from McGill University:

↦ Firstly, in spite of everything, we confirmed the influence of the bed friction number on the recirculation zone downstream expansions, though we brought two fundamental new results. Firstly, a distinction is necessary between the local bed friction number $S(x)$ and the global bed friction number S. This distinction is comparable to the one between a flow Reynolds number and a particulate Reynolds number based an obstacle length scale, though S and Re compare different forces in the flow. The (local) bed friction number $S(x)$ is derived using the mixing layer width: its comparison to a critical value tells on the state of the vortices advected in the mixing layer and their stability. It can be associated to the flow Reynolds number derived using the hydraulic diameter, which value tells if the flow is laminar or turbulent, and gives information on the turbulence intensity. The (global) bed friction number S is derived using a fixed length scale, the expansion width, a characteristic of the flow geometry. It informs on the equilibrium between the different forces exerted on the free-stream and on the size of the recirculation. It can be associated to a particulate Reynolds number which values inform on the shape and size of the wake downstream of an obstacle.

↦ Secondly, we have shown that the bed friction number S meaning is to quantify the intensity of the bottom friction and its importance in the momentum and energy balances. To refer to the flow regimes corresponding to small or high S, the names “frictional / non-frictional regimes” used by [Chu et al., 2004] are far more appropriate than the names “shallow / deep water flows” used formerly [Babarutsi et al., 1989].

↦ Indeed, and this is the third point, our work establishes and explains the role of a second dimensionless parameter, the relative water depth h/d. This parameter informs on the intensity of the vertical confinement compelling the large scale vortices to take a diameter proportional to the water depth.

↦ Finally, we showed that a third dimensionless parameters, the expansion ratio R_b, has

an influence comparable to the two former ones, by contributing both to the head losses and the kinetic energy redistribution.

As a brief, according to the values of the dimensionless parameters, the flow follows different regimes:
$\mapsto$ according to the bed friction S values, the flow can be non-frictional (small S) or frictional (large S)
$\mapsto$ according to the relative water depth, the flow can be vertically unconfined (large h/d) or confined (small h/d)

Non-frictional, unconfined expansions are similar to backward-facing steps. Confined, non-frictional flows are leaded by the confinement: the recirculation length increases as h/d decreases. Frictional, confined flows are leaded by the bottom friction: the recirculation length decreases as S increases.

Prospects

In the short term, some aspects of our problem that could not be addressed during the Ph.D could be investigated.
→ Firstly, in all probability, a more accurate empirical correlation can be derived using more sophisticated and appropriate regression techniques, which was not performed due to a lack of time.
→ Then, additional experiments with higher roughness would be interesting, notably to investigate the transition between the different regimes and to determine if an "unconfined and frictional" regime exists. Such experiments are difficult as additional roughness such as bumps in a tear plate (our study) or strings laid transversally on the bottom (literature) create additional eddies which are affected by the vertical confinement: the value of the Darcy coefficient is then difficult to determine and is a function of the water depth. The use of uniform canopies (artificial grass for example) could be a solution.
→ Afterwards, our experiments confirmed the correlation between the vertical confinement (h/d) and the size of large scale vortices of vertical axis but a quantitative correlation, in the form $\Lambda = f(h/d)$-all other paramters being kept equal- would be interesting to understand more deeply the role of these vortices on the momentum/kinetic energy distribution.
→ Finally, technical solutions to avoid backwater effects encountered during the experiments with small expansion ratio must be sought to allow investigating small R_b values and understand more deeply the non-monotonic influence of this parameter.

In the medium or long terms, a more precise characterization of the different cells (gyres) in the recirculation zone could be undertaken. Then, the implications of our results on sediment deposition could be investigated. Otherwise, our results could be used to evaluate the ability of numerical simulation tools. Saint-Venant's shallow water equations are expected to give good results in the frictional regime - provided they reproduce correctly the dissipation in the recirculation zone - but the confined/non−frictional regime is still a challenge due to the role of detached, large vortices. Our experiments could be also a test case for 3D LES or DNS, more complex than the backward facing step, especially if the free-surface reconstruction is undertaken. And yet, it would be interesting to check in the literature concerning the backward facing if a lateral confinement was present in some data, which could explain some discrepancies on the recirculation length. Finally, our results could be applied to the retention or deposition reservoirs [Dufresne et al., 2010], where a central jet separates two recirculation zones which interact with each other.

Appendix A

The influence of the each term in Eq.(6.21) in CHAP.6.

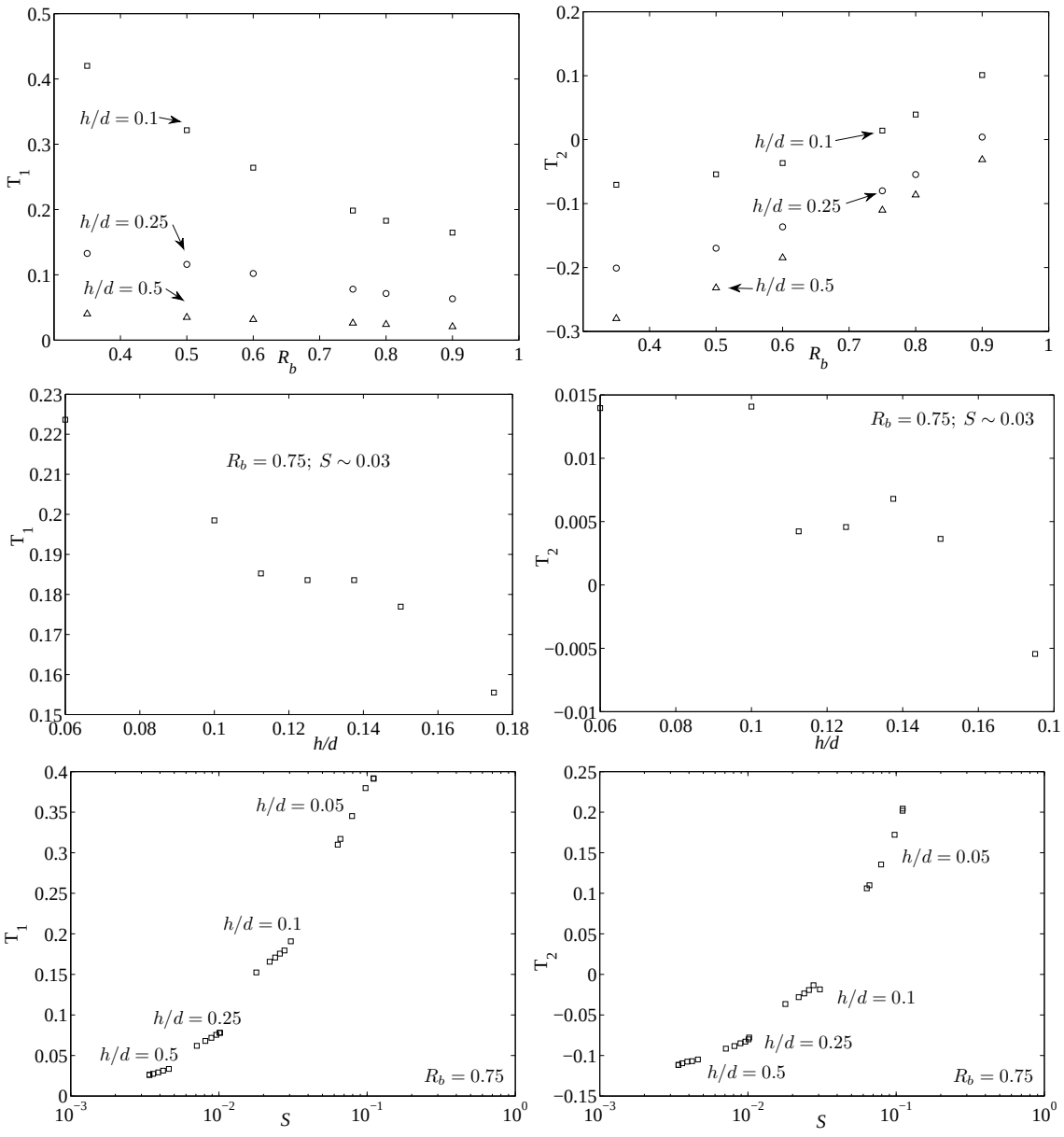

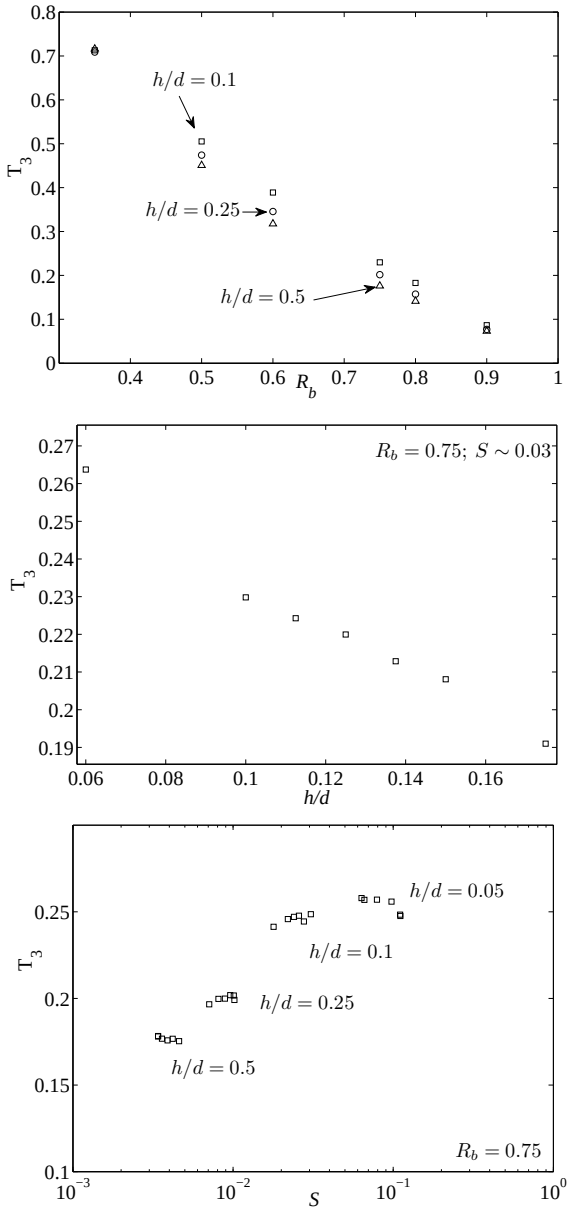

Bibliography

[Abbott and Kline, 1962] Abbott, D. E. and Kline, S. J. (1962). Experimental investigation of subsonic turbulent flow over single and double backward facing steps. *Journal of Fluids Engineering*. 84(3), 317–325.

[Adams and Johnston, 1988] Adams, E. and Johnston, J. (1988). Effects of the separating shear layer on the reattachment flow structure part 1: Pressure and turbulence quantities. *Experiments in Fluids*, 6(6):400–408.

[Alavian and Chu, 1985] Alavian, V. and Chu, V. (1985). Turbulent exchange flow in shallow compound channel. In *Proc., 21st Congress of IAHR Melbourne*, pages 446–451, Melbourne, Australia.

[Altai and Chu, 1997] Altai, W. and Chu, V. (1997). Retention time in recirculating flow. In *Environmental and Coastal Hydraulics: Protecting the Aquatic Habitat*, pages 9–14. ASCE.

[Armaly et al., 1983] Armaly, B. F., Durst, F., Pereira, J. C. F., and Schounung, B. (1983). Experimental and theoretical investigation of backward-facing step flow. *Journal of Fluid Mechanics*, 127:473–496.

[Babarutsi and Chu, 1991] Babarutsi, S. and Chu, V. (1991). Dye-concentration distribution in shallow recirculating flows. *Journal of hydraulic engineering*. 117(5), 643–659.

[Babarutsi et al., 1989] Babarutsi, S., Ganoulis, J., and Chu, V. (1989). Experimental investigation of shallow recirculating flows. *Journal of hydraulic engineering*. 115(7), 906–924.

[Babarutsi et al., 1996] Babarutsi, S., Nassiri, M., and Chu, V. (1996). Computation of shallow recirculating flow dominated by friction. *Journal of hydraulic engineering*, 122(7):367–372.

[Bell and Mehta, 1990] Bell, J. and Mehta, R. (1990). Development of a two-stream mixing layer from tripped and untripped boundary layers. *AIAA J.* 28(12), 2034–2042.

[Biancafiore et al., 2011] Biancafiore, L., Gallaire, F., and Pasquetti, R. (2011). Influence of confinement on a two-dimensional wake. *Journal of Fluid Mechanics*. 688, 297–320.

[Biancofiore, 2014] Biancofiore, L. (2014). Crossover between two-and three-dimensional turbulence in spatial mixing layers. *Journal of Fluid Mechanics*, 745:164–179.

[Bijvelds et al., 1999] Bijvelds, M., Kranenburg, C., and Stelling, G. (1999). 3d numerical simulation of turbulent shallow-water flow in square harbor. *Journal of Hydraulic Engineering*, 125(1):26–31.

[Biswas et al., 2004] Biswas, G., Breuer, M., and Durst, F. (2004). Backward-facing step flows for various expansion ratios at low and moderate reynolds numbers. *Journal of fluids engineering*, 126(3):362–374.

[Blanckaert et al., 2012] Blanckaert, K., Duarte, A., Chen, Q., and Schleiss, A. (2012). Flow processes near smooth and rough (concave) outer banks in curved open channels. *Journal of Geophysical Research: Earth Surface (2003–2012)*, 117(F4).

[Booij and Tukker, 2001] Booij, R. and Tukker, J. (2001). Integral model of shallow mixing layers. *J. Hydraulic Research*. 39(2), 169–179.

[Bradshaw and Wong, 1972] Bradshaw, P. and Wong, F. (1972). The reattachment and relaxation of a turbulent shear layer. *Journal of Fluid Mechanics*, 52(01):113–135.

[Champagne et al., 1976] Champagne, F. H., Pao, Y. H., and Wygnanski, I. J. (1976). On the two-dimensional mixing region. *Journal of Fluid Mechanics*, 74:209–250.

[Chandrsuda and Bradshaw, 1981] Chandrsuda, C. and Bradshaw, P. (1981). Turbulence structure of a reattaching mixing layer. *Journal of Fluid Mechanics*. 110, 171–194.

[Chatelain et al., 2014] Chatelain, M., Han, L., Rivière, N., and Mignot, E. (2014). Physics of shallow recirculation zones downstream lateral expansions. In *Proc., Int. Conference on Fluvial Hydraulics - River Flow 2014*, pages 701–709, Lausanne, Switzerland.

[Chen and Jirka, 1995] Chen, D. and Jirka, G. H. (1995). Experimental study of plane turbulent wakes in a shallow water layer. *Fluid Dynamics Research*, 16(1):11.

[Chen et al., 2004] Chen, J., Jönsson, P., Tamura, M., Gu, Z., Matsushita, B., and Eklundh, L. (2004). A simple method for reconstructing a high-quality ndvi time-series data set based on the savitzky–golay filter. *Remote sensing of Environment*, 91(3):332–344.

[Cheng and Constantinescu, 2014] Cheng, Z. and Constantinescu, G. (2014). Spatial development of a constant-depth shallow mixing layer in a long channel. In *Proc., Int. Conference on Fluvial Hydraulics - River Flow 2014*, pages 155–164, Lausanne, Switzerland.

[Chu and Babarutsi, 1988] Chu, V. and Babarutsi, S. (1988). Confinement and bed friction effects in shallow turbulent mixing layers. *J. Hydraul. Eng.* 114, 1257–1274.

[Chu et al., 2004] Chu, V., Liu, F., and Altai, W. (2004). Friction and confinement effects on a shallow recirculating flow. *Journal of Environmental and Engineering Science*. 3(5),463–475.

[Chu et al., 1983] Chu, V., Wu, J., and Khayat, R. (1983). Stability of turbulent shear flows in shallow channels. In *Proc. of the 20th Congress of IAHR*, pages 128–133, Moscow, Russia.

[Chu et al., 1991] Chu, V., Wu, J., and Khayat, R. (1991). Stability of turbulent shear flows in shallow channels. *Journal of Hydraulic Engineering*. 117(10), 1370–1388.

[Chu and Jirka, 1986] Chu, V. H. and Jirka, G. H. (1986). Surface buoyant jets and plumes. *Encyclopedia of fluid mechanics*,, VI(C6).

[Constantinescu, 2013] Constantinescu, G. (2013). Les of shallow mixing interfaces :a review. *Environmental Fluid Mechanics*. 14(5), 971–996.

[De Serres et al., 1999] De Serres, B., Roy, A. G., Biron, P. M., and Best, J. L. (1999). Three-dimensional structure of flow at a confluence of river channels with discordant beds. *Geomorphology*, 26(4):313–335.

[Dey and Nath, 2009] Dey, S. and Nath, T. K. (2009). Turbulence characteristics in flows subjected to boundary injection and suction. *Journal of engineering mechanics*, 136(7):877–888.

[Dubief and Delcayre, 2000] Dubief, Y. and Delcayre, F. (2000). On coherent-vortex identification in turbulence. *Journal of Turbulence*, page N11.

[Dufresne et al., 2010] Dufresne, M., Dewals, B. J., Erpicum, S., Archambeau, P., and Pirotton, M. (2010). Classification of flow patterns in rectangular shallow reservoirs. *Journal of Hydraulic Research*, 48(2):197–204.

[Fiedler et al., 1991] Fiedler, H., Kim, J.-H., and Köpp, N. (1991). The spatially accelerated mixing layer in a tailored pressure gradient. *European journal of mechanics. B, Fluids*, 10(4):349–376.

[Gibson and Younis, 1983] Gibson, M. and Younis, B. (1983). Turbulence measurements in a developing mixing layer with mild destabilising curvature. *Experiments in Fluids*, 1(1):23–30.

[Goring and Nikora, 2002] Goring, G. and Nikora, V. (2002). Despiking acoustic doppler velocimeter data. *J. Hydraul. Eng.* 128(1), 117-126.

[Han et al., a] Han, L., Mignot, E., and Rivière, N. Shallow mixing layer downstream a sudden expansion. Submitted online 03, October, 2014.

[Han et al., b] Han, L., Mignot, E., and Rivière, N. The turbulent viscosity concept downstream an open-channel sudden expansion. Prepared to be Submitted online.

[Hauet, 2006] Hauet, A. (2006). *Estimation de débit et mesure de vitesse en rivière par Large-Scale Particle Image Velocimetry*. PhD thesis, Institut National Polytechnique de Grenoble-INPG.

[Hertzberg and Ho, 1995] Hertzberg, J. and Ho, C. (1995). Three-dimensional vortex dynamics in a rectangular sudden expansion. *Journal of Fluid Mechanics*. 289, 1-27.

[Hurther and Lemmin, 2001] Hurther, D. and Lemmin, U. (2001). A correction method for turbulence measurements with a 3d acoustic doppler velocity profiler. *Journal of Atmospheric and Oceanic Technology*, 18(3):446–458.

[Jovic and Driver, 1994] Jovic, S. and Driver, D. (1994). Backward-facing step measurement at low reynolds number, reh=5000. *NASA Tech. Mem.* 108807.

[Kasagi and Matsunaga, 1995] Kasagi, N. and Matsunaga, A. (1995). Three-dimensional particle-tracking velocimetry measurement of turbulent statistics and energy budget in a backward facing step flow. *International Journal of Heat and Fluid flow*. 16, 477–485.

[Kitoh et al., 2007] Kitoh, A., Sugawara, K., Yoshikawa, H., and Ota, T. (2007). Expansion ratio effects on three-dimensional separated flow and heat transfer around backward-facing steps. *Journal of Heat Transfer*, 129(9):1141–1155.

[Langendoen et al., 1994] Langendoen, E. J., Kranenburg, C., and Booij, R. (1994). Flow patterns and exchange of matter in tidal harbours. *Journal of Hydraulic Research*, 32(2):259–270.

[Largeau and Moriniere, 2007] Largeau, J. and Moriniere, V. (2007). Wall pressure fluctuations and topology in separated flows over a forward-facing step. *Experiments in fluids*, 42(1):21–40.

[Le et al., 1997] Le, H., Moin, P., and Kim, J. (1997). Direct numerical simulation of turbulent flow over a backward-facing step. *Journal of Fluid Mechanics*, 330:349–374.

[Lesieur, 1997] Lesieur, M. (1997). *Turbulence in Fluids*. Kluwer Academic, Norwell, U.S.A.

[Li and Djilali, 1995] Li, X. and Djilali, N. (1995). On the scaling of separation bubbles. *JSME Int. J. Series B.* 38(4), 541–548.

[Loucks and Wallace, 2012] Loucks, R. B. and Wallace, J. M. (2012). Velocity and velocity gradient based properties of a turbulent plane mixing layer. *Journal of Fluid Mechanics*, 699:280–319.

[Lyn and Rodi, 1994] Lyn, D. and Rodi, W. (1994). The flapping shear layer formed by flow separation from the forward corner of a square cylinder. *Journal of Fluid Mechanics*. 267, 353–376.

[Margolis and Lumley, 1965] Margolis, D. and Lumley, J. L. (1965). Curved turbulent mixing layer. *Physics of Fluids (1958-1988)*, 8(10).

[McLelland and Nicholas, 2000] McLelland, S. J. and Nicholas, A. P. (2000). A new method for evaluating errors in high-frequency adv measurements. *Hydrological Processes*, 14(2):351–366.

[Mignot et al., 2009] Mignot, E., Barthelemy, E., and Hurther, D. (2009). Double-averaging analysis and local flow characterization of near-bed turbulence in gravel-bed channel flows. *Journal of Fluid Mechanics*, 618:279–303.

[Mignot et al., 2014a] Mignot, E., Doppler, D., Rivière, N., Vinkovic, I., Gence, J., and Simoens, S. (2014a). Analysis of flow separation using a local frame axis: Application to the open-channel bifurcation. *Journal of Hydraulic Engineering*. 140(3), 280–290.

[Mignot et al., 2011] Mignot, E., Hurther, D., and Barthelemy, E. (2011). Double-averaging turbulence characteristics in flows over a gravel bed. *Journal of Hydraulic Research*, 49(5):703–704.

[Mignot et al., 2014b] Mignot, E., Vinkovic, I., Doppler, D., and Rivière, N. (2014b). Mixing layer in open-channel junction flows. *Environmental Fluid Mechanics*. 14(5), 1027–1041.

[Nassiri and Babarutsi, 1997] Nassiri, M. and Babarutsi, S. (1997). Computation of dye concentration in shallow recirculating flow. *Journal of Hydraulic Engineering*, 123(9):793–805.

[Nezu and Nakagawa, 1993] Nezu, I. and Nakagawa, H. (1993). Turbulence in open-channel flows. In *IAHR monographs series*, Balkema, Rotterdam.

[Nikora and Goring, 1998] Nikora, V. I. and Goring, D. G. (1998). Adv measurements of turbulence: Can we improve their interpretation? *Journal of Hydraulic Engineering*, 124(6):630–634.

[Noh and Woodward, 1976] Noh, W. and Woodward, P. (1976). Slic (simple line interface calculation). In van de Vooren, A. and Zandbergen, P., editors, *Proceedings of the Fifth International Conference on Numerical Methods in Fluid Dynamics June 28-July 2, 1976 Twente University, Enschede*, volume 59 of *Lecture Notes in Physics*, pages 330–340. Springer Berlin Heidelberg.

[Ouellet et al., 1986] Ouellet, Y., Dupuis, P., and Soulaimani, A. (1986). Modélisation d'un éoulement tourbillonnaire en régime permanent. *Canadian Journal of Civil Engineering*, 13(3):310–318.

[Ouillon and Dartus, 1997] Ouillon, S. and Dartus, D. (1997). Three-dimensional computation of flow around groyne. *Journal of hydraulic Engineering*, 123(11):962–970.

[Peltier, 2011] Peltier, Y. (2011). *Physical modelling of overbank flows with a groyne set on the floodplain*. Theses, Université Claude Bernard - Lyon I.

[Peltier et al., 2014] Peltier, Y., Erpicum, S., Archambeau, P., Pirotton, M., and Dewals, B. (2014). Meandering jets in shallow rectangular reservoirs: Pod analysis and identification of coherent structures. *Experiments in Fluids*, 55(6):1–16.

[Peltier et al., 2013] Peltier, Y., Rivière, N., Proust, S., Mignot, E., Paquier, A., and Shiono, K. (2013). Estimation of the error on the mean velocity and on the reynolds stress due to a misoriented adv probe in the horizontal plane: Case of experiments in a compound open-channel. *Flow Measurement and Instrumentation*, 34(0):34 – 41.

[Plesniak et al., 1996] Plesniak, M. W., Mehta, R. D., and Johnston, J. P. (1996). Curved two-stream turbulent mixing layers revisited. *Experimental thermal and fluid science*, 13(3):190–205.

[Pope, 2008] Pope, S. (2008). *Turbulence flows*. Cambridge University Press, Cambridge, United Kingdom.

[Ramamurthy et al., 1991] Ramamurthy, A., Balachandar, R., and Ram, H. G. (1991). Some characteristics of flow past backward facing steps including cavitation effects. *Journal of fluids engineering*, 113(2):278–284.

[Raupach et al., 1996] Raupach, M., Finnigan, J., and Brunei, Y. (1996). Coherent eddies and turbulence in vegetation canopies: The mixing-layer analogy. *Boundary-Layer Meteorology*, 78(3-4):351–382.

[Rhoads and Sukhodolov, 2008] Rhoads, B. L. and Sukhodolov, A. N. (2008). Lateral momentum flux and the spatial evolution of flow within a confluence mixing interface. *Water Resources Research*, 44(8):n/a–n/a.

[Rivière et al., 2008] Rivière, N., Badin, B., Bomchil, Y., and Proust, S. (2008). Recirculation zones downstream open channel expansions. In *Proc. of the 4th international conference on fluvial hydraulics-RiverFlow 2008*, Izmir, Turkey.

[Riviere et al., 2011] Riviere, N., Gautier, S., and Mignot, E. (2011). Experimental characterization of flow reattachment downstream open channel expansions. In *Proceedings of the 34th World Congress of the International Association for Hydro- Environment Research and Engineering*, pages 3745–3752, Brisbane, Australia.

[Rouse and Appel, 1965] Rouse, H. and Appel, D. W. (1965). *Advanced Mechanics of Fluids*. Wiley, New York, U.S.A., print edition.

[Ruderich and Fernholz, 1986] Ruderich, R. and Fernholz, H. H. (1986). An experimental investigation of a turbulent shear flow with separation, reverse flow, and reattachment. *Journal of Fluid Mechanics*, 163:283–322.

[Schmitt, 2007] Schmitt, F. G. (2007). About boussinesq's turbulent viscosity hypothesis: historical remarks and a direct evaluation of its validity. *Comptes Rendus Mécanique*, 335(9):617–627.

[Sherry et al., 2010] Sherry, M., Lo Jacono, D., and Sheridan, J. (2010). An experimental investigation of the recirculation zone formed downstream of a forward facing step. *Journal of Wind Engineering and Industrial Aerodynamics*, 98(12):888–894.

[Simoens et al., 2007] Simoens, S., Ayrault, M., and Wallace, J. M. (2007). The flow across a street canyon of variable width-part 1: kinematic description. *Atmospheric Environment*, 41(39):9002–9017.

[Strom and Papanicolaou, 2007] Strom, K. B. and Papanicolaou, A. N. (2007). Adv measurements around a cluster microform in a shallow mountain stream. *Journal of Hydraulic Engineering*, 133(12):1379–1389.

[Sukhodolov et al., 2010] Sukhodolov, A., Schnauder, I., and Uijttewaal, W. (2010). Dynamics of shallow lateral shear layers: experimental study in a river with a sandy bed. *Water Resour. Res.* 46, W11519.

[Talstra, 2011] Talstra, H. (2011). *Large-scale turbulence structures in shallow separating flows*. PhD thesis, Technische Universiteit Delft, Delft, Netherlands.

[Tennekes and Lumley, 1972] Tennekes, H. and Lumley, J. (1972). *A First Course in Turbulence*. Cambridge University Press, Massachusetts.

[Tihon et al., 2001] Tihon, J., Legrand, J., and Legentilhomme, P. (2001). Near-wall investigation of backward-facing step flows. *Experiments in fluids*, 31(5):484–493.

[Toschi et al., 2006] Toschi, F., Kobayashi, H., Piomelli, U., and Iaccarino, G. (2006). Backward-facing step calculations using the shear improved smagorinsky model. In *Proceedings of the Summer Program*, page 87. Citeseer.

[Uijttewaal and Booij, 2000] Uijttewaal, W. and Booij, R. (2000). Effects of shallowness on the development of free-surface mixing layers. *Physics of Fluids*. 12(2), 392–402.

[Uijttewaal and Tukker, 1998] Uijttewaal, W. S. J. and Tukker, J. (1998). Development of quasi two-dimensional structures in a shallow free-surface mixing layer. *Experiments in Fluids*, 24(3):192–200.

[Van Prooijen and Uijttewaal, 2002] Van Prooijen, B. and Uijttewaal, W. (2002). A linear approach for the evolution of coherent structures in shallow mixing layers. *Physics of Fluids*. 4(12), 4105–4114.

[Voulgaris and Trowbridget, 1997] Voulgaris, G. and Trowbridget, J. (1997). Evaluation of the acoustic doppler velocimeter (adv) for turbulence measurements. *J. Atmos. Oceanic Technol.* 15, 272–289.

[Wang et al., 2011] Wang, G., Chen, D., Wang, X., and Xia, J. (2011). Effect of shallowness on sediment deposition in recirculation zones. *Journal of Hydraulic Engineering*. 137(9), 976–985.

[Weitbrecht et al., 2008] Weitbrecht, V., Socolofsky, S. A., and Jirka, G. H. (2008). Experiments on mass exchange between groin fields and main stream in rivers. *Journal of Hydraulic Engineering*, 134(2):173–183.

[Welch, 1967] Welch, P. D. (1967). The use of fast fourier transform for the estimation of power spectra: a method based on time averaging over short, modified periodograms. *IEEE Transactions on audio and electroacoustics*, 15(2):70–73.

[White and Nepf, 2007] White, B. and Nepf, H. (2007). Shear instability and coherent structures in shallow flow adjacent to a porous layer. *Journal of Fluid Mechanics*. 593, 1–32.

[Winterwerp, 2005] Winterwerp, J. (2005). Reducing harbor siltation. i: Methodology. *Journal of Waterway, Port, Coastal, and Ocean Engineering*, 131(6):258–266.

[Wolanski et al., 1984] Wolanski, E., Imberger, J., and Heron, M. L. (1984). Island wakes in shallow coastal waters. *Journal of Geophysical Research: Oceans*, 89(C6):10553–10569.

[Wu et al., 2013] Wu, Y., Ren, H., and Tang, H. (2013). Turbulent flow over a rough backward-facing step. *International Journal of Heat and Fluid Flow*, 44:155–169.

[Wygnanski and Fiedler, 1970] Wygnanski, I. and Fiedler, H. (1970). The two-dimensional mixing region. *Journal of Fluid Mechanics*. 41(2), 327–361.